



**HAL**  
open science

# Trapping and Reliability investigations in GaN-based HEMTs

Agostino Benvegnù

► **To cite this version:**

Agostino Benvegnù. Trapping and Reliability investigations in GaN-based HEMTs. Electronics. Université de Limoges; Università degli studi (Padoue, Italie), 2016. English. NNT : 2016LIMO0064 . tel-01643704

**HAL Id: tel-01643704**

**<https://theses.hal.science/tel-01643704>**

Submitted on 21 Nov 2017

**HAL** is a multi-disciplinary open access archive for the deposit and dissemination of scientific research documents, whether they are published or not. The documents may come from teaching and research institutions in France or abroad, or from public or private research centers.

L'archive ouverte pluridisciplinaire **HAL**, est destinée au dépôt et à la diffusion de documents scientifiques de niveau recherche, publiés ou non, émanant des établissements d'enseignement et de recherche français ou étrangers, des laboratoires publics ou privés.



Université  
de Limoges

ECOLE DOCTORALE SCIENCES ET INGÉNIERIE POUR L'INFORMATION

Discipline: Électronique des Hautes Fréquences, Photonique et Systèmes



UNIVERSITÀ  
DEGLI STUDI  
DI PADOVA

SCUOLA DI DOTTORATO DI RICERCA IN: Ingegneria dell'Informazione

INDIRIZZO: Scienza e Tecnologia dell'Informazione

CICLO XXVIII

Submitted in fulfilment of the requirements for  
the *Degree of Doctor of Philosophy*

# **Trapping and Reliability Investigations in GaN-based HEMTs**

by

**Agostino Benvegnù**

Advisors: Denis Barataud, Enrico Zanoni and Raymond Quéré

Dissertation committee:

Olivier Latry, Assistant professor (HDR) at University of Rouen, Referee

Nathalie Malbert, Professor at University of Bordeaux 1, Referee

Dominique Baillargeat, Professor at University of Limoges, XLIM, President

Denis Barataud, Professor at University of Limoges, XLIM, Examiner

Gaudenzio Meneghesso, Professor at University of Padova, Examiner

Raymond Quéré, Professor at University of Limoges, XLIM, Examiner

Jean-Luc Roux, Engineer at CNES Toulouse, Examiner

Olivier Jardel, Engineer at Thalès Alenia Space Toulouse, Invite

Didier Floriot, Engineer at UMS Semiconductors, Invite

Jean-Luc Muraro, Engineer at Thalès Alenia Space Toulouse, Invite

September 28<sup>th</sup>, 2016



# Copyright

This work is licensed under the Contract:

"Attribution-NonCommercial-NoDerivs 3.0 Unported (CC BY-NC-ND 3.0)"

Available online: <http://creativecommons.org/licenses/by-nc-nd/3.0/>







*To my family & friends*

*« A winner is a dreamer who never gives up! »*

*Nelson Mandela*



## **Acknowledgements**

I'd like to begin by thanking my supervisors Professor Denis Barataud and Professor Raymond Quéré from the University of Limoges and Professor Enrico Zanoni from the University of Padova for their advice and continuing support throughout my Ph.D. thesis.

In addition, to the director of the XLIM, Professor Dominique Baillargeat, for welcoming me to the XLIM Research Institute and presiding over the dissertation committee. I'd like to thank the jury members, Professor Olivier Latry, Professor Nathalie Malbert, Professor Gaudenzio Meneghesso, Jean-Luc Roux, Dr. Jean-Luc Muraro, Dr. Olivier Jardel and Dr. Didier Floriot, for reviewing this dissertation.

Having worked on my Ph.D. at both the University of Limoges and Padova and Thales Alenia Space, I got the chance to meet a lot of people who guided me, supported me and inspired me. I would like to express my sincere gratitude to them because the success of this work would not have been the same without them. I would like to thank all the Ph.D. students of Limoges, Arnaud, Julien, Pierre, Karthik, Clement, Lotfi, Nicolas, Paul, Johann and Yoann, for introducing me to the RF world and for being my family both in the laboratory and also during daily life. I am extremely grateful to my department secretary Marie Claude Lerouge for her patience and her kindness.

And many thanks to all my colleagues in Brive, Anthony, Frederique, Romain, Amed and Karim, for having hosted me and for the good times we spent together. Special thanks to Dr. Sylvain Laurant for supporting me and for the long days spent performing LSNA measurements.

A sincere thanks to the microelectronic group of University of Padova, Isabella, Carlo, Riccardo, Antonio, Stefano and Davide, for introducing me to the HEMT world and for always being ready to help me. Special thanks go to Professor Matteo Meneghini for his willingness and for the many discussions on the physics of electronic semiconductors.

I'd also like to thank Dr. Dominique Langlez for welcoming me to the LEMMIC group at Thales Alenia Space. I would like to thank Dr. Jean-Luc Muraro for his involvement and for always setting a good mood.

I am also thankful to my roommates, Claudio, Thomas and Alexander, who made the first floor of 19th Boulevard Gambetta a very fun place and for the organization of many pizza parties in our living room.

And many thanks to my family, Mum, Dad and Simone, for giving me the opportunity to be here.

And last, but certainly not least, I'd like to thank Francesca for supporting this long-distance relationship and for always being there for me.

# Table of contents

<b>1</b>	<b>Background</b> .....	<b>1</b>
1.1	Introduction .....	1
1.2	GaN based semiconductors.....	1
1.2.1	Two-dimensional electron gas.....	3
1.3	GaN technology for satellite equipment .....	6
1.4	GH50-10 process.....	7
1.5	Conclusion.....	8
<b>2</b>	<b>Investigation of trapping phenomena</b> .....	<b>9</b>
2.1	Introduction .....	9
2.2	Basics of trapping phenomena .....	9
2.3	Trapping characterization methodology .....	13
2.3.1	Pulsed I/V characterization.....	13
2.3.2	Drain current transient spectroscopy .....	23
2.3.3	Nonlinear microwave drain current transient spectroscopy .....	31
2.3.4	Low-frequency dispersion measurements .....	57
2.4	Identification of deep-levels .....	61
2.5	Conclusions .....	64
<b>3</b>	<b>Nonlinear Electro-Thermal model of AlGa<sub>N</sub>/Ga<sub>N</sub> HEMT</b> .....	<b>68</b>
3.1	Introduction .....	68
3.2	Modeling methods for HEMTs.....	68
3.3	Modeling methodology .....	70
3.4	Device modeling process .....	71
3.4.1	Small-signal model.....	71
3.4.2	Nonlinear model .....	78
3.4.3	Nonlinear trapping and thermal current source model .....	84
3.4.4	Model validation.....	96
3.5	Conclusion.....	99
<b>4</b>	<b>Time-domain large-signal reliability investigation of AlGa<sub>N</sub>/Ga<sub>N</sub> HEMT</b> .....	<b>101</b>
4.1	Introduction .....	101
4.2	Reliability Testing.....	102

4.2.1	Analysis of reliability .....	102
4.2.2	Accelerated life test .....	103
4.2.3	Physical failure mechanisms .....	106
<b>4.3</b>	<b>Time-domain continuous RF waveform monitoring under stress overdrive condition.....</b>	<b>110</b>
4.3.1	Time-domain continuous RF waveform stress set-up .....	111
4.3.2	Reliability test procedure.....	114
4.3.3	Time-domain stress test results .....	118
<b>4.4</b>	<b>Conclusion .....</b>	<b>134</b>
<b>5</b>	<b>Conclusion .....</b>	<b>136</b>
<b>6</b>	<b>Publications .....</b>	<b>139</b>
<b>7</b>	<b>References .....</b>	<b>141</b>

## **Thesis overview**

The excellent physical properties of Gallium Nitride (GaN), Aluminium Nitride (AlN) and related alloys (AlGaN) make the solid-state electronic devices based on an AlGaN/GaN heterojunction the most interesting candidate for the next generation of power electronics, in particular for space applications. Unfortunately, this young technology suffers from reliability difficulties and memory effects (i.e. charge-trapping phenomena). In the last decades, much effort has been devoted to investigating the reliability and trapping effects of this technology. These investigations have identified several physical and technological challenges and have contributed to improve the maturity of the technology. The most significant effort to develop this technology for space applications was made by the American and European space agencies: the national aeronautics and space administration (NASA) and the European space agency (ESA). In particular, in Europe, this research was initially funded through national agencies, innovative component development activities at ESA and EU defense initiatives, such as the Korrigan, and great<sup>2</sup> (GaN Reliability Enhancement and Technology Transfer Initiative) projects [1], [2]. An important step towards using the European GaN technology in satellites has been done by ESA with the first in-orbit demonstration of an X-band transmitter using GaN monolithic microwave integrated circuit (MMIC) technology on board the PROBA-V mission. This transmitter has now been successfully operating in space for image and data transmission for more than 24 months, as shown in [2]. Among the industries supported by ESA and French space agency (centre national d'études spatiales (CNES)), Thales Alenia Space in Toulouse has currently developed a new generation of RF Front-End chain in GaN (MMIC) technology.

In this context, the present joint Ph.D. collaboration between the XLIM laboratory and the University of Padova was developed in order to make some improvements in reliability measurements and trapping characterization.

This work was supported on the one hand by the Thales Alenia Space in Toulouse through the "DEFIS-RF" ANR project (ANR-13-CHIN-0003) under the supervision of Dr. Jean-Luc Muraro and on the other hand by the French space agency (CNES) through contract 131223/00 under the supervision of Jean-Luc Roux. This joint Ph.D. collaboration has benefited from two different environments based on both the



university and industrial approaches. Moreover, this Ph.D. research has brought together the knowledge and skills of distinguished universities, namely, the University of Padova and the University of Limoges, the former on reliability and the latter on RF device modeling.

The main topics of this Ph.D. research concerned the characterization and the modeling of charge-trapping dynamic dispersion and reliability studies with an advanced time-domain methodology of GaN-based high electron mobility transistors.

Chapter 1 includes a brief introduction to the properties and capabilities of GaN technology and its promising applications in the space world.

In Chapter 2, a new investigation of charge-trapping is discussed from DC to radio-frequency operation mode, based on pulsed I/V measurements, DC and RF drain current measurements, and low-frequency dispersion measurements. An extensive analysis of the main charge-trapping mechanisms and the related deep levels identified in state-of-art GaN-based high electron mobility transistors are presented.

In Chapter 3, the determination and validation of a nonlinear electro-thermal AlGaN/GaN model for CAD application is described with a new additive thermal trap model to take into account the nonlinear dynamic behavior of trap states and their associated temperature variation.

In Chapter 4, an advanced time-domain methodology is introduced to investigate device reliability and determine its safe operating area for different overdrive conditions and different output load impedance conditions.

Lastly, the key points and the novel experimental results of this Ph.D. research are presented.



# 1 Background

## 1.1 Introduction

In this first part of this chapter a brief overview of the properties and capabilities of the more promising wide band-gap semiconductors based on AlGaN/GaN high-electron mobility transistors for the gamut of power electronics applications, from power conditioning to microwaves, is presented. In the second part, the potential usage of this technology in satellite equipment for telecommunications, navigation, Earth observation and science missions is illustrated.

## 1.2 GaN based semiconductors

The greatest scientific and technological revolution of the last century has no doubt changed the world. Nowadays, the need of communication and data processing are fulfilled thanks to the field effect transistor (FET) introduced in the beginning of 20<sup>th</sup> century. Its principle was filed by Julius Lilienfeld in 1925. After the Second World War, at AT&T Bell Labs, William Shockley at the head of a research group decided to attempt the building of a triode (transistor's precursor) like solid-state electronic device.

Later, the history of solid-state electronic devices was marked by the introduction of the high-electron mobility transistor (HEMT). The HEMT was first demonstrated by *Mimura et al.* at Fujitsu Labs in 1980 [3]. The invention of the HEMT represented the latest triumph of band-gap engineering and molecular beam epitaxy. Moreover, the HEMT in III-V compound semiconductors was based on the concept of modulation doping first demonstrated by *Dingle et al.* at Bell Labs in 1978 [4]. A modulation-doped structure creates a two-dimensional electron gas at the interface between two semiconductors of different band-gaps, which is the principle of a heterostructure device.

Today, RF and microwave applications are satisfied by different mature semiconductor technologies, such as Si, GaAs, and other III-V semiconductors. However, the wide band-gap semiconductors, in particular those based on GaN, are the most promising technologies for the next generation applications in communications, signal processing, electrical power management and imaging. Its performance has attracted attention as a highly promising

material for electronic applications because of its excellent transport properties, high critical electric field, robustness and thermal stability when compared to GaAs.

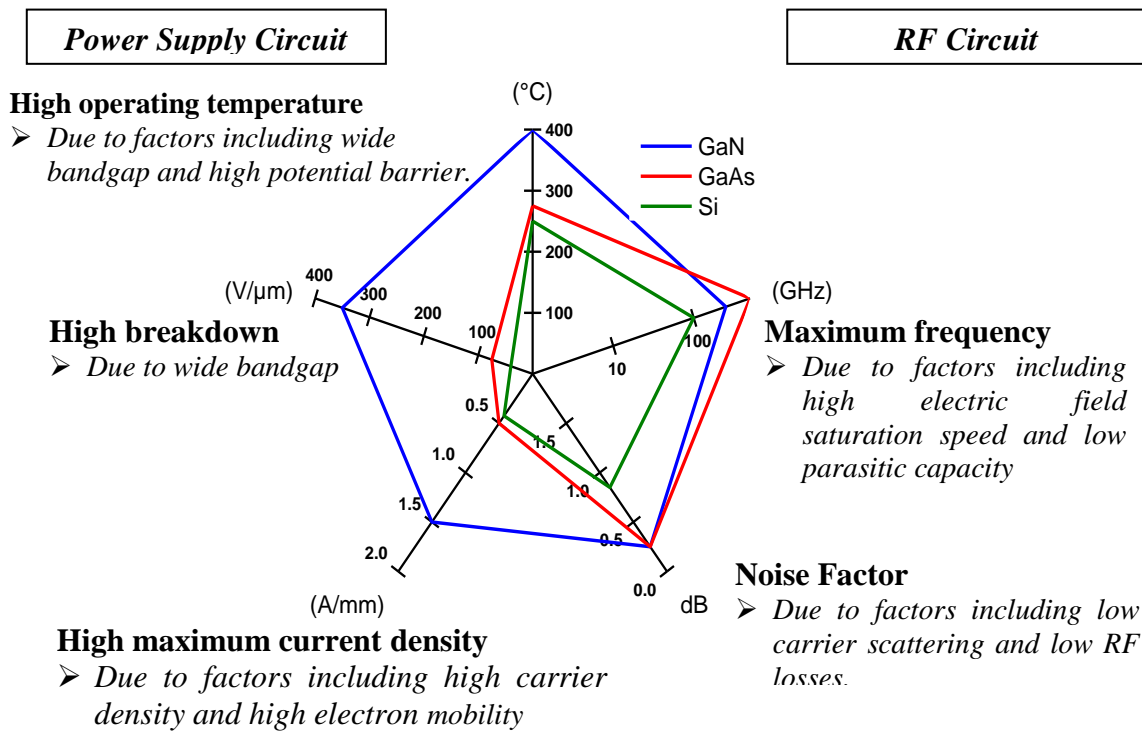


**Figure 1-1: Comparison of GaN with Si and GaAs semiconductors [5].**

TABLE 1

COMPARISON OF THERMAL AND ELECTRONIC PROPERTIES FOR DIFFERENT SEMICONDUCTORS AND HETEROSTRUCTURES [6]

Characteristic	Silicon	Gallium Arsenide	Indium Phosphide	Silicon Carbide	Gallium Nitride
Bandgap (eV)	1.1	1.42	1.35	3.25	3.49
Electron Mobility at 300 °K (cm <sup>2</sup> /Vs)	1500	8500	5400	700	1000-2000
Saturated Electron Velocity (x10 <sup>7</sup> cm/s)	1	1.3	1	2	2.5
Critical Breakdown Field (MV/cm)	0.3	0.4	0.5	3	3.3
Thermal Conductivity (W/cm °K)	1.5	0.5	0.7	4.5	>1.5
Relative Dielectric Constant $\epsilon_r$	11.8	12.8	12.5	10	9

The GaN-based devices currently have advantages for high-cost microwave applications where device performance is more critical. When compared with other highly commercialized

semiconductors such as Si and GaAs, GaN-based semiconductors have five key advantages: high operating temperatures, high critical electric field, high current densities, high-speed switching, and low on-resistances. A schematic comparison of these five figures of merit is given in Figure 1-1. These different materials can be compared using the Johnson figure of merit (JFoM), which gives a power-frequency limit based on material properties:

$$JFoM = \frac{v_{sat} E_{BD}}{2\pi} \quad (1-1)$$

where  $v_{sat}$  is the saturation velocity and  $E_{BD}$  is the electric field at which impact ionization initiates breakdown. The GaN JFoM is approximately 27.5 times higher than Si and more than 10 times better than GaAs [7]. Si and GaAs materials are expected to be replaced by wide-band gap GaN material due to the increase of power and frequency request for future communication applications. The GaN material demonstrates promising superior performances over its competitors as shown in Table 1, due to piezoelectric and spontaneous polarization induced effects, the two-dimensional electron gas (2DEG) sheet carrier concentration ( $n_s$ ) of AlGaN/GaN structure is very high (experimental values up to  $10^{13} \text{ cm}^{-2}$ ) in comparison with III-V semiconductors. Furthermore, an exciting prospect in the near future is the monolithic integration of GaN HEMT and III-V CMOS devices to give a new lease on life to Moore's Law. The lack of bulk GaN source material has to the need for GaN growth on mismatched substrates such as Si, SiC and sapphire. Moreover, the development of GaN for RF electronics was significantly aided by the intense development of light-emitting diodes (LEDs).

### 1.2.1 Two-dimensional electron gas

As described in the previous section, the unique feature of AlGaN/GaN HEMTs is 2DEG channel formation. The sheet carrier density and the confinement of the two-dimensional electron gas located close to the interface of undoped and doped AlGaN/GaN heterostructures is due to the bending of the bands. The accumulation of attracted mobile carriers (electrons in the case of a positive sheet charge  $\sigma$ ) in this two-dimensional electron gas is confined in a quantum well along the heterojunction and relies both on piezoelectric and spontaneous polarization induced effects, as shown in Figure 1-2. The piezoelectric effects can exert a substantial influence on the concentration and distribution of free carriers in strained group-III nitride heterostructures. Indeed, in AlGaN/GaN based transistor structures, the piezoelectric

polarization of the strained AlGa<sub>N</sub> barrier layer is more than five times that of AlGaAs/GaAs structures, which corresponds to an increasing current density. The very high mobility of confined electrons in the quantum well and high saturation velocity associated to GaN make up the key feature of AlGa<sub>N</sub>/GaN HEMTs.

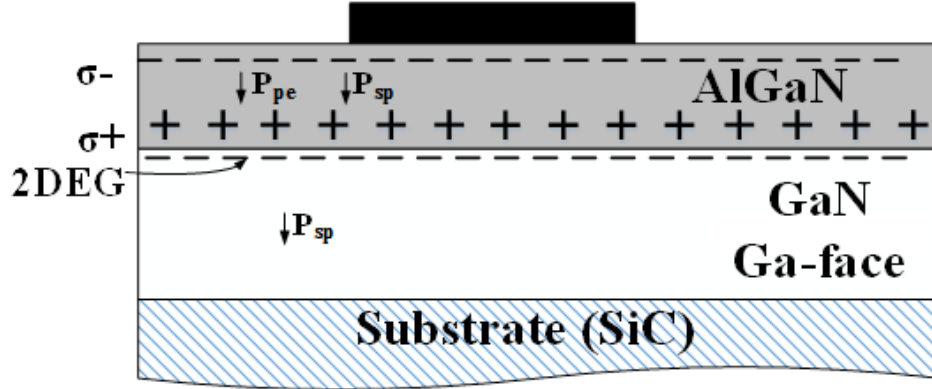


**Figure 1-2: Polarization and charges in AlGa<sub>N</sub>/GaN HEMTs [5].**

The induced sheet charge  $\sigma$  created at the interface between the AlGa<sub>N</sub> layer and the GaN layer of AlGa<sub>N</sub>/GaN heterostructures grown along the [0001] direction ( $c$ -axis) (GaN), shown in Figure 1-2, can be written as the sum of spontaneous and piezoelectric polarization charges at AlGa<sub>N</sub> and GaN layers (the piezoelectric polarization  $P_{PE-GaN}$  is considered negligible).

$$|\sigma| = |P_{SP-AlGaN} + P_{PE-AlGaN} - P_{SP-GaN}| \quad (1-2)$$

In order to compensate this induced positive sheet charge at the AlGa<sub>N</sub> interface, an accumulation of free electrons will appear at the GaN interface, as illustrated in Figure 1-2. The sheet electron concentration  $n_s(x)$  can be calculated by using the total bound sheet charge  $\sigma(x)$  (illustrated in Figure 1-3) and the following equation [8]:

$$n_s(x) = \frac{\sigma(x)}{q} - \frac{\epsilon_0 \epsilon_r(x)}{q^2 d} [q\Phi_b(x) + E_F(x) - \Delta E_c(x)] \quad (1-3)$$

where  $\sigma$  is the polarization induced sheet charge density,  $q$  is the electron charge, ( $\epsilon_0$ ,  $\epsilon_r$ ) are the vacuum and relative permittivities,  $d$  is the thickness of the AlGa<sub>N</sub> barrier,  $q\phi_b$  is the Schottky barrier of the gate contact on top of AlGa<sub>N</sub>,  $E_F$  is the position of the Fermi level with respect to the edge of the GaN conduction band energy, and  $\Delta E_c(x)$  is the offset of conduction band energy at the AlGa<sub>N</sub>/GaN interface.

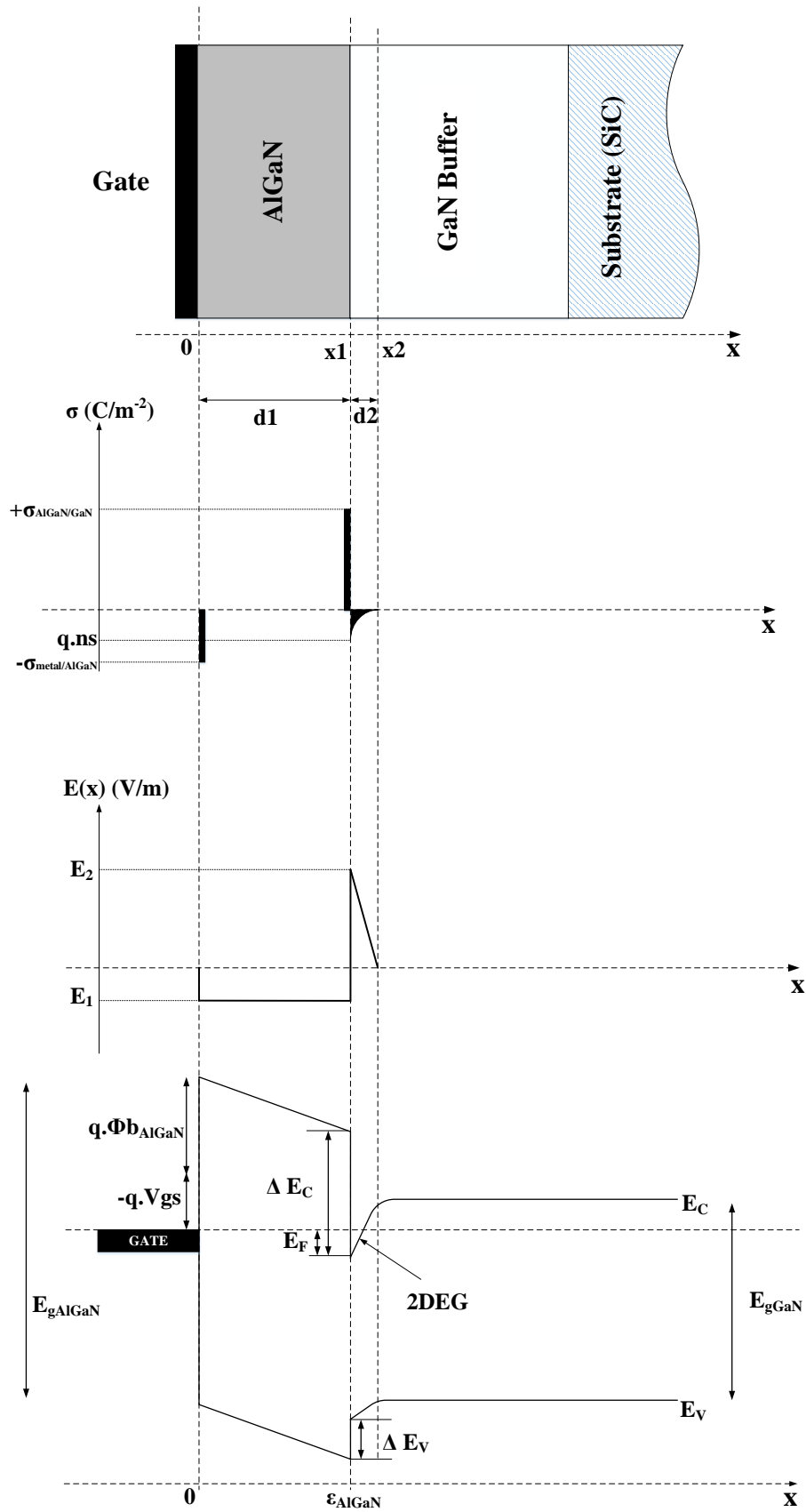
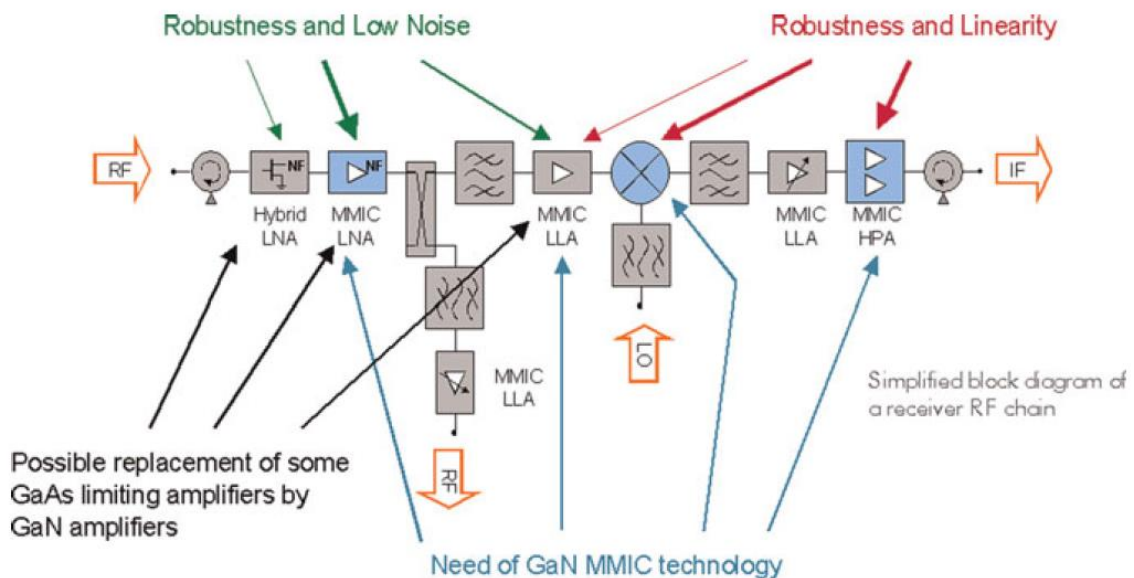


Figure 1-3: Charge distribution, electric field and energy band diagram of an AlGaN/GaN HEMT heterostructure [5].

### 1.3 GaN technology for satellite equipment

As already mentioned, GaN technology is currently under development and qualification not only for high power amplifier (HPA) module but also for other applications like low noise amplifier (LNA), mixer and local oscillator in a space environment. This technology offers significant advantages for space industries in terms of size reduction/integration, DC power consumption, linearity and RF power.

Solid-state power transistors have, over the past 40 years, started to replace vacuum technology in the vast majority of microwave systems, but the revolution is not complete. In particular, the high RF power microwave and millimeter-wave radar and communications transmitter applications are dominated by microwave tubes for frequency capabilities greater than 100 GHz, and for high device operating temperature capabilities greater than about 250 °C. Nowadays, at lower frequency ranges (L/C/S band), GaN-based solid state power amplifiers (SSPA) obtain impressive RF performance, such as for a Galileo-like navigation satellite 230 W [9], a 170 W L-Band achieved by Thales Alenia Space [10] and the 80 W C-band, which are comparable to a travelling-wave amplifier tube (TWTA) solution but with a smaller size and more flexible architecture.



**Figure 1-4: Improvements along the RF chain of satellite receivers [11].**

The improvements along the RF chain of satellite receivers are shown in [11], the majority of the functions of the equipment can be replaced by GaN technology with a reduction in the number of MMICs, thus lower equipment cost and increased robustness and linearity of HPA, LNA and mixer modules.



## 1.4 GH50-10 process

In this thesis, the modeled and characterized device is an  $8 \times 250 \mu\text{m}$  AlGaIn/GaN GH50-10 HEMTs (from the UMS foundry). A schematic cross section of the active region of a GH50-10 transistor is shown in Figure 1-5.

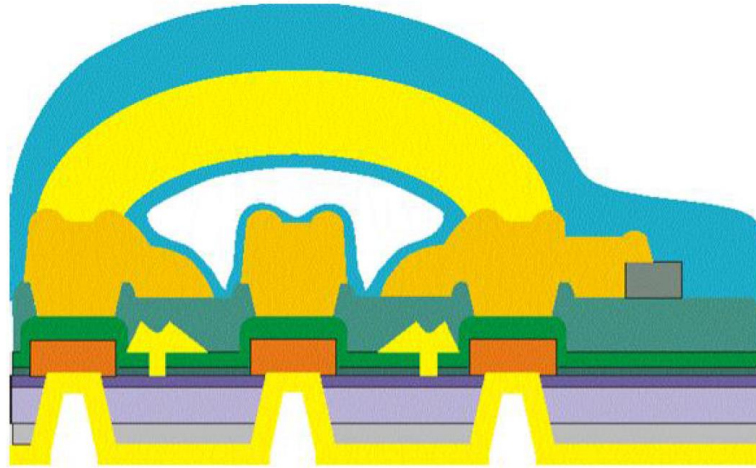


**Figure 1-5: Schematic cross section of the active region of GH50-10 transistor [12].**

The major features of the GH50-10 process extracted from [12] are the following:

- HEMT MOCVD active layer on 3-inch semi-insulating SiC substrate with high sheet-resistance uniformity
- Isolation by ion implantation
- $0.5 \mu\text{m}$  T and  $\Gamma$  shaped gold gate with diffusion barriers with low resistance suitable for high frequency operation. The gate foot lithography is made with an e-beam whereas the gate head lithography is made with an I-line stepper.
- $30\Omega/\text{sq}$  TaN resistors,  $640\Omega/\text{sq}$  semiconductor resistors and  $1000\Omega/\text{sq}$  TiWSi resistors
- Thick gold electroplating for interconnects and line reinforcement
- Air bridges to overcome device topography
- SiN-protection of the wafer front side
- $100 \mu\text{m}$  substrate thickness with via interconnects for source contacting / connection to ground pads
- Power density  $5 \text{ W/mm}$  @  $2 \text{ GHz}$
- Operating frequencies up to  $6 \text{ GHz}$
- Operating voltage  $V_{\text{ds}} = 50 \text{ V}$
- Maximum voltage  $V_{\text{dsmax}} = 150 \text{ V}$
- Pinch-off voltage  $V_{\text{p}} = -2.2 \text{ V}$

- Drain saturation current  $I_{dss} = 420 \text{ mA/mm}$
- Transconductance  $G_m = 190 \text{ mS/mm}$  @  $V_{gs} = 0\text{V}$
- Gate and Drain leakage currents  $I_{gl}, I_{dl} < 200 \text{ }\mu\text{A/mm}$  @  $V_{ds} = 50 \text{ V}, V_{gs} = -7 \text{ V}$

## 1.5 Conclusion

This chapter briefly introduced the properties and advantages of GaN in microwave systems with a particular emphasis on space applications. An example of an RF chain of a satellite receiver was presented, but is currently under development to replace most of the functions of the equipment with GaN technology. The presented Ph.D. research was focused on this context, more specifically on HPA modules. At the end of this chapter, further details on the technology process of the studied GaN device was also presented.

## 2 Investigation of trapping phenomena

### 2.1 Introduction

The AlGaN/GaN HEMTs, as described in the first chapter, have shown impressive performance in terms of high electron mobility, high power density, high cut-off frequency and high thermal conductivity. As a consequence, HEMT devices should replace the preceding technologies in most RF and power commercial markets. However, GaN technology suffers severely from dispersion phenomena called trapping effects that, combined with thermal effects (self-heating), limit their initial expectation.

The aim of this chapter is the understanding of the trapping phenomena, in particular the reduction of their effects during real operation mode using appropriate bias conditions.

This chapter presents a detailed trap investigation protocol to obtain a complete overview of trap behavior from DC to radio-frequency operation mode based on combined pulsed I/V measurements, DC and RF drain current measurements and low-frequency (LF) dispersion measurements. The thermal pulsed I/V measurement technique is used to determine the thermal resistance, something which is necessary to calculate the Arrhenius plot. Finally, a discussion and comparison of the Arrhenius plot results of these trap investigation techniques are depicted.

### 2.2 Basics of trapping phenomena

Traps, in solid-state physics, are any locations within a material (generally in a semiconductor) that limit the movement of holes (i.e., energy levels, related to the absence of an electron/hole within a crystal structure and present between the forbidden energy-gap of semiconductor). Trapping effects have required many years to be understood in several semiconductor technologies like FET and GaAs MESFETs. However, in spite of extensive investigation of trapping phenomena, the physics of the active defects is not completely understood in GaN HEMTs. So, a deep knowledge of the origin of the traps, their location, and the physical mechanisms of a trap are important for the optimization of the performance of these devices. The GaN material contains high densities of defects, mostly due to crystalline imperfections, which result from the growth of the material (like impurities in the crystal lattice, dangling bonds on the surface, and lattice mismatches with foreign substrates

such as SiC and sapphire and impurities in the crystal lattice) and the processing of the device.

These imperfections generate trap centers within the band-gap of a semiconductor that facilitate the creation of a free electron in the conduction band and a hole in the valence band. These processes need a smaller amount of energy than a direct band-to-band transition. There are two types of traps: donors and acceptors. A donor-like state can be both positive (ability to emit an electron) or neutral (when filled). Acceptor-like states can be both negative (possibility of capturing an electron) or neutral (when empty).

The defects can be classified in terms of their energy level: the traps with an energy-level close to the conduction or valence bands ( $<1\text{eV}$ ) are called shallow-level traps, which are responsible for parasitic doping effects. Traps with an energy level deeper within the forbidden band-gap are called deep level traps. The process of trapping and de-trapping follows the Shockley–Read–Hall theory [13]–[15] which describes the interactions between the free-carriers (electrons and holes) and the generation/recombination mechanisms for a deep level transition to or from a band (as illustrated in Figure 2-1).

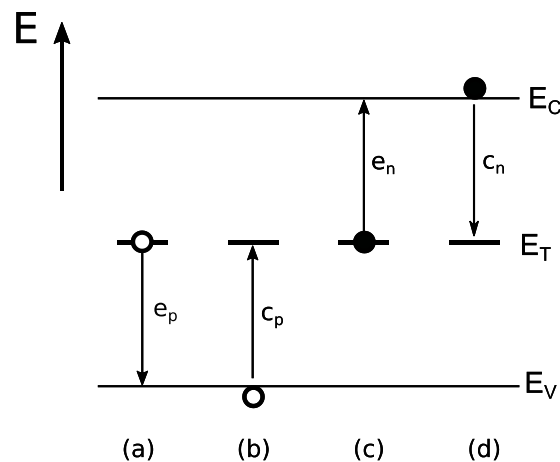


**Figure 2-1: The basic processes of transition: (a) hole emission (an electron jumps from the valence band to the trapped level), (b) hole capture (an electron drops from an occupied trap to the valence band, and a hole disappears), (c) electron emission (an electron jumps from the trapped level to the conduction band) and (d) electron capture (an electron drops from the conduction band to an unoccupied trap).**

In particular, we focus only on the traps related to the conduction band, the same argument can be used for the valence band. To calculate the rate of an occupied trap's density or a function of time, an analysis of the capture and emission processes needs to be considered.

Considering all recombination–generation processes, the overall occupancy trap rate in the conduction band is equal to

$$\frac{\partial n_T}{\partial t} = (c_n(N_T - n_T) - e_n n_T) \quad (2-1)$$

where  $c_n$ ,  $N_T$ ,  $n_T$  and  $e_n$  are respectively the electron capture rate, the number of defect states, the number of defect states filled with electrons and the electron emission rate. In thermal equilibrium where every process is balanced by its inverse process, in Equation (2-1) the number of emitted electrons from traps must be equal to the number of those captured (thus  $\partial n_T / \partial t = 0$ ). Therefore, the relationship between the capture and the emission rate for the conduction band can be defined as

$$\frac{e_n}{c_n} = \left( \frac{N_T}{n_T} - 1 \right) \quad (2-2)$$

The occupancy probability of trap's energy level is given by the Fermi-Dirac distribution:

$$\frac{N_T}{n_T} = \frac{1}{1 + \exp\left(\frac{E_T - E_F}{kT}\right)} \quad (2-3)$$

where  $E_T$  is the energy level,  $E_F$  is a reference energy called the Fermi level,  $k$  is the Boltzmann constant (in  $\text{eV T}^{-1}$ ) and  $T$  is the temperature (in K). Considering the Fermi equations, Equation (2-2) can be rewritten as

$$\frac{e_n}{c_n} = \exp\left(\frac{E_T - E_F}{kT}\right) \quad (2-4)$$

The capture rate of electrons  $c_n$ , which represents the ratio of the trapped electrons density to unoccupied trap states, can be expressed as

$$c_n = \sigma_n v_n n \quad (2-5)$$

where  $\sigma_n$ ,  $v_n$  and  $n$  represent respectively the capture cross-section, the thermal velocity of the electrons, and the number of free-electrons in the conductance band. The last two parameters can be expressed as

$$v_n = \left( \frac{3kT}{m^*} \right)^{1/2} \quad (2-6)$$

and

$$n = N_c \exp\left(-\frac{E_C - E_F}{kT}\right) \quad (2-7)$$

The conduction-band effective density of state  $N_c$  is expressed as

$$N_c = 2M_c \left( \frac{2\pi m^* kT}{h^2} \right)^{3/2} \quad (2-8)$$

where  $m^*$  is the effective mass of the electron,  $h$  is the Planck's constant, and  $M_c$  is the number of conduction band minima.

Substituting Equations (2-5), (2-6), (2-7) and (2-8) in to Equation (2-4), we obtain the expression of emission electron rate of deep level:

$$\frac{1}{\tau_n} = e_n = \gamma T^2 \sigma_n \exp\left(-\frac{E_n}{kT}\right) \quad (2-9)$$

where

$$\gamma = 2\sqrt{3}(2\pi)^{3/2} k^2 m^* h^{-2} \quad (2-10)$$

and

$$\sigma_n = \sigma_\infty \exp\left(\frac{\Delta E_\sigma}{kT}\right) \quad (2-11)$$

where  $\tau_n$  represents the electron emission time constant,  $\sigma_\infty$  the capture cross section at  $T = \infty$ ,  $E_n$  the apparent activation energy, which is in this case may significantly differ from the zero-field binding energy of the trap with respect to the conduction-band, and  $\Delta E_\sigma$  is the activation energy of the capture cross-section.

In order to obtain the properties of traps (such as their physical location in the structure of the device), it is necessary to extrapolate the Arrhenius plots of the traps and their signatures in terms of activation energies and capture cross-sections. The determination of the emission time constant for different techniques, drain current transient (DCT) and LF dispersion measurements, is fully discussed in the following.

The activation energy and capture cross-section parameters are the fundamental characteristics of a trapping center. In fact, a comparison with other identified activation energies and capture cross-sections in different devices can help to understand the mechanisms of charge-trapping and to determine the location of the trapping centers in a device.

In GaN-based transistors, the parasitic charge moving of the traps on the surface and/or in the bulk affects the density of the 2DEG channel, causing a modulation of the drain current that is

determined by the effective channel thickness as well as the output conductance and transconductance in the low-frequency range [16]. For this reason, an advanced trapping characterization protocol is proposed in the following paragraph and is based on:

- Pulsed I/V measurements, carried out at several quiescent bias points to quantify the current-collapse (CC), to obtain a preliminary characterization and to understand which trapping mechanisms may affect the transistor's performance [17];
- DC and RF drain current transient spectroscopy [18], [19] through stretched multi-exponential fitting of the DCT measurements [20] can provide information about the activation energy and capture cross-section of the trap levels;
- Output conductance frequency dispersion and transconductance frequency dispersion [21], [22] based on low-frequency 2-port S-parameter measurements can provide information on the characteristics of the trap levels (such as  $E_A$  and  $\sigma_c$ ) promoted by small-signal excitation at a fixed bias point.

## 2.3 Trapping characterization methodology

### 2.3.1 Pulsed I/V characterization

Pulsed I/V measurement is carried out to obtain a preliminary and quick characterization in order to understand which trapping mechanisms may affect the transistor's performance. This technique is very useful because it allows distinguishing the trapping effects from the thermal effects (normally these effects have time constants with the same order of magnitude) and then evaluate only the electrical phenomena of a trap state. One of the most common trap effects is called CC [23], as shown in Figure 2-2.

The  $I_D$ - $V_D$  characteristics in Figure 2-2 obtained before and after the application of a high drain bias with quiescent point Q' show a dynamic increase of the knee voltage and a decrease of the drain current due to large gate-drain voltage swings [24], [25]. These two phenomena are still sufficient to cause a substantial reduction in output power (shown in Figure 2-2), where the maximum output power is proportional to the product of the maximum current and voltage swings and in Class A is equal to

$$p \cong \frac{1}{8} \Delta V \Delta I \quad (2-12)$$

Thus, these CC effects are related to the presence of deep level which promotes the specific trapping phenomena. The main effects related to CC are the gate-lag effect and the drain-lag effect [26].

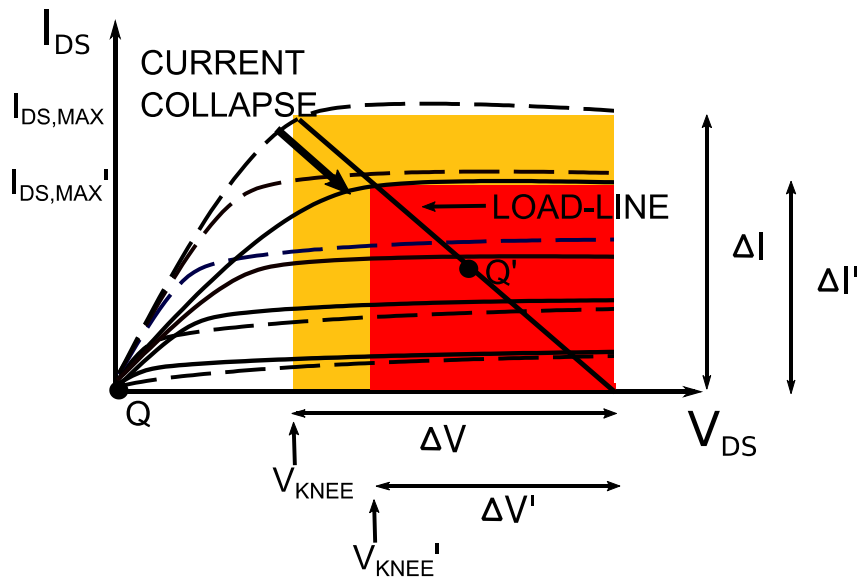


**Figure 2-2: Schematic of  $I_D$ - $V_D$  characteristics before (dashed curves) and after (full curves) the application of a high drain bias. The maximum device output power with and without trap effects is plotted in red and yellow rectangles respectively.**

The **gate-lag effect** is a delayed response of the drain current when a gate voltage variation is applied and this is due principally to two mechanisms [17], [27]. The first one has been associated with the ionized donor states located on the surface between the gate and the drain electrodes [25], [28] which influence the series resistances in the source and drain access regions. The ionized donor states can capture a free electron and thus reduce the 2DEG density. *Vetury et al.*[25] explains that the extension of the depletion region is due to the increase of ionized donor states. This effect can be modeled as a second virtual gate when a negative gate pulse is applied. The de-trapping transient associated to this effect shows a slow constant time (in the order of milliseconds-seconds) [27]. The mechanism of a virtual gate is shown in Figure 2-3.



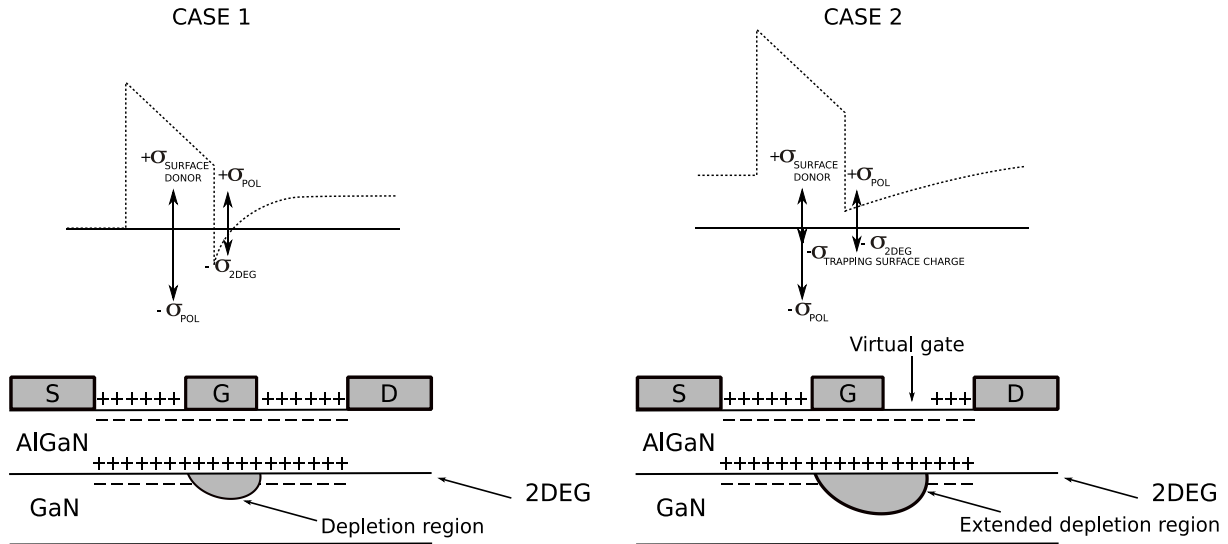


**Figure 2-3: Schematic of gate-lag mechanism: (case 1) presence of ionized donor traps, (case 2) trap charged with reduction of the 2DEG density [25].**

The second one is related to the positive shift of the pinch-off voltage for negative gate bias that is due to charge trapping under the gate [17]. These traps are normally located in the AlGaIn or GaN layers and have faster de-trapping kinetic processes.

In a recent work [29], using a simple simulation framework, it has been demonstrated that a passivation dielectric that minimizes surface leakage and creates a high density of shallow traps at the surface is necessary to minimize the formation of a virtual gate and eliminate gate-lag phenomena. The use of a passivation layer and gate field plating in the last generation of GaN-based transistors has allowed the almost complete reduction of gate-lag effects.

The **drain-lag effect** is a delayed response of the drain current induced when a very high drain voltage and very negative gate voltage (higher than the pinch-off voltage  $V_P$ ) during DC pulses are applied. It produces a modulation of the depletion layer into the active region due to free electrons' being injected into the buffer. The drain-lag mechanism is explained in Figure 2-4 when the drain pulse is applied. Figure 2-4 shows the impact of traps related to the buffer on the 2DEG channel when the drain pulsed is applied: (1) the initial state, the device is at equilibrium  $N_d^+ = N_a^-$  the density of ionized donors is equal to the density of ionized acceptor when  $E=0$ . (2) A very high drain voltage and very negative gate voltage are applied. They produce a very strong vertical electric field due to the high drain voltage and high leakage current due to very negative gate voltage. These two phenomena induce a capture of free-electrons in the 2DEG channel by the donor trap, thus the density of ionized donors is reduced to  $N_d'^+$  and becomes neutral. (3) The device comes back to initial state when the  $V_{GS}$  and  $V_{DS}$  are pulsed down. The device is no longer submitted to a strong vertical electric field

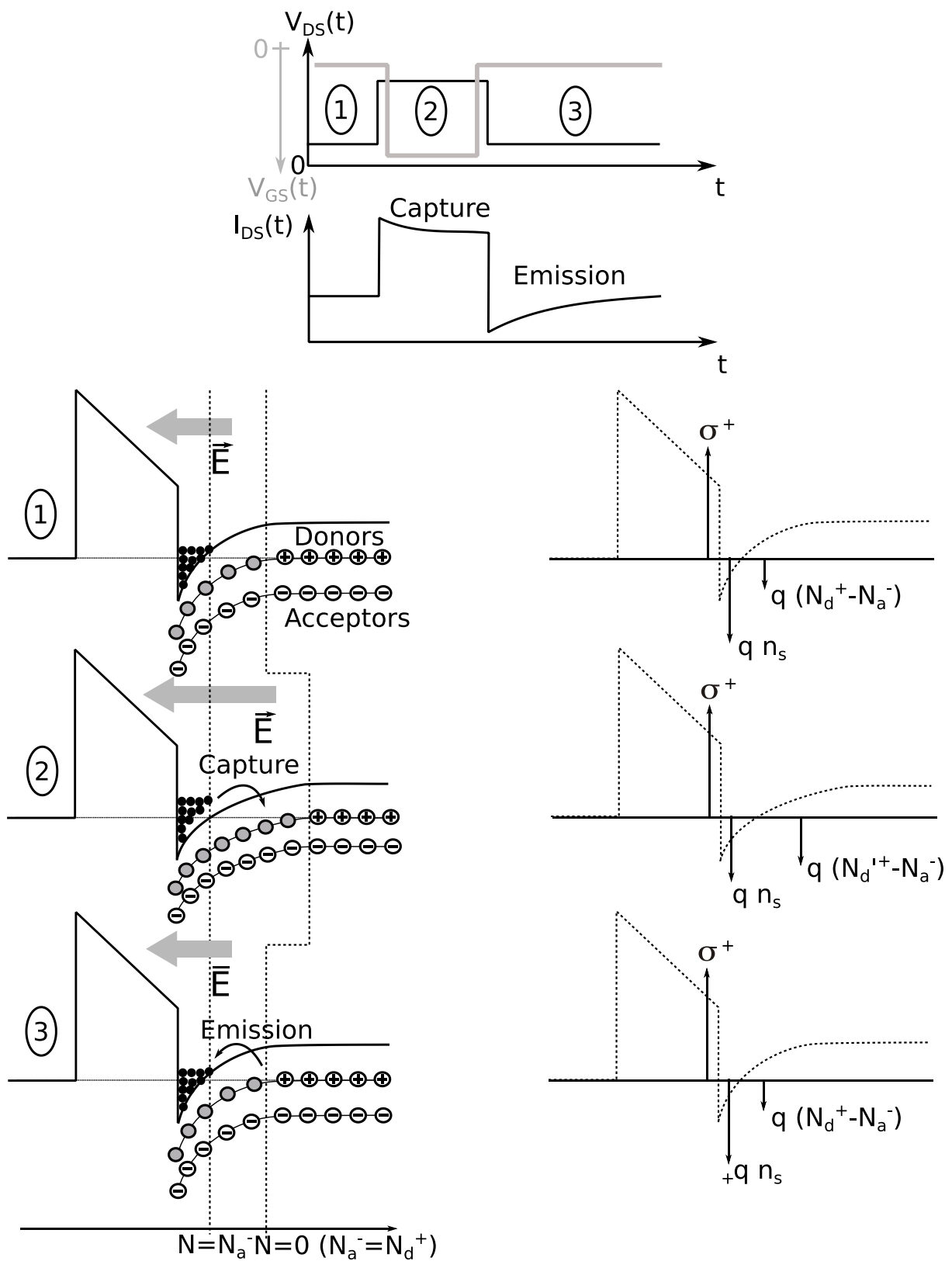


**Figure 2-4: Schematic of trapping and de-trapping process of traps located in the buffer (hypothesis  $N_D > N_A$ ) [5], [30].**

and high leakage current, so the captured electrons in the last step are re-emitted with a slow emission process. Therefore, the capture and emission processes are asymmetric. Hence, in a GaN-based transistor the capture time constants are in the order of a few nanoseconds and the emission time constants on the order of a few microseconds to minutes.

### 2.3.1.1 Pulsed measurement test bench

A schematic of the set-up used for pulsed I/V characterization is shown in Figure 2-5. The set-up is based on a 250V/10A pulsed I/V BILT AMCAD system [31]. The pulsed I/V measurements obtained with this set-up can be used for trapping investigation and the extraction of a nonlinear current source model of the transistor. The gate and drain current measurements are made using differential voltage measurements at the terminals of a resistance into the gate ( $10\ \Omega$ ) and drain ( $0.5\ \Omega$ ) probe respectively. The pulse generation and the voltage/current measurement are synchronized by an internal trigger. In the system, it is possible also to consider parasitic effects (introduced by the cable, connector, bias tees...) with a special DC calibration. This DC calibration consists of measuring the resistance path from probe head (I/V original reference planes) to on-wafer probing. The use of bias tees is conditioned by the type of device under test (DUT), e. g. it is recommended for transistors with large areas. It must also be considered that the use of bias tees introduces a degradation of the  $I_D$ - $V_D$  characteristic especially in the ohmic region.

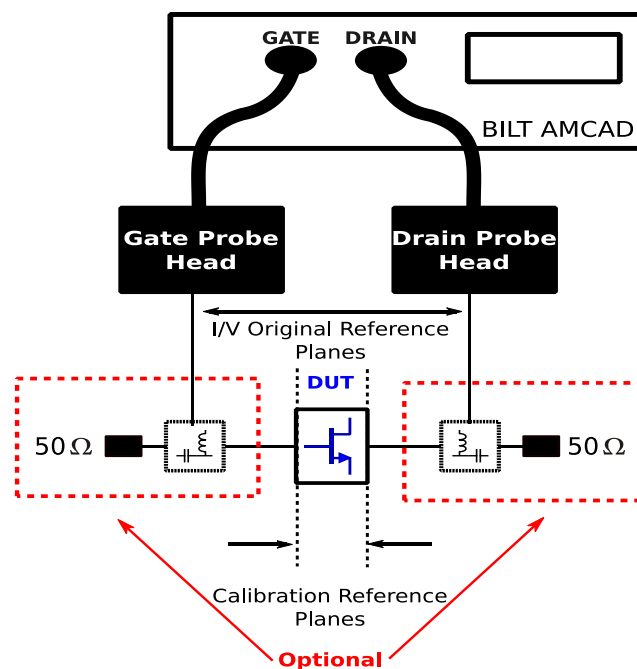


**Figure 2-5: Block diagram of pulsed I/V experimental set-up.**

The principle of pulsed I/V measurements is shown in Figure 2-6. Pulsed I/V measurements are carried out in quasi isothermal conditions. Therefore, the gate and drain of the device are pulsed from a quiescent-bias point  $(V_{GQ}, V_{DQ})$  corresponding to a fixed trapping state to the measurement-bias point  $(V_{GM}, V_{DM})$ . In order to overcome the self-heating effect and therefore to investigate principally the electrical phenomena due to the trapping effects, the pulse-width of the gate and drain are chosen as small as possible, within the limit of pulse generation. Moreover, the duration of the pulse period must be much longer than the pulse-width, so as to be sure that the device returns to its steady-state conditions. The timing specification used for the following pulsed I/V measurement is described in Figure 2-7 with a pulse duty cycle (defined as  $PW_{GATE}/PERIOD$ ) equal to 99 and the I/V TRACE WINDOW represents the part of the pulse employed to determine the average currents and voltages for every measurement-bias point.

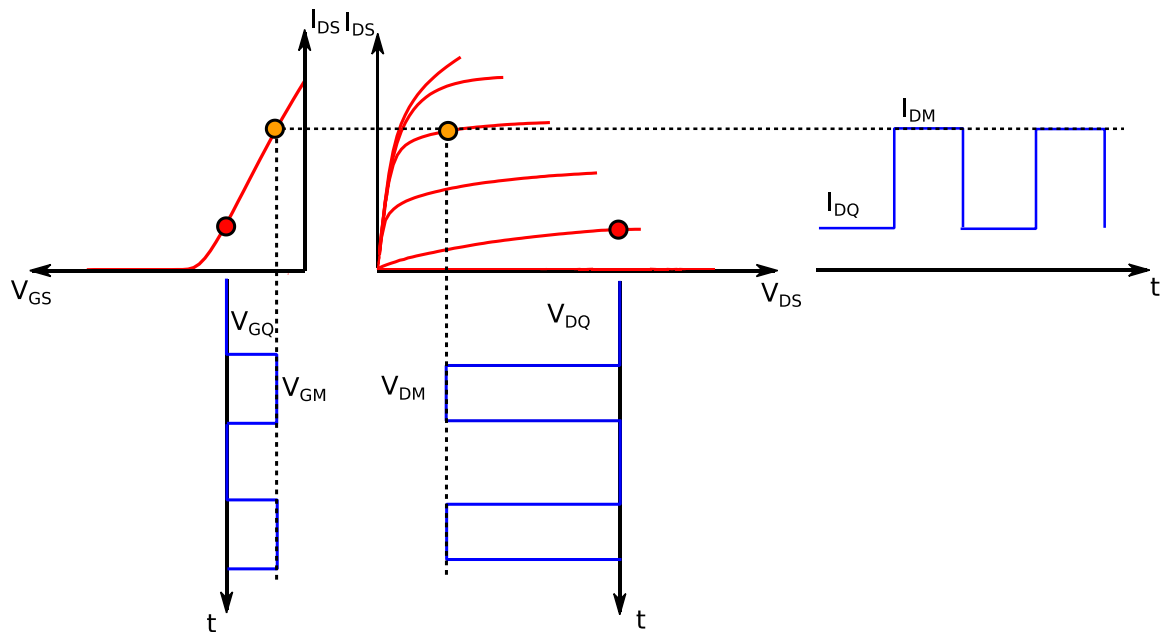


**Figure 2-6: Principle of pulse I/V measurement.**

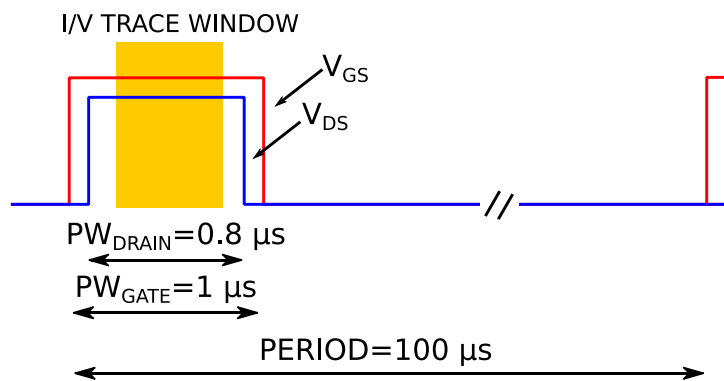


**Figure 2-7: Pulse timing diagram of pulse I/V measurement.**

### 2.3.1.2 Pulsed I/V characterization for trapping investigation

In order to identify and quantify the trapping effects a specific trapping pulsed I/V protocol has been developed, based on pulsed I/V characterization for different quiescent bias points:

- Q<sub>1</sub>: ( $V_{GQ}, V_{DQ}$ )=(0V,0V) which corresponds to negligible electron trapping;
- Q<sub>2</sub>: ( $V_{GQ}, V_{DQ}$ )=( -5V,0V) which may favor the trapping of electrons under the gate region (gate-lag);
- Q<sub>3</sub>: ( $V_{GQ}, V_{DQ}$ )=( -5V,40V) which may favor the trapping of electrons under the gate-drain region (drain-lag);
- Q<sub>4</sub>: ( $V_{GQ}, V_{DQ}$ )=( -1.9V,40V) which is representative of electron trapping under class AB bias condition ( $I_{DS}$ =50mA at  $V_{DQ}$ =40V).

Figure 2-8(a) reports the results of pulsed  $I_D$ - $V_D$  characterization and Figure 2-8(b) shows the  $g_m$  variation (extracted from  $I_D$ - $V_G$  measurements). The results of pulsed  $I_D$ - $V_D$  measurements indicate that the device is less sensitive to gate-lag than to drain-lag: the gate filling pulse  $V_{GQ}$  has a negligible effect on the device characteristics, while the application of  $V_{DQ}$  induces a strong CC and degrades the  $R_{ON}$  value. By comparing the OFF-state quiescent bias point (-5V, 40 V) with the SEMI-ON state, class AB bias condition (same  $V_{DQ}$  but  $V_{GQ}$ =-1.9 V), it can be noticed that the CC is relatively unchanged but the  $R_{ON}$  degradation is enhanced.

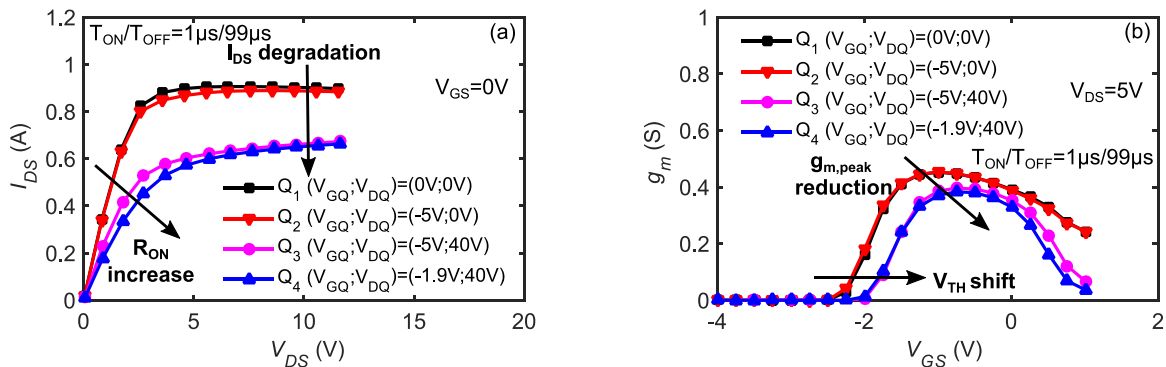


**Figure 2-8: (a)  $I_D$ - $V_D$  and (b)  $g_m$  (derived from  $I_D$ - $V_G$ ) pulsed characterizations for different quiescent bias points of  $8 \times 250 \times 0.5 \mu m^2$  AlGaIn/GaN HEMT.**

Transconductance ( $g_m$ ) measurements, shown in Figure 2-8(b), show that the drain-lag (point Q<sub>3</sub>) induces both a positive threshold voltage shift and a reduction in  $g_m$  (-15% at peak and more pronounced at higher  $V_{GS}$ ). The Q<sub>4</sub> quiescent point presents the same threshold voltage shift and a slightly more pronounced decrease in  $g_m$  with respect to Q<sub>3</sub>. The threshold voltage shift and a reduction in  $g_m$  for Q<sub>3</sub> and Q<sub>4</sub> quiescent point conditions suggest that CC is related to negative charge trapping both under the gate and in the access regions.

One figure of merit to evaluate and quantify the impact of trapping effects on the device's characteristics is the slump ratio (SR), defined as the saturation drain current in trapping conditions such as  $Q_2$ ,  $Q_3$  and  $Q_4$  measured at  $(V_{GM}; V_{DM}) = (0V; 10V)$  divided by the saturation drain current in negligible trapping condition  $Q_1$  measured at  $(V_{GM}; V_{DM}) = (0V; 10V)$ .

Table 2 summarizes the drop of saturation current due to CC. Notice that the SR has a strong decrease in the drain-lag and Class AB operation bias point. This indicates that traps excited by a high electric field will cause dispersion in RF performance.

TABLE 2  
SLUMP RATIO UNDER PULSED I/V

	COLD ( $Q_1$ )	GATE-LAG ( $Q_2$ )	DRAIN-LAG ( $Q_3$ )	CLASS AB BIAS ( $Q_4$ )
$I_{DS(V_{GM}; V_{DM})=(0V; 10V)}(A)$	0,90	0,88	0,66	0,65
SR	//	0,98	0,73	0,72

### 2.3.1.3 Pulsed I/V characterization for channel temperature investigation

In order to estimate the junction temperature of GaN-based HEMTs, something which is essential to determine the Arrhenius plot, an electrical methodology to determine the thermal resistance is used [32]. This methodology is based on pulsed I/V measurements, which uses a small pulse-width. Thus, the self-heating of the device can be assumed negligible and the junction temperature can be considered dependent of the dissipated power of the quiescent bias point. The extraction of  $R_{TH}$  consists in the characterization of the on-resistance ( $R_{ON}$ ) and saturation drain current ( $I_{DS,SAT}$ ) variations with respect to the temperature and is based on two steps:

- **Thermal calibration.**  $R_{ON}$  and  $I_{DS,SAT}$  are measured at cold quiescent bias point condition  $(V_{GQ}, V_{DQ})=(0V, 0V)$  and at different chuck temperatures. At this condition, there is no dissipated power and the channel temperature can be considered the same as the chuck temperature.

The thermal pulsed I/V measurements are carried out in cold network condition  $(V_{GQ}, V_{DQ})=(0V, 0V)$  and for 25°C-150°C temperature range (Figure 2-9(a)).

- **Dissipation power calibration.** In this case,  $R_{ON}$  and  $I_{DS,SAT}$  are measured at a fixed chuck temperature (25°C) and the pulses are issued from different quiescent bias

points. The power dissipation and consequently the channel temperature are set by the quiescent bias point ( $V_{GQ}$   $V_{DQ}$ ). The pulsed I/V measurements are carried out at various bias points ( $V_{GQ}=-1V$ ,  $V_{DQ}= 4-40V$ ) and at 25°C chuck temperature (Figure 2-9(b)).

This technology has very slow trapping phenomena. Hence, between successive measurements a relaxation period is applied to the device without any electric bias. The estimated  $R_{ON}$  and  $I_{DS,SAT}$  in Figure 2-10 present for both conditions a linear relationship with temperature and power dissipation: a negative slope for  $I_{DS,SAT}$  and a positive slope for  $R_{ON}$ . The thermal resistance can be defined classically as the relationship between the channel temperature and power dissipation [33]:

$$R_{TH} = \frac{\Delta T}{\Delta P_{DISS}} \quad (2-13)$$

Thus, the thermal resistance is simply the ratio of the slope of the temperature and of the power dissipation. The thermal resistance can be extracted from the linear region ( $R_{ON}$ ) and from the saturation region ( $I_{DS,SAT}$ ). In our case the thermal resistance is determined from the saturation region ( $I_{DS,SAT}$ ) because the linear region, where  $R_{ON}$  is calculated, has a parasitic effect introduced by the bias tees. The thermal resistance extracted from the  $I_{DS,SAT}$  measurement is estimated to be 14 C°/W.

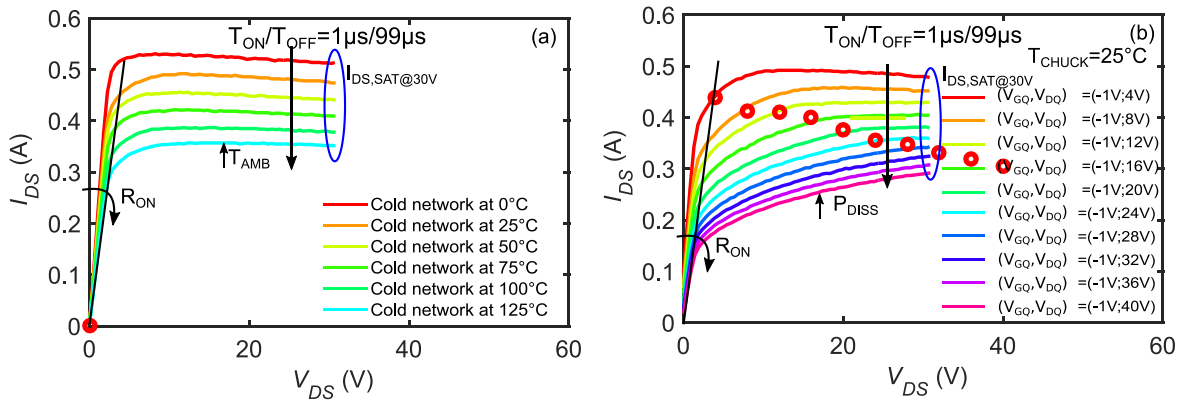


**Figure 2-9: (a) Pulsed I/V characteristics (@ $V_{GS}=-1V$ ) at cold network ( $V_{GQ}$ ,  $V_{DQ}$ )=(0V,0V) with zero power condition (in red circles) and at different chuck temperatures. (b) Pulsed I/V characteristics (@ $V_{GS}=-1V$ ) from various bias points ( $V_{GQ}=-1V$ ,  $V_{DQ}= 4-40V$ ) (in red circles) and at a chuck temperature equal to 25°C.**

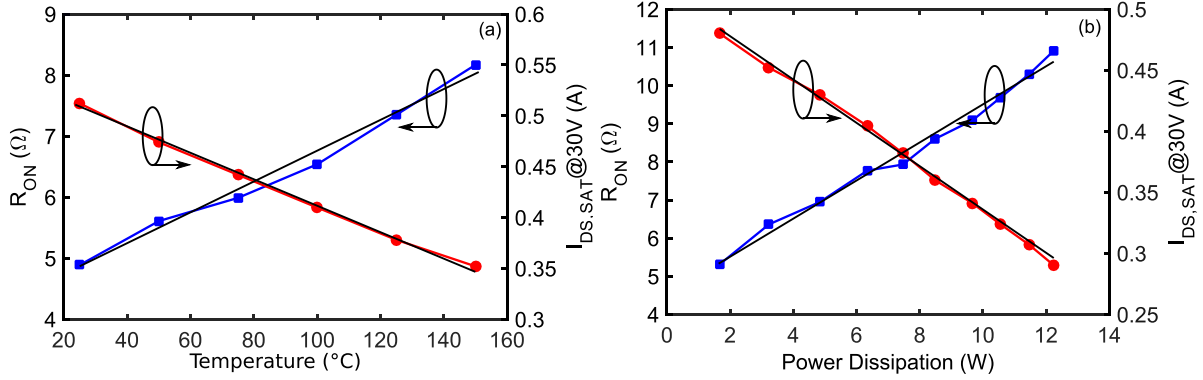


**Figure 2-10: (a) Extracted pulsed  $I_{DS,SAT}$  (@ $V_{DS}=30V$ ) and  $R_{ON}$  as a function of chuck temperature  $T_{AMB}$  (@  $P_{DISS}=0$  W), (b) Extracted pulsed  $I_{DS,SAT}$  (@ $V_{DS}=30V$ ) and  $R_{ON}$  versus power dissipation.**

The measured device is soldered onto a copper tungsten mount. The 3-D finite-element simulations with ANSYS software are performed separately on a  $0.5 \times 8 \times 250 \mu m^2$  AlGaIn/GaN HEMT (Figure 2-11) and on a copper tungsten mount (Figure 2-12). The overall thermal resistance obtained by the finite-element simulations is

$$R_{TH\_ANSYS} = R_{DEVICE} + R_{MOUNT} = \frac{15}{2.5} + \frac{25}{4} \cong 12.25 \text{ } ^\circ C/W \quad (2-14)$$

In the first approximation, the channel temperature determined with these two techniques gives similar results. Thus, the estimated thermal resistance is validated with 3-D finite-element simulations.

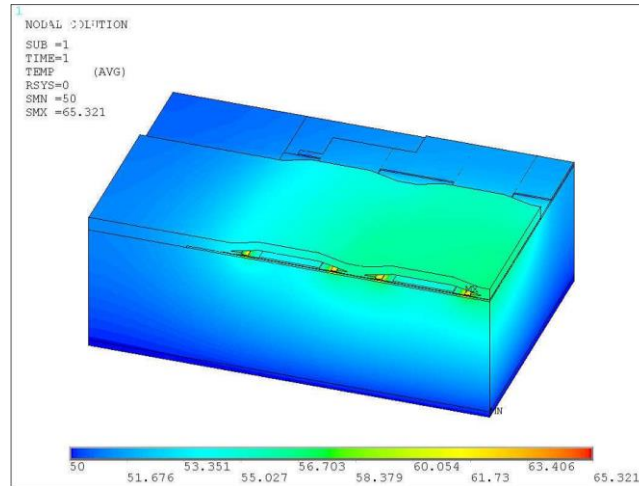


**Figure 2-11: Thermal resistance for a  $0.5 \times 8 \times 250 \mu m^2$  AlGaIn/GaN HEMT by 3-D finite element simulation with ANSYS software for a dissipated power equal to 2.5 W.**



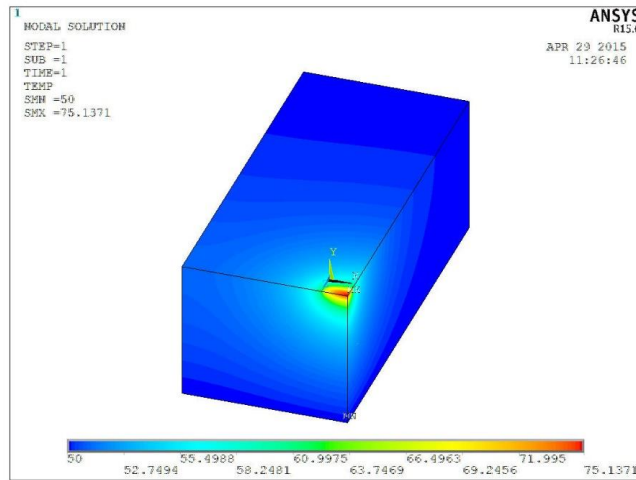


**Figure 2-12: Thermal resistance for a copper tungsten mount by 3-D finite element simulation with ANSYS software for a dissipated power equal to 4 W.**

### 2.3.2 Drain current transient spectroscopy

The previous pulsed I/V characterization is very useful for investigating the CC. But, its measurement window ( $<1$  ms) does not provide any information about the dynamic behavior of the trap state. For this reason, DCT spectroscopy [18]–[20], [34]–[36], known as current mode deep level transient spectroscopy (I-DLTS), is used to investigate the time evolution of carriers in the trapping process and therefore to identify the associated deep level.

#### 2.3.2.1 Drain current transient set-up

The experimental set-up used for DCT measurements is shown in Figure 2-13. In this set-up, the drain current transient is determined by measuring the differential voltage on a resistive load ( $R_{\text{SENSE}}=10\Omega$ ) connected between the drain of transistor and the drain pulser (Agilent 33220A arbitrary waveform generator). The drain pulse signal is linearly amplified to reach the required values of drain current and voltage. The digital sampling oscilloscope (Tektronix TDS 645C) and gate pulser (Agilent 33220A arbitrary waveform generator) are triggered by a synchronous pulsed signal generated by a drain pulser. The delay introduced by the linear DC PA (FLC voltage amplifier) has a negligible effect on the synchronized biasing and DC measurement of the transistor.

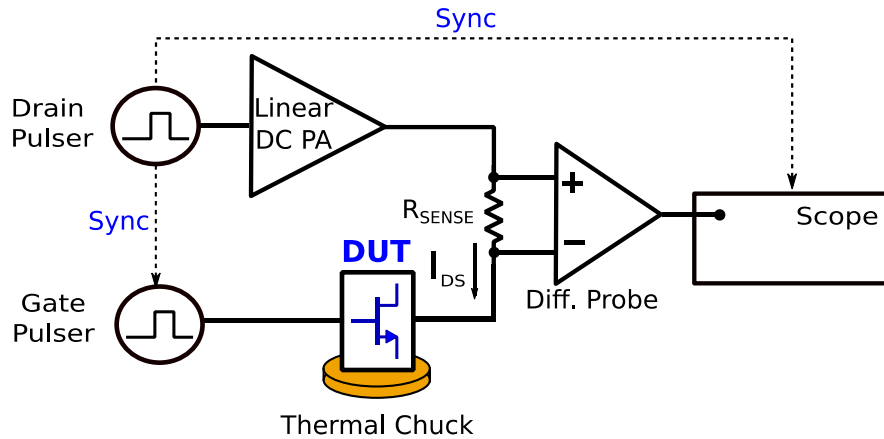


**Figure 2-13: Block diagram of thermal DCT measurement set-up.**

The principle of drain current measurement technique is shown in Figure 2-14. The device is biased for 100 s in filling condition ( $V_{GS,F}; V_{DS,F}$ ), thus inducing a specific trapping state. Subsequently, the device is switched to a different bias point in a low-field and low-power on-state ( $V_{GS,M}; V_{DS,M}$ ); the recovery of drain current related to charge de-trapping is measured over 7 time decades (from 10  $\mu$ s to 100 s) with multiple recording techniques by means of a digital sampling oscilloscope. The measured drain current transients are later elaborated with dedicated fitting to obtain the associated time-constant spectrum.

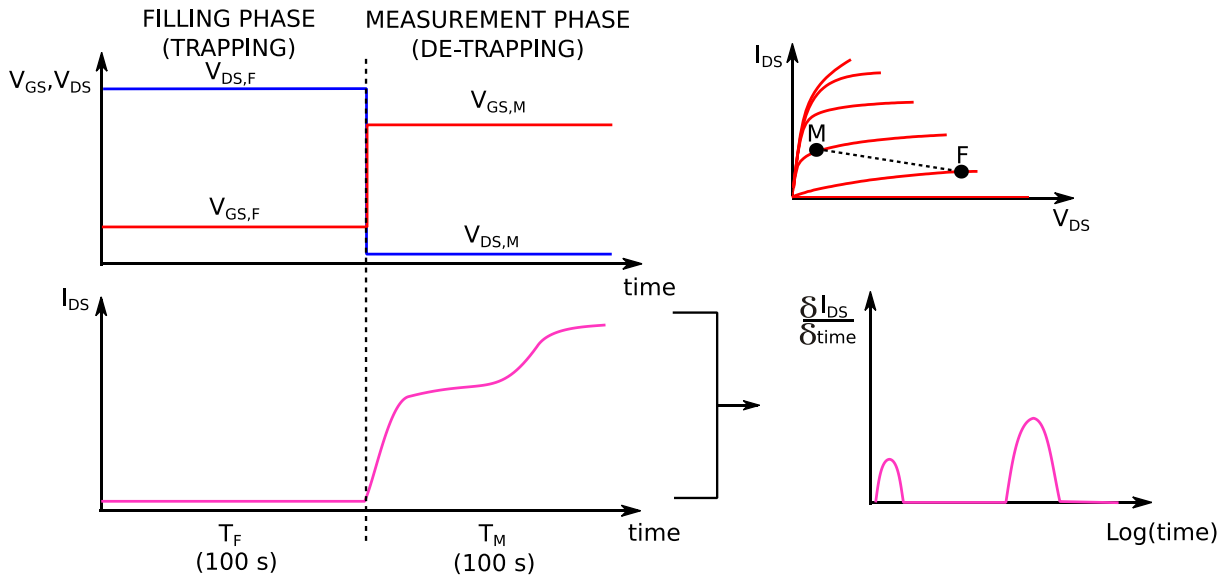


**Figure 2-14: Principle of the drain current transient measurement technique: the device is biased for 100 s in filling condition ( $V_{GS,F}; V_{DS,F}$ ), then it is biased in de-trapping condition ( $V_{GS,M}; V_{DS,M}$ ), for another 100 s to measure drain current transient and to obtain a trapping analysis with the related time-constant spectrum [37].**

### 2.3.2.2 Time constant extraction methodology

In the literature, several mathematical approaches to fit the de-trapping transient data and to extrapolate both time constants and trap amplitudes are reported:

- **polynomial:** the fitting of transient data with a polynomial function and the extrapolation of time constant from the peak of associated drain current derivative [20];
- **multi-exponential:** the fitting of transient data with a least mean square function by the sum of 100 exponentials with fixed time constants and variable amplitude coefficients, and the determination of the time constant by the analysis of the peak of associated drain current derivative [18];
- **stretched multi-exponential:** the fitting of the data by a stretched multi-exponential function and the determination of the time constant by the analysis of the peak of the derivative that corresponds to the time constant of the de-trapping behavior [20].

*Bisi et al.* [20] implemented and compared these three methods to evaluate which method has the best performance and precision in determining the time constant. The comparison of the different fitting algorithms is depicted in Figure 2-15. It appears that the three methods involve three different behaviors: the quasi-ideal exponential transient labeled “T1” in Figure 2-15 is correctly detected by all fitting methods. On the contrary, the “T2D” process has a complex stretched multi-exponential behavior. In this case, it is only with the stretched multi-exponential fitting that the time constants are correctly extracted: the polynomial and the multi-exponential fits present spectral dispersion introducing additional parasitic components in more to the real time constant. In conclusion, the best method in terms of precision and physical sense is the stretched multi-exponential fit. Following these considerations, this method has been adopted to extract the time constant in our study. The stretched multi-exponential function can be expressed as

$$I_{DS,fitting}(t) = \sum_i^N A_i e^{-\left(\frac{t}{\tau_i}\right)^{\beta_i}} + I_{DS,final} \quad (2-15)$$

where  $A_i$ ,  $\tau_i$  and  $\beta_i$ , are fitting parameters corresponding respectively to the trap amplitude, time constant and stretching parameter ( $0 < \beta_i < 1$ ) of  $N$  detected charge-trappings. In the trapping (de-trapping) behavior,  $A_i > 0$  ( $A_i < 0$ ) corresponds to emission and  $A_i < 0$  ( $A_i > 0$ )

corresponds to the capture process. These parameters are numerically calculated and the plot obtained gives a time constant spectrum [20].

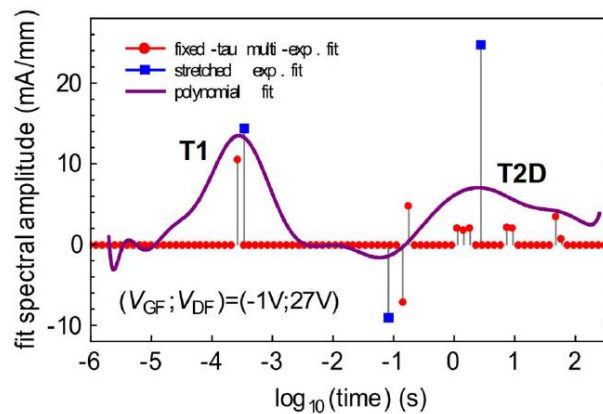


**Figure 2-15: Comparison between the three data fitting solutions: though the pure-exponential T1 process is correctly detected by all the fitting methods, the non-exponential T2D signal is properly detected only by stretched exponential fit, since its detection by polynomial fit and fixed-tau-multi-exponential fit is affected by spectral dispersion [20].**

Another point that strongly affects the DCT results is the choice of the de-trapping bias point. The de-trapping bias point (or measuring-bias point) can be chosen in the linear region or in the saturation region, depending on the intended application of the device, i.e., in the linear region for switch operation mode and in the saturation region for RF operation mode.

As shown by *Bisi et al.* [20] in Figure 2-16, the choice of the de-trapping bias point can impact the transient results. The device measured in the linear region presents one weak emission process, on the contrary the transient measured in the saturation region presents two emission processes. This difference in the measured peaks is due to the fact that the DUT in *Bisi et al.* [20] are sensitive principally to the threshold voltage. This threshold voltage shift impacts the value of the current more seriously in the saturation region than in the linear (ohmic) region.

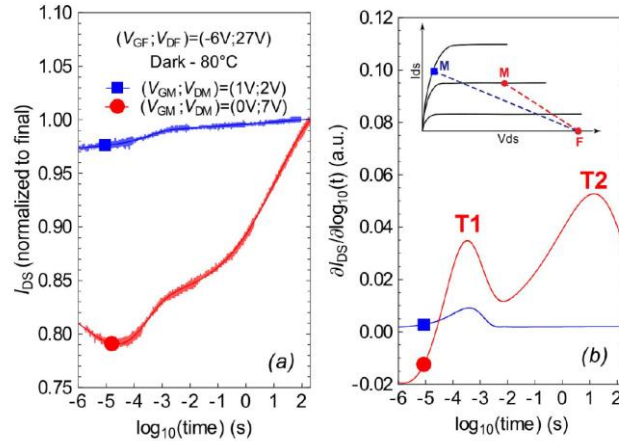


**Figure 2-16: (a) Drain current transients performed in the linear and saturation regions and (b) related differential signals: in good agreement with pulsed measurement, transients recorded in linear region detect only a weak emission process, while those recorded in saturation region reveal much higher current collapse and the presence of two emission processes-labeled T1 and T2 [20].**

### 2.3.2.3 Drain current transient results

To achieve complementary information about the CC, DCT measurements are carried out, starting from three different filling bias conditions  $(V_{GS,F}; V_{DS,F})$  (corresponding to the quiescent bias points used in the previously described pulsed I/V measurements). The results are shown in Figure 2-17. The OFF-state condition defined by  $(V_{GS,F}; V_{DS,F}) = (-5V; 10V)$  induces negligible trapping. The emission process “E4” shows a high drain voltage dependence and clearly appears for the two following conditions: OFF-state defined by  $(V_{GS,F}; V_{DS,F}) = (-5V; 40V)$  and SEMI-ON state defined by  $(V_{GS,F}; V_{DS,F}) = (-1.9V; 40V)$ . Furthermore, the emission process “E2” and the capture process “E3” are mostly induced by the  $(V_{GS,F}; V_{DS,F}) = (-1.9V; 40V)$  bias condition. In order to investigate the properties of traps for the SEMI-ON state, the DCT measurements are carried out at different temperatures. Therefore, the determined time constants with applied temperature correction (the determination of the thermal resistance is presented in Section 2.3.1.3) allows us to determine the activation energy  $E_A$  and the capture cross-section  $\sigma_c$  by using Equation (2-9). The time spectrum analysis and Arrhenius plot are represented in Figure 2-18(b) and Figure 2-18(c), respectively. The analysis for the SEMI-ON state is very interesting because it gives information about which traps will affect the class AB operation bias point of the transistor in a power amplifier. It can be noticed that all emission and capture processes “E2”, “E3” and “E4” will take place in this class AB operation bias point. The Arrhenius plot analysis will be discussed in Section 2.4.

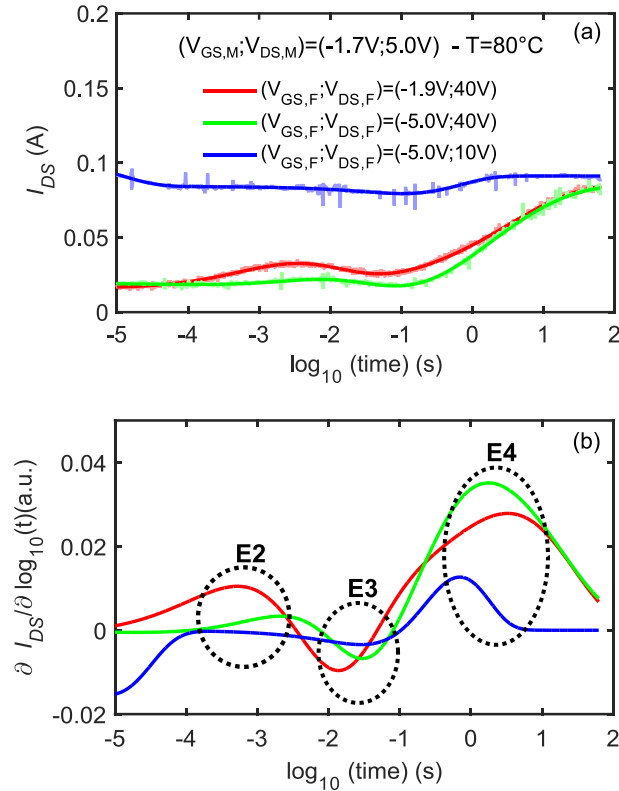


**Figure 2-17: (a) DCT recorded and fitting for three different trapping conditions at  $80^\circ\text{C}$ . (b) Related time spectrum analysis (measured for a  $8 \times 250 \times 0.5 \mu\text{m}^2$  AlGaIn/GaN HEMT).**

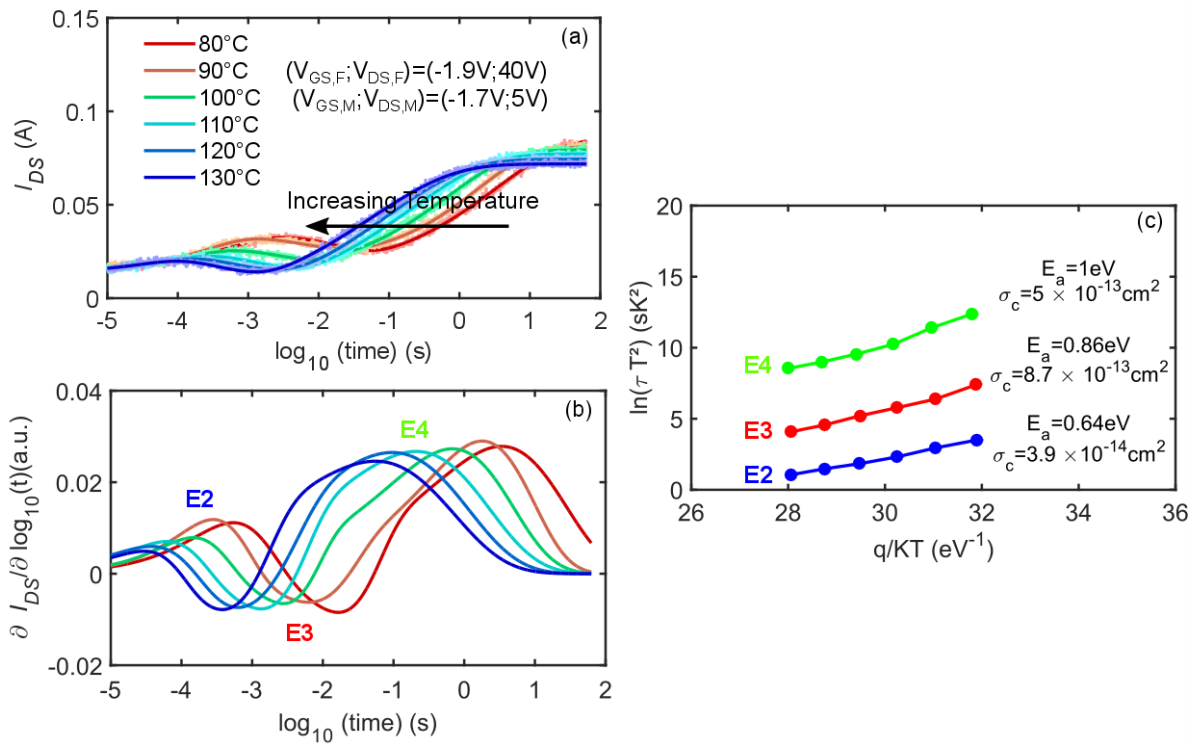


**Figure 2-18: (a) DCT recorded and fitting in SEMI-ON state condition for  $80^\circ\text{C}$  to  $130^\circ\text{C}$  temperature range, (b) related time spectrum analysis and (c) related Arrhenius plot.**

### 2.3.2.4 Filling Time Dependence

To obtain more information on the dynamic behaviour of trap, the evolution of the “E2”, “E3”, and “E4” time spectrum results is reported versus the duration of the filling pulse in Figure 2-19(a). For this investigation, the trapping phenomena were induced by applying  $(V_{GS,F}, V_{DS,F}) = (-1.9V, 40V)$  at constant temperature ( $100^\circ C$ ). The width of filling time varies from  $100 \mu s$  to  $100 s$ . As described in Figure 2-19, the “E4” amplitude increases with time and saturates for a long pulse width. This behavior can be explained by two possible hypotheses. The first one is related to the presence of linear line defects, possibly due to dangling bonds along dislocation core sites. As described in [38], the concentration of the ionized defects has a logarithmic dependency on the duration of the filling pulse ( $t_p$ ) according to the following formula:

$$n_T(t_p) = c_n \tau N_T \ln \left( 1 + \frac{t_p}{\tau} \right) \quad (2-16)$$

where  $c_n$ ,  $\tau$  and  $N_T$  respectively represent the capture probability, the characteristic time for the capture barrier build-up and the total concentration of the defects. Before the saturation of trap occupancy, the charge filling-time may produce a reduction in the capture rate due to the repulsive interaction between the free electrons and the increased negatively charged traps. The second one is related to the presence of acceptor-like traps, where the filling-time is associated with the emission of holes to the valence-band [39]. Simultaneously, the “E2” amplitude decreases when the pulse width increases up to a value which corresponds to the saturation of ionized trap “E4”. The evolution of “E4” and “E2” amplitudes with the filling time suggests that there may exist an equilibrium between the ionization of the two trap states.

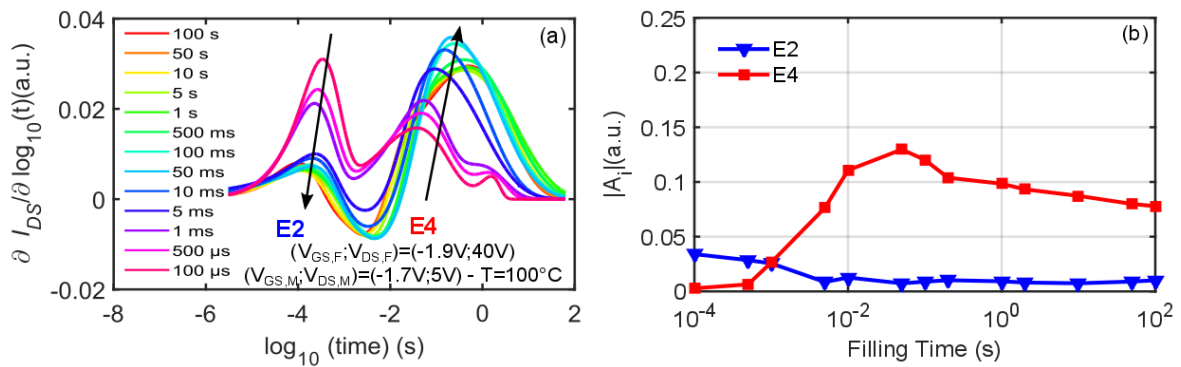


**Figure 2-19: (a) E2 and E4 time spectrum analysis and (b) related amplitude processes dependency on the filling pulse duration.**

### 2.3.2.5 Capture Mechanism: Dependence on Gate Bias and Temperature

To further investigate the trapping behavior due to the RF working conditions, a complete analysis of the dependence of the CC on the gate quiescent bias point (swept from -5V to -1.5V) is performed. It allows emulating the RF sweep condition (that corresponds to a constant DC value of  $V_{DS}$  and an increase DC value of  $I_{DS}$  with the increase of input power level). The results of this CC analysis (evaluated at  $V_{GS}=0V$  and  $V_{DS}=10V$ ) are summarized in Figure 2-20. It shows that for the OFF-state ( $V_{GS} < -2.4V$ ) the CC is constant and for the ON-state ( $V_{GS} > -2.4V$ ) the CC increases significantly with the drain current  $I_{DS}$ . These variations cannot be due to the temperature increase when the drain current increases because Figure 2-20 proves that the CC does not depend on the temperature of the device. The CC increase for the ON-state can rather be attributed to the injection of hot electrons towards traps located in the buffer. This hypothesis is also proposed in [40], which demonstrated an increase of the amplitude of the process with an increase of the gate quiescent bias point. It was then demonstrated that the CC is strongly correlated to the value of the gate quiescent bias conditions in the ON- state.

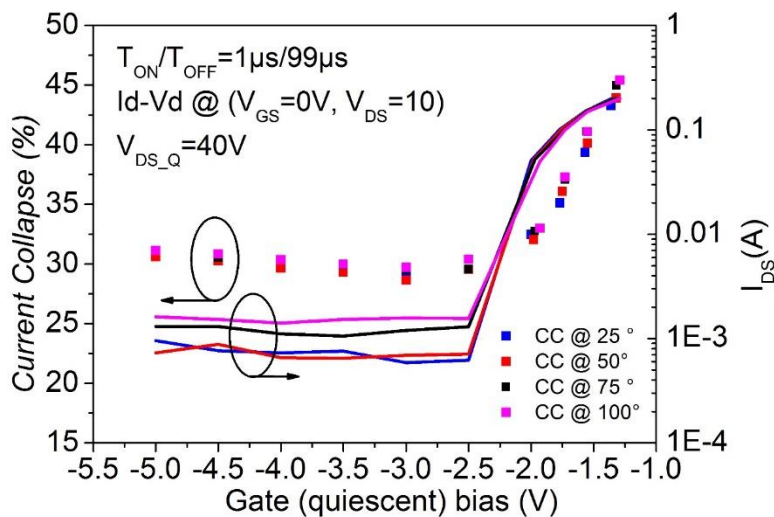


**Figure 2-20: Thermal dependence of CC and  $I_{DS}$  on the gate quiescent bias point for a 40 V drain quiescent bias point.**

The CC measured with this method should possibly be attributed to the trap “E4” which makes a major contribution to the overall current collapse of the transient, as shown in Figure 2-17.



### 2.3.3 Nonlinear microwave drain current transient spectroscopy

In the last years, many research groups [41]–[46] have shown that the nonlinear dynamics of the dispersion effects play a major role in the modification of the large-signal performances when the device is fed by modulated signals like RF pulses or telecommunications signals.

The time constants associated to these dynamic effects can cover a large range of values from tenths of ns to several minutes and are related to the characteristics of the RF signal in a very complex way.

In order to get an insight into the impact of the trapping effects responsible for the modifications in the RF performance, a drain current analysis under RF operation mode is used. The analysis of the charge-trapping through the bias drain current monitoring during RF excitation is of fundamental importance as it provides information about the nonlinear dynamics of the trapping effects in the RF large-signal operation mode. Moreover, this information can be introduced into a CAD model to predict the RF dispersion of the devices.

In this case, the previously developed trapping investigation techniques (such as pulsed I-V, drain current transient spectroscopy, and admittance spectroscopy) can give complementary information. All these methods suffer from the fact that the device does not work under real large-signal conditions. In this section, the RF trapping analysis is carried out with different combinations of DC and RF signal excitations to involve different trapping effects:

- Pulsed RF drain current transient measurement (DC continuous and RF pulse);
- Pulsed DC and RF drain current transient measurement (DC pulse and RF pulse);
- CW RF drain current transient measurement (DC continuous and CW RF).

#### 2.3.3.1 Pulsed RF drain current transient measurement

The first set of measurements used for the trapping investigation due to RF excitation is based on drain current evaluation when a RF pulse is applied. Thus, this trapping analysis technique can be applied to GaN-based HEMT for radar application.

##### 2.3.3.1.1 Pulsed RF drain current transient set-up

The experimental set-up used for both RF waveforms and drain current measurements is shown in Figure 2-21. In order to characterize the DUT under a single pulse measurement, the RF signal must have the shape shown in Figure 2-22. This pulse has a variable width (PW)

and magnitude. The total acquisition time, which allows monitoring the average drain current, has a range between ms to tenths of seconds in order to identify very slow de-trapping phenomena.

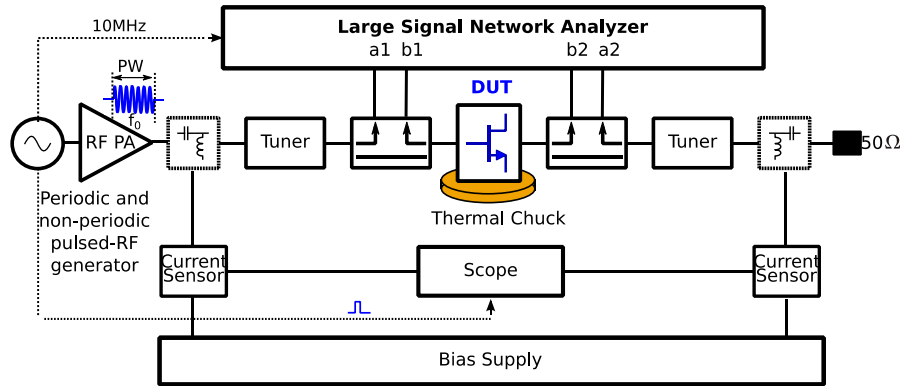


**Figure 2-21: Block diagram of the RF experimental set-up based on LSNA system.**

Moreover, the measurement algorithm requires the periodicity of the RF pulse which is contradictory with this approach. In order to overcome this difficulty, a two-step characterization protocol has been developed. It allows managing the large duration of the transients, which can run from seconds to hundreds of seconds.

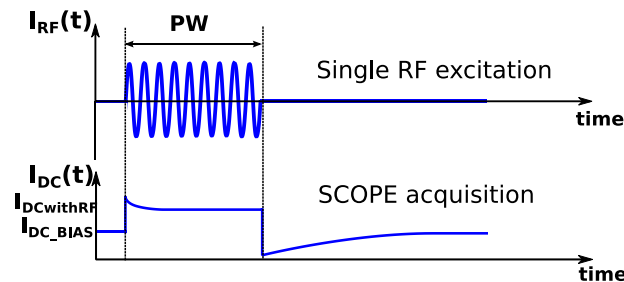


**Figure 2-22: Drain current measurement principle for RF trapping characterization for a single pulse RF excitation.**

The first step of the measurement method consists in performing CW time-domain large-signal load-pull RF measurements using the LSNA. The details of LSNA set-up and calibration are depicted in Section 4.3.1. The time-domain RF voltages and currents and the CW power performance are obtained by the LSNA at the DUT planes. Of course, the output tuner allows modifying the RF loading of the device and thus the shapes of the drain and gate voltages and currents which could impact the trapping effects.

The second step consists in the measurement of the slow transient variations of the bias drain current when a single pulse large-signal excitation is applied or removed. Typical RF PWs range from 1 ms to 200 ms, which is sufficient to excite the traps, as the de-trapping time constants are much slower than the trapping ones. One assumes that the load conditions do

not differ between the CW conditions in the first step of measurement and the single RF filling pulse in the second step. This ensures that the large-signal RF waveforms are very close in the two experiments. The quiescent point is applied to the DUT by means of two external bias tees connected to the DC power supply. The DC-path frequency bandwidth of these bias tees allows applying pulses of 200 ns time duration (a value below the time constants sought in the single pulse experiment). The broadband current sensor (120 MHz 5 A AC/DC hall current probe) connected to a digital sampling scope Tektronix DPO7054 (500 MHz bandwidth, 10 GS/s, 8 bit) allows the measurement of the drain current when the RF input signal is turned OFF. The whole system is calibrated in DC by comparison of its measurement with a DC ampmeter. The results are analyzed through the mathematical approach described in Section 2.3.2.2 to extract the time constants of the traps.

All the measurements are performed on-wafer with a probe station equipped with a thermal chuck. The devices are soldered onto a copper tungsten mount which is assembled on the chuck thanks to a thermal paste. The temperature of the chuck is recorded through a temperature sensor assembled at the base of the transistor mounting.

### 2.3.3.1.2 Pulsed RF drain current transient measurements' results

Several studies on DC trapping effects in GaN transistor have noticed that some parameters play a fundamental role for the traps such as filling bias conditions, filling time and temperature [18], [20]. The objective of this research is to investigate the influence of the following RF measurements' parameters on the charge trap behavior:

- Input power level;
- PW;
- Output load impedance;
- Temperature.

In Figure 2-23, CW time-domain load-pull characterization of the transistor operating in class AB ( $I_{DS}=25$  mA/mm at  $V_{DS}=40$  V) at a frequency of 4 GHz is presented for two different output load impedances:

- Impedance corresponding to the matching of the transistor for maximum PAE (shown in Figure 2-23 in solid line)  $Z_{LOAD\_maxPAE}(f_0) = 20.5 + j44 \Omega$ .
- Fifty Ohm impedance (shown in Figure 2-23 in solid line with circle)  $Z_{LOAD\_50\Omega}(f_0) = 50\Omega$  corresponding to a mismatched impedance for the transistor considered.

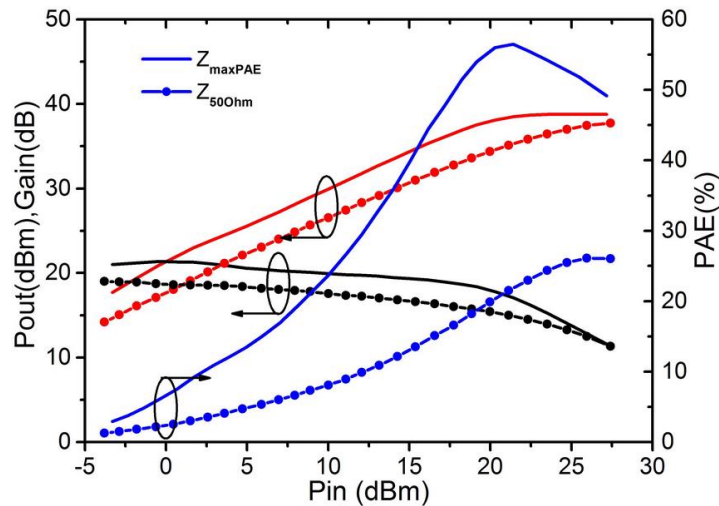


**Figure 2-23: RF power performances measured at 4 GHz (class AB operation mode), in solid line, for maximum PAE at impedance equal to  $Z_{LOAD\_maxPAE}(f_0) = 20.5 + j44 \Omega$  and in solid line with circle for impedance equal to  $Z_{LOAD\_50\Omega}(f_0) = 50 \Omega$ .**

### 2.3.3.1.2.1 Input power level dependence

Bias drain current measurements at different single pulse RF input power levels are performed for a fixed PW= 200 ms, as shown in Figure 2-24. Figure 2-24 shows the value of the average drain current immediately after the cut-off of the RF excitation. This reveals an increasing number of electrons trapped when the input power increases. The load-cycle shown in the insert of Figure 2-24 exhibits drain voltage excursion up to 80 V at maximum output power and a drain current excursion up to 1.5 A.

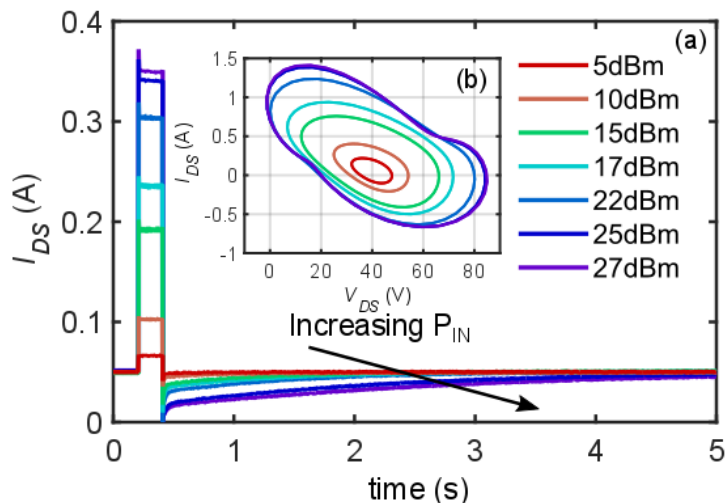


**Figure 2-24: (a) Bias drain current measurements during single pulse excitation for fixed PW=200 ms,  $Z_{LOAD\_maxPAE}$  and at 25°C. While the time range measurement is 10 s, results are shown for a reduced time range to exhibit the linear shape of the pulses. (b) Corresponding extrinsic CW output load-lines derived from wave measurement at  $f_0$ ,  $2f_0$  and  $3f_0$ .**

The results obtained for fixed PW,  $Z_{load\_maxPAE}$  and input power variation are summarized in Figure 2-25. They indicate the presence of two traps in the trapping/de-trapping process. At relatively low input power only the trap, labeled “T1” in the Figure 2-25(b), is observed. As the input power increases, the number of electrons trapped increases as previously mentioned and the trap, labeled as “T2” in Figure 2-25(b), becomes predominant. Moreover, for the high compression gain ( $P_{in} = 25$  dBm (7 dB comp.) and  $P_{in}=27$  dBm (9 dB comp.)), there can be observed a saturation of drain current during the pulse (in Figure 2-24) that produces an equivalent saturation of the CC (in Figure 2-25(a)) evaluated at 1 ms after the RF pulse is OFF. This indicates that the majority of the traps are ionized under such high compression levels. It must be noted that for an input power above 22 dBm a decrease of the magnitude of “T1” is observed while the magnitude associated with “T2” keeps increasing. Moreover, the “T1” has an emission time constant significantly lower than “T2”.

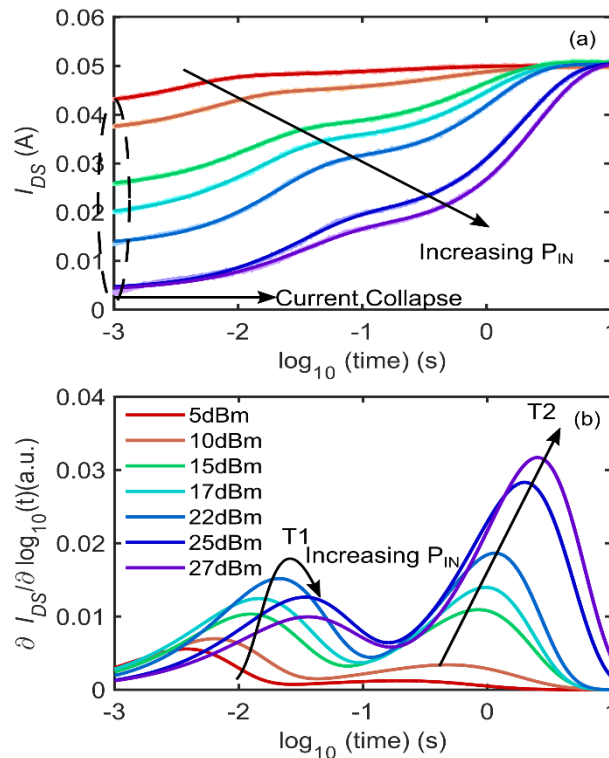


**Figure 2-25: (a) De-trapping drain current transient measurements and stretched multi-exponential fitting (PW=200 ms,  $Z_{LOAD\_maxPAE}$  and at 25°C). (b) Time constant analysis of de-trapping transient.**

The increasing magnitude of the peak associated to “T2”, as shown in Figure 2-25(b), indicates that the ionization of this trap appears for large voltage excursion. This is due to a selective ionization of those deep level traps which are located in the buffer [28]. The detailed mechanism of the physical process remains to be determined. Moreover, the decrease of the magnitude of the peak associated to “T1” for input power above 22 dBm suggests that some

of the electrons trapped at this level are re-emitted during the 200 ms RF pulse. More surprisingly, the time constants of the traps are increasing when the power level is increased. This is in contradiction with Shockley-Read-Hall model: the expected increase of the temperature of the device which should lead to a decrease of those time constants.

### 2.3.3.1.2.2 Pulse-width dependence

Bias drain current transient measurements are carried out, in order to achieve complementary information on the trapping phenomena (“T1” and “T2”), for a PW variation from 1 ms to 200 ms at fixed  $P_{in}=25$  dBm (7 dB comp.) as shown in Figure 2-26.

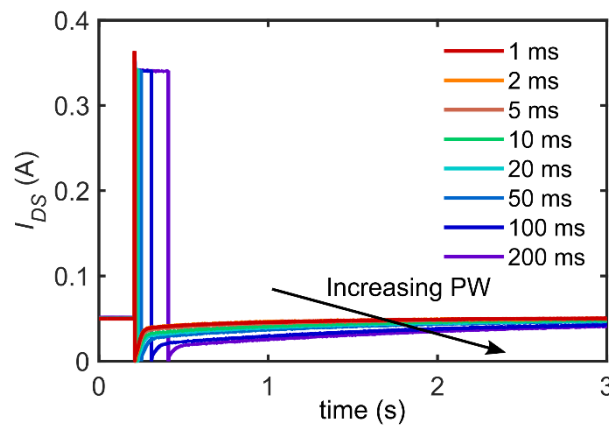


**Figure 2-26: Bias drain current measurements during single pulse excitation for different PWs and at fixed  $P_{in}=25$  dBm,  $Z_{LOAD\_maxPAE}$  and  $25^{\circ}C$ . While the time range measurement is 10 s, results are shown for a reduced time range to exhibit the linear shape of the pulses.**

As in the previous section, the two trap emission processes: “T1” and “T2” are identified in Figure 2-27. The time constant associated to “T1” is constant with the PW duration and its amplitude decreases with the PW duration while the time constant and amplitude associated to “T2” increase with PW duration. Moreover, the initial and final values of the drain current variations remain constant whatever the PW is. Also, the sum of the amplitudes  $A_i$  of “T1” and “T2” is constant with PW variations (as shown in Figure 2-27(a)). One can conclude that the number of electrons trapped, for PWs above 1ms, depend only on the input power. However, the results shown in Figure 2-27 clearly demonstrate that the PW changes the repartition of these electrons between the two trap phenomena at the end of the RF pulse. This is due to the fact that the capture time constant of “T2” is in the range of the duration of the pulses. Once again this measurement clearly confirms that the trapping process and not the higher temperatures reached during RF excitation is responsible for the CC. A careful examination of Figure 2-27(b) and Figure 2-28(b), reveals that the time constant of “T1” does

not change with the PW. Considering the extreme sensitivity of this time constant to temperature changes, this signifies that the temperature at 1 ms after the RF OFF is the same for all the PW considered. For a filling pulse of 1 ms “T1” are completely ionized while most of “T2” are not ionized. Therefore, when the PW increases some of the electrons captured by “T1” are re-emitted and captured by “T2” before they are finally released in the channel with emission time constant of “T2”. This experiment clearly demonstrates the strong interaction between the two trap phenomena. This remains to be modeled through physical simulation.

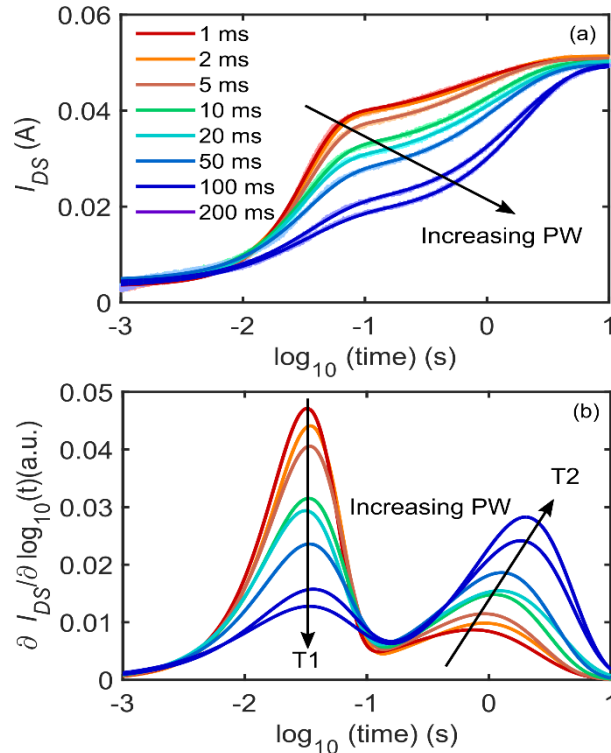


**Figure 2-27: De-trapping drain current transient measurements and stretched multi-exponential fitting ( $P_{in}=25$  dBm,  $Z_{LOAD\_maxPAE}$  and at  $25^{\circ}C$ ). (b) Time constant analysis of de-trapping transient.**

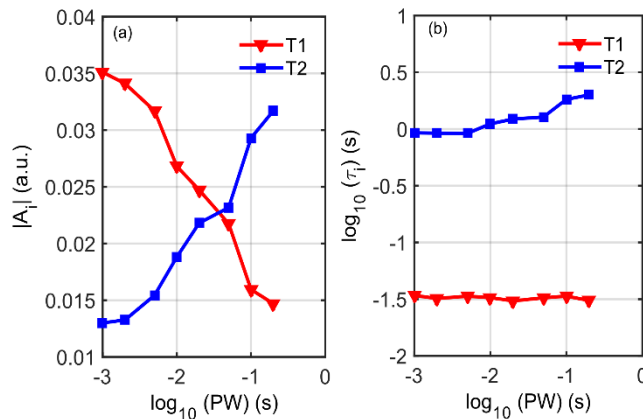


**Figure 2-28: (a) “T1” and “T2” amplitude processes versus PW durations (b) “T1” and “T2” time constant processes versus PW durations.**

### 2.3.3.1.2.3 Output load impedance dependence

To study the trapping phenomena as a function of the output load impedance, two different load impedances are chosen: the maximum of PAE impedance (that is normally the one chosen for HPA design) and one of  $50 \Omega$ . Results for maximum PAE impedance have been presented previously.

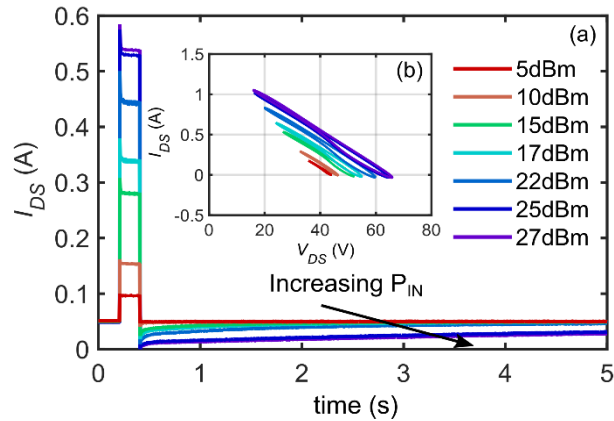


**Figure 2-29: (a) Bias drain current measurements during single pulse excitation for fixed  $PW=200$  ms,  $Z_{LOAD\_50\Omega}$  and at  $25^\circ\text{C}$ . While the time range measurement is 100 s, results are shown for a reduced time range to exhibit the linear shape of the pulses. (b) Corresponding extrinsic CW output load-lines derived from wave measurement at  $f_0$ ,  $2f_0$  and  $3f_0$ .**

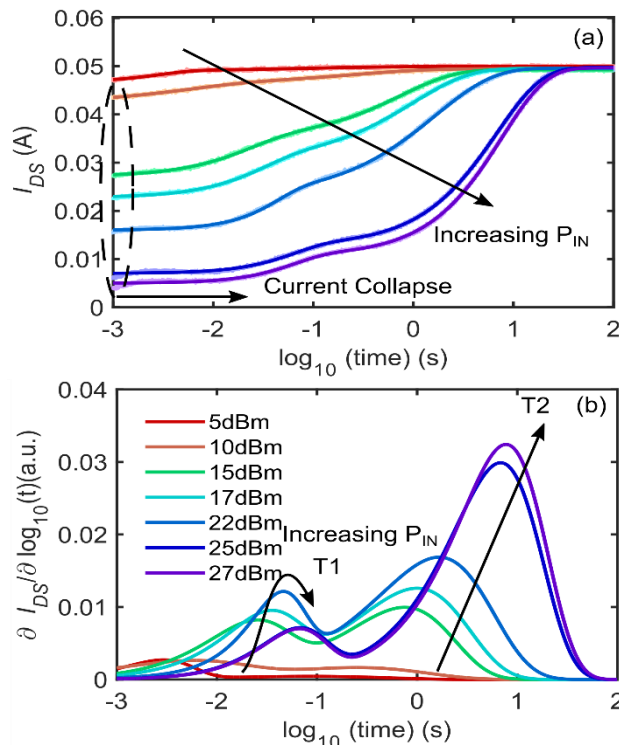


**Figure 2-30: (a) De-trapping drain current transient measurements and stretched multi-exponential fitting ( $PW=200$  ms,  $Z_{LOAD\_50\Omega}$  and at  $25^\circ\text{C}$ ). (b) Time constant analysis of de-trapping transient.**



In Figure 2-29, the bias drain current measurement at different RF input power levels (for fixed  $PW=200$  ms and  $Z_{LOAD\_50\Omega}$ ) is reported. The time constant spectrum in Figure 2-30(b) shows the presence of “T1” and “T2”. The amplitude and time constant of “T1” and “T2” have a similar trend to the traps in case of maximum PAE impedance, with lower time constants (the experimental values are compared in Section 2.3.3.1.4).

### 2.3.3.1.2.4 Temperature dependence

Temperature dependence was investigated using single pulse RF measurement at maximum of PAE impedance, at fixed  $PW=200$  ms and fixed  $P_{in}=25$  dBm (7dB comp.) for several temperatures. The results described in Figure 2-31 therefore indicate that for fixed 25 dBm input power level, the drain current value during single pulse RF excitation has decreased slightly with the increase of temperature. Figure 2-32(a) shows that the CC at 1 ms after RF OFF decreases with the increase of temperature because the emission process is activated by temperature and at that time a number of electrons have already been released.

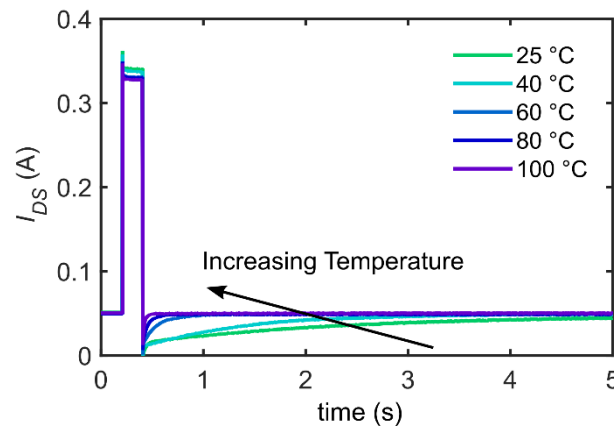


**Figure 2-31: Bias drain current measurements during single pulse excitation for different temperatures at fixed  $P_{in}=25$  dBm,  $PW=200$  ms and  $Z_{LOAD\_maxPAE}$ . While the time range measurement is 10 s, results are shown for a reduced time range to exhibit the linear shape of the pulses.**

The time constant spectrum in Figure 2-32(b) shows that the peak related to “T2” shifts leftwards when the temperature increases and this shift is in agreement with DCT. In this case only the “T2” is activated for temperatures above  $40^{\circ}\text{C}$ . At  $25^{\circ}\text{C}$ , it can be observed that “T1” is detected and that the amplitude of “T2” peak for this temperature is lower than expected. As already observed, there is a strong interaction between the two trapping phenomena “T1” and “T2”; the fact that the trap “T1” is present at  $25^{\circ}\text{C}$  suggests that there is a transfer of electrons from trap “T1” to trap “T2” at  $25^{\circ}\text{C}$ , indeed the amplitude of “T2” peak is increased and “T1” has disappeared at  $40^{\circ}\text{C}$ , thus “T1” may be not a trap signature.

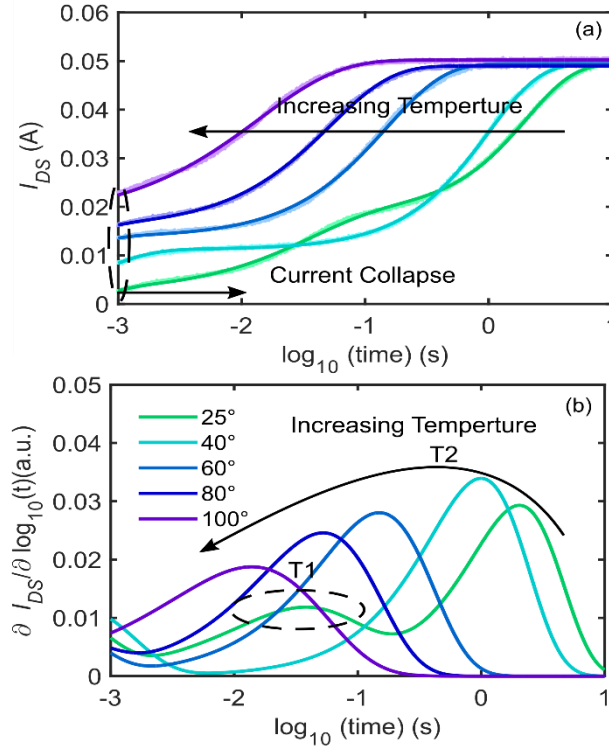


**Figure 2-32: (a) De-trapping drain current transient measurements and stretched multi-exponential fitting ( $P_{in}=25$  dBm,  $PW=200$  ms &  $Z_{LOAD\_maxPAE}$ ). (b) Time constant analysis of de-trapping transient.**

### 2.3.3.1.3 Comparison of the RF pulse and DC pulse trapping effects

#### 2.3.3.1.3.1 Gate DC pulse drain current transient set-up

To investigate the CC due to single pulse RF excitation, the DC drain current pulse technique is used. This technique is based on single gate pulsing from semi-on state ( $V_{G\_QP}$  in Figure 2-33) to on-state voltage ( $V_{G\_PULSE}$  in Figure 2-33). By choosing  $V_{G\_QP}$  and  $V_{D\_QP}$  in such a way that the quiescent bias point is the same as for the single RF pulse experiment, the initial trap state of the device is the same for the two experiments. The on-state gate voltage is selected in order to get the same value of the drain current as the average one obtained when the DUT is driven by single pulse RF excitation. The drain voltage is fixed to the same value of class AB quiescent point. This technique is already used in [47] to explain the CC and the attendant trapping effects under RF excitation.

The measurement set-up (in Figure 2-33) is based on the use of an Agilent 33220A arbitrary waveform generator for gate pulsing and a BILT AMCAD power supply to apply the DC drain value. The drain and gate voltages are applied to the DUT by means of two external bias tees with RF port connected to  $50 \Omega$ . Therefore, the state of the device is the same as in the

previous experiment apart from the fact that there is no RF signal applied. The bias drain current is measured with a large bandwidth current sensor (120 MHz 5 A AC/DC current probe) connected to a digital sampling scope Tektronix TDS 5104 (1 GHz bandwidth, 5 GS/s, 8 bit). The output pulse signal generated by the gate pulse power supply (Sync signal in Figure 2-33) is used to trigger the digital sampling scope. The system was controlled remotely and automatically by a SCILAB program.

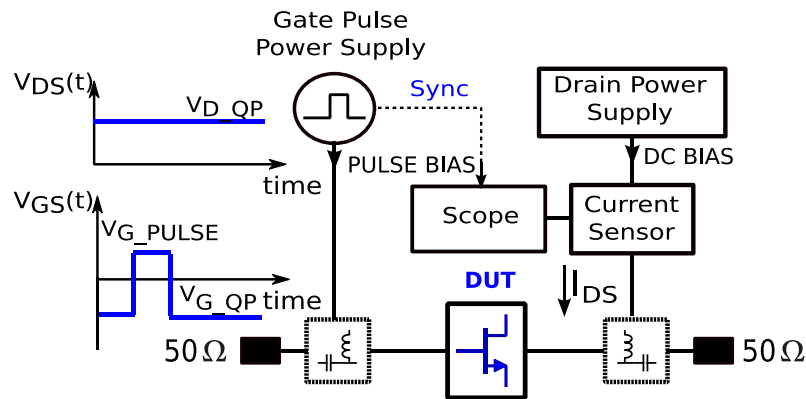


**Figure 2-33: Block diagram of experimental set-up for gate DC pulse mode.**

### 2.3.3.1.3.2 Gate DC pulse drain current transient measurements' results

The DC investigation is carried out on the same device by means of the drain current pulse technique based on gate DC pulse mode (described in the following), to highlight the de-trapping transient characteristics when a gate DC pulse and constant drain voltage are applied.

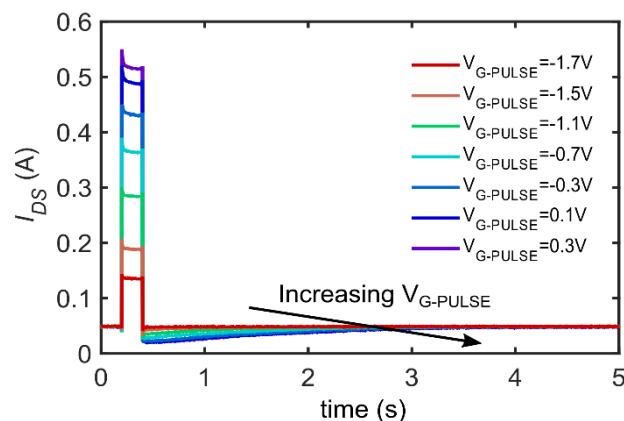


**Figure 2-34: Bias drain current measurements during single gate pulse excitation for different gate voltage values during the pulse, at fixed PW=200 ms and with RF port of bias tees connected to 50 Ω. While the time range measurement is 10 s, results are shown for a reduced time range to exhibit the linear shape of the pulses.**

As shown in Figure 2-33, the RF port of the bias tees are connected to  $50 \Omega$  to ensure that the transistor is in the same RF loading as in the single pulse RF measurement with  $50 \Omega$  load impedance.

The results of this DC investigation are summarized in Figure 2-34. The values of  $V_{G\_QP}$  and  $V_{D\_QP}$  are chosen to bias the device in class AB operation mode ( $-1.98 \text{ V}$  and  $40 \text{ V}$  for gate voltage and drain voltage respectively, for this GaN technology). The results of de-trapping transient for different gate pulse voltage values are presented in Figure 2-35. The magnitude of the CC (in Figure 2-35(a)) and the time constant associated to “T2” (in Figure 2-35(b)) show a significant increase with an increase of  $V_{G\_PULSE}$ . This increase can rather be attributed to the injection of hot electrons towards traps located in the buffer [40]. This is the same mechanism seen with pulsed I/V measurement in Section 2.3.2.5. It can be observed that the CC at 1 ms after the gate DC pulse is OFF increases with the amplitude of the gate filling pulse.

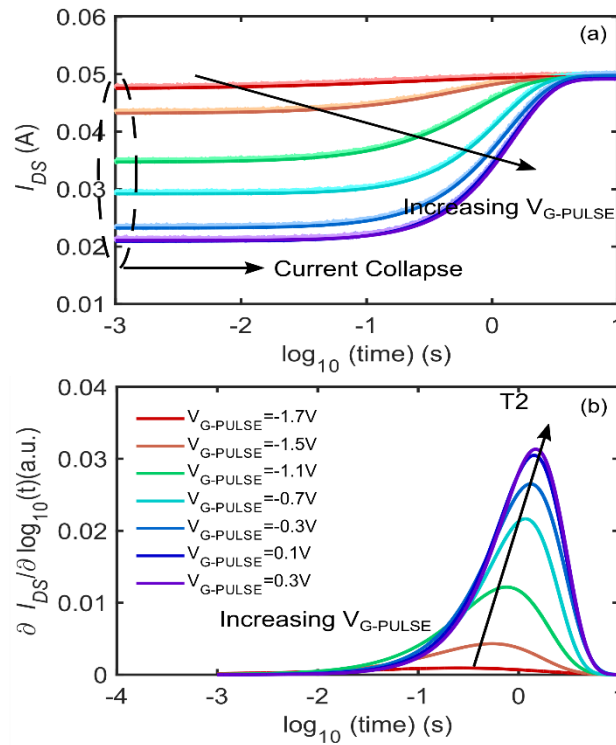


**Figure 2-35: (a) De-trapping drain current transient measurements and stretched multi-exponential fitting for different gate voltage values during the pulse (PW=200 ms & RF port of bias tees connected to  $50 \Omega$ ). (b) Time constant analysis of de-trapping transient.**

### 2.3.3.1.4 Discussion of the results

The results of comparing the CCs, trap amplitudes and time constants as a function of variations in the values of the drain current pulses are summarized in Figure 2-36. It can be observed that at high drain currents there are large differences in the amplitudes and time constants of the “T2” time spectrum between pulse DC measurements and pulse RF measurements.

This is due to the fact that the DC testing has a fixed drain voltage value and thus the electric field is constant. In RF testing the high gate and the high drain voltage excursions are applied simultaneously and promote very deep trapping processes [28]. The results of comparing the trap amplitudes and time constants as functions of the input power level variation for different output load impedances are presented in Figure 2-37. For high gain compression, the “T2” time constants in  $Z_{LOAD\_50\Omega}$  case are quite one decade higher than in the  $Z_{LOAD\_maxPAE}$  case. This appears to be in disagreement with the fact that for  $P_{in}=25$  dBm the extrinsic drain voltage excursion is 50 V (in Figure 2-29(b)) for the  $Z_{LOAD\_50\Omega}$  case and in the  $Z_{LOAD\_maxPAE}$  case is equal to 80 V (in Figure 2-24(b)). Thus, a higher drain voltage excursion results in a slower relaxation time. But in this case the drain current level during single pulse RF excitation is higher. For the time being, it is difficult to draw a general conclusion about the impact of RF voltage and current excursions on the emission time constants.

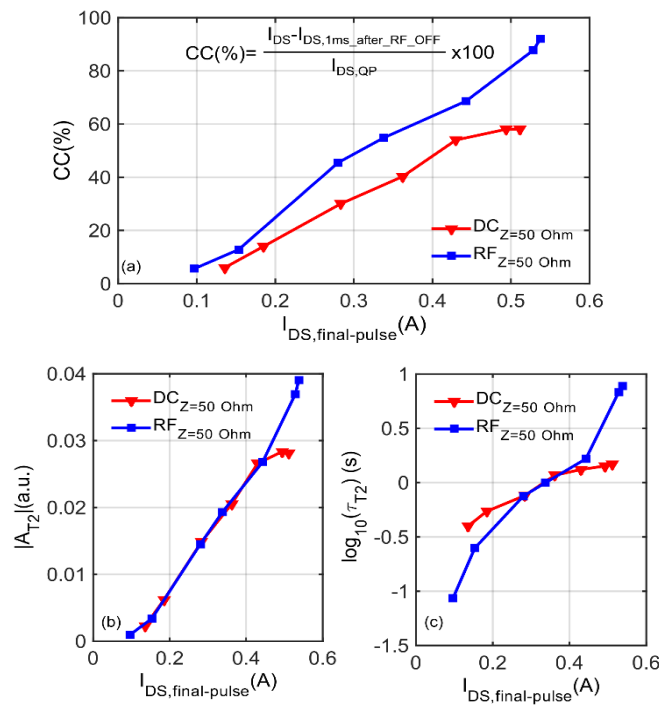


**Figure 2-36: Comparison of (a) CC, (b) “T2” amplitude and (c) “T2” time constant between DC drain current pulse measurement in red and 50 load impedance single pulse RF measurement in blue.**

The logarithmic dependence of the “T2” amplitude on the PW, as shown in Figure 2-28(b), should be related to the presence of linear line defects, possibly due to dangling bonds along the dislocation core sites as reported in [38]. The previous hypothesis is also strengthened by the observed logarithmic dependence of the time constant on the RF input power level (Figure 2-37(b)). The time constant range and the peak amplitude of trap “T2” suggest that this is related to the deep level “E4” detected in Section 2.3.3.2.2.3.

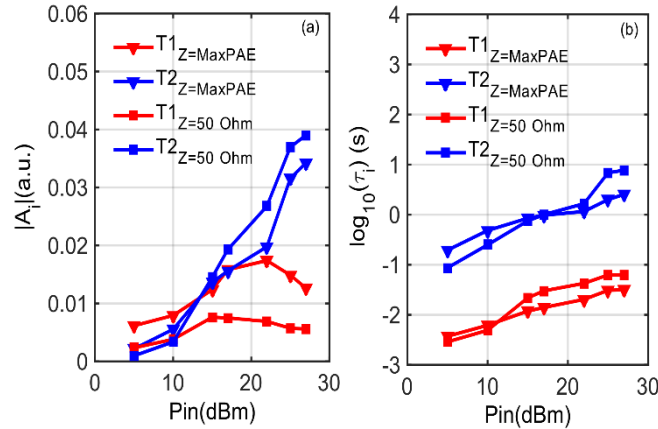


**Figure 2-37: Comparison of (a) trap amplitude and (b) time constant between single pulse RF measurement as a function of input power levels for different output load impedance: maximum of PAE (solid line with triangle) and 50 Ω (solid line with square).**

### 2.3.3.2 Pulsed DC and RF drain current transient measurement

The pulsed RF drain current transient measurement described in the previous section has shown its limitations in the evaluation of de-trapping effect in the way that the de-trapping condition after RF OFF is fixed by the continuous DC bias point of class AB condition and ambient temperature. In this section, the classic pulsed DC drain current transient measurements described in Section 2.3.2 are adapted, adding an RF excitation in filling condition to allow the microwave trapping characterization methodology (for determining  $E_A$  and  $\sigma_c$ ).

#### 2.3.3.2.1 Experimental Set-up

The set-up used for the analysis of the trap responsible for RF dispersion effects is shown in Figure 2-38. The device is initially kept in a trapping condition by applying both a DC filling pulse ( $V_{DF}$ ;  $I_{DF}$ ) and an RF filling pulse for 100 s, thus inducing a specific trapping state. Subsequently, the RF excitation is switched OFF and the device is biased in the saturation region ( $V_{DM}$ ;  $I_{DM}$ ) for another 100 s to evaluate the de-trapping transient, as shown in Figure

2-39. The recovery of drain current related to charge de-trapping is measured over 5 time decades (from 1 ms to 100 s) with a current sensor connected to a digital sampling scope. Thereafter, the de-trapping transient results are fitted with a stretched multi-exponential function to extrapolate the time constant from the peak of the  $\partial I_{DS}/\partial \log(t)$  curves.

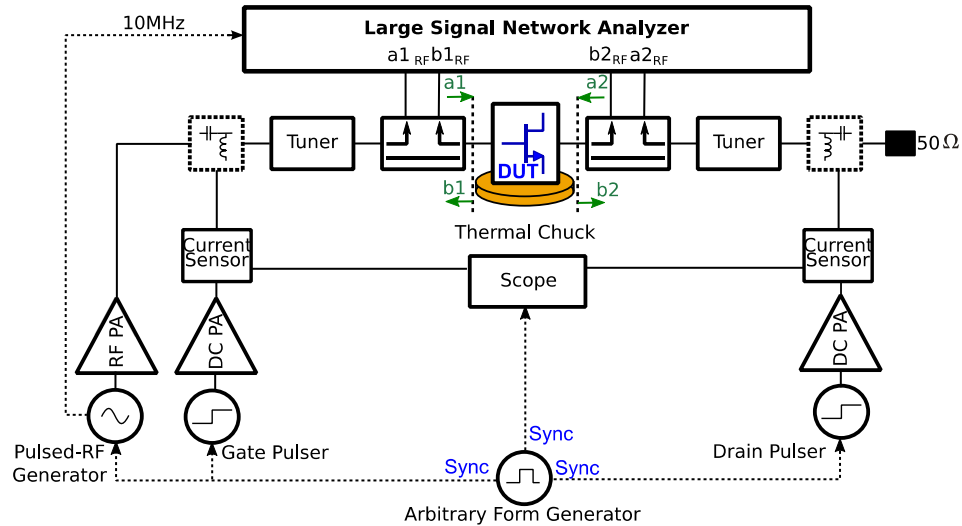


**Figure 2-38: Block diagram of microwave drain current spectroscopy set-up.**

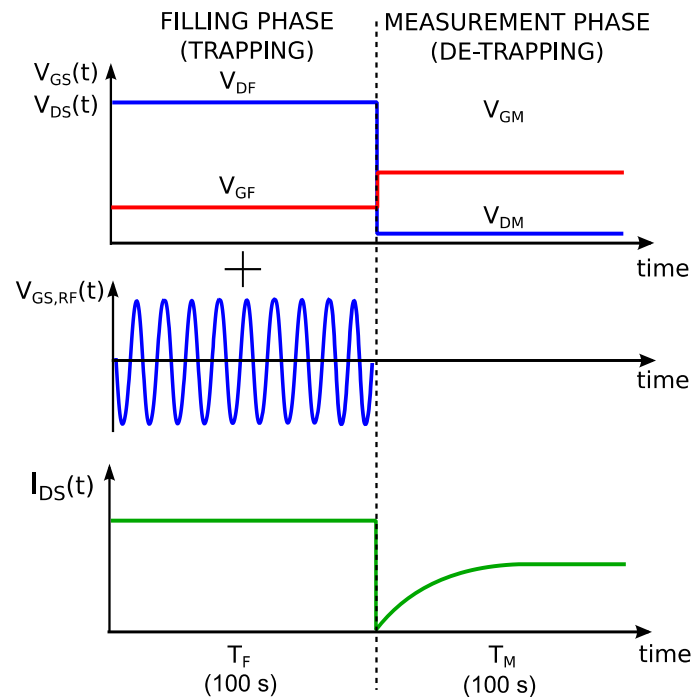


**Figure 2-39: Timing diagram of microwave drain current spectroscopy.**

The RF waveforms are continuously measured at the DUT planes during the filling phase using an LSNA. The generation of DC (by gate and drain pulsers) and RF (by pulsed-RF generator) excitations and the measuring of the DC current and RF waveforms are synchronized by an arbitrary waveform generator.

### 2.3.3.2.2 Experimental Results and Discussion

For this trapping investigation the  $8 \times 250 \mu\text{m}$  GH 50-10 AlGaIn/GaN HEMT was operated in class AB ( $I_{\text{DS}}=25 \text{ mA/mm}$  at  $V_{\text{DS}}=40 \text{ V}$ ) at a frequency of 4 GHz for an optimum PAE impedance  $Z_{\text{LOAD\_opt,PAE}}(f_0)=19.5+j68\Omega$ . The CW RF power performance (shown in Figure 2-40) was measured before the trapping investigation. One of the trapping mechanisms responsible of the modification of the large-signal RF performance is shown in Figure 2-41. The  $I_{\text{D}}-V_{\text{G}}$  characterization is performed before and several times after 100 s of RF stress at  $P_{\text{in}}$  equal to 27 dBm in class AB operation mode – this input power corresponds to a high compression level of 12 dB. The results of  $g_{\text{m}}$  (derived from  $I_{\text{D}}-V_{\text{G}}$ ) measurements in Figure 2-41 show a threshold voltage ( $V_{\text{TH}}$ ) positive shift after RF stress. This  $V_{\text{TH}}$  positive shift indicates an accumulation of negative charges trapped under gate region [20]. In order to further investigate the trapping phenomena responsible for the  $V_{\text{TH}}$  shift, microwave drain current transient measurements are carried out. In the following, we investigate the influence of the bias point ( $V_{\text{DM}}$ ;  $I_{\text{DM}}$ ) in de-trapping condition, the input power level and the temperature on the dynamic behavior of the charge-trapping.

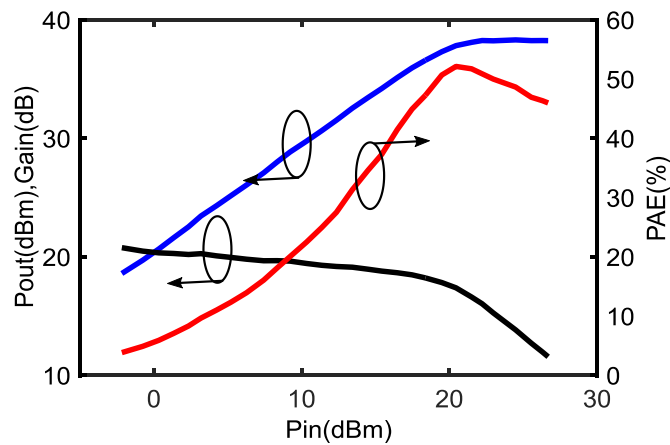


**Figure 2-40: RF power performances at 4 GHz (class AB operation mode) for maximum PAE at  $Z_{\text{LOAD\_opt,PAE}}(f_0)=19.5+j68\Omega$ .**



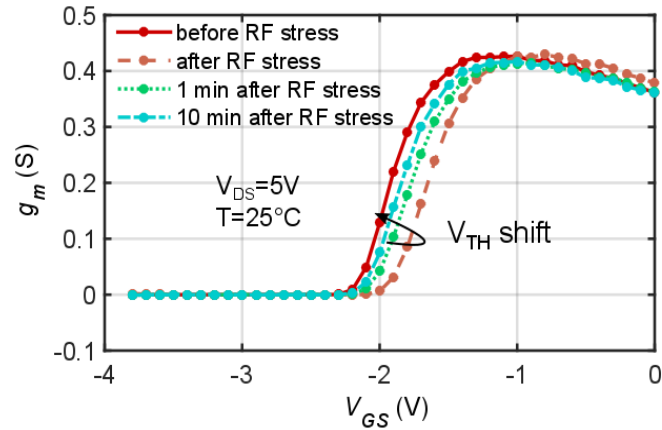


**Figure 2-41: Variation of  $g_m$  (derived from  $I_D$ - $V_G$  characteristic) before and after 100 s of RF stress at  $P_{in}$  equal to 27 dBm in class AB operation mode.**

### 2.3.3.2.2.1 Bias point dependence in de-trapping condition

The dependence of the de-trapping behavior is investigated by drain current transient measurements for different bias point ( $V_{DM}$ ;  $I_{DM}$ ) in the de-trapping condition as shown in Figure 2-42. The trap state is fixed with a DC filling bias condition equal to ( $V_{DF}$ ;  $I_{DF}$ )=(40 V; 50 mA) and with a RF filling condition with  $P_{in}$  equal to 27 dBm. The shape of the current in Figure 2-42 shows that for a fixed  $I_{DS}$  and an increase of  $V_{DS}$ , the de-trapping processes are accelerated. In the same way, for a fixed  $V_{DS}$  and increase of  $I_{DS}$  the time constants become faster. These accelerations of emission process are firstly due to the increase of the power dissipation for fixed  $V_{DM}$ , leading to an increase of the operating temperature of device, and secondly to the Poole-Frenkel effect when  $V_{DM}$  increases. Indeed, the measurement results in Figure 2-43 obtained for a fixed  $I_{DS}$  show that the emission rate increases exponentially with the square root of the applied field, according to the Poole-Frenkel model [48]. In Figure 2-43 the error bar indicates the estimated variation of de-trapping time constant due to the channel temperature increases. In the following measurements, ( $V_{DM}$ ;  $I_{DM}$ )= (5 V; 100 mA) is chosen. The low drain voltage allows to minimize the electric-field effect during the monitoring while a drain current equal to 100 mA allows a better investigation of trapping effects.

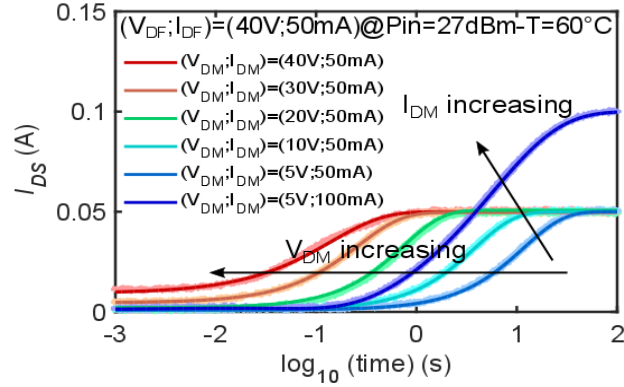


**Figure 2-42: De-trapping drain current transient measurements and stretched multi-exponential fitting for different bias points  $(V_{DM}; I_{DM})$  in de-trapping condition with a DC filling bias condition of  $(V_{DF}; I_{DF}) = (40\text{ V}, 50\text{ mA})$  and an RF filling condition of  $P_{in}$  equal to 27 dBm.**

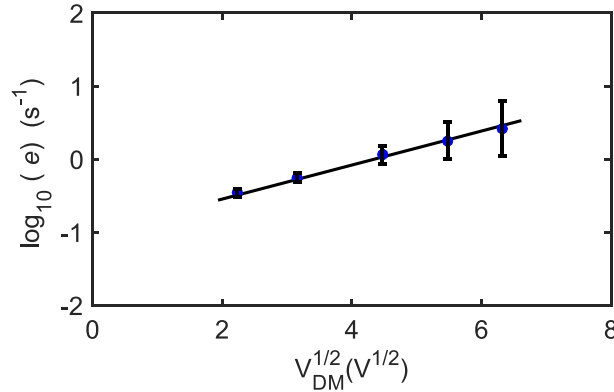


**Figure 2-43: Emission rate as a function of the square root of the applied voltage  $(V_{DM})$  during the de-trapping condition for a fixed  $I_{DS}$  equal to 50 mA (min-max time constants variation with junction temperature estimation reported on the error bars).**

### 2.3.3.2.2.2 RF Input power level dependence

In order to investigate the trapping effects due to DC and RF excitations, the drain current measurements are carried out firstly with no RF excitation and then with increasing RF input power, as shown Figure 2-44(a). The associated load-lines responsible to RF trapping effects are illustrated in Figure 2-44(c). In particular, the de-trapping drain current transient measurements and the associated time constant analysis are depicted respectively in Figure 2-44(b) and Figure 2-44 (d). The DC mode gives rise to two trapping phenomena: one capture process and one emission process labeled, respectively, “E3” and “E4”. The capture process “E3” disappears with an increase of input power. The increase of CC versus  $P_{in}$  at 1 ms after the filling phase, which corresponds consequently to the increase of “E4” trap density, is due to the fact that more and more trap centers “E4” have been excited by the increasing electric field (capture process). The electric field increases promote an increase in the high gate and

high drain voltage excursions [42]. The trap centers “E4” are possibly located in the buffer [28].

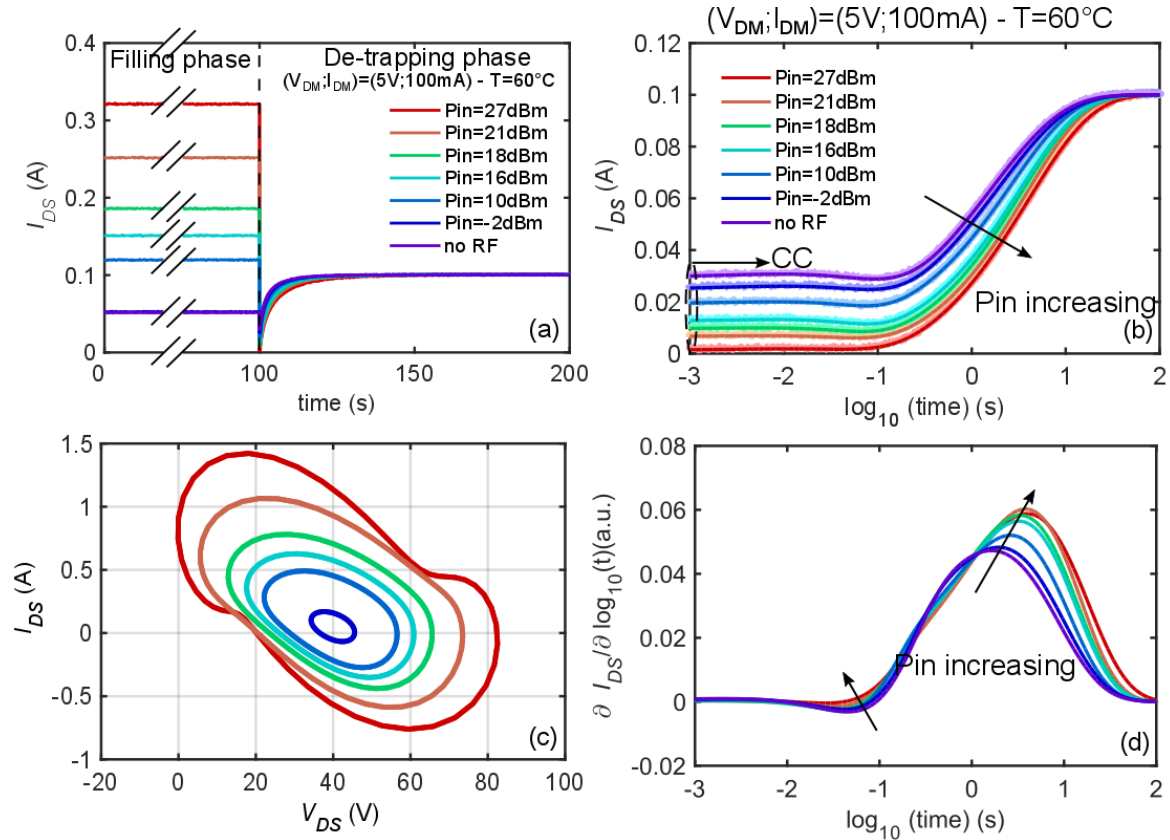


**Figure 2-44: (a) Drain current measurements recorded with and without a variable level of RF excitation at  $60^\circ\text{C}$ . (c) Corresponding extrinsic output load-lines derived from waveforms at  $f_0$ ,  $2f_0$  and  $3f_0$  measured at 90 s after starting RF pulse. (b) De-trapping drain current transient measurements and stretched multi-exponential fitting without RF excitation and with an increase to power input level at  $60^\circ\text{C}$ . (d) Related time spectrum analysis of de-trapping transient.**

In the time range [100 ms – 100 s] “E4” emission process is observed and shown in Figure 2-44(d). The electric field is fixed by the bias point  $(V_{DM}; I_{DM})$  and does not vary. Moreover, the junction device temperature can be considered as stabilized (i.e. determined only by the bias point  $(V_{DM}; I_{DM})$ , and independent of the previous filling excitations). Then, we do not expect the emission time constant to vary with the different previous filling excitations. In Figure 2-44(d), it is observed that the emission time constant has only a small variation in the time range [ $\sim 2.5$  –  $\sim 6$  s] with increasing input power level and exhibits a saturation when the input power level is above 21 dBm. This emission time constant variation is negligible with respect to the ones of Arrhenius plot in Figure 2-47, which is equal to two decades with only  $40^\circ\text{C}$  temperature variation. Thus, to a approximation, only the amplitude of current recovery varies, due to the increasing of ionized trap density with respect to  $P_{in}$  in the filling phase. In

Figure 2-44(b), it is also possible to evaluate the impact of the trapping effect due to DC and RF excitations: the CC at 1 ms after filling condition and the “E4” trap density for a RF filling pulse at Pin equal to 27 dBm are 25% more important than the DC ones.

### 2.3.3.2.2.3 Temperature dependence

For a deeper understanding of the properties of the involved levels “E3” and “E4”, the drain current transients are measured at several temperatures in DC and RF filling conditions (with Pin equal to 27 dBm), in Figure 2-45(a), respectively, Figure 2-46(a), to extrapolate the Arrhenius plot. The results of the Arrhenius plot shown in Figure 2-47 present two trap signatures, namely “E3” and “E4”, obtained from DC excitation with apparent activation energies of 0.73 eV and 0.75 eV and capture cross section of  $1.4 \times 10^{-15} \text{ cm}^2$  and  $1.4 \times 10^{-14} \text{ cm}^2$ . Figure 2-45 shows also that the trap “E3” gives only a minor contribution to overall temperature de-trapping transients. One trap signature “E4” is identified from the RF excitation with activation energy 0.85 eV and cross section  $9.4 \times 10^{-15} \text{ cm}^2$ . The Arrhenius plot results are corrected to consider device self-heating.

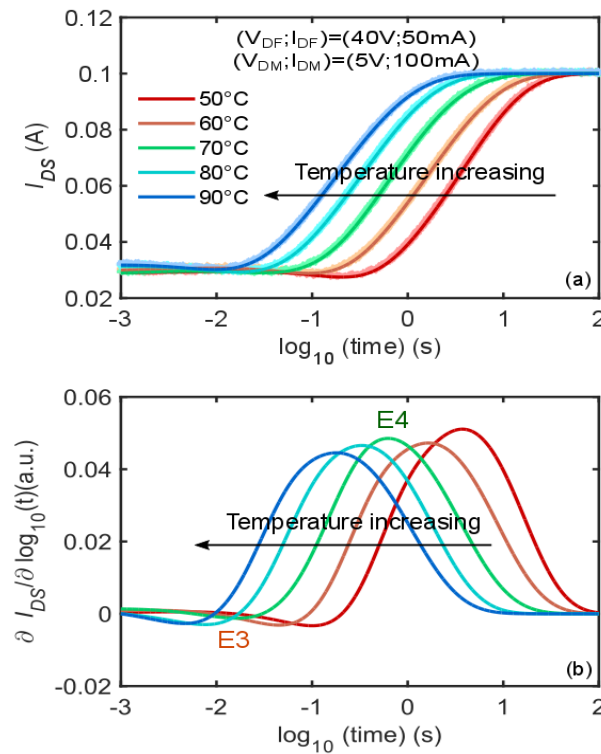


**Figure 2-45: (a) De-trapping drain current measurement recorded and stretched multi-exponential fitting without RF excitation ( $V_{DF}; I_{DF}$ )=(40 V; 50 mA) for 50°C to 90°C temperature range, (b) Related time spectrum analysis of de-trapping transient.**

As was noticed in the last section, the emission process “E4” obtained from RF excitation presents a similar dynamic behavior to the one obtained from DC excitation. Remarkably, the trap signal amplitude is higher under RF excitation, while the time constant is longer. Thus, we suppose that level “E4” obtained from DC excitation and from RF excitation has the same nature, while the density of the ionized traps changes with the excitation conditions.

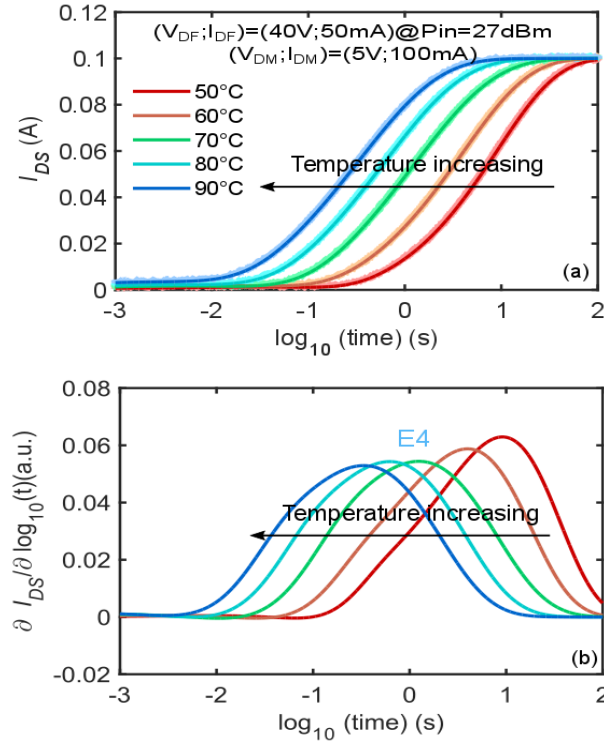


**Figure 2-46: (a) De-trapping drain current measurement recorded and stretched multi-exponential fitting at  $(V_{DF}; I_{DF}) = (40\text{ V}; 50\text{ mA})$  with RF  $P_{in} = 27\text{ dBm}$  for  $50^\circ\text{C}$  to  $90^\circ\text{C}$  temperature range, (b) Related time spectrum analysis of de-trapping transient.**

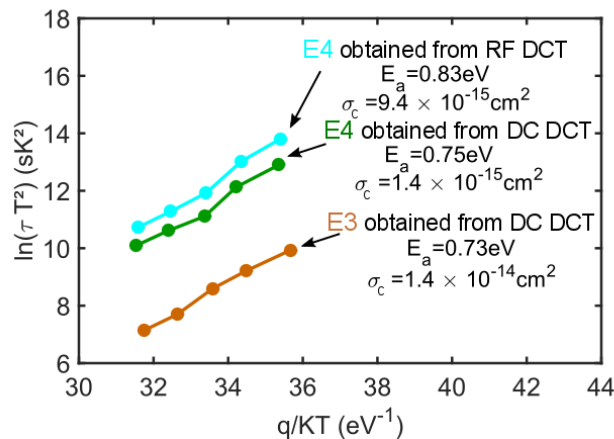


**Figure 2-47: Arrhenius plot of the signature detected from RF excitation ( $P_{in} = 27\text{ dBm}$ ) and DC excitation with apparent activation energies ( $E_A$ ) and capture cross sections ( $\sigma_c$ ).**

### 2.3.3.3 CW RF drain current transient measurement

One way to characterize these trapping phenomena on new SSPA generation based on AlGaIn/GaN HEMTs under CW large-signal excitations is based on multiple and consecutive power sweep measurements and a drain current transient measurement after the last power sweep. The set-up used for these characterizations is shown in Section 2.3.3.1.1 based on an LSNA system, but it is possible use a cheaper solution based on VNA and a scope.

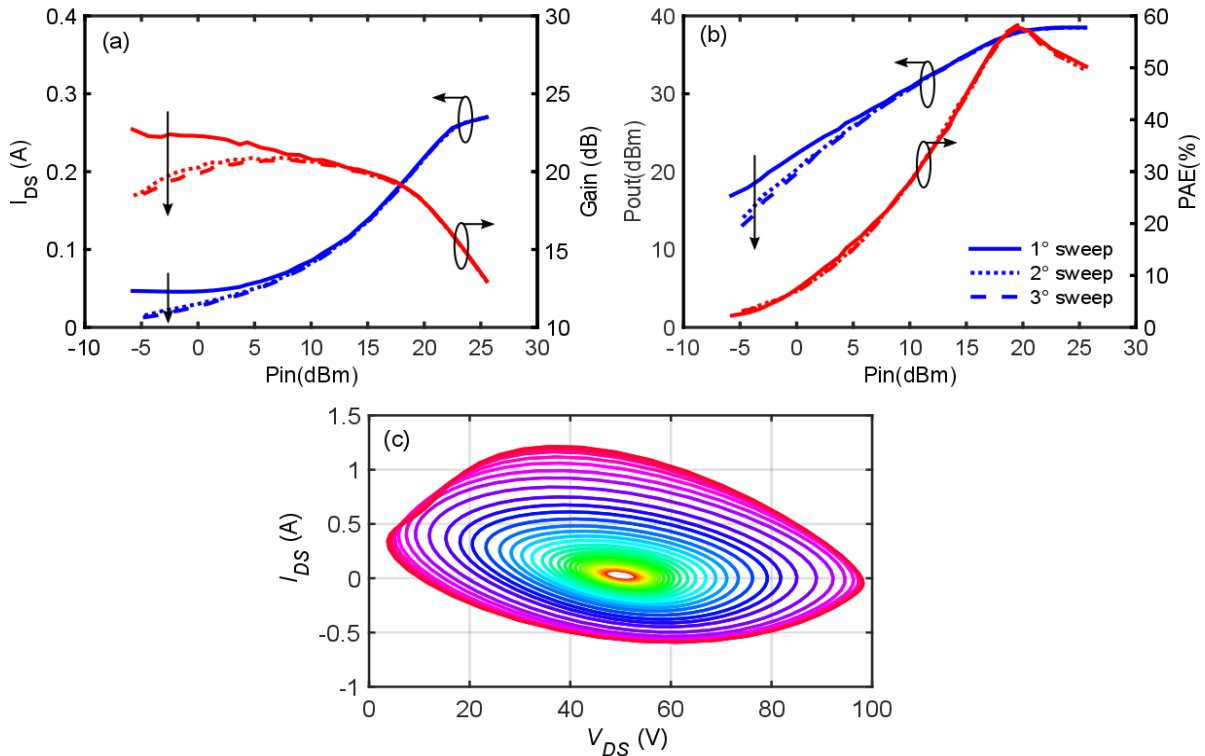


**Figure 2-48: Three consecutive RF power performances until 10 dBc measured at 4 GHz (class AB operation mode) for maximum PAE at impedance equal to  $Z_{LOAD\_maxPAE}(f_0) = 22.5 + j58\Omega$ . Corresponding extrinsic CW output load-lines derived from wave measurement at  $f_0$ ,  $2f_0$  and  $3f_0$  of the first power sweep.**

In order to understand how the class operation mode is sensitive to trapping effects, we have carried out three consecutive power sweep measurements up to 10 dB compression in class AB operation mode ( $I_{DS} = 25$  mA/mm at  $V_{DS} = 50$  V) at a frequency of 4 GHz and for an impedance corresponding to the matching of the transistor for maximum PAE  $Z_{LOAD\_maxPAE}(f_0) = 22.5 + j58\Omega$ . The measurement results in Figure 2-48 (a) and (b) show principally that after the first power sweep, the output power, gain and drain current present an important drop for low input power level due to trapping phenomena which are excited by varying large-signal excitations in high compression gain, as shown by the CW output load-lines in Figure 2-48(c). Subsequently, the second and third power sweeps indicate that the

device changes its class operation mode from class AB to class B. This class operation changing is due to trapping effects which impacts the drain current at low input power. Indeed, as shown in Figure 2-49, the extrinsic CW output load-lines at an input power level equal to -5 dBm present a strong reduction for the second and third power sweeps.

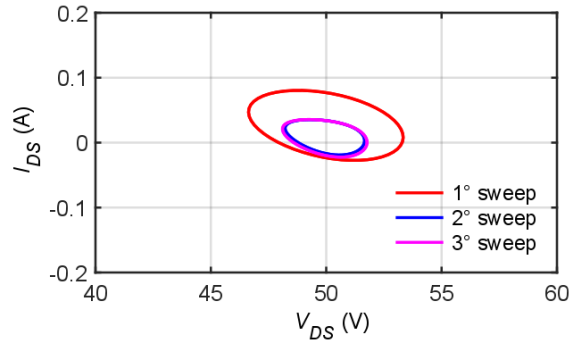


**Figure 2-49: Extrinsic CW output load-lines derived from wave measurement at  $f_0$ ,  $2f_0$  and  $3f_0$  for  $P_{IN}=-5$  dBm for the three power sweeps.**

In order to further investigate the effect of the bias point on these trapping phenomena, two consecutive power sweep measurements and drain current transient measurements are carried out for fixed  $I_{DS}$  and for fixed  $V_{DS}$  conditions. The analysis of the recovery drain current transient measurements by the multiexponential fit (in Equation (2-15)), already used in the last sections, allows to extract the time constant.

To analyze the RF degradation due to trapping effects, the figures of merit, for a fixed input power level ( $P_{IN}$ ) are defined as

$$I_{DS} \text{ DROP}(P_{IN}) = \frac{I_{DS,1SWEEP}(P_{IN}) - I_{DS,2SWEEP}(P_{IN})}{I_{DS,1SWEEP}(P_{IN})} \cdot 100 \quad (2-17)$$

$$\text{Gain DROP}(P_{IN}) = \text{Gain}_{1SWEEP}(P_{IN}) - \text{Gain}_{2SWEEP}(P_{IN}) \quad (2-18)$$

$$\text{Pout DROP}(P_{IN}) = \text{Pout}_{1SWEEP}(P_{IN}) - \text{Pout}_{2SWEEP}(P_{IN}) \quad (2-19)$$

and the time constant.

The first characterization consists of an RF performance measurements for a fixed  $I_{DS}$  equal to 50 mA and an increasing  $V_{DS}$ , first 30 V, then 40 V and 50 V. As shown in Figure 2-50 and more clearly summarized in Table 3, the power gain, drain current and output power decrease at low input power level with respect to the increasing of  $V_{DS}$ . It must be noticed that the trapping effects and consequently their time constants decrease with increasing  $V_{DS}$  due to the Poole–Frenkel effect, as shown in Section 2.3.3.2.2.1.

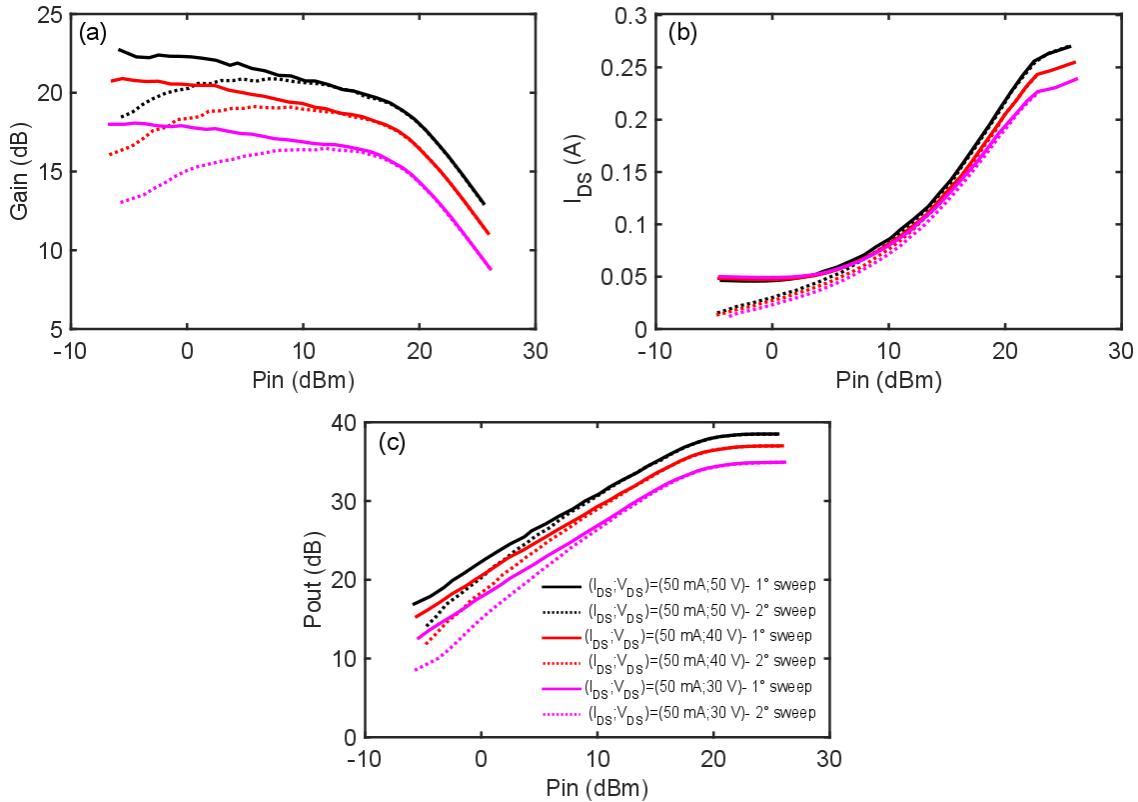


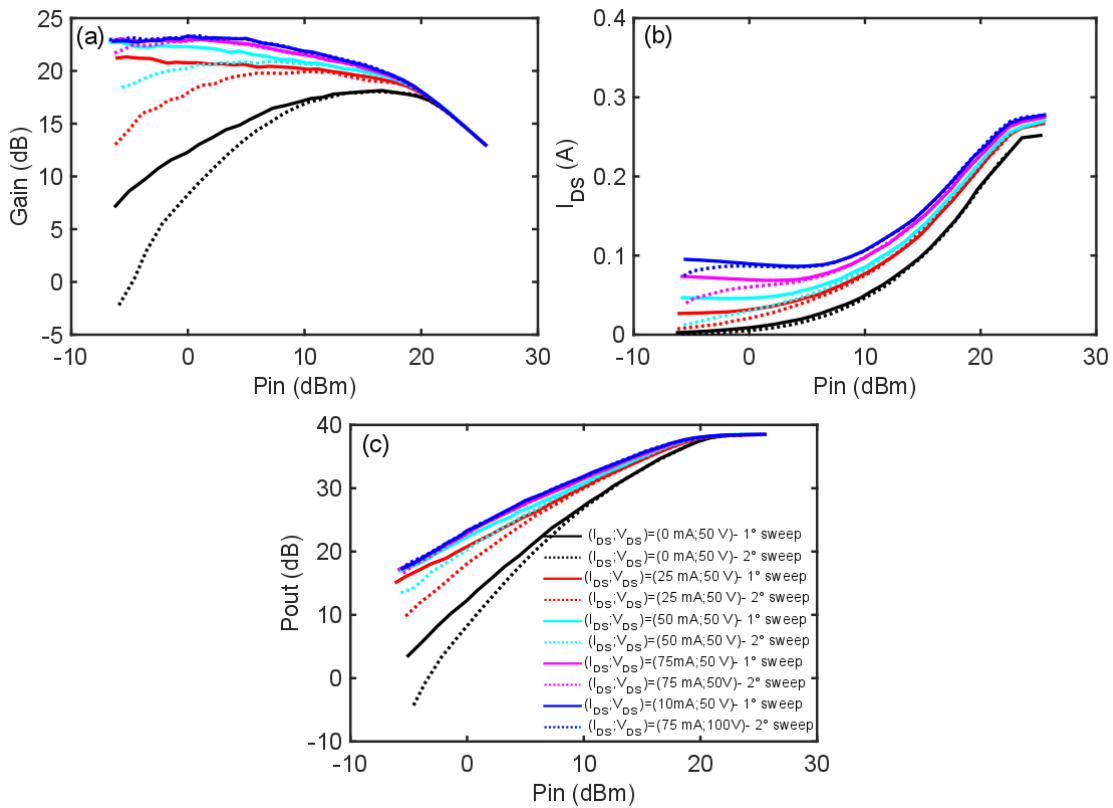
**Figure 2-50: Two consecutive (a) gain, (b) drain current and (c) output power performances for fixed  $I_{DS}=50$  mA and different  $V_{DS}$  equal to 30 V, 40 V and 50 V.**

The second characterization consists of RF performance measurements for a fixed  $V_{DS}$  equal to 50 V (thus for a fixed electric field) with increasing values of  $I_{DS}$  equal to 0 mA, 25 mA, 50 mA, 75 mA and 100 mA. In this case, the drop of power gain, drain current and output power decreases when  $I_{DS}$  increases down to practically 0 for a drain current for 100 mA, as shown in Figure 2-51 and more clearly summarized in Table 4. This can be explained in two ways:

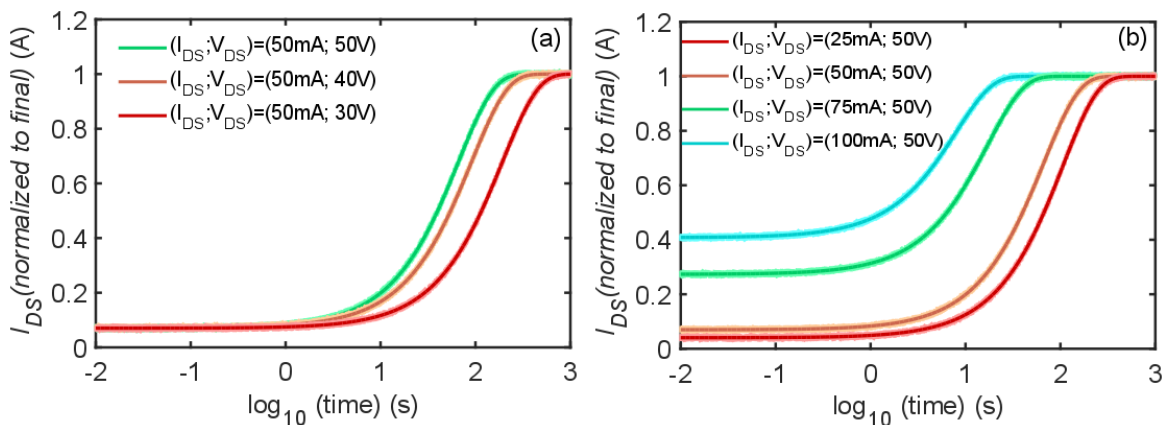
- For high  $I_{DS}$  values the power gain is in the saturation region at lower input power level, as shown in Figure 2-53, thus the variation of bias drain current due to the trapping effect from A to A' does not impact the power gain because it is still in the saturation region. Therefore, the gain is desensitized to trapping effects. Another way is that in the linear gain region, the variation of bias drain current due to the trapping effect from B to B' corresponds to a large drop of the power gain.
- An increase of  $I_{DS}$  corresponds to an increase of the operating temperature of the device, which produces a time constant activation as shown in Figure 2-52(b). Thus, the recovery gain time depends principally on the device's operating temperature.



Following these considerations, it is suggested to bias the device at  $I_{DS}$  equal to 100 mA in order to reduce the trapping effects.



**Figure 2-51: Two consecutive (a) gain, (b) drain current and (c) output power performances for fixed  $V_{DS}=50$  V and different  $I_{DS}$  equal to 0 mA, 25 mA, 50 mA, 75 mA and 100 mA.**



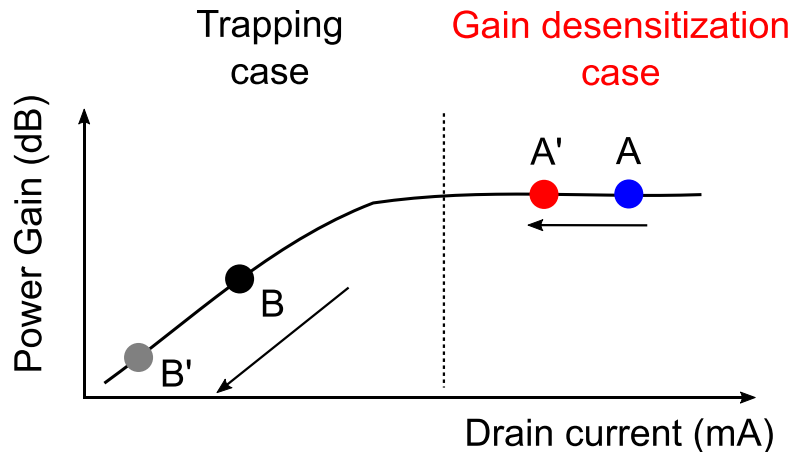
**Figure 2-52: Recovery drain current transient measurement after second power sweep with varying of  $V_{DS}$  (a) and  $I_{DS}$  (b).**

TABLE 3  
FIGURE OF MERIT AT FIXED  $I_{DS}$

$V_{DS}$ (V)	$I_{DS}$ DROP (%) [Pin=-5dBm]	Gain DROP (dB) [Pin=-5dBm]	Pout DROP (dBm) [Pin=-5dBm]	Time constant (s)
30	76.3	4.47	2.58	186.2
40	68.8	4.16	2.53	93.32
50	57.6	3.97	1.69	65.31

TABLE 4  
FIGURE OF MERIT AT FIXED  $V_{DS}$

$I_{DS}$ (mA)	$I_{DS}$ DROP (%) [Pin=-5dBm]	Gain DROP (dB) [Pin=-5dBm]	Pout DROP (dBm) [Pin=-5dBm]	Time constant (s)
0	//	11.9	14.1	//
25	65.4	6.85	5.36	106.6
50	57.6	3.97	1.69	65.3
75	36.5	0.38	0.48	17.5
100	21.9	0	0	8



**Figure 2-53: Schematic of trapping effect on power gain as a function of the drain current.**

With this technique, we demonstrated that it is possible to control the trapping phenomena by choosing the value of the bias point and thus identify a trapping desensitization operating zone. Indeed for  $(I_{DS}; V_{DS})=(100 \text{ mA}; 50 \text{ V})$  the gain drop is cancelled and the time constant is noticeably reduced, so the trapping effect can be considered neutralized. Whereas for very low  $I_{DS}$  the RF performances are more impacted, with the consequence that the trapping effects are exacerbated. Lastly, one notices that the trapping effect are more sensitive to varying  $I_{DS}$  than to varying  $V_{DS}$ .

### 2.3.4 Low-frequency dispersion measurements

The output conductance and transconductance of GaN HEMTs have been observed to change significantly at low-frequencies (10 Hz - 100 MHz) [16], [49]. So, in order to gather complementary information on trapping effects under class AB biasing, the dispersion of the LF Y-parameters are investigated through measurements of the small-signal S-parameters in the 100 Hz to 1 GHz frequency range. These S-parameter measurements were carried out at several temperatures using an Agilent E5061b LF-HF vector network analyzer [50] to determine the dispersion of  $g_d(f)$  and  $g_m(f)$ . As illustrated in Figure 2-54, the  $V_{GS}$  is applied to an external LF bias tee with a DC port connected to the power supply and the RF port connected to port 2 of the VNA. In order to cover the broadband from 100 Hz to 1 GHz LF Y-parameter measurements are performed in two sub-bands: with an LF home-made resistive bias tee [49] from 100 Hz to 10 MHz and with a commercial bias tee (Picosecond 5546) from 10 MHz to 1 GHz. The characteristics of the bias tees in terms of return and insertion loss are shown in Figure 2-55. The drain terminal is connected to an internal bias system (port 1) in the network analyzer. An on-wafer SOLT calibration is performed at each individual temperature.

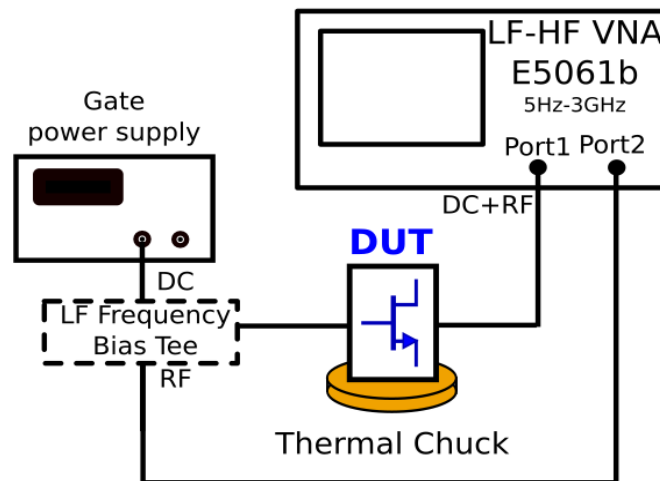


**Figure 2-54: Block diagram of the LF Y-parameters measurement set-up in 2-port configuration for the characterization of  $g_d(f)$  and  $g_m(f)$ .**

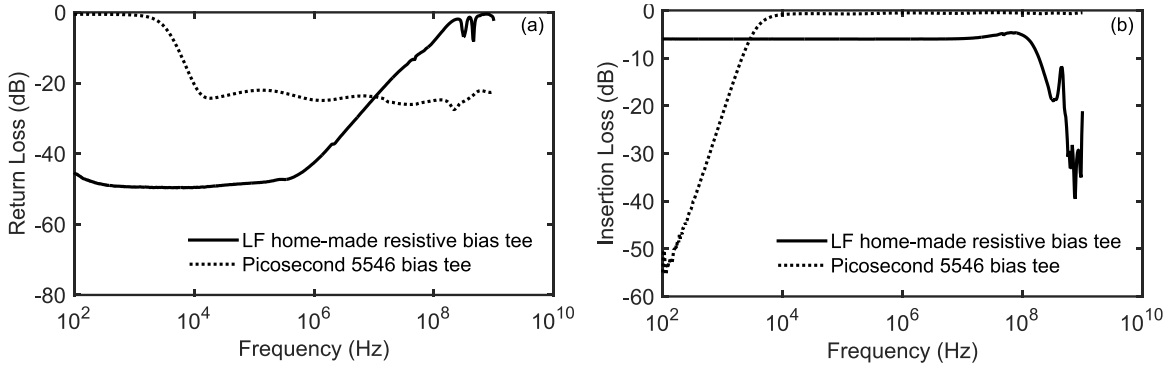


**Figure 2-55: (a) Return loss and (b) insertion loss of LF bias tees used for LF Y-parameter measurements.**

So, the Y-parameters are calculated from measured S-parameters [51]. Empirically, the effect of carrier trapping on the frequency dispersion of the output conductance and transconductance can be modeled as reported in [21]. The dispersion effects are taken into account with an additional voltage dependent current source (which represents the injection mechanism in trap state) in an RC circuit as shown in Figure 2-56.

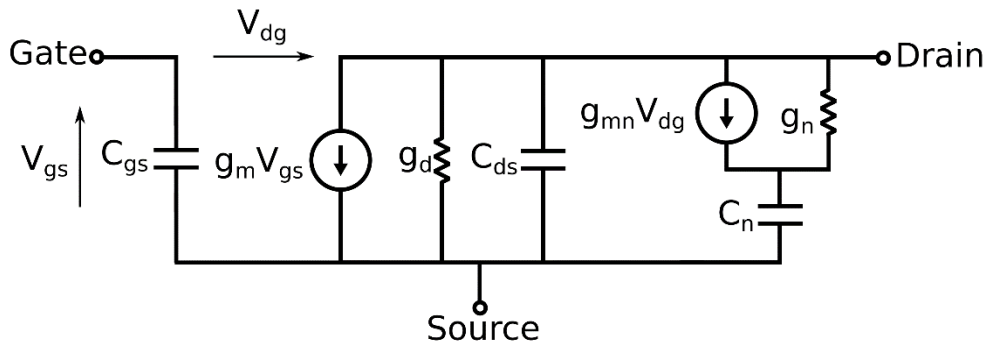


**Figure 2-56: Empirically equivalent circuit model for output conductance and transconductance dispersions.**

According to this small-signal model at low-frequency,  $g_m(f)$  and  $g_d(f)$  can be deduced from the Y-parameters of the DUT, respectively  $Y_{21}$  and  $Y_{22}$  parameters by the following equations:

$$Y_{21}(\omega) = \left( g_m - \frac{g_{mn}(\omega\tau_n)^2}{1+(\omega\tau_n)^2} \right) - j \frac{g_{mn}(\omega\tau_n)}{1+(\omega\tau_n)^2} \quad (2-20)$$

$$Y_{22}(\omega) = \left( g_d + \frac{(g_{mn} + g_n)(\omega\tau_n)^2}{1+(\omega\tau_n)^2} \right) + j \frac{(g_{mn} + g_n)(\omega\tau_n)}{1+(\omega\tau_n)^2} \quad (2-21)$$

$\tau_n = C_n/g_n$  corresponds to the time constant of the trapping process. For the determination of the time constants, the derivative forms of the imaginary part of  $Y_{21}$  and  $Y_{22}$  are used. In this way,

the time constants due to  $g_m(f)$  dispersion can be determined either from the peak values of the imaginary part of  $Y_{21}$  ( $f_{\text{imag}[Y_{21}]}=1/2\pi\tau_n$ ) and the time constants due to  $g_d(f)$  dispersion can be determined from the peak values of the imaginary part of  $Y_{22}$  ( $f_{\text{imag}[Y_{22}]}=1/2\pi\tau_n$ ). The number of traps of  $g_m(f)$  ( $g_d(f)$ ) is defined by the number of peaks of the imaginary part of  $Y_{21}$  ( $Y_{22}$ ) or by the number of inflexion points of the real part of  $Y_{21}$  ( $Y_{22}$ ) [9]. As has been demonstrated, the peak values of the imaginary parts of  $Y_{21}$  and  $Y_{22}$  at several temperatures allows determining the  $E_A$  and  $\sigma_c$  (associated respectively to  $g_m(f)$  and  $g_d(f)$  dispersion) using the Arrhenius formula (2-11) and substituting the emission rate with the reciprocal of the time constant ( $e_n=1/\tau_n$ ). A temperature correction is applied to determine  $E_A$  and  $\sigma_c$ .

### 2.3.4.1 LF Y-parameter measurement results

LF Y-parameter measurements for the SEMI-ON state ( $V_{GS}; V_{DS}$ )= $(-1.9V, 40V)$  were carried out at different temperatures to obtain the Arrhenius plots shown in Figure 2-57 and Figure 2-58. This analysis is focused only on  $Y_{21}$  and  $Y_{22}$  because the experimental data of  $Y_{11}$  and  $Y_{12}$  do not show any dispersion. The Y-parameters, depicted in Figure 2-57 and Figure 2-58, show that above 100 MHz, the contribution of the intrinsic capacitances of the small-signal model is not negligible. The  $Y_{21}$ -measurement shows two distinct transition frequencies in  $\text{Real}[Y_{21}]$  and two distinct peaks in  $\text{Imag}[Y_{21}]$ , proving that  $g_m(f)$  dispersion presents two trapping phenomena. The peak of the imaginary part of  $Y_{21}$  corresponds to the transitions in the transconductance (the real part of  $Y_{21}$ ). Figure 2-57(a) shows a significant decrease of the transconductance ( $\text{Real}[Y_{21}]$ ) amplitude with the increase of the temperature due to thermal effects. On the one hand, the first transition appears at LF (approximately 5-10 KHz for 80°C). On the other hand  $\text{Real}[Y_{21}]$  increases when the frequency decreases. The conclusion of these two last observations is that the trap (labeled “E2”) can be associated to an emission process. Considering that  $\text{Real}[Y_{21}]$  decreases when the frequency decreases and considering that the time constant of trap “E1” is approximately 1 $\mu$ s, the trap “E1” can be associated to a capture process. Output conductance dispersion for the same device is presented in Figure 2-58. The real part of  $Y_{22}$  ( $\text{Real}[Y_{22}]$ ) corresponding, to a first approximation, to the output conductance, shows one inflexion point. So  $g_d(f)$  dispersion presents one trap that corresponds to trap “E2” found by  $g_m(f)$  dispersion according to [52].

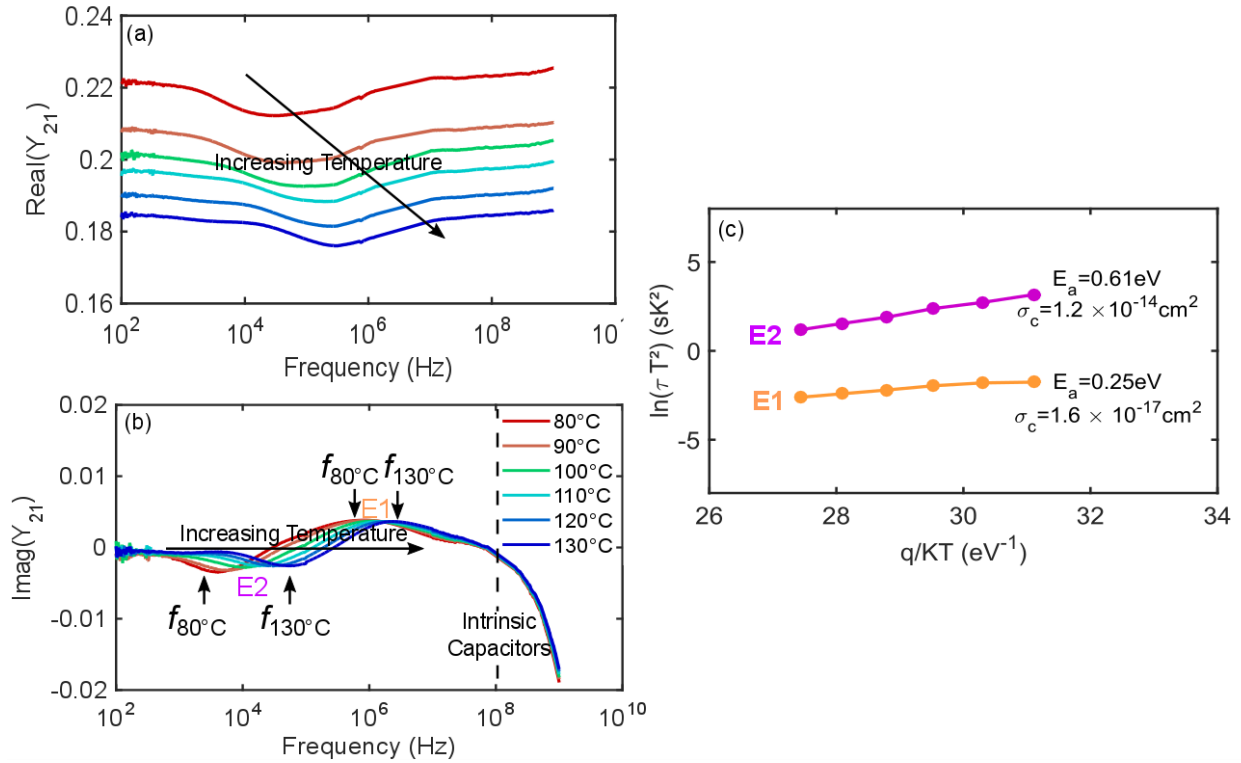


**Figure 2-57:** (a) Real  $[Y_{21}]$  versus frequency for 80°C to 130°C temperature range, (b) Imag $[Y_{21}]$  versus frequency for 80°C to 130°C temperature range and (c) related Arrhenius plot .

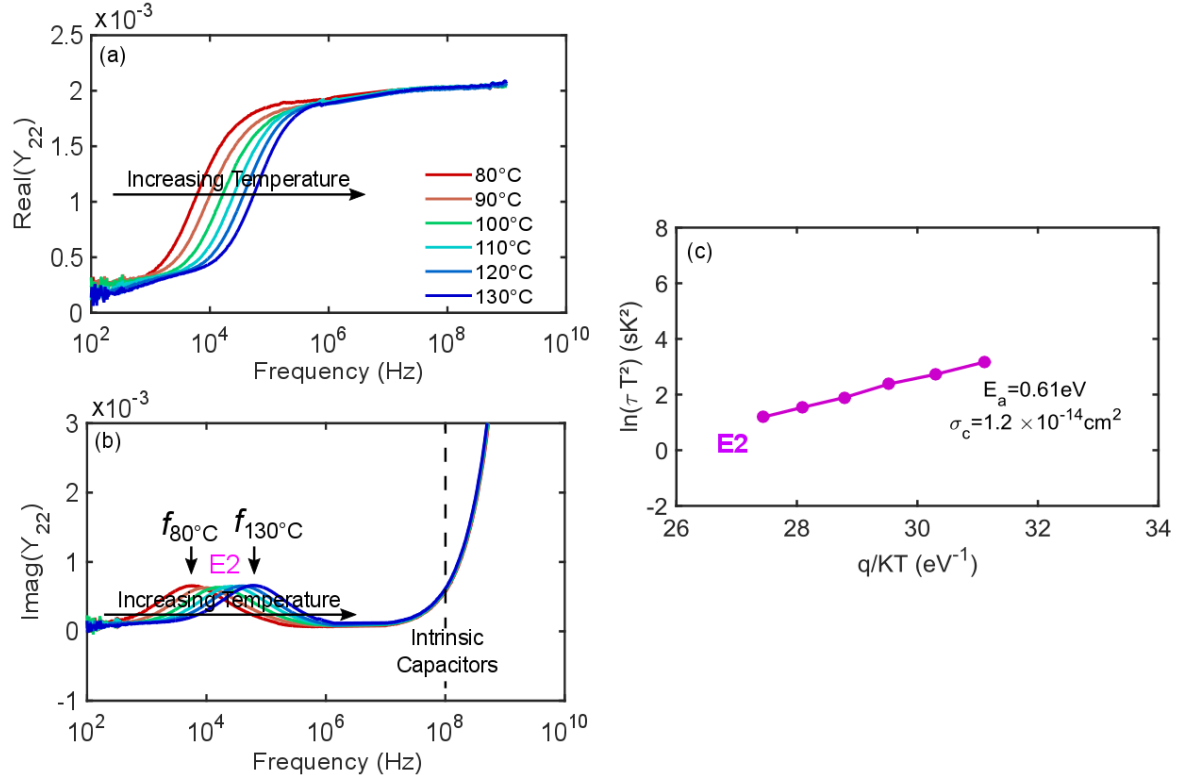


**Figure 2-58:** (a) Real  $[Y_{22}]$  versus frequency for 80°C to 130°C temperature range, (b) Imag  $[Y_{22}]$  versus frequency for 80°C to 130°C temperature range and (c) related Arrhenius plot.

Moreover, for the process “E2” we found the same time constants by  $g_d(f)$  and  $g_m(f)$  dispersions. Thus, the traps “E1” and “E2” are promoted by two mechanisms: the first one appears only when the small-signal is applied to the gate port, this suggests that the trap is located under the gate. The second trapping mechanism is due to hot electrons as explained in Section 2.3.2.5. The transconductance and output conductance frequency dispersions promoted by the process “E2” can be explained in this way: if the de-trapping time constant is much higher than the signal period (the traps are frozen), the traps cannot respond as quickly as the applied voltage. On the other hand, when the de-trapping time constant is of the same order as the signal period, trapped electrons due to the injection of highly energetic (hot) electrons are emitted and they participate in the RF current-carrying process giving rise to frequency dispersion in the device.

## 2.4 Identification of deep levels

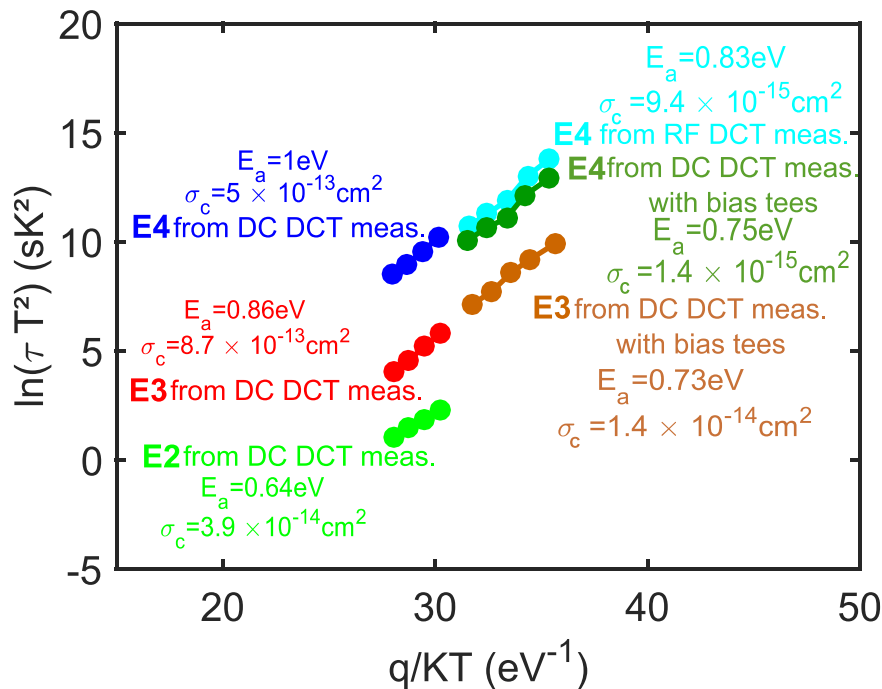


**Figure 2-59: Summary of Arrhenius plot of the deep levels, obtained from different drain current transient measurements performed during the research for this thesis.**

A summary of the Arrhenius plot obtained from different drain current transient measurements performed during the research for this thesis is shown in Figure 2-59. The deep levels “E4”=1 eV, “E3”=0.86 eV and “E2”=0.64 eV are identified by DC drain current transient measurements carried out using the set-up at the University of Padova described in Section 2.3.2.1. The deep levels “E4”=0.75 eV, and “E3”=0.73 eV are identified with DC drain current transient measurements and the deep level “E4”=0.83 eV is identified with RF

drain current transient measurements carried out using the set-up at the XLIM laboratory described in Section 2.3.3.2.1. All XLIM laboratory measurements are carried out with use of bias tees. Thus, due to the parasitic effects of the bias tees, the drain current recording is started at 1 ms. Therefore, the trapping effect labeled “E2” is outside of the time windows for the measurements and it cannot be detected. Moreover, the differences between the  $E_A$  and  $\sigma_c$  of deep level “E4” between DC drain current transient measurements carried out at the University of Padova and at the XLIM laboratory can be explained by the fact that the characterized DUTs came from the same technology but different production runs. In conclusion, the deep levels “E3” and “E4” detected by the conventional DC DLTS measurement set-up and by the DC DLTS measurement set-up with bias tees involve the same trap-center.

In order to understand and interpret the possible physical origin of a trap, the trap properties ( $E_A$  and  $\sigma_c$ ) are compared to deep levels previously reported in the literature, which are summarized in Figure 2-60 and Table 5.

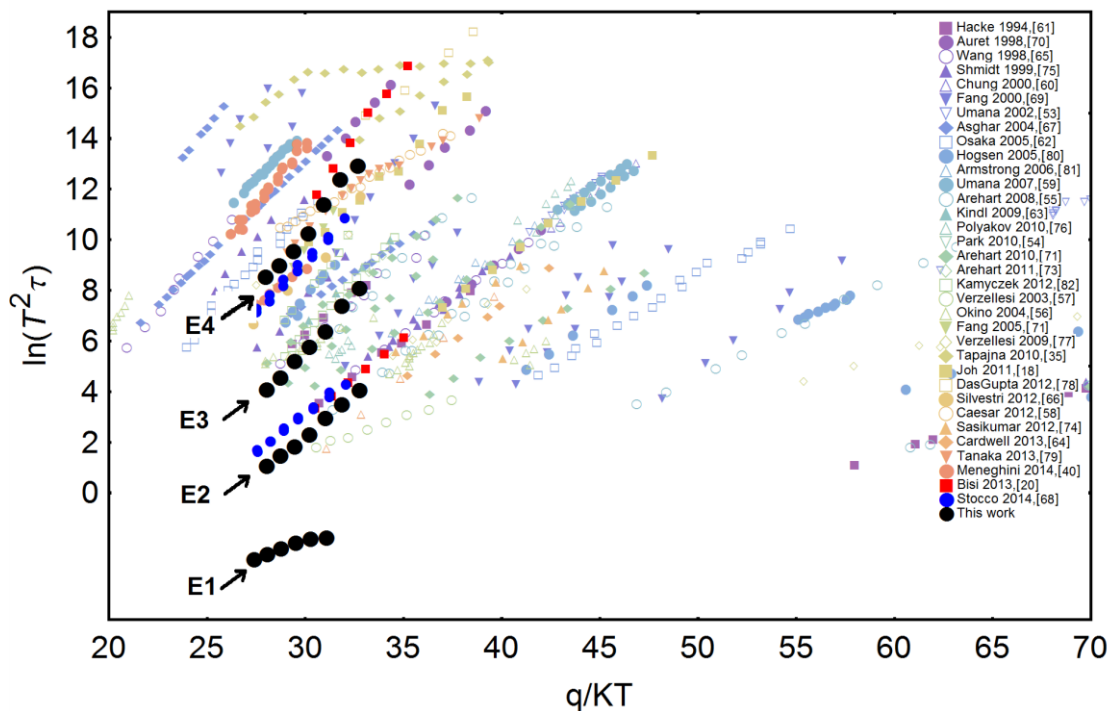


**Figure 2-60: Arrhenius plot of deep levels “E1”, “E2”, “E3” and “E4” detected within this thesis research. Presentation of trap states reported in previous papers for comparison (data taken from [20] and references therein).**



TABLE 5  
 DATABASE OF DEEP LEVELS IN GaN-BASED DEVICES (DATA TAKEN FROM [20] AND REFERENCES THEREIN)

reference papers	Analyzed samples	Deep level energy (eV)	Interpretations
Umana-Membreno [53], Park [54], Arehart [55]	various GaN-based devices	EC-0.09/0.27	Nitrogen vacancies
Okino [56]	AlGaIn/GaN HEMTs	EC-0.34	Possible AlGaIn surface
Verzellesi [57]	AlGaIn/GaN HEMTs	EV+0.3	Surface
Umana-Membreno [53]	n-GaN	EC-0.355	Mg impurities
Caeser [58], Tapajna [35]	various GaN-based devices	EC-0.44/0.45	C/O/H impurities, possibly in nitrogen substitution position
Umana-Membreno [59], Arehart [55], Chung [60], Hacke [61], Osaka [62], Kindl [63]	various GaN-based devices	EC-0.5/0.69	Nitrogen antisites
Cardwell [64]	AlGaIn/GaN HEMTs	EC-0.57	influenced by Fe dopant
Wang [65]	n-GaN	EC-0.58	C or H impurities
Wang [65], Meneghini [40]	various GaN-based devices	EC-0.62/0.66	GaN native defect
Okino [56]	AlGaIn/GaN MIS-HEMTs	EC-0.68	Surface
Silvestri [66]	HEMT	EC-0.72	Fe dopant
Asghar [67]	GaN pn diode	EC-0.76	Nitrogen antisites
Stocco [68]	AlGaIn/GaN HEMT	EC-0.80	Gallium vacancy
Fang [69]	n-type GaN on sapphire	EC-0.89	Nitrogen antisites
Auret [70], Fang [71]	various GaN-based devices	EC-0.95/1.02	Treading dislocation
Arehart [55], Arehart [72]	various GaN-based devices	EC-1.28	Carbon interstitial defect
Arehart [55], Arehart [72]	various GaN-based devices	EC-2.6/2.64	$V_{Ga}$ or $V_{Ga-H}$ or $V_{Ga-2H}$
Arehart [73]	AlGaIn (Al 30%)	EC-3.11	Cation vacancy
Sasikumar [74], Arehart [55]	various GaN-based devices	EC-3.2/3.22	Residual Mg acceptor
Arehart [55], Arehart [72]	various GaN-based devices	EC-3.22/3.28	$C_N$ substitution
Arehart [73]	AlGaIn (Al 30%)	EC-3.93	Mg impurities

From Table 5 and [37], the defects are principally due to:

- **native defects** in GaN with Gallium vacancy ( $V_{Ga}$ ) as acceptor level and Nitrogen vacancy ( $V_N$ ) as donor level.

- high presence of **hydrogen** impurities in GaN (complexes with  $V_{Ga}$  and C-H).
- **carbon** atoms can be incorporated with gallium substitutionals ( $C_{Ga}$ ) or nitrogen substitutionals ( $C_N$ ) in order to obtain a highly insulating GaN layer.
- **oxygen** impurity in nitrogen substitutional ( $O_N$ ) that has a shallow donor level.
- **iron** impurities is commonly presented in GaN technology to reach a semi-insulating GaN.

The overall Arrhenius plot provided by I-DLTS, transconductance and output-conductance frequency dispersion measurements is shown in Figure 2-60. From Figure 2-60, the emission process “E2” obtained from DCT measurements is characterized by  $E_A=0.64\text{eV}$  and  $\sigma_c=3.9\times 10^{-14}\text{cm}^2$ . The emission trap process obtained from transconductance and output-conductance frequency dispersion measurements is characterized by  $E_A=0.61\text{eV}$  and  $\sigma_c=1.2\times 10^{-14}\text{cm}^2$ . For the first time, to our knowledge, the correspondence of the trap characteristics allows concluding that the same trap level “E2” is determined from the two different measurements. Moreover, the imaginary parts of  $Y_{21}$  and the  $Y_{22}$  in Figure 2-57 and Figure 2-58 show a rightward shift of the peaks when the temperature increases. This frequency shift, from 5 kHz (at 80°C) to 65 kHz (at 130°C), converted in the time-domain corresponds to the same time constant shift observed in the DCT measurements (Figure 2-18(a)) when the temperature increases. This level “E2” is supposed to be due to a native defect of GaN, based on comparison with previous reports [20], [40], [68]. The level “E3” ( $E_A=0.86\text{eV}$ ;  $\sigma_c=8.7\times 10^{-13}\text{cm}^2$ ) obtained from DCT measurements, reveals a similar signature to the deep levels already associated to nitrogen-related defects [19], [35], [61], [72] present in the GaN layer. The level “E4” ( $E_A=1\text{eV}$ ;  $\sigma_c=5.0\times 10^{-13}\text{cm}^2$ ) characterized by DCT measurements, shows a correspondence with the signature of the deep levels associated to extended defects in GaN [7], [20], [27], [62]. Finally, the level “E1” ( $E_A=0.25\text{eV}$ ;  $\sigma_c=1.6\times 10^{-17}\text{cm}^2$ ) characterized by LF  $Y_{21}$  measurements, shows again a correspondence with the signature of the deep levels associated to nitrogen-related defects [30], [31].

## 2.5 Conclusions

In this chapter, a detailed and innovative investigation of the trapping processes in AlGaIn/GaN HEMTs from DC to radio-frequency range is described. The first part of this chapter introduced the theoretical concepts on electron capture/emission phenomena needed to understand and characterize the trap mechanism and the determination of an Arrhenius plot.

Successively, the methods and the associated set-ups for the trapping investigation developed during the research for this Ph.D. thesis have been presented. This trapping investigation is based on combined pulsed I/V measurements (which provide an identification of the possible trap position), DCT investigation (which provide data on the large-signal voltage steps de-trapping transient, suitable for deep level analysis), nonlinear microwave DCT investigation (which provide the RF deep level analysis) and LF transconductance and output-conductance measurements (which provide small-signal trap analysis). The conclusions of this chapter on trapping investigation are summarized below:

- The pulsed I/V measurements under class AB bias condition detected a shift in the threshold voltage, a significant increase in the resistivity of the gate–drain access region, and a decrease in the transconductance peak. Moreover, pulsed I/V characterization carried out at several temperatures shows that the CC increases when the gate quiescent bias point increases (due to hot electrons), in accordance with [83].
- The properties of the trap responsible for CC are investigated with DC DCT. This technique has evidenced three traps with the following activation energies: “E4”=1 eV, “E3”= 0.86 eV and “E2”=0.64 eV.
- The transconductance and output-conductance frequency technique principally identified a trap level “E2”=0.61 eV which has been found to have a good matching with the trap level “E2” identified by the DC DCT technique. The trap level “E2” corresponds to the faster trap phenomena detected by the DC DCT technique. The trap level “E2” is supposed to be due to a native defect in GaN. The features of the pulsed I/V measurement suggest that these defects are located in the GaN buffer layer.
- The DC DCT technique is very powerful because of the sensitivity of the drain current to the trap parameter analysis. The time constant and amplitude of the traps are determined from the Arrhenius plot for trapping or de-trapping phenomena. Real-time trapping behavior is observed thanks to accurate records over a 7-decade time scale allowing the investigation of slow and fast trapping phenomena.
- The transconductance and output-conductance frequency dispersion technique can provide trap information ( $E_A$  and  $\sigma_c$ ) using small-signal excitations close to real CW RF operation mode. This trapping determination method (LF  $Y_{21}$  and LF  $Y_{22}$ ) is based on the 2-port S-parameters measurement that directly provides information about the current corresponding to  $g_m$  and  $g_d$  (to a first approximation). The advantage of this method lies in the sensitivity of  $g_m$  and  $g_d$  to the drain-lag trapping effects. LF Y-

parameter characterization is very accurate because it is based on the use of VNA measurements. This method provides a fast characterization of trapping phenomena but suffers from the lack of a quantitative determination of the trap density. The complexity of the LF dispersion characterization and the scarcity of its analysis makes it difficult to determine at the moment a detailed theoretical model of trap “E1”. But, the technique for determining the activation energies and capture cross-sections for the detected traps, based on temperature-dependent measurements of the imaginary parts of  $Y_{22}$  and  $Y_{21}$ , is demonstrated.

- The nonlinear microwave DCT measurements allow investigating the trapping characteristics corresponding to the nonlinear RF dynamics of the dispersion effects in GaN HEMTs. The method consists of the measurement and analysis of de-trapping drain current transients after 100 ns of RF excitation.
- It is demonstrated how the choice of bias point in the de-trapping condition allows accelerating the slow emission process for the increase in power dissipation and for the Poole–Frenkel effect.
- The nonlinear microwave DCT measurement results show also that the increase of the load-line excursions produce a stronger impact of the de-trapping behavior in terms of CC after RF OFF and trap amplitude. Therefore, an increase in the RF level involves the excitation of more and more “E4” trap centers. The trapping mechanism due to RF excitation is attributed to a positive threshold voltage shift that indicates a negative charge-trapping under the gate region.
- The comparison between the DC and RF testing results demonstrated that the impact of trapping phenomena appears more severe under single pulse large-signal RF excitation than under only single pulse DC excitation.
- The nonlinear microwave DCT load-pull measurements for two different output load impedances (maximum of PAE and mismatched impedances) have revealed that the trapping phenomena impact is lower when the transistor is optimally matched at its output port to reach maximum PAE performance.
- The nonlinear microwave DCT analysis has evidenced the deep level “E4”=0.75 eV. The level “E4” is also detected in DC excitation but with an increase of the density of the ionized traps.
- The nonlinear microwave DCT results have put in evidence the sensitivity of the traps to the:

- Input power level;
  - Pulse-width;
  - Temperature;
  - Load impedance;
  - Operating bias point.
- The nonlinear microwave DCT measurements have demonstrated that it is possible to control the trapping phenomena by choosing the value of operating bias point and thus identify a trapping desensitization operating zone.

In conclusion, in this chapter we have identified the trap levels present in this commercial GaN GH50 technology from UMS foundry due principally to native defects of the GaN. Moreover, we have also demonstrated the strong impact on the RF performance of the trapping effects and their sensitivity to many factors. Thus, this thesis research has identified a way to make the SSPA insensitive to trapping effects in real RF operating conditions, by choosing the correct operating bias point value in order to reach the trapping desensitization operating zone.

## 3 Nonlinear Electro-Thermal model of AlGaIn/GaN HEMT

### 3.1 Introduction

The new SSPA generation based on AlGaIn/GaN HEMTs is currently under development for replacing the preceding technologies. As described in the previous chapter, GaN technology is still subject to memory effects, such as trapping and thermal effects. The aim of electrical modeling is to allow designers to simulate the nonlinear behavior of the device under complex electrical signals. Thus, it is of fundamental importance to provide a compact model in CAD tools which takes into account the dispersion phenomena of GaN-based HEMT in order to predict correctly the RF performance during real RF operating conditions. The resultant nonlinear electro-thermal AlGaIn/GaN HEMT model including large-signal dynamic trapping effects becomes a necessary tool for designers to assess the performance of the high efficiency solid state power amplifier required by the market [84].

In this chapter a modeling methodology for AlGaIn/GaN HEMTs is presented, in particular our contribution with respect to previous works [30], [41]. This contribution mainly consists in the introduction of a new additive thermal-trap model which takes into account the dynamic behavior of trap states and their associated temperature variation and the validation of the model at different temperatures. The building of the new thermal-trapping model is based on the large trapping investigation and measurements carried out in the last chapter.

### 3.2 Modeling methods for HEMTs

There are different kinds of models that can be less or more complex according to the goal of modeling the device. For example, for understanding the physical phenomena, such as the charging mechanisms between the semi-conductor layers due to trapping and thermal effects, a *physical model* is used. This model is described by physical laws and includes technological parameters (e.g., device layout, doping, and layer size). The physical model is generally performed using 2-D solving of charge transport equations for the electrical characteristics. In the case of thermal simulation, a 3-D finite element simulation involves meshes with thousands of nodes in order to take into account the various effects. This modeling approach requires a heavy simulation load and does not fit with circuit simulation.

A *phenomenological model* or *compact transistor model* allows decreasing the number of parameters used. The purpose of the model is to reproduce the phenomena involved in the device, with a simplification of the complexity of the physical structure. This modeling approach is proposed in [85] and depicted in Figure 3-1. This model is also called a semi-physical model because the equations are determined from the physics (in the case of definition of the diodes) or following a mathematical law for a better modeling of the phenomenon (e.g.,  $C_{GS}$  and  $C_{GD}$ ) and a better convergence of the model. With the emerging new generations of characterization methods and instruments, a new type of model is developed that is called a *behavioral model*. This behavioral model [86] is based on the neural network (NN) approach [87] and/or X-parameter measurements [88], [89] and it can be determined directly from large-signal measurements. It also allows more rapid determination and correct prediction of the physical phenomena involved in the device. But it does not provide access to the model parameters, as it is described by a large number of parameters which have no direct physical meaning. Behavioral models are considered “black box” models, where only the responses of the component to some controlled stimuli are known, and are consequently validated only under the operating conditions measured. For research purposes, we have chosen the phenomenological or compact model, which provides a good trade-off between simulation speed and modeling flexibility.

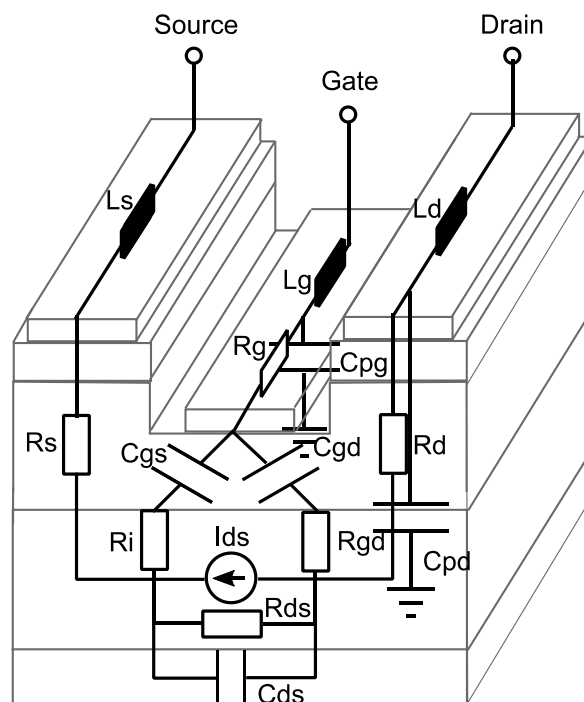


**Figure 3-1: Identification of intrinsic and extrinsic parameters based on physical structure of HEMT for a phenomenological model.**

### 3.3 Modeling methodology

The equivalent device circuit used to describe the nonlinear AlGaIn/GaN HEMT characteristic including trapping and thermal effects is shown in Figure 3-2. The modeling methodology flow, required for a complete device extraction is based on four different steps, as shown in Figure 3-3.

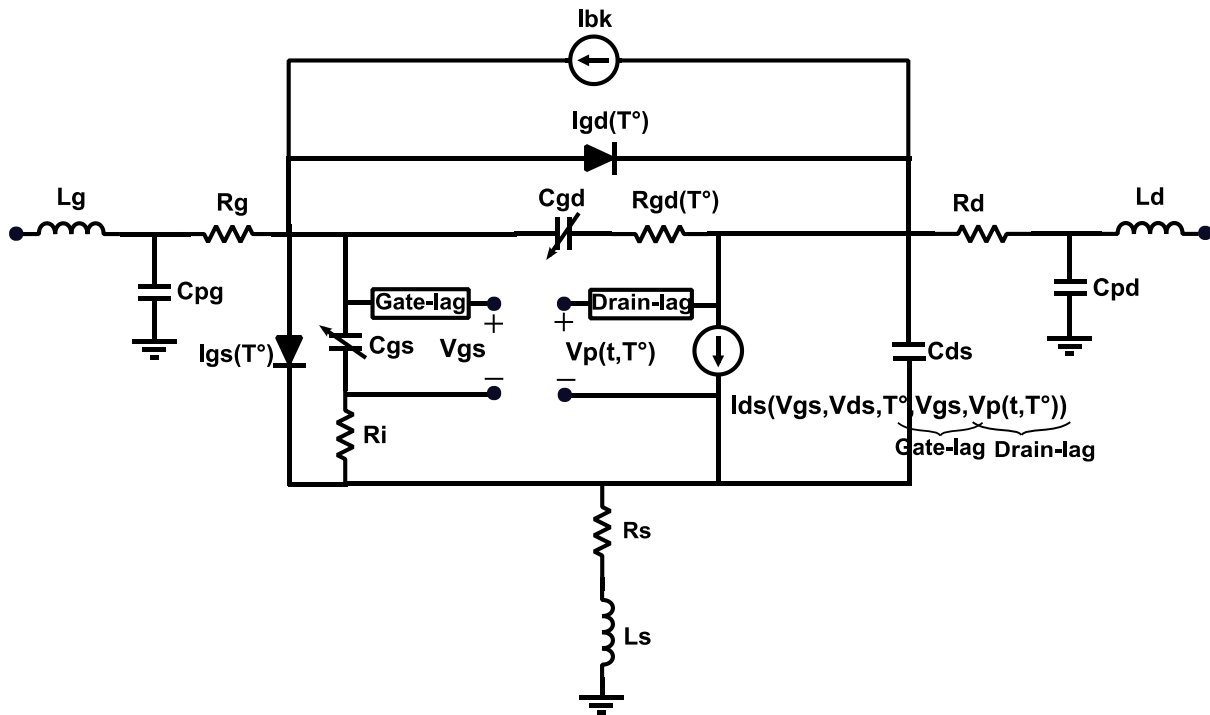


Figure 3-2: Structure of the nonlinear model including trapping and thermal effects.

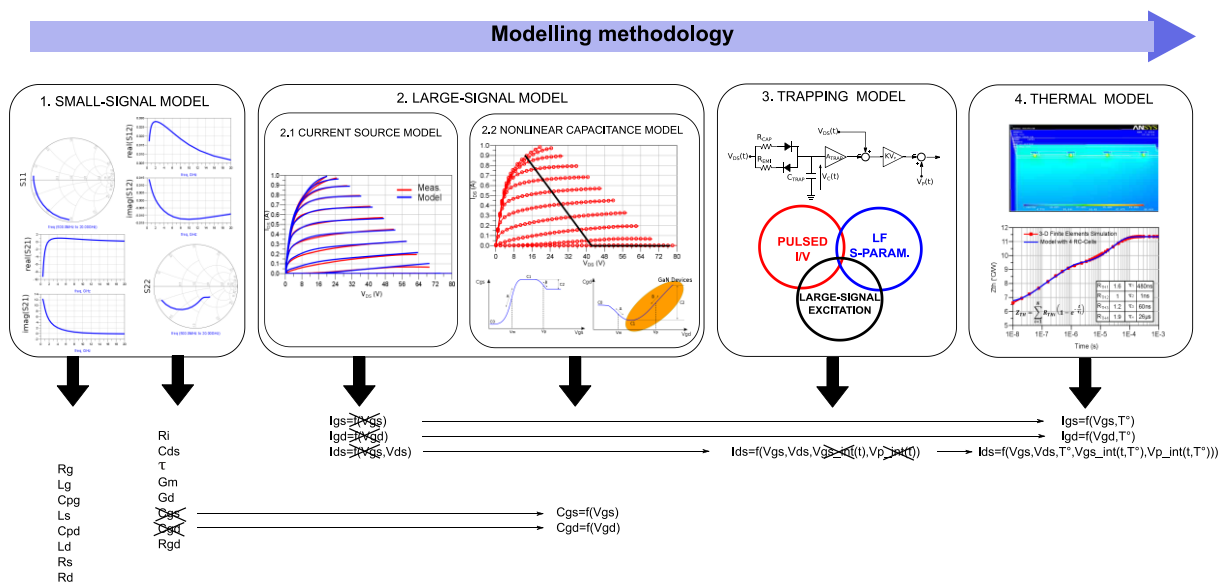


Figure 3-3: Modeling methodology flow for the extraction of a nonlinear model including trapping and thermal effects.



The method for parameters extraction shown in Figure 3-3 is developed as follows

1. Determination of extrinsic ( $R_g$ ,  $L_g$ ,  $C_{pg}$ ,  $R_d$ ,  $L_d$ ,  $C_{pd}$ ,  $R_s$  and  $L_s$ ) and intrinsic ( $C_{gs}$ ,  $C_{gd}$ ,  $C_{ds}$ ,  $R_i$ ,  $R_{gd}$ ,  $G_m$ ,  $G_d$  and  $\tau$ ) parameters of small-signal model for a fixed bias point.
2. Determination of the large-signal model:
  - 2.1. Definition of drain current source, gate-source diode and gate-drain diode by the fitting of pulsed I/V characteristic.
  - 2.2. Extraction of nonlinear capacitances  $C_{GS}$  and  $C_{GD}$  from S-parameter measurements at different bias points located on an ideal load-line.
3. Addition of the trapping modeling blocks that modulate the instantaneous drain current value through the variation of intrinsic gate voltage and pinch-off voltage.
4. Addition of the thermal dependency of the drain current source, trapping model, gate-source diode and gate-drain diode.

### 3.4 Device modeling process

#### 3.4.1 Small-signal model

The equivalent small-signal model or linear model of HEMT is shown in Figure 3-4. It is composed of two kinds of parameter: the intrinsic and the extrinsic parameters. The last one corresponds to the parasitic elements due to access lines and metallization.

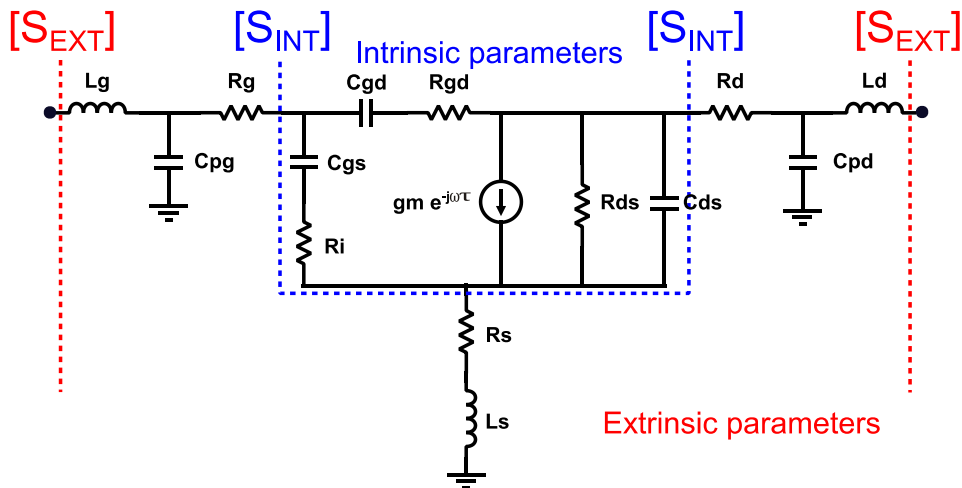


**Figure 3-4: Equivalent small-signal model of HEMT.**

The quality of the nonlinear model is strongly dependent on the accuracy of the extrinsic parameters. Thus, for the extraction of the small-signal model, an optimization method

(developed in XLIM laboratory) is used [30]. The small-signal model is extracted from small-signal pulsed S-parameter measurements.

### 3.4.1.1 Pulsed S-parameters measurements

The S-parameters are measured under pulsed condition to extract the small-signal model at fixed quiescent bias point close to real operation condition. The measurement set-up is similar to the previously described pulsed I/V test bench in 2.3.1.1 with the addition of a pulsed VNA (Rohde & Schwarz ZVA40 and ZVAX modules) to measure pulsed S-parameters as shown in Figure 3-5. An on-wafer calibration is performed to obtain the pulsed S-parameters at both ports of the DUT. This calibration is performed in CW mode (SOLT, TRM, etc...) because the pulsed calibration can deteriorate due to the linearity and dynamic range of the receiver's mixer and the losses due to the internal switch in the ZVAX.

The principle of pulsed S-parameter measurements consists of generating the RF signal for each measurement bias point ( $V_{GS,M}; V_{DS,M}$ ) of the pulsed I-V network and performing the S-parameters acquisition as depicted in Figure 3-6. Thus as previous discussed, the thermal and trap states are fixed by the quiescent bias point ( $V_{GS,Q}; V_{DS,Q}$ ). The pulsed RF signal is synchronized with the pulsed I/V excitation with a reference signal generated by the pulsed I/V system (BILT AMCAD). The dynamic range from CW to pulsed mode decreases when the duty cycle of the pulses is reduced as indicated in Equation (3-1).

$$reduction (dB) = -20 \cdot \log \left[ \frac{Pulse\ period}{Pulse\ width} \right] \quad (3-1)$$

Thus, the pulse-period and pulse-width are chosen in order to limit the dynamic reduction while maintaining a quasi-isothermal state and a fixed trapping state. The measurement condition for pulsed S-parameter measurements are summarized in Figure 3-7 (1  $\mu$ s of RF pulse-width, 1.2  $\mu$ s of gate pulse-width and 1.4  $\mu$ s of drain pulse-width with an identical pulse period of 10  $\mu$ s).

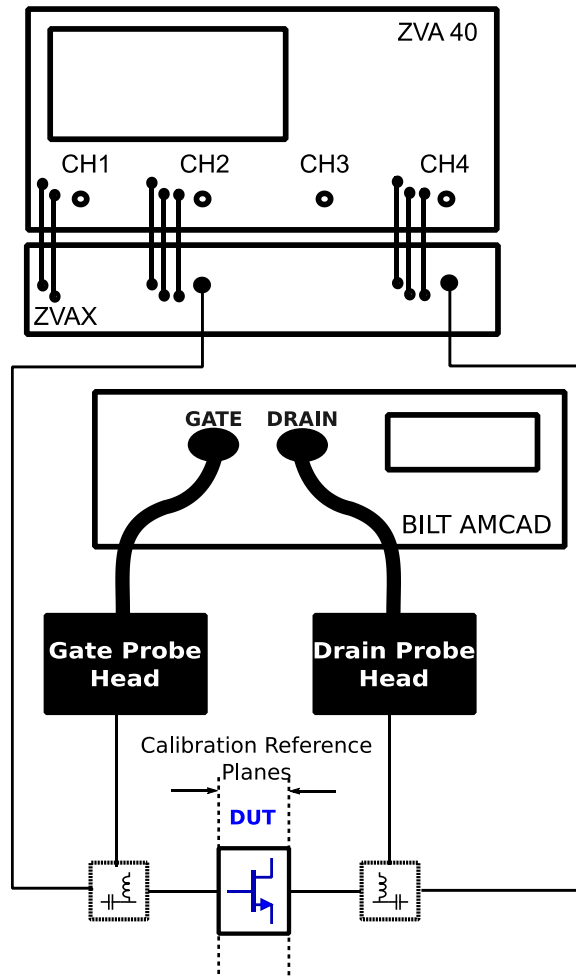


Figure 3-5: Block diagram of pulsed S-parameters experimental set-up.

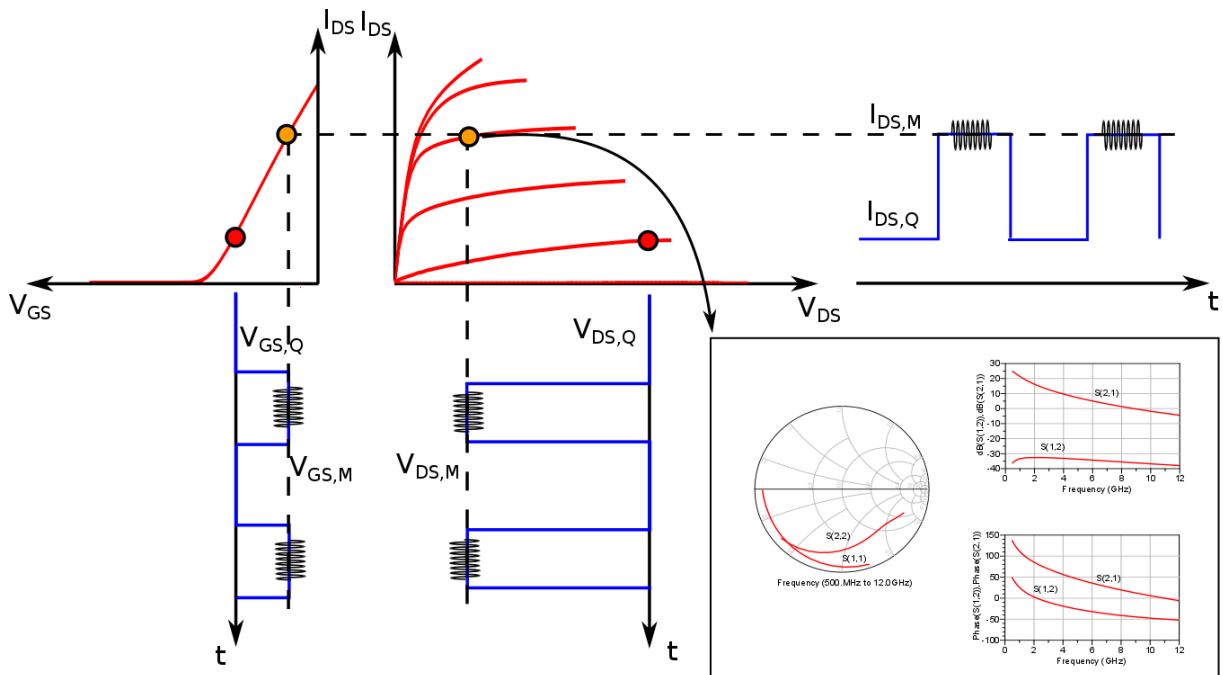
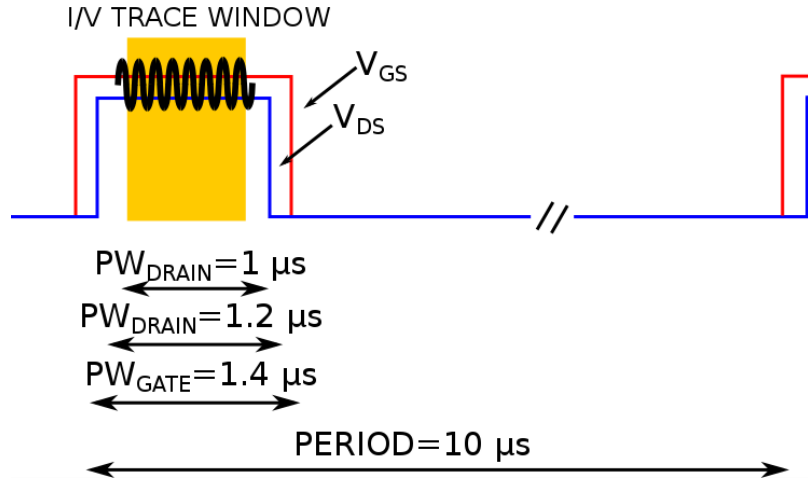


Figure 3-6: Principle of pulse S-parameter measurement.



**Figure 3-7: Pulse timing diagram of pulse S-parameter measurement.**

### 3.4.1.2 Extraction of the small-signal model

The method for the model extraction allows the direct determination of extrinsic parameters provided the intrinsic parameters are frequency independent. The procedure is the following:

- The intrinsic admittance parameters  $[Y_{INT}]$  are obtained from the measured S-parameters by successive transformation of the matrix of measured S-parameters (as depicted in Figure 3-8).
- Then, the extrinsic parameters are analytically calculated at each frequency, from the  $[Y_{INT}]$  matrix using the following equations:

$$Cgd = \frac{-Im(Y_{12})}{\omega} \left[ 1 + \left( \frac{Re(Y_{12})}{Im(Y_{12})} \right)^2 \right] \quad (3-2)$$

$$Rgd = \frac{-Re(Y_{12})}{(Cgd \cdot \omega)^2} \left[ 1 + \left( \frac{Re(Y_{12})}{Im(Y_{12})} \right)^2 \right] \quad (3-3)$$

$$Cgs = \frac{Im(Y_{11}) + Im(Y_{12})}{\omega} \left[ 1 + \left( \frac{Re(Y_{11}) + Re(Y_{12})}{Im(Y_{11}) + Im(Y_{12})} \right)^2 \right] \quad (3-4)$$

$$Gd = Re(Y_{12}) + Re(Y_{22}) \quad (3-5)$$

$$Cds = \frac{Im(Y_{12}) + Im(Y_{22})}{\omega} \quad (3-6)$$

$$Ri = \frac{Re(Y_{11}) + Re(Y_{12})}{(Cgs \cdot \omega)^2} \left[ 1 + \left( \frac{Re(Y_{11}) + Re(Y_{12})}{Im(Y_{11}) + Im(Y_{12})} \right)^2 \right] \quad (3-7)$$

$$Gm = \sqrt{(A^2 + B^2)(1 + Ri^2 Cgs^2 \omega^2)} \quad (3-8)$$

$$\tau = \frac{-1}{\omega} \cdot \arctan \left[ \frac{B + A \cdot Ri \cdot Cgs \cdot \omega}{A - B \cdot Ri \cdot Cgs \cdot \omega} \right] \quad (3-9)$$

where:

$$A = \text{Re}(Y_{21}) - \text{Re}(Y_{12}) \quad (3-10)$$

$$B = \text{Im}(Y_{21}) - \text{Im}(Y_{12}) \quad (3-11)$$

An optimization algorithm process allows adjusting the extrinsic parameters in order the intrinsic parameters be frequency independent, thus validating the small-signal circuit topology [30].

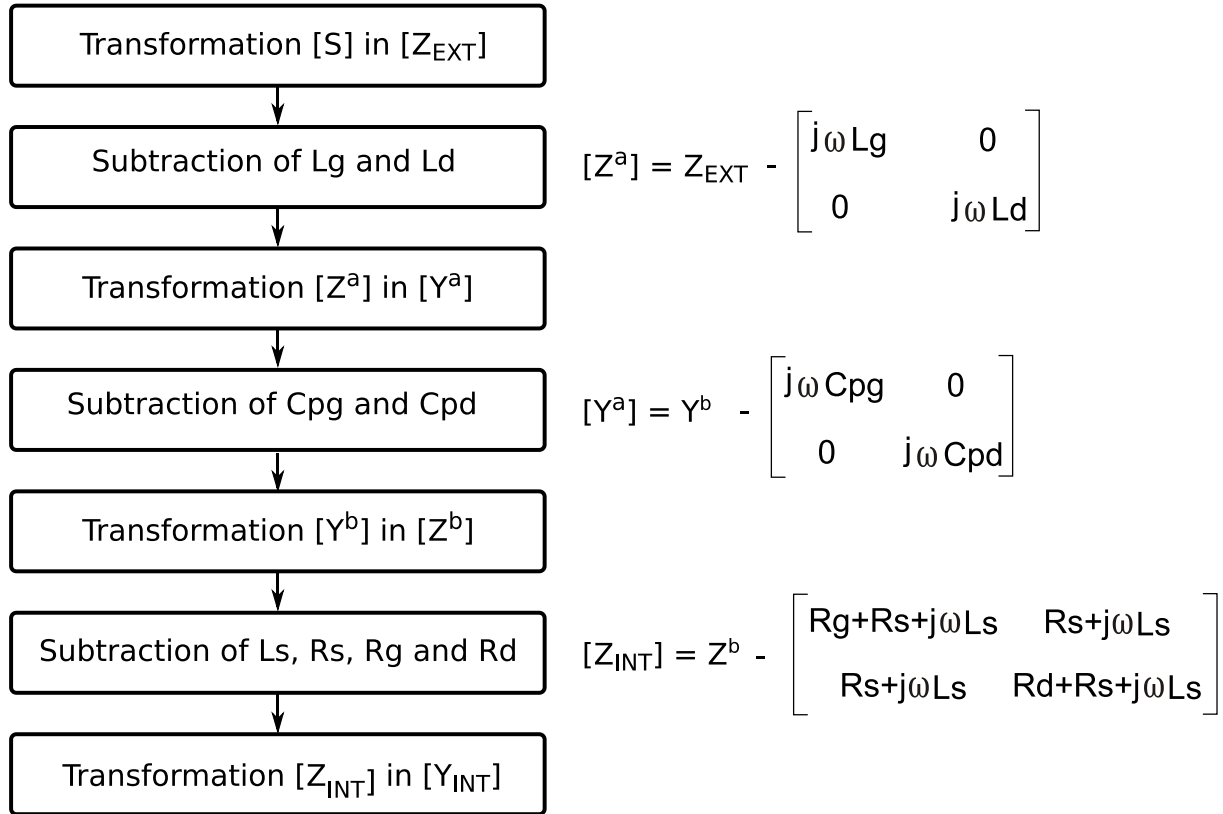


**Figure 3-8: Extraction algorithm used to determine the intrinsic Y-parameters matrix [90].**

Generally, the extraction methods used to determine the extrinsic parameters are based on S-parameter measurements at different bias point conditions [91]. A simplified approach used in [92] for a first determination of intrinsic parameters, was adapted for the GaN device in collaboration with K. Kahil [ K. Kahil personal communication] at the XLIM laboratory for use in this research thesis. LF S-parameter measurements allow estimating the ranges of values of the intrinsic parameters, which are introduced in the optimization loop in order to determine the extrinsic parameters. In the LF range, the extrinsic parameters, in Figure 3-4, can be considered negligible, therefore the intrinsic parameter equations (3-2)-(3-11) become

$$Cgd = \frac{-Im(Y_{12})}{\omega} \quad (3-12)$$

$$Rgd = \frac{-Re(Y_{12})}{(Cgd \cdot \omega)^2} \quad (3-13)$$

$$Cgs = \frac{Im(Y_{11}) + Im(Y_{12})}{\omega} \quad (3-14)$$

$$Gd = Re(Y_{12}) + Re(Y_{22}) \quad (3-15)$$

$$Cds = \frac{Im(Y_{12}) + Im(Y_{22})}{\omega} \quad (3-16)$$

$$Ri = \frac{Re(Y_{11}) + Re(Y_{12})}{(Cgs \cdot \omega)^2} \quad (3-17)$$

$$Gm = Re(Y_{21}) \quad (3-18)$$

$$\tau = \frac{-1}{\omega} \cdot \arctan \left[ \frac{B + A \cdot Ri \cdot Cgs \cdot \omega}{A - B \cdot Ri \cdot Cgs \cdot \omega} \right] \quad (3-19)$$

where:

$$A = Re(Y_{21}) - Re(Y_{12}) \quad (3-20)$$

$$B = Im(Y_{21}) - Im(Y_{12}) \quad (3-21)$$

These equations are applied to the LF CW S-parameters measured at  $(I_{DS}; V_{DS}) = (50 \text{ mA}; 40 \text{ V})$ , using the set-up in Section 2.3.4. The intrinsic parameter results extracted using this approach are shown in Figure 3-9.

It can be observed from the previous results that this LF approach give good results and provides thermally dependent intrinsic parameters. Thus, they constitute very good starting values for the global optimization of the S-parameters at higher frequencies which include the parasitic access.

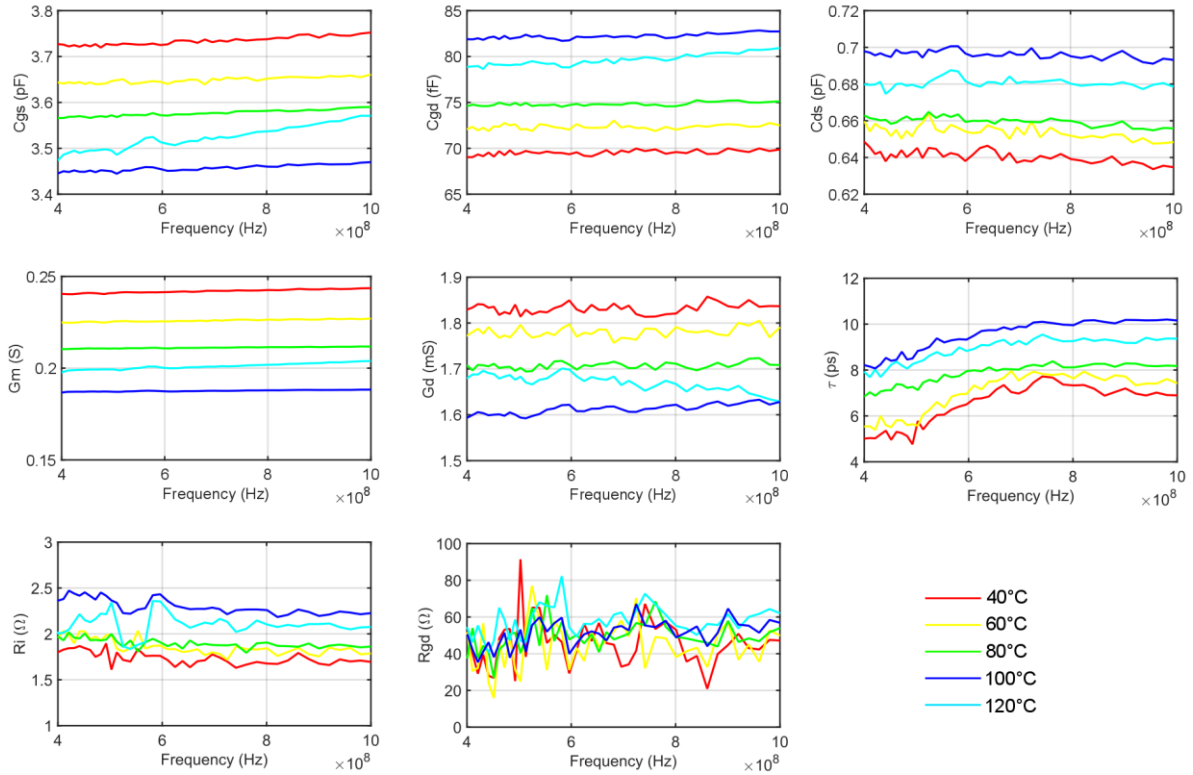


**Figure 3-9: The intrinsic parameter results extracted by LF S-parameters measured at  $(I_{DS}; V_{DS})=(50 \text{ mA}; 40 \text{ V})$  for different temperatures.**

### 3.4.1.3 Extraction of extrinsic and intrinsic parameters

The bias dependent small-signal parameters are extracted for I/V network issued from a quiescent bias point equal to the one used in the RF condition. The quiescent bias point chosen for the determining the small-signal model corresponds to  $(I_{DS,Q}; V_{DS,Q})= (50 \text{ mA}, 40 \text{ V})$ .

TABLE 6  
VALUES OF EXTRINSIC AND INTRINSIC PARAMETERS AT  
 $(I_{DS,Q}; V_{DS,Q})= (I_{DS,M}; V_{DS,M})= (50 \text{ mA}, 40\text{V})$  &  $T_{CHUCK}=25^\circ\text{C}$

EXTRINSIC PARAMETERS							
$R_g$ ( $\Omega$ )	$R_d$ ( $\Omega$ )	$R_s$ ( $\Omega$ )	$L_g$ (pH)	$L_d$ (pH)	$L_s$ (pH)	$C_{pg}$ (pF)	$C_{pd}$ (fF)
0.4	0.9	0.2	39.5	34	2	0.52	1.69
INTRINSIC PARAMETERS							
$C_{gs}$ (pF)	$C_{gd}$ (fF)	$R_i$ ( $\Omega$ )	$R_{gd}$ ( $\Omega$ )	$C_{ds}$ (pF)	$\tau$ (ps)	$g_m$ (mS)	$g_d$ (mS)
3.88	66.3	1.55	73	57.6	3.97	245	1.69

The pulsed S-parameter measurements are carried on all measurement bias points of the I/V network under quiescent bias point  $(I_{DS,Q}; V_{DS,Q}) = (50 \text{ mA}, 40 \text{ V})$ . The values of the elements of the small-signal equivalent circuit obtained at a bias point  $(I_{DS,M}; V_{DS,M}) = (50 \text{ mA}, 40 \text{ V})$ , are summarized in Table 6 and a comparison between the measured and modeled S-parameters is given in Figure 3-10. Once the extrinsic elements are determined the process can be repeated for the set of bias points chosen to obtain the multi-bias small-signal circuit.

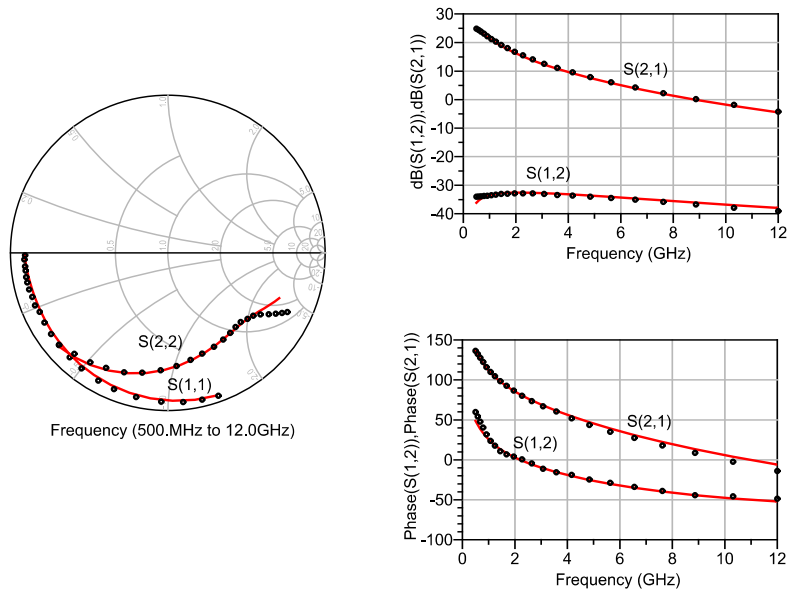


**Figure 3-10: Measurements (red solid line) and simulation results (black dotted line) of pulsed S-parameter measurements at  $(I_{DS,Q}; V_{DS,Q}) = (I_{DS,M}; V_{DS,M}) = (50 \text{ mA}, 40 \text{ V})$  from 0.5 GHz to 12 GHz.**

### 3.4.2 Nonlinear model

The nonlinear HEMT model includes the intrinsic nonlinear current sources shown in Figure 3-11. It consists of the access resistances ( $R_g, R_d, R_s$ ), the main drain current source  $I_{DS}$ , the two Schottky gate diodes ( $I_{GS}, I_{GD}$ ) and the breakdown current source  $I_{BK}$ .

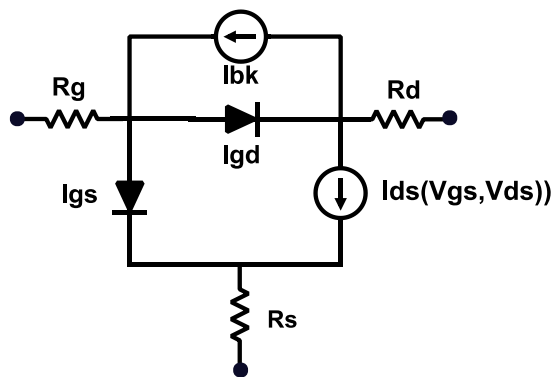


**Figure 3-11: Intrinsic nonlinear current sources of HEMT.**



### 3.4.2.1 Nonlinear current source model

The fundamental effect of FET is described by a nonlinear current source controlled by  $V_{DS}$  and  $V_{GS}$ . The model (derived from the model proposed by Tajima [93]) has been modified to take into account the HEMT effect as shown in [90]. Moreover, an accurate current source model has been developed in the XLIM laboratory by *Jardel et al.* [94], which allows to predict the  $I_{DS}$ - $V_{DS}$  characteristic for positive and negative values of the drain voltage. The model equations are:

$$I_D = I_{DS} - I_{GD} = I_{DSS} \cdot dhyp[V_{DSN} + A \cdot V_{DSN}^3] \cdot V_{GSN} \quad (3-22)$$

with

$$V_{GSN} = V_{GSNlin} \cdot \left[1 + \frac{V_{P0}}{v_p}\right]^N \quad (3-23)$$

$$V_{DSN} = \frac{V_{DS}}{V_{DSN} \cdot [1 + W \cdot (V_{GSN} - 1)]} \quad (3-24)$$

$$v_p = V_{P0} + above[-V_{DS}, \beta_{NEG}, 0] + P \cdot V_{DS} \quad (3-25)$$

$$V_{GSNlin} = above \left[ \frac{V_{GCOM} + v_p}{above(V_{SATPOS} + v_p + v_{P0}, V_{SATNEG}, \frac{-v_p}{v_{P0}})}, \alpha_{vp}, 0 \right] \quad (3-26)$$

$$V_{GCOM} = under \left[ \frac{1}{2} V_{GS} + under \left( \frac{V_{GS}}{2}, S_{SAT1POS}, V_{GSAT1POS} \right), S_{SAT1POS}, V_{GSAT1POS} \right] \quad (3-27)$$

$$V_{DSN} = \frac{V_{DS}}{V_{DSN} \cdot [1 + W \cdot (V_{GSN} - 1)]} \quad (3-28)$$

$$\alpha_{vp} = above(under(-V_{DS}, S_{SATNEG}, V_{SATNEG}), 10^{-4}, -g_{Msmooth}) \quad (3-29)$$

$$A = cval(A_{POS}, A_{NEG}, V_{DS}, R_{HO}) \quad (3-30)$$

$$W = cval(W_{POS}, W_{NEG}, (V_{GS} + V_{P0}), R_{HO}) \quad (3-31)$$

Equations (3-22)-(3-31) are composed of continuous mathematical functions: the function *dhyp* (Equation (3-22)) allows reconstructing the envelope of the current (it is similar to a hyperbolic tangent). The function *cval* (Equation (3-30)) allows changing the value of the variable  $a$  when the third parameter  $V$  reaches 0 V, with a “smooth” transition, the nature of which is governed by the parameter  $\alpha_{TRVAL}$ . Lastly, the functions *above* (Equation (3-26)) and *under* (Equation (3-27)) allow a saturation at the values  $x_n$  and  $x_p$  respectively, with a “smooth” transition governed by the parameter  $a$ . An example of the behavior of the last two

functions for different values of the parameter  $a$  and for a given  $x_n$  and  $x_p$  equal to 1 are shown in Figure 3-12.

$$dhyp(x) = \frac{x}{\sqrt{1+x^2}} \quad (3-32)$$

$$cval(x_{POS}, x_{NEG}, V, \alpha_{TRVAL}) = \frac{x_{POS} - x_{NEG}}{2} \cdot \tanh(\alpha_{TRVAL} \cdot V) + \frac{x_{POS} - x_{NEG}}{2} \quad (3-33)$$

$$hypfneg(x) = \begin{cases} \frac{1}{2 \cdot (\sqrt{1+x^2} - x)} & \text{if } x > 1 \\ -1 \\ \frac{-1}{2 \cdot x \cdot \left(1 + \sqrt{1 + \frac{1}{x^2}}\right)} & \text{else} \end{cases} \quad (3-34)$$

$$above(x, a, x_n) = \begin{cases} x + a \cdot hypfneg\left(\frac{-(x+x_n)}{a}\right) & \text{if } x > -x_n \\ -x_n + a \cdot hypfneg\left(\frac{(x+x_n)}{a}\right) & \text{else} \end{cases} \quad (3-35)$$

$$under(x, a, x_p) = \begin{cases} x_p - a \cdot hypfneg\left(\frac{(x_p-x)}{a}\right) & \text{if } x > x_p \\ x - a \cdot hypfneg\left(\frac{(x-x_p)}{a}\right) & \text{else} \end{cases} \quad (3-36)$$

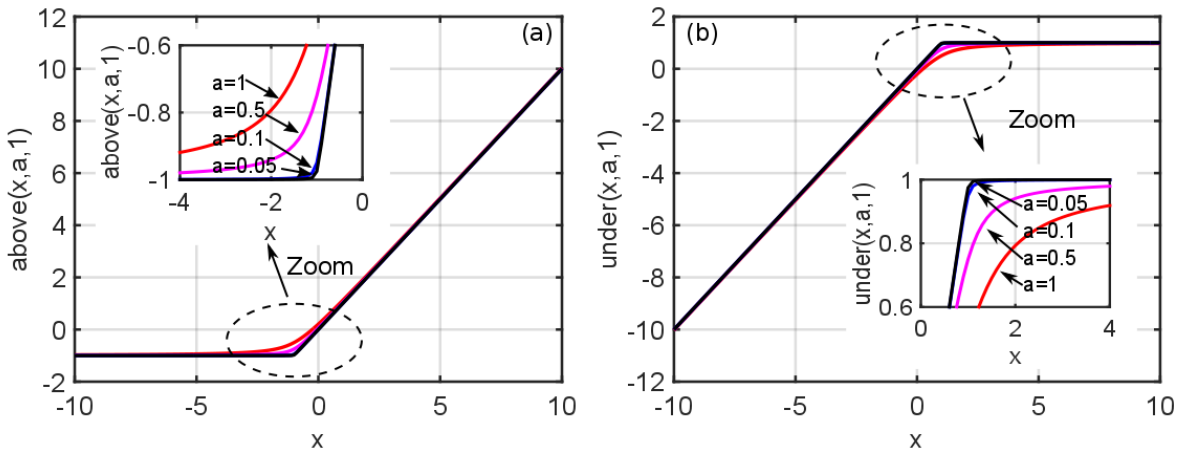


**Figure 3-12:** Comparison of the function (a)  $above(x,a,x_n)$  with  $x_n$  equal to 1 and varying the value of the parameter  $a$  and of the function (b)  $under(x,a,x_p)$  with  $x_p$  equal to 1, also varying  $a$ .

The output current source modeled by 19 parameters is therefore more accurate than the modified Tajima model which is modeled by only 13 parameters. In the following, the description of the parameter roles in the non-linear model equations is given by

- $I_{DSS}$ : drain current saturation;
- $P$ : output conductance parameter (gd);
- $V_{p0}$ : pinch-off voltage;

- $V_{dsp}$ : slope in the ohmic area (corresponds to  $R_{ON}$ );
- $W_{pos}$ : curvature of knee zone (for positive drain voltages values);
- $W_{neg}$ : curvature of knee zone (for negative drain voltages values);
- $A_{neg}$ : linear slope in the ohmic area (for negative drain voltage values);
- $A_{pos}$ : linear slope in the ohmic area (for positive drain voltages values);
- $V_{sat1pos}$ : gate voltage for first gm saturation (at high  $V_{GS}$  values and for positive drain voltages values);
- $S_{sat1pos}$ : smoothness of gm saturation due to the value of the parameter  $V_{sat1pos}$ ;
- $V_{sat2pos}$ : gate voltage for second gm saturation (at halfway  $V_{GS}$  values and for positive drain voltages);
- $S_{sat2pos}$ : smoothness of current saturation governed by the parameter  $V_{sat2pos}$ ;
- $N$ : curvature of gm in the middle of I/V network;
- $S_{satneg}$ : smooth of current saturation (for negative drain voltages);
- $V_{satneg}$ : gate voltage for current saturation;
- $gm_{smth}$ : smoothing around pinch-off voltage area;
- $\rho$ : smooth transition between the two parameters of the function *cval*.

The parameter values of nonlinear current source model are determined from pulsed I/V measurements in hot condition and are shown in Table 7.

TABLE 7  
PARAMETER VALUES OF OUTPUT CURRENT SOURCE

<b>OUTPUT CURRENT SOURCE</b>							
IDSS	P	Vp0	Vdsp	Wpos	Wneg	Apos	Aneg
0.95	0.0009	1.54	2.73	1.5	0	0.01	0.01
Ssat1pos	Ssat2pos	Vsat1pos	Vsat2pos	N	Ssatneg	Vsatneg	gm <sub>smth</sub>
0.02	0.85	5	1.72	2.08	0.87	0.993	0.14
Rho							
1							

The gate contact is modeled by the gate-drain and gate-source diode equations including both forward and reverse conductions of gate current. The diodes are modeled by the classical equations:

$$I_{gs} = I_{S_{gs}} \cdot \left[ e^{\frac{q \cdot V_{gs}}{N_{gs} \cdot k \cdot T}} - 1 \right] \quad (3-37)$$

$$I_{gd} = I_{S_{gd}} \cdot \left[ e^{\frac{q \cdot V_{gd}}{N_{gd} \cdot k \cdot T}} - 1 \right] \quad (3-38)$$

The parameter values for the gate-drain and gate-source diodes are extracted from pulsed I/V measurements in hot condition for high gate-source voltages and are shown in Table 8.

TABLE 8  
PARAMETER VALUES OF GATE-DRAIN AND GATE-SOURCE DIODE

<b>GATE-DRAIN AND GATE-SOURCE DIODE</b>			
$I_{S_{gs}}$	$N_{gs}$	$I_{S_{gd}}$	$N_{gd}$
$1.12 \cdot 10^{-14}$	1.5	$1.6 \cdot 10^{-14}$	1.5

The drain-to-gate breakdown phenomenon is modeled by a current source  $I_{bk}$ , which gives an exponential increase in the gate-to-drain current when the breakdown voltage  $V_{GD}$  is reached. For modeling this exponential increase a soft quasi-exponential function (*exp\_soft*) is used to improve the simulation convergence [94].

$$I_{bk} = I_{av_{gd}} \cdot [exp\_soft(\alpha_{gd} V_{ds})] \quad (3-39)$$

However, for the GaN technology studied in this thesis, the nonlinear breakdown source is not considered because the breakdown voltages are far beyond the operating voltages.

### 3.4.2.2 Nonlinear capacitances model

The gate-to-source and gate-to-drain capacitances  $C_{gs}$  and  $C_{gd}$  present a nonlinear dependence on both control voltages  $V_{GS}$  and  $V_{GD}$  [94] which can be modeled with a one dimensional model. Moreover, the one dimensional capacitance model provides better convergence than 2D models. Thus, the nonlinear  $C_{gs}$  and  $C_{gd}$  are extracted under operation condition which for power amplifier application, are along the ideal large-signal operating load-line. Generally, from the multi-bias measured S-parameters, the resulting values of  $C_{gs}$  and  $C_{gd}$  along the estimated load-line behave similarly to the one shown in Figure 3-13. These shapes can be precisely fitted with hyperbolic tangent equations:

$$C_{gx} = C_0 + \frac{C_1 - C_0}{2} [1 + \tanh(a(V_{gx} + V_m))] - \frac{C_2}{2} [1 + \tanh(b(V_{gx} + V_p))] \quad (3-40)$$

where  $C_{gx}$  and  $V_{Gx}$  stand for the gate-to-x capacitance and voltage, respectively, i.e. ( $C_{gs}$  and  $V_{GS}$ ) or ( $C_{gd}$  and  $V_{GD}$ ). The seven modeling parameters ( $C_0$ ,  $C_1$ ,  $C_2$ ,  $a$ ,  $b$ ,  $V_p$  and  $V_m$ ) are different for each of the capacitance models.

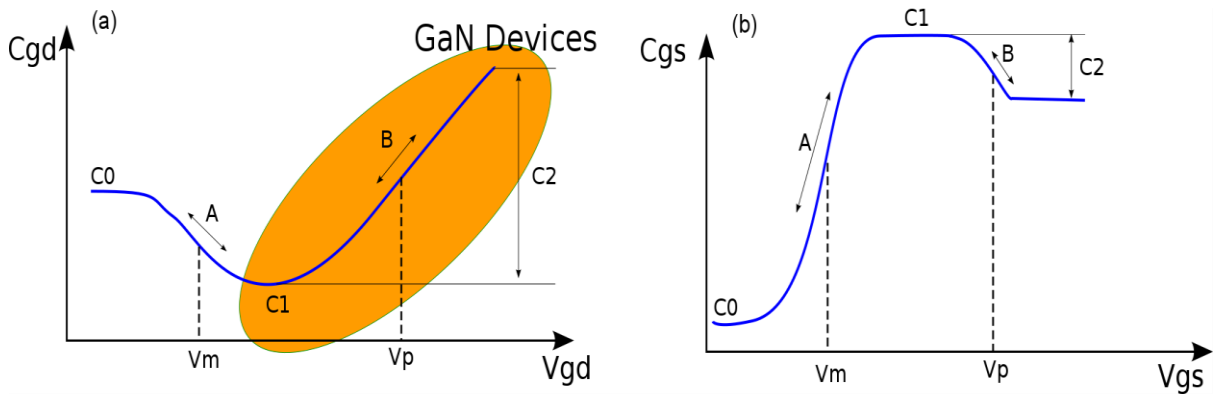


**Figure 3-13: Typical shapes of (a)  $C_{gd}$  VS  $V_{GD}$  and (b)  $C_{gs}$  VS  $V_{GS}$ .**

The  $C_{gs}$  and  $C_{gd}$  parameters are extracted from multi-bias pulsed S-parameter measurements issuing from the I/V hot network bias point ( $I_{DS,Q}$  ;  $V_{DS,Q}$ )= (50 mA, 40V). The comparison between of the extracted  $C_{gs}$  and  $C_{gd}$  values along the estimated load-line and the modeled  $C_{gs}$  and  $C_{gd}$  are shown in Figure 3-14. The values of the different parameters of the  $C_{gs}$  and  $C_{gd}$  models are shown in Table 9.

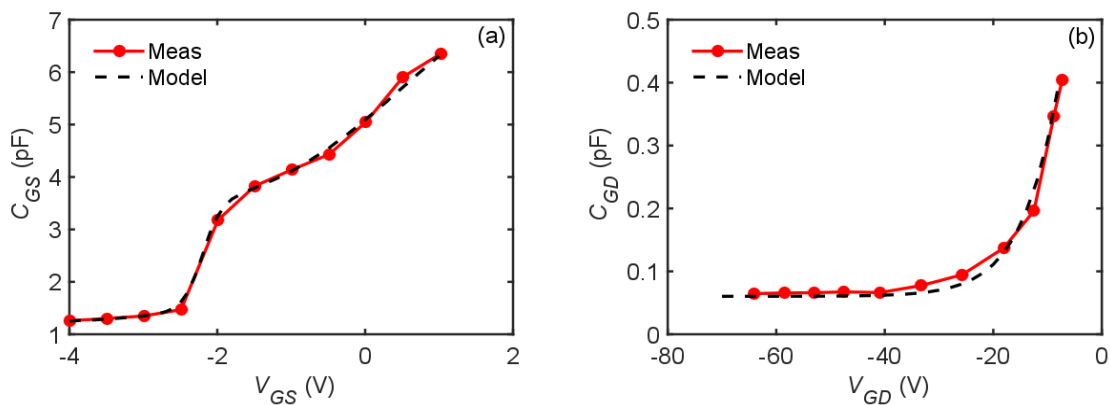


**Figure 3-14: Comparison of experimental (red solid line with circle) values and modeled (black dotted line) values of (a)  $C_{GS}$  and (b)  $C_{GD}$  versus  $V_{GS}$  and  $V_{GD}$ , respectively, along the estimated load-line.**

TABLE 9  
PARAMETER VALUES OF  $C_{GS}$  AND  $C_{GD}$

Parameter values of $C_{gs}$ 1D equation						
$C_0$ (pF)	$C_1$ (pF)	$C_2$ (pF)	A	B	$V_m$ (V)	$V_p$ (V)
1.2	3.2	-5	4	0.5	2.2	-0.5
Parameter values of $C_{gd}$ 1D equation						
$C_0$ (pF)	$C_1$ (pF)	$C_2$ (pF)	A	B	$V_m$ (V)	$V_p$ (V)
0.06	2.84	10	0.083	1	-4	-3

### 3.4.3 Nonlinear trapping and thermal current source model

As already established, AlGaIn/GaN HEMTs are still subject to memory and thermal effects. In particular, these trapping effects that have been deeply studied in the previous chapter present a nonlinear dynamic variation of the dispersion effects under modulated signals such as RF pulses. This dynamic behavior plays a major role in the modification of its large-signal performance. Moreover, self-heating also plays a major role under large-signal operation mode of transistors and affects their reliability. Indeed, several parameters such as carrier mobility and saturation velocity, are sensitive to temperature, leading to a reduction of drain current and power gain. Furthermore, traps are also very sensitive to temperature. So, there is a need to integrate the nonlinear RF dynamic effects and their thermal variation into a large-signal electro-thermal HEMT model.

The trapping effects are modeled through the modulation of the drain current source by gate and drain stimulus. The AlGaIn/GaN model employed an intrinsic output current given by Equation (3-41). It is a nonlinear parametric function of the instantaneous intrinsic gate and drain voltages  $V_{GS}(t)$  and  $V_{DS}(t)$ , temperature, intrinsic gate voltage that corresponds to the gate-lag effect and intrinsic pinch-off voltage  $V_{P0\_INT}$  that corresponds to the drain-lag effect. These gate-lag and drain-lag components have a strong dependency on the trap charge, firstly, and on the temperature, secondly.

$$I_{DS}(t) = f_{NL} \left( V_{GS}(t), V_{DS}(t), T^{\circ}, V_{GS\_INT}, V_{P0\_INT}(t), V_C(t), T^{\circ} \right) \quad (3-41)$$

Thus, the gate-lag and the drain-lag effects are modeled by adding trap sub-circuits to the nonlinear circuit model that dynamically modify the actual gate and pinch-off control voltages, respectively.

In the following part the trapping model based on gate-lag and drain-lag sub-circuits and the parameter extraction of the drain-lag model will be presented. Lastly, the temperature dependent parameters of the current source and trapping model will be determined.

#### 3.4.3.1 The gate-lag sub-circuit

The gate-lag sub-circuit, that is depicted in schematic form in Figure 3-15, operates as an envelope detector on the gate-to-source voltage  $V_{GS}(t)$  so as to modify itself and calculate the new intrinsic gate-to-source voltage  $V_{GS\_INT}(t)$  of the current source by the charging/discharging of the capacitance  $C_{TRAP}$  according to a physical exponential law.

During a capture process that corresponds to a decrease of  $V_{GS}$ , the capacitance  $C_{TRAP}$  charges through the resistance  $R_{CAP}$  (with a capture time constant  $\tau_{CAP} \cong R_{CAP} \cdot C_{TRAP}$  as  $R_{CAP} \ll R_{EMI}$ ). In contrast, during an emission process, which corresponds to an increase of  $V_{GS}$ , the capacitance  $C_{TRAP}$  discharges through the resistance  $R_{EMI}$  (with an emission time constant  $\tau_{EMI} \cong R_{EMI} \cdot C_{TRAP}$ ). This model also takes into account the following assumption of a strong dissymmetry of GaN technology between the capture and emission time constants. The capture time constant is assumed to fall into the nanoseconds-microseconds range while the emission time constant is assumed to fall into the microseconds-seconds range in GaN HEMTs.

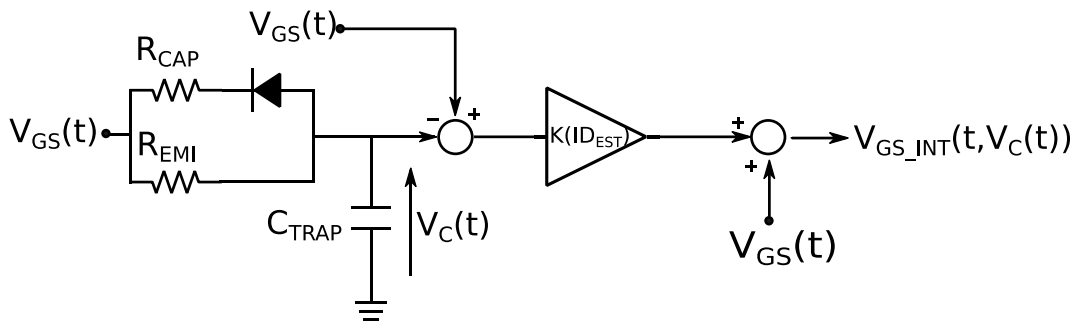


**Figure 3-15: Schematic of gate-lag model [94].**

Finally, the intrinsic actual gate-to-source voltage  $V_{GS\_INT}(t)$  is calculated as the instantaneous capacitor voltage  $V_C(t)$  multiplied by a factor  $k$  shown in Figure 3-15. This factor controls the amplitude of the trap and is calculated as

$$k(ID_{EST}) = krel \cdot ID_{EST}(V_{GS}) \cdot A_{DL} \quad (3-42)$$

with

$$ID_{EST}(V_{GS}) = Gm_{DC} \cdot [V_{GS} - V_{PINCH-OFF}] \quad (3-43)$$

where  $Gm_{DC}$  and  $A_{DL}$  are fitting parameters while  $krel$  is the sum of each trap contribution  $krel_n$  in the case of  $n$  different trap states.

$$krel = \sum_1^n krel_n \quad (3-44)$$

Therefore, the instantaneous gate control voltage  $V_{GS\_int}$  obtained from the gate-lag model is defined by the following equation:

$$V_{GS\_int} = V_{GS} + k(ID_{EST}) \cdot (V_{GS} - V_C) \quad (3-45)$$

So that the actual drain current will be expressed as

$$I_{DS} = f(V_{GS\_int}, V_{ds}) \quad (3-46)$$

The gate-lag effect in this AlGaN/GaN technology has been reduced strongly by passivation and field plate as shown in Section 2.3.1.2. Thus, the gate-lag model is not implemented in our intrinsic output current source model.

### 3.4.3.2 The drain-lag sub circuit

As already shown in the previous chapter, the drain-lag effect still remains the main trap phenomenon that affects the large-signal operation mode. Thus, this paragraph focuses on the development of an accurate additive trap model mainly based on the recent work of *Jardel et al.* [41]. The model implemented in this thesis allows predicting the dynamic behavior of trap states from DC to the radio-frequency operation mode. The trap dynamic behavior is taken into account by the modification of correction term to the pinch-off voltage. The pinch-off voltage shift has been identified in this technology as the main cause of the trapping effects during RF large signal operation as shown in Figure 2-41. The nonlinear current source equations presented in Section 3.4.2.1 have been modified in order to add a correction term to the pinch-off voltage ( $V_{P0}$ ) formulation and also to the parameter  $I_{DSS}$  (determining the steady state current). To ensure, as much as possible a physical behavior summarized by the expression of the density of carriers in the channel as shown in Equation (3-47), both contributions are written in order to maintain the proportionality relationship between  $V_{P0}$  ( $V_{TH}$  in Equation (3-47)) and  $I_{DSS}$  ( $qn_s$  in Equation (3-47)).

$$qn_s(E_f, V_{GS}) = C_0[V_{GS} - V_{TH}] \quad (3-47)$$

The new nonlinear current source equations taking into account the trapping effects are

$$I_D = I_{DSS,TRAP} \cdot dhyp[V_{DSN} + A \cdot V_{DSN}^3] \cdot V_{GSN} \quad (3-48)$$

$$v_p = V_{P0INT}(t, V_c(t)) + above[-V_{DS}, \beta_{NEG}, 0] + P \cdot V_{DS} \quad (3-49)$$

$$I_{DSS,TRAP} = I_{DSS} \cdot \left( \frac{V_{P0INT}(t, V_c(t))}{V_{P0}} \right) \quad (3-50)$$

where  $V_{P0INT}(t, V_c(t))$  is the instantaneous output voltage of the drain-lag sub-circuit depicted in Figure 3-16. This thermal-trap model is based on the same charging/discharging principle



as the gate-lag model. The instantaneous capacitor voltage  $V_C(t)$  modifies the pinch-off voltage in order to control the nonlinear drain current source. In the model, the amplitude of the capture and emission processes of each trap is controlled by the  $A_{TRAP}$  parameter whereas the constant factor  $KV_P$  is used to adjust the weight of all trap effects into  $V_{P0\_INT}(t)$ .

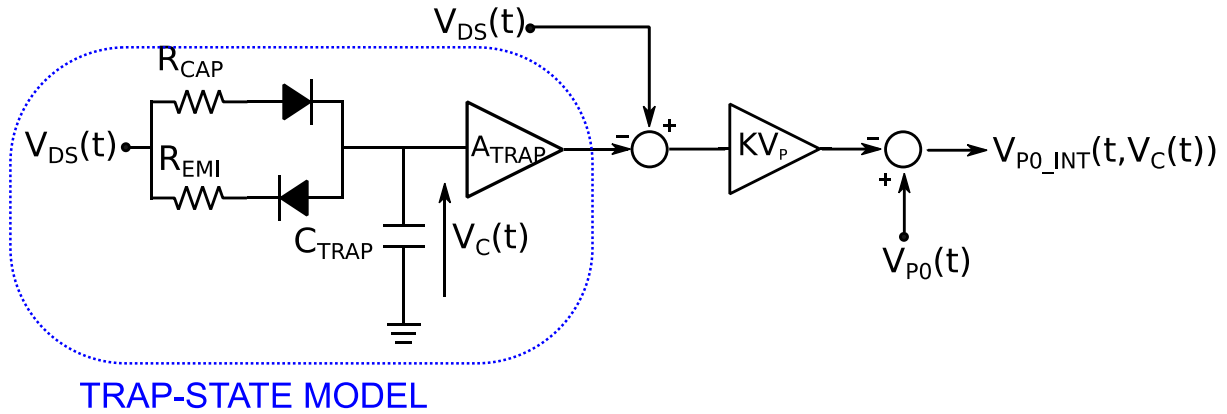


**Figure 3-16: Schematic of drain-lag model.**

An example of a chronogram of the drain-lag impact observed in dynamic I/V conditions is presented in Figure 3-17. It shows the evaluation of the internal voltages in the drain-lag model. For this example  $V_{DS,HIGH}$  is assumed large enough to involve a capture process and the pulse-width is large enough to observe emission and capture process:

- 1) The emission process appears when the drain voltage varies from  $V_{DS,HIGH}$  to  $V_{DS,LOW}$ , the diode of the drain-lag sub-circuit is blocked and the capacitor  $C_{TRAP}$  is discharged through  $R_{EMI}$  with an associated time constant  $\tau_{EMI}$ . The instantaneous capacitor voltage is multiplied by  $A_{TRAP,EMI}$  and subtracted from  $V_{DS}$ . The resulting transient is multiplied by  $KV_P$  and subtracted from  $V_{P0}$ . The final output voltage  $V_{P0\_INT}$  directly shapes the transient of the  $I_{DS}$  drain current.
- 2) The capture process appears when the drain voltage varies from  $V_{DS,LOW}$  to  $V_{DS,HIGH}$  assuming that the emission process is completed. The diode of the drain-lag sub-circuit conducts and the capacitor  $C_{TRAP}$  is charged through  $R_{CAP}$  with an associated time constant  $\tau_{CAP}$ . The instantaneous capacitor voltage is multiplied by  $A_{TRAP,CAP}$  and subtracted from  $V_{DS}$ . The resulting transient is multiplied by  $KV_P$  and subtracted from  $V_{P0}$ . The final output voltage  $V_{P0\_INT}$  directly shapes the transient of the  $I_{DS}$  drain current.

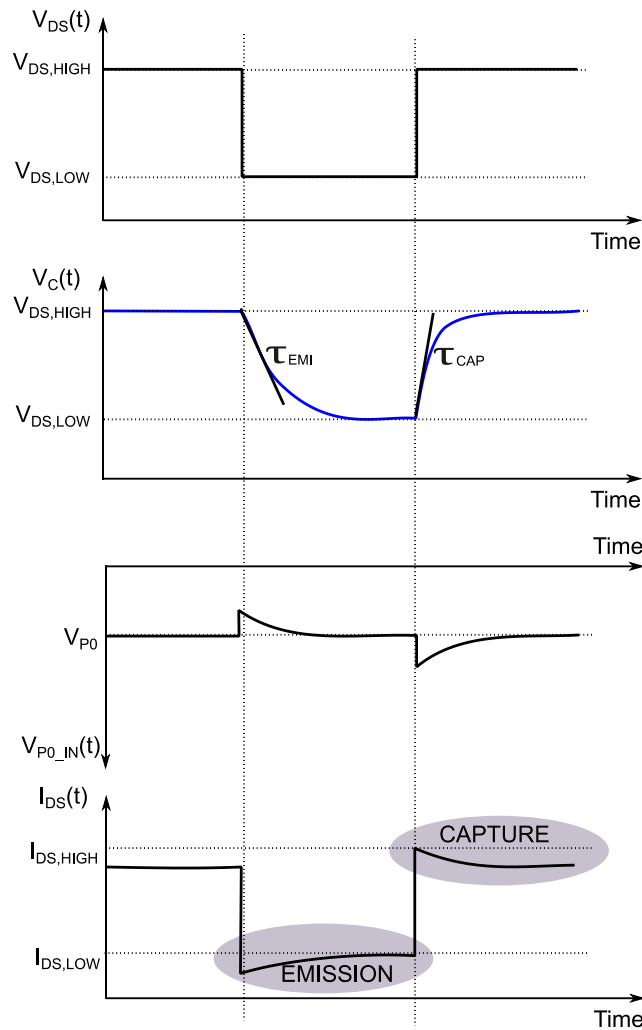


**Figure 3-17: Chronogram of internal voltages and drain current in the drain-lag sub-circuit model.**

### 3.4.3.3 Extraction of drain-lag sub-circuit

The method for the drain-lag model extraction is based on pulsed I/V measurements, LF CW S-parameter measurements and DCT measurements. It is possible to identify one trap state from LF CW S-parameter measurements and two other different trap states from DCT measurements. Therefore, three trap states are modeled in the drain-lag sub-circuit. The trap state sub-circuit model is represented in Figure 3-16.

The first step of the extraction method is based firstly on LF CW S-parameter measurements. It consists more specifically in the output conductance frequency dispersion analysis that is very sensitive to the drain-lag phenomenon. This characterization allows determining the time constant of trap by the frequency peak value of imaginary part of  $Y_{22}$ , as demonstrated in Section 2.3.4. Then, it is easy to implement the trap model with the deduced time constants ( $\tau = R_{EMI} \times C_{TRAP}$ ) from the results of the measurements of the imaginary part of  $Y_{22}$ . This low-

frequency S-parameter measurements method has the major advantage, in addition to pulsed I/V measurements, of making the traps only dependent on the biasing of the transistor. Figure 3-18 shows the comparison of low-frequency  $Y_{22}$ -parameter variation between measured and simulated results at 80°C. In the following, this trapping phenomenon is labeled “E2”.

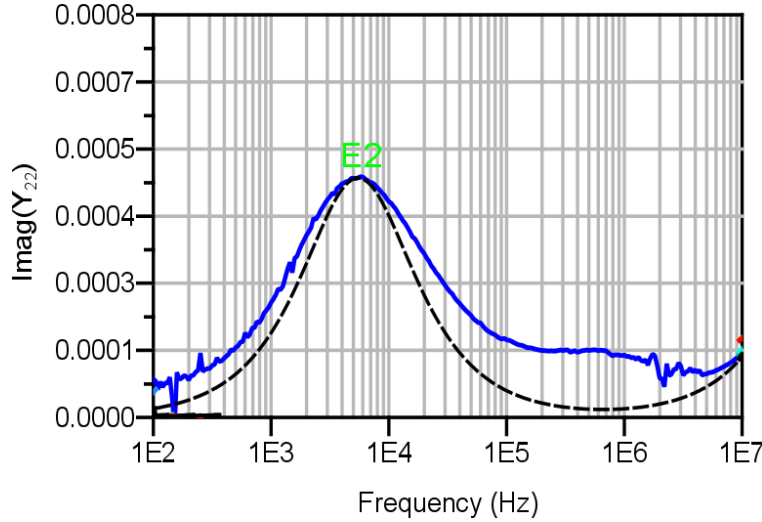


**Figure 3-18: Measurement (blue solid line) and simulation results (black dotted line) of imaginary part of  $Y_{22}$  from 100 Hz to 10 MHz frequency range at  $I_{DS}=25$  mA/mm and  $V_{DS}=40$  V at 80°C.**

The second step of modeling the trap consists of analyzing the bias drain current measured during DC excitation. The trap model described in *Jardel et al.* [41], is then modified to simplify and make easier the extraction of the parameter values of the drain-lag model ( $A_{TRAP}$  and  $\tau$  in Figure 3-16) by fitting the drain current transient measurement results after stress DC condition. The stretched multi-exponential function used to fit the measured results is described by Equation (2-15). The measurement and simulation results of drain current analysis consists in 100 s of DC filling pulse ( $V_{DF}; I_{DF}$ )=(40V;50mA) and another 100 s in the DC de-trapping condition ( $V_{DM}; I_{DM}$ )=(5V;100mA) are shown in Figure 3-19. In particular, the de-trapping transient simulation exhibits the CC after the transition and the time constants of the two trapping phenomena: the capture process labeled “E3” and the emission process labeled “E4” (the impact of “E3” is minimal). The capture process is implemented with negative trap amplitude. The modeling of the drain current is realized on ADS software using a transient simulation. In order to simplify the parameter extraction of the drain-model for modeling the drain current transient, we have added a diode branch with  $R_{EMI}$  in this way the  $\tau_{EMI}=R_{EMI} \times C_{TRAP}$ . Therefore, the emission time constant does not depend on  $R_{CAP}$ . This modification is used only for the trap state model that issues from DCT measurement.

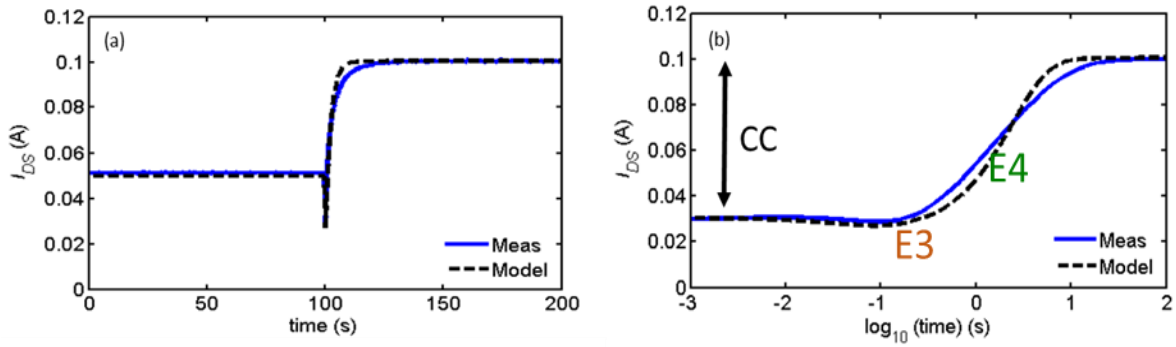


**Figure 3-19:** (a) Drain current measurement (blue solid line) and simulation results (black dotted line) for 100 s device is biased under DC filling pulse ( $V_{DF}; I_{DF}$ )=(40V; 50 mA), subsequently biased for another 100 s in the de-trapping condition ( $V_{DM}; I_{DM}$ )=(5 V; 100 mA) at 60°C. (b) De-trapping transient measurements (blue solid line) and simulation results (black dotted line) at 60°C.

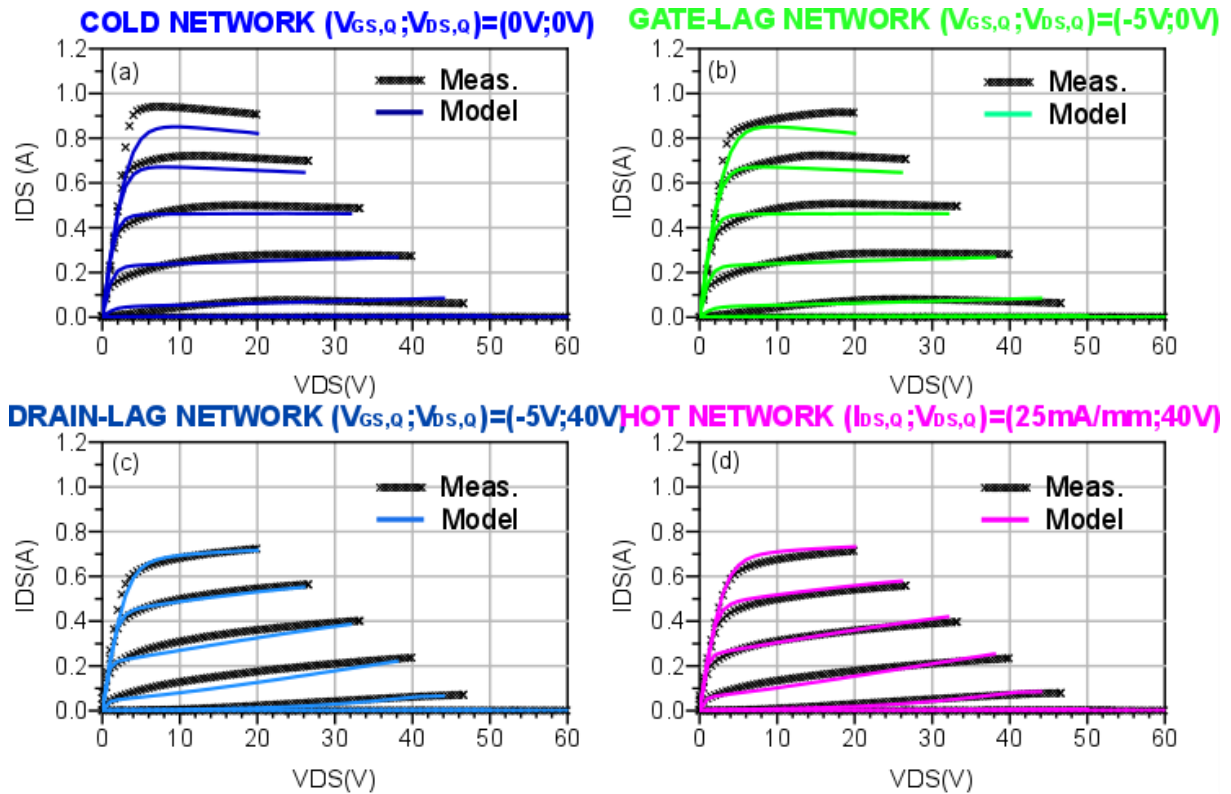


**Figure 3-20:** Measurement (crosses) and simulation results (solid line) of pulsed I/V characteristic in (a) cold condition, (b) gate-lag condition, (c) drain-lag condition and (d) hot condition with  $T_{ON}/T_{OFF}=1\mu s/99\mu s$  and  $V_{GS}$  from 0V to -4V (-0.5V/step).

Lastly, the amplitudes of the trap density  $A_{TRAP}$  and pinch-off voltage correction term  $KV_P$  (in Figure 3-16) are refined to predict the correct dispersion level of pulsed I/V measurements at different quiescent points, drain current transient measurement excitations, and low-frequency CW S-parameter measurements. A virtual pulsed test bench is realized on ADS software using a transient simulation to obtain the pulsed I/V characteristic of the model. The comparison of measured and modeled pulsed I/V characteristics at different quiescent bias

points is shown in Figure 3-20. As shown in Figure 3-20 the model shows a good match with the measurements in drain-lag and hot conditions. However, in cold and gate-lag conditions, the amplitude of the drain current for a high gate voltage is not attained (the trap amplitude is too weak for high gate voltages).

### 3.4.3.4 Thermal electrical model extraction

The trap states are strongly sensitive to the device's operating temperature. It is then necessary to accurately estimate the junction temperature to predict the dynamic behavior of the traps at several temperatures.

In order to model the temperature evolution, the thermal analog circuit shown in Figure 3-21 is used. The temperature rises exponentially as a function of time for a fixed dissipated power. Thus, a suitable electrical representation consists of parallel R-C cells with different time constants ( $\tau_n = R_n \times C_n$ ). The dissipated power, calculated in the intrinsic current source, is represented as a current source in the input of the R-C network, and the self-heating is implemented by the output circuit voltage. The ambient temperature is associated with an initial voltage. The junction temperature device is dependent on the power dissipation by adding the room temperature as a voltage source.

To estimate the thermal impedance versus time, a 3-D finite-element simulation with ANSYS software was performed by applying a dissipated power of 2.25 W/mm. Thus, the equivalent thermal RC-network model is determined by the 3-D finite-element simulation, as shown in Figure 3-22. The 3-D finite element simulations were provided by R. Sommet.

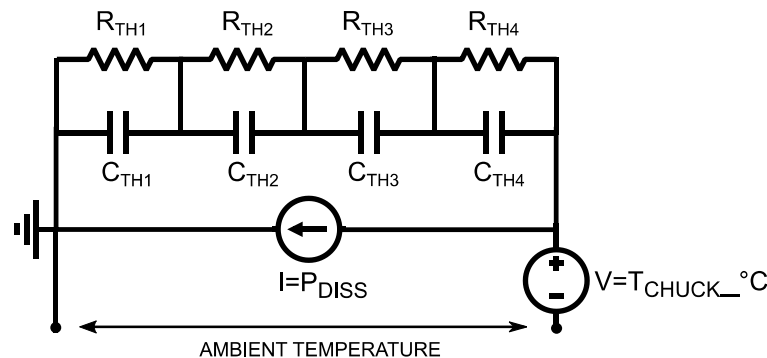


**Figure 3-21: Thermal analog circuit implemented in the nonlinear current source model.**

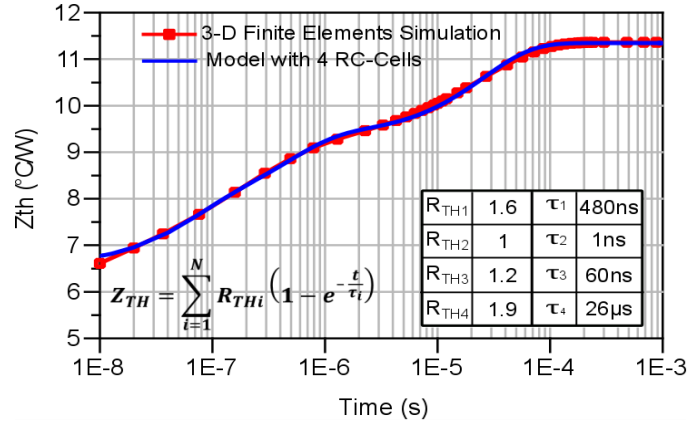


**Figure 3-22: Thermal impedance versus time. The solid line with square in red corresponds to 3-D finite element simulation for a dissipated power equal to 2.25 W/mm obtained by ANSYS software. The solid line in blue corresponds to the values given by the electrical model with four RC cells.**

#### 3.4.3.4.1 Thermal dependence of output current source

The thermal dependence of the output current source is extracted from pulsed I/V network measurements in hot condition ( $V_{DS,Q}$ ;  $I_{DS,Q}$ )=(40 V; 50 mA) at different temperatures as shown in Figure 3-23. It can be observed that the saturation drain current decreases when the temperature increases. It can be also seen that the pinch-off shifts leftward with an increase in temperature. In order to model the thermal variation of the pulsed  $I_{DS}$ - $V_{DS}$  and  $I_{DS}$ - $V_{GS}$  characteristics a thermal linear dependency is applied on the drain current saturation parameter, output conductance parameter and pinch-off voltage parameter:

$$I_{DSS} = I_{DSS0} \cdot (1 + \alpha_{I_{DSS}} \cdot T) \quad (3-51)$$

$$P = P_0 \cdot (1 + \alpha_{P_0} \cdot T) \quad (3-52)$$

$$V_{P0} = V_{P00} \cdot (1 + \alpha_{V_{P0}} \cdot T) \quad (3-53)$$

The parameters for the thermal dependence of the output current source are shown in Table 10.

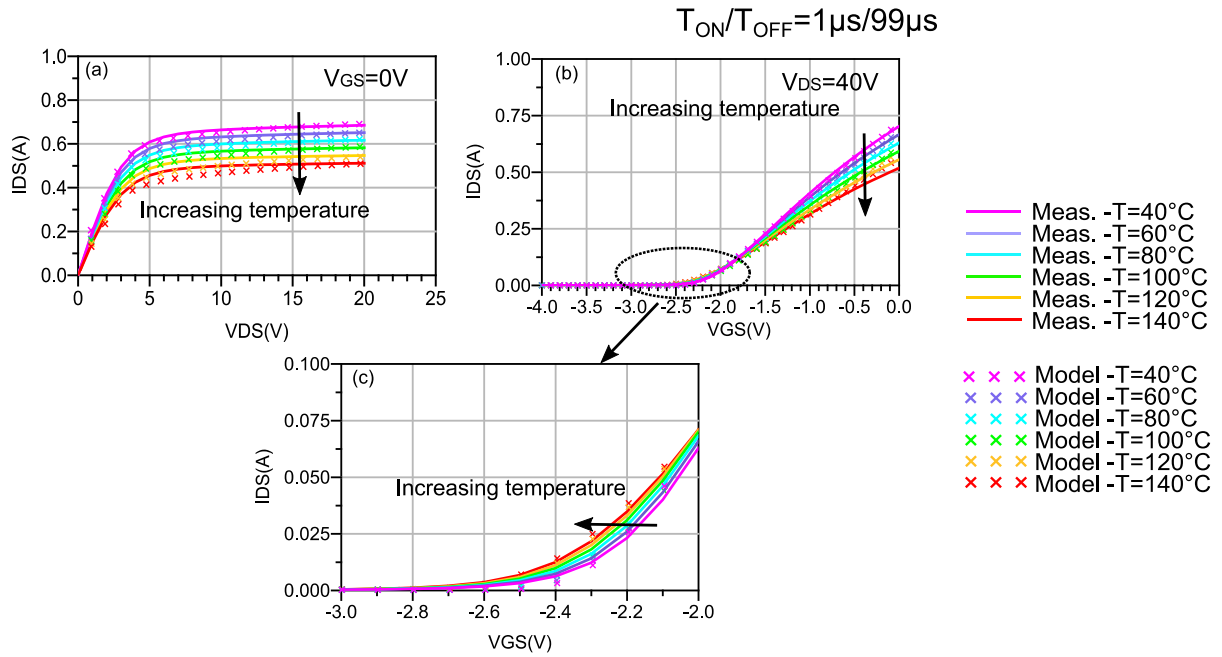


**Figure 3-23: Measurement (solid line) and simulation results (crosses) at several temperatures of pulsed (a)  $I_{DS}$ - $V_{DS}$  characteristic in hot condition ( $V_{DS,Q}; I_{DS,Q}$ )=(40V;50mA) at  $V_{GS}=0V$ , (b)  $I_{DS}$ - $V_{GS}$  characteristic at  $V_{DS}=40V$  and (c) zoom of  $I_{DS}$ - $V_{GS}$  characteristic at  $V_{DS}=40V$ .**

TABLE 10  
THERMAL DEPENDENCY PARAMETERS OF OUTPUT CURRENT SOURCE

$I_{DSS0}$	$\alpha I_{DSS}$	$P_0$	$\alpha P_0$	$VP_0$	$\alpha VP_0$
1.02	-0.0025	0.0001	-0.00001	1.6	0.0008

### 3.4.3.4.2 Thermal-trap model

In the thermal-trap model, it is assumed that each defect is represented by a capacitance  $C_{TRAP}$  and that the values of the resistances  $R_{CAP}$  and  $R_{EMI}$  determine respectively the capture and emission time constants [95]. Hence, a change of capture/emission time constant due to an increase of temperature corresponds to a change of capture/emission resistance. Therefore, in this drain-lag model, the temperature dependence of the traps is incorporated into the capture  $R_{CAP}(T^\circ)$  and emission  $R_{EMI}(T^\circ)$  resistances. Assuming that the trap density does not change with temperature, the multiplying factor  $A_{TRAP}$  remains constant with respect to the temperature variation. This model also makes the assumption of a strong dissymmetry of GaN technology between the capture and emission time constants. Indeed, the capture time constant usually falls into the nanoseconds-microseconds range during the trapping phase while the emission time constant falls into the microseconds-seconds range during the de-trapping phase in GaN HEMTs. With this assumption on the capture time constants, the

temperature dependence of the capture process is not applied. To summarize, three charge-trapping RC networks coupled with diodes were implemented in thermal drain-lag model. The first one takes into account the small-signal dispersion that has a fast emission time constant (in the microseconds-milliseconds range) as trap phenomenon “E2”. The second and third RC networks are used to model the slow dispersion due to the large-signal operation mode, where the associated slow time constants are in the milliseconds-minutes range, such as trap phenomena “E3” and “E4”.

The new drain-lag sub-circuit including the thermal dependence is shown in Figure 3-24. Each resistance follows a thermal dependence as given in Equation (3-54).

$$R_{EMI}(T) = R_{EMI0} \cdot e^{(\alpha_{EMI} \cdot T)} \quad (3-54)$$

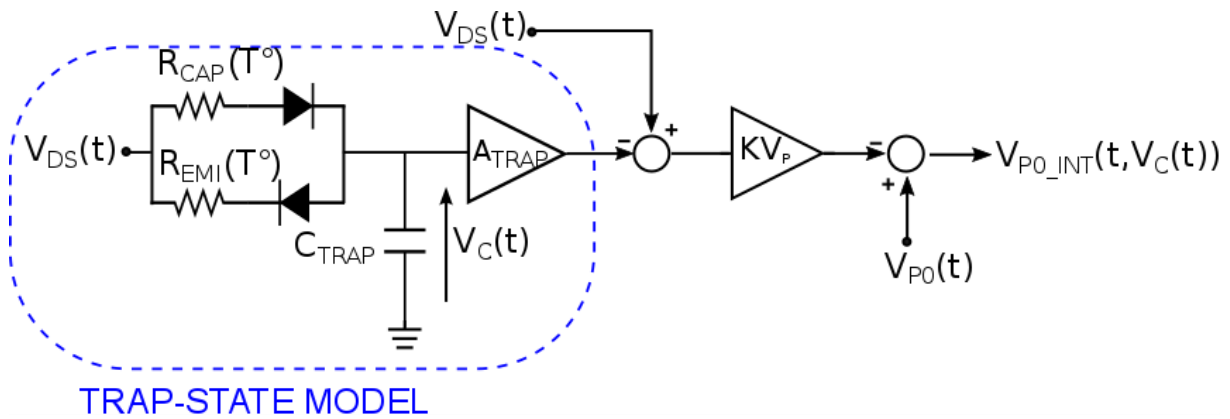


**Figure 3-24: Schematic of thermal drain-lag model.**

TABLE 11  
THERMAL DEPENDENCE OF EMISSION RESISTANCES

$R_{EMI0\_E2}$	$\alpha_{EMI\_E2}$	$R_{EMI0\_E3}$	$\alpha_{EMI\_E3}$	$R_{EMI0\_E4}$	$\alpha_{EMI\_E4}$
0.015	-0.0055	4.7	-0.076	101.5	-0.065

The thermal activation of traps “E2”, “E3” and “E4” and therefore their emission resistance variations are determined by LF  $Y_{22}$  measurements for “E2” and DCT measurements for “E3” and “E4” at different temperatures. The parameter values of Equation (3-54) are shown in Table 11 for the three traps identified. In the case of capture process “E3” during the de-trapping transient, as described before, the trap amplitude ( $A_{TRAP}$ ) is assumed to be negative, so as to predict the drain current reduction. Consequently, the thermal dependence of the trap is applied to  $R_{EMI}$  to produce the correct temperature variation of the emission process.

The leftward frequency shift of trap “E2” and the rightward time constant shift of trap “E3” and “E4” with increasing temperature are correctly modeled.

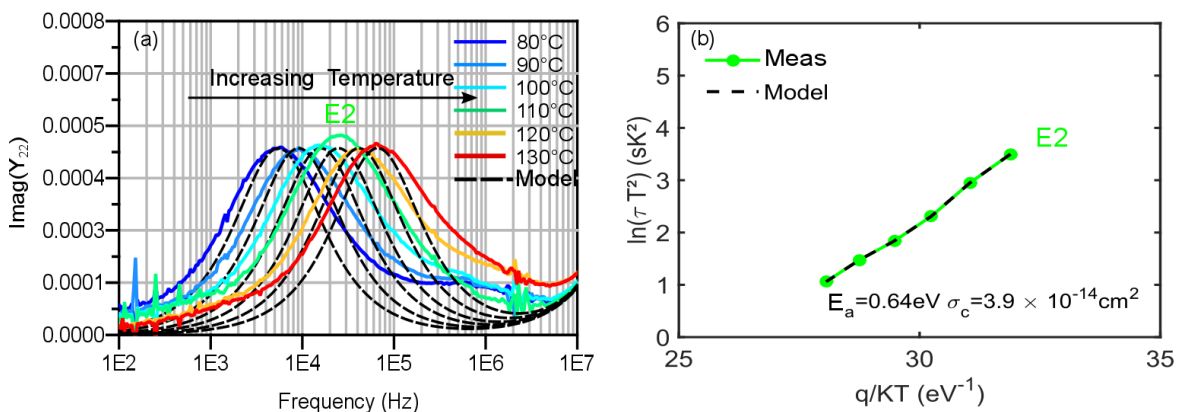


Figure 3-25(a) compares the LF  $Y_{22}$ -parameter of the measured and simulated results when the temperature varies from 80°C to 130°C.

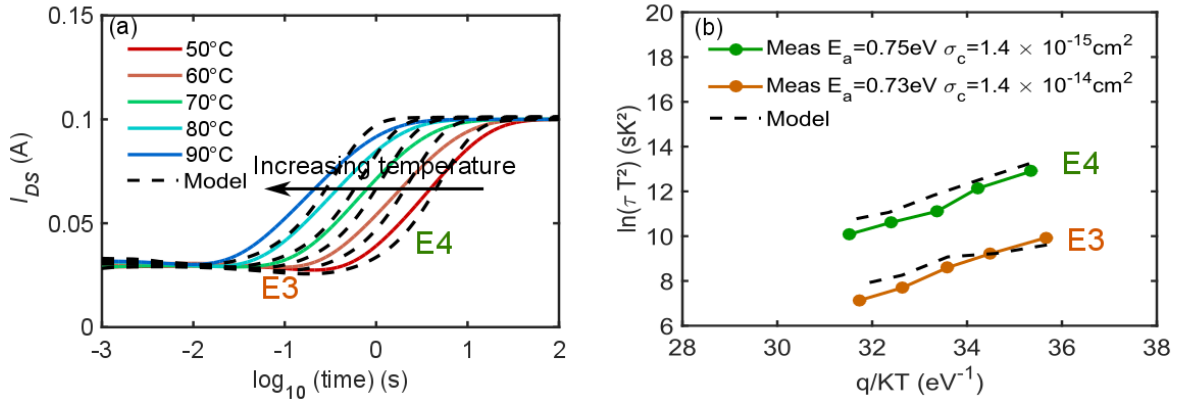
Figure 3-26(a) presents the comparison of DCT measurements and corresponding transient simulation for DC pulse excitation (shown in Figure 2-14) with the two voltage levels ( $V_{DS,F}; I_{DS,F}$ )=(40 V; 50 mA) and ( $V_{DS,M}; I_{DS,M}$ )=(5 V; 100 mA) at different temperatures.

Figure 3-27(a) compares the measurement and envelope simulation results of GaN HEMT driven by an RF pulse signal (corresponding to a 27 dBm input average power) at different temperatures. In this experiment, the GaN HEMT is also biased with a synchronized DC pulse signal with voltage levels ( $V_{DS,F}; I_{DS,F}$ )=(40 V; 50 mA) and ( $V_{DS,M}; I_{DS,M}$ )=(5 V; 100 mA). For both DCT comparison results are only shown during the de-trapping transients as shown in Figure 3-26(a) and Figure 3-27(a) and demonstrated a good agreement between measured and simulated results validating the new developed electro-thermal model with the new thermally dependent trapping model.

This new model accurately predicts the increase of average drain current due to the slow emission processes after DC transition and after cut-off of the pulsed RF excitation. Thanks to the determination of the trapping model parameter assisted with stretched multi-exponential fitting, the de-trapping phenomena shown in Figure 3-26(a) and in Figure 3-27(a) improved the model accuracy with respect to [41]. Moreover, for each trapping analysis simulation, the related Arrhenius plot is determined by substituting the simulated emission rate in the Arrhenius formula (2-11). The good agreement between the measured and simulated Arrhenius plots of the “E2”, “E3” and “E4” trap signatures are shown in Figure 3-25(b), Figure 3-26(b) and Figure 3-27(b).



**Figure 3-25: (a) Measurement (solid line) and simulation results (black dotted line) of imaginary part of  $Y_{22}$  from 100 Hz to 10 MHz frequency range at  $I_{DS} = 25$  mA/mm and  $V_{DS} = 40$  V for different temperatures. (b) Related Arrhenius plot.**



**Figure 3-26: (a) DCT Measurement (clear solid line) and simulation results (black dotted line) of de-trapping average drain current transients in  $(V_{DS,M}; I_{DS,M})=(5V;50mA/mm)$  condition after 100 s in  $(V_{DS,F}; I_{DS,F})=(40V;25mA/mm)$  for different temperatures. (b) Related Arrhenius plot.**

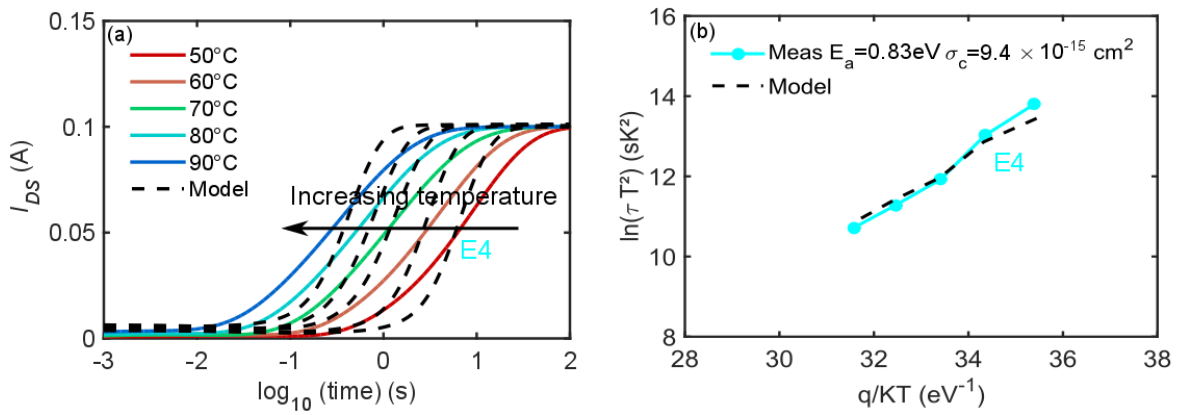


**Figure 3-27: (a) DCT Measurement (clear solid line) and simulation results (black dotted line) of de-trapping average drain current transients in  $(V_{DS,M}; I_{DS,M})=(5V;50mA/mm)$  condition after 100 s in  $(V_{DS,F}; I_{DS,F})=(40V;25mA/mm)$  for different temperatures and when the HEMT is driven by a pulse signal (27 dBm input average power). (b) Related Arrhenius plot.**

### 3.4.4 Model validation

The thermal nonlinear model is firstly validated under small-signal excitation for the bias point corresponding to the RF application operation mode  $(I_{DS}; V_{DS})=(50 \text{ mA}, 40V)$ . Indeed, some model parameters are adjusted (e.g.  $C_{GS}$ ,  $C_{GD}$ ,  $g_m$  and  $g_d$ ) during the successive nonlinear modeling phases. Finally, the comparison between measured and simulated S-parameters are shown in Figure 3-28.

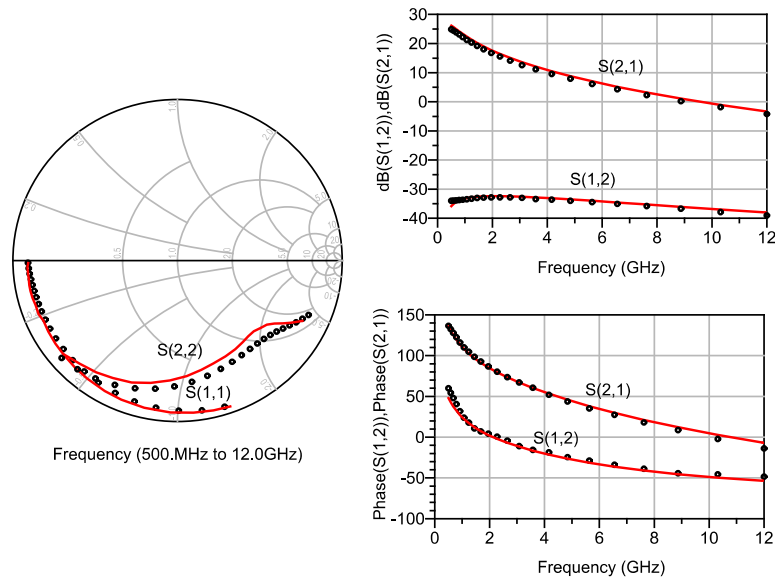


**Figure 3-28: Measurement (red solid line) and simulation results (black dotted line) of pulsed S-parameter measurement at  $(I_{DS,Q} ; V_{DS,Q}) = (I_{DS,M} ; V_{DS,M}) = (50 \text{ mA}, 40\text{V})$  from 0.5 GHz to 12 GHz frequency range.**

The more important model validation step is the one performed under large-signal operating mode. In this case, the nonlinear model is expected to be as faithful as possible to the RF measurement. Figure 3-29 shows the good agreement between the measured CW RF performances for 4 GHz in class AB operation mode ( $I_{DS} = 25 \text{ mA/mm}$  at  $V_{DS} = 40 \text{ V}$  for a fixed temperature of  $25^\circ\text{C}$  and maximum PAE impedance  $Z_{loadMAXPAE}(f_0)$  equal to  $20.5 + j44 \Omega$ ) and the electro-thermal model with thermal drain-lag circuits.

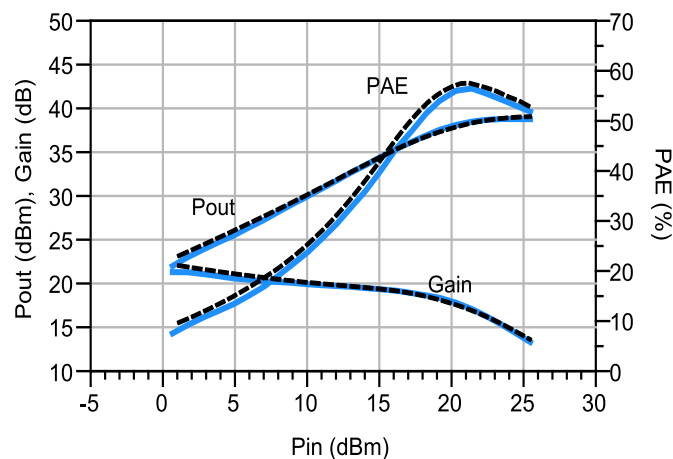


**Figure 3-29: Measurements (blue solid line) and simulation results (black dotted line) of the CW RF performances in class AB operation mode at 4 GHz, temperature  $25^\circ\text{C}$  and  $Z_{loadMAXPAE}(f_0) = 20.5 + j44 \Omega$ .**

To validate the large-signal dynamic, the drain current transient measurements during pulsed-DC and pulsed-RF excitation are compared with new model in Figure 3-30. This comparison shows that the increase of average drain current, time constant and trap amplitude after the

filling phase with respect to the input power's increasing is correctly modeled and is due to the capture and emission trap process excited by gate and drain large-signal voltage excursions during the RF excitation.

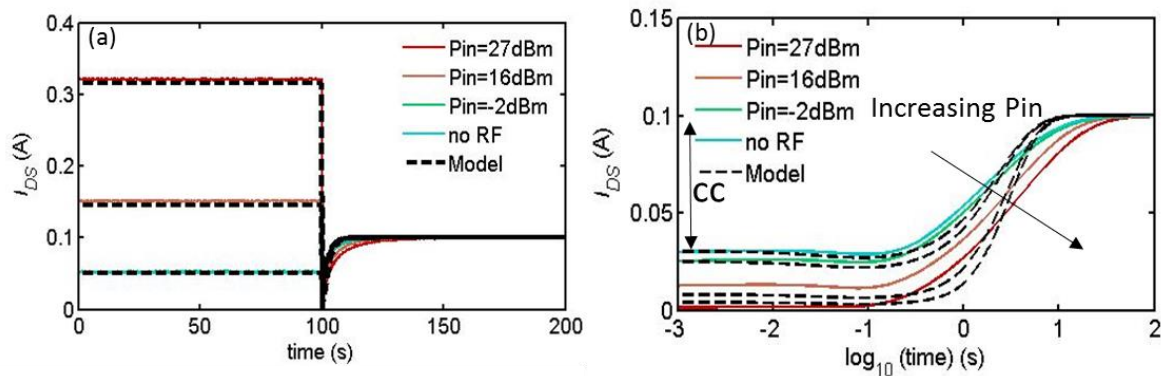


**Figure 3-30: (a) Drain current measurement (solid line) and simulation results (black dotted line) of 100s under DC filling pulse ( $V_{DS,F}$ ;  $I_{DS,F}$ )=(40V;50mA) and different input power and without input power and after another 100 s under de-trapping condition ( $V_{DS,M}$ ;  $I_{DS,M}$ )=(5V;100mA) at 60°C. (b) De-trapping transient measurements (solid line) and simulation results (black dotted line) at 60°C.**

Unfortunately, the model has an inconsistency in the trap modeling. It can be observed with the comparison of LF  $Y_{22}$  parameter measurements and the simulation results presented in Figure 3-31. This figure shows that the simulated results of the real part of  $Y_{22}$ , when “E2”, “E3” and “E4” trap models are activated, do not agree with the measurement results. But it can be noted that the  $g_d$  value determined from the measurement is closer to the  $g_d$  value determined from the simulation with “E2” only activated. This inconsistency of the trapping model during small-signal operation mode can be explained firstly by the model’s simplicity and secondly by the fact that we simulate several trapping phenomena detected with different operating modes which may be not involved during this operation mode. At the moment, the role of the trapping phenomena in LF  $Y$ -parameter dispersion is not completely clear, so complementary physical simulations are necessary to understand these trapping phenomena and consequently propose a new trap model which agrees with the LF  $Y_{22}$ -parameter measurements.

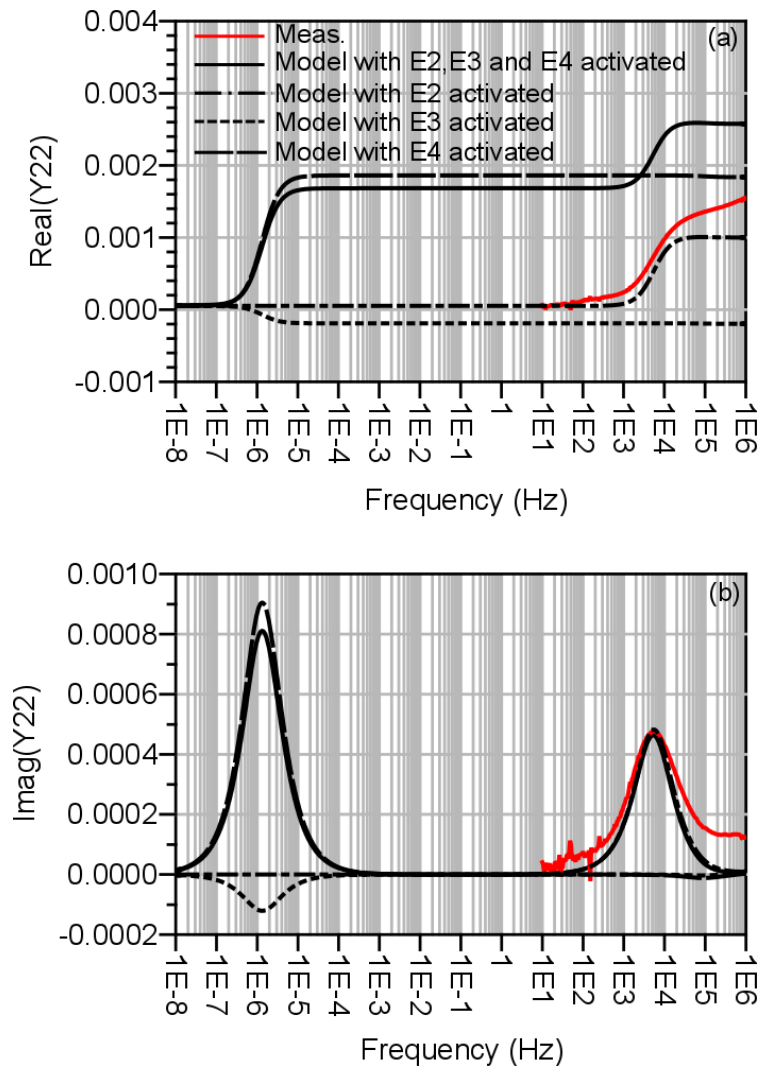


**Figure 3-31: (a) Measurement (red solid line), simulation results (black solid line) with all traps activated and modeling (black dotted line) with different traps activated of (a) real and (b) imaginary parts of  $Y_{22}$  at  $I_{DS}=25$  mA/mm and  $V_{DS}=40$  V at  $80^\circ\text{C}$ .**

### 3.5 Conclusion

This chapter presents a method and an operating process to extract the nonlinear electro-thermal AlGaIn/GaN model for CAD application with a new additive thermal-trap model to take into account the dynamic behavior of the trap states and their associated temperature variation. The extraction of a nonlinear electro-thermal model of AlGaIn/GaN HEMT and its performance evaluation are based on pulsed I/V measurements, multi-bias pulsed S-parameter measurements and pulsed large-signal measurements. In particular, a new method for the extraction method of the intrinsic parameters is used. It is based on LF S-parameter measurements. One challenge of this work is to propose a new thermal-trap model which takes into account the dynamic behavior and to reach a good agreement for low-frequency small-signal CW S-parameter results on the one hand and for large-signal pulsed-RF results

on the other hand at different temperatures. This thermal-trap model allows accurately predicting the physical temperature activation of the traps and also the thermal signature of the traps. It is also demonstrated that the extrapolation of trap model parameters by stretched multi-exponential function of drain current transient measurements during pulsed-RF excitations allows greatly improving the low-frequency simulations of the drain current. The presented thermal-trap model correctly models the pinch-off voltage shift due to trapping phenomena and temperature. Unfortunately, the trap model has an inconsistency in the simulation of real part of  $Y_{22}$ . A possible perspective for the continuation of this research would certainly be the resolution of the trap model's inconsistency, but also the introduction of a pulse-width dependence into the trap amplitude and time constant parameters of the thermal-trap model for radar and telecommunication applications.

# 4 Time-domain large-signal reliability investigation of AlGaIn/GaN HEMT

## 4.1 Introduction

As is well established, AlGaIn/GaN HEMTs are a promising candidate for RF power applications in space equipment due to their excellent performance. However, this technology requires extensive study of its reliability and its conditions of use. Reliability is a prerequisite for space equipment, because it must work for at least 15 years (satellite operating lifetimes can range from five to ten years for Earth observation missions and up to eighteen years for telecommunication satellites [2]). Moreover, the power amplifier is a circuit function that must work under constraining operating conditions (high currents, high temperatures, high-frequency operation, high gate-source and drain-source voltage excursions, and high power). Therefore, reliability aspects are of paramount importance. So, the wear out failure mechanisms must be understood and modeled to achieve some advances for design tools. One of the failure mechanisms recently identified in GaN HEMTs is the generation of deep levels due to a trapping effect which is extensively discussed in Chapter 2.

The aim of this chapter is to report an advanced time-domain methodology to investigate the device reliability and determine its safe operating area (SOA). This methodology was applied (by the Thales Alenia Space company) in order to carry out a further assessment of GH 50-10 AlGaIn/GaN for the SiC HFET technology already qualified [96]. The presented technique is based on the continued monitoring of the RF waveforms and DC parameters in order to assess the degradation of the transistor characteristics in RF power amplifiers. Moreover, a complete characterization protocol is associated to the time-domain methodology in order to obtain a nonlinear electro-thermal model that takes into account the RF performance variations during the RF stress and its degradation. This reliability model can be used by designers to predict the RF degradation during real RF overdrive operation conditions in the design phase.

The first part of the chapter provides an overview of reliability test methodology and failure mechanisms.

The second part presents first the set-up to determine the time-domain large-signal RF waveforms and secondly the complete characterization protocol for the reliability investigation.

The last part of this chapter shows the reliability results carried out in class AB operation mode under RF power step-stress and 240 hours RF life stress with time-domain waveform monitoring at high drain bias voltages and overdrive conditions (12 dB compression) for two different output load impedances corresponding to the optimum of PAE and to a mismatched impedance.

## 4.2 Reliability Testing

Before presenting an accelerated reliability testing of AlGaIn/GaN HEMTs, the following section summarizes some basic concepts to understand reliability analysis.

### 4.2.1 Analysis of reliability

The reliability of a population of devices ( $R$ ) is defined as the number of devices  $N(t)$  surviving until the time ( $t$ ) divided by the total number of devices  $N$  (i.e.  $R = N(t)/N$ ). The cumulative failure distribution function  $F(t)$  is the probability that an item operating at time  $t=0$  under the stated condition, fails at or before time  $t$ . Therefore, it is defined as  $F(t) = 1 - R(t)$ . Its derivative represents the failure probability distribution function  $f(t) = \partial F(t)/\partial t$  and the probability of device failure between  $t$  and  $t + \partial t$  is equal to  $f(t)\partial t$ . The mean time to failure (MTTF) is the average time to first failure under the specified experimental condition. It is calculated by integrating between 0 and  $\infty$  the device lifetime (i. e.  $t \cdot f(t)\partial t$ ) as shown in the following equation:

$$MTTF = \int_0^{\infty} t \cdot f(t) \partial t \quad (4-1)$$

For electronic devices generally two specific probability distribution function are considered the “lognormal” and the “Weibull” [97] in order to analyze reliability results and to characterize the failure mechanism. The measurement of reliability for semiconductors generally involves failure rates. The evolution of the failure rates for a population of semiconductor components (or any other sort of population) as a function of time is described by the “bathtub” curve [98] in Figure 4-1. In particular, the Weibull distribution is used to mimic the “bathtub” curve.



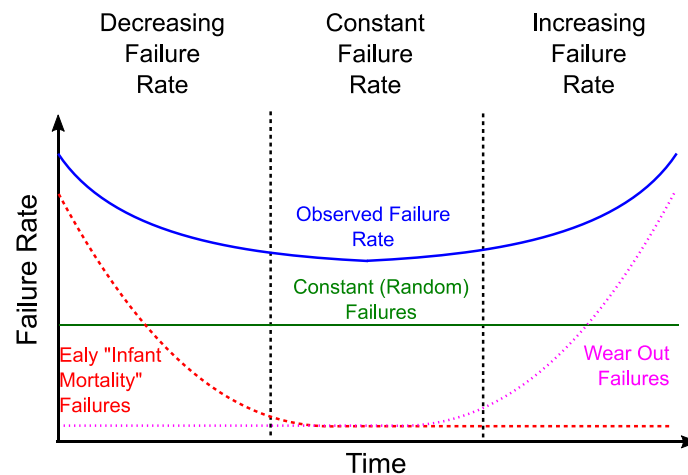


**Figure 4-1: Bathtub curve describing the time dependence of failure rate for an electronic device.**

The initial region that begins at time zero when a device begins to be used is characterized by a high but rapidly decreasing failure rate. This region is known as the early failure period or “infant mortality” period. “Infant mortality” failures are due to defects of the component occurring before the expected end of life. Defect-related problems are principally induced by manufacturing flaws (such as a missing process step, contamination, undetected excursions, wide variation, fabrication processes...). In order to weed out those defects, the manufacturers will often perform a “burn in” on all components. In the next region, the failure rate remains roughly constant and low. This period of a low failure rate is usually identified as the “random” failure period, and it characterizes the useful life of components where the lowest failure rate occurs. Finally, the failure rate begins to increase as materials wear out and degradation occurs at an ever increasing rate. This is known as the “wear out” failure period. End of life wear out refers to the natural process where components will begin to develop faults and problems. Gradual degradation in the parameters of a device is typically mimicked with accelerated life-test conditions.

#### 4.2.2 Accelerated life test

Satellite communication systems (such as HPAs) are expected to have a long life and it is quite impractical to measure their reliability under ordinary conditions. Accelerated tests are used to obtain reliability predictions in a much shorter time than that required to produce a significant number of failures under normal operating conditions. So in general, the median time to failures are extrapolated by means of an accelerated factor [99] to induce a specific electrical constraint, such as

- Temperature acceleration,

- Current acceleration (one of the principal wear out failure mechanisms is electro-migration),
- Voltage acceleration (involves the transistor but also the overall components around it, such as MIM capacitors sensitive to breakdown voltage, the voltage acceleration subsequently induces an electric field acceleration),
- RF bias acceleration (one of major failure mechanisms is hot carrier injection).

In order to determine the MTTF, the corresponding acceleration law depends on the involved failure mechanism (e.g. accelerated by temperature), the Arrhenius law is adopted and the MTTF is given by

$$MTTF = \gamma_0 \exp\left(\frac{E_a}{kT}\right) \quad (4-2)$$

where  $\gamma_0$  is constant,  $E_a$  is the activation energy (eV),  $k$  is Boltzmann's constant and  $T$  is absolute temperature (K). Both  $\gamma_0$  and  $E_a$  depend on the specific failure mechanism involved. The definition of "failure" is one of the most subjective and arbitrary aspects in measuring reliability, yet it is necessary to evaluate the median time to failure. The failure can be defined as, e.g., a reduction in the drain current by 10%, a increase in the leakage current by 10%, a reduction in gain by 1 dB, a reduction in output power by 1 dBm, a reduction in gain compression by 1 dBc.

An example of accelerated testing of GaN-based heterojunction field effect transistors submitted to a three high temperatures operating life test is shown in Figure 4-2. Cumulative failure rates are recorded and the MTTF for each of the three temperatures is established. The Arrhenius plots of the MTTF determined at three different temperatures is shown in Figure 4-2, which leads to an activation energy of about 2 eV and an extrapolated MTTF value greater than  $10^7$  hours at 150 °C.

In the following, we summarize the main accelerated life tests:

- **HTS** (high temperature storage test): The device is unbiased and stored at different temperatures. This test allows studying the thermal activation of the failure mechanism.
- **HTO** (high temperature operating-life test): The device is biased under normal conditions and stored at different temperatures. This allows studying the combined effects of thermal and electrical stresses.

- **HTRB** (high temperature reverse bias): The device is biased under reverse condition close to breakdown voltage at high temperature. This allows to study the effects of high electric fields and temperatures.

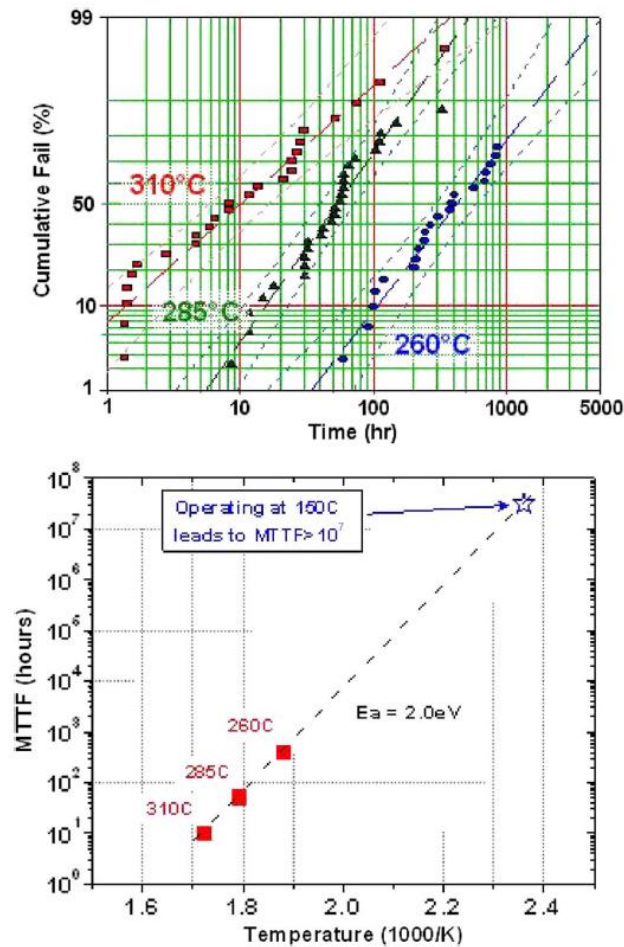


**Figure 4-2: (Top) Three-temperature (3T) lifetime test data showing the cumulative failure rates versus time obtained at three different temperatures, namely, 180 °C, 285 °C, and 310 °C. The  $\sigma$  values for 180 °C and 285 °C are approximately 1 but that at 310 °C is 1.5, which might imply contribution by infant failure. (Bottom) Arrhenius plot of the MTTF determined at three different temperatures, namely, 180 °C, 285 °C, and 310 °C, which lead to an activation energy of about 2 eV and an extrapolated MTTF value greater than 10<sup>7</sup> hours at 150 °C [100].**

In particular, the HTO test can be performed under either DC or RF operating conditions. Normally, DC testing is used for a preliminary investigation of the reliability, which is, in general, easier to set up and less expensive. In the other way, the RF life test can drive the device in real working conditions.

In order to induce an accelerated degradation, these tests are performed with step-stress techniques (e.g., reverse gate step-stress,  $V_{DS}$  step-stress,  $P_{IN}$  step-stress and  $V_{DS}$  step-stress with fixed  $P_{IN}$ ).

### 4.2.3 Physical failure mechanisms

As a relatively new semiconductor technology, a lot of research groups have devoted much effort to the identification and understanding of the failure mechanisms of AlGaN/GaN HEMTs. In the following, we discuss some of the key failure mechanisms presented in the literature which have been identified through DC and/or RF characterization techniques. A recent publication, *Meneghesso et al.* [26] has highlighted failure mechanisms identified on GaN based HEMTs. They are reported on a cross-section in Figure 4-3. These mechanisms have never been clearly identified in the other semiconductors.

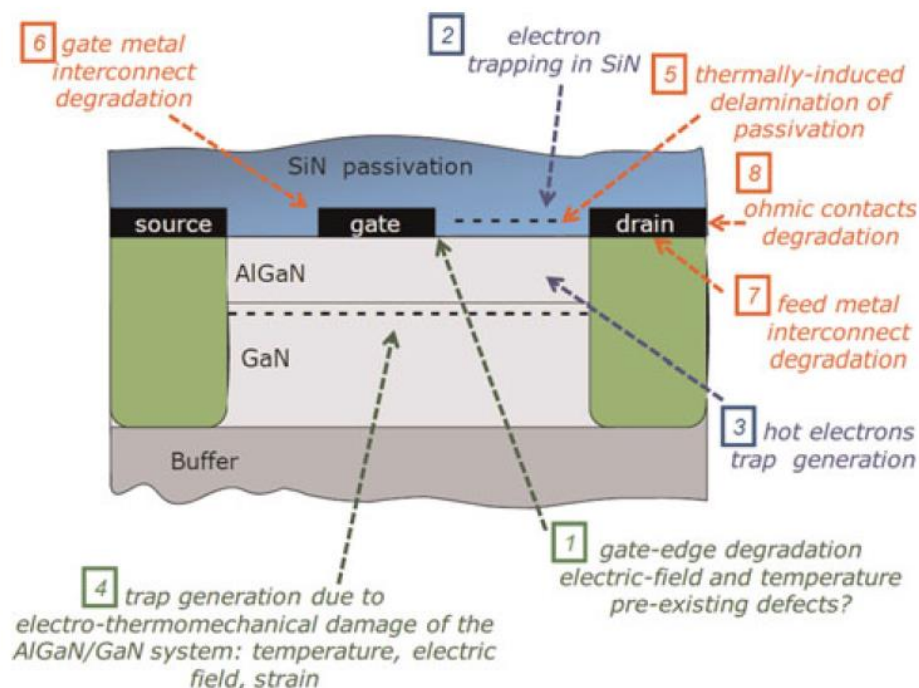


**Figure 4-3: Failure mechanisms recently identified on GaN HEMTs. Mechanisms identified in red (5, 6, 7, 8) are thermally activated mechanisms. Mechanisms 2 and 3 are related to the presence of hot electrons under high bias conditions. Mechanisms 1 and 4 (green) are peculiar to GaN devices due to the polar and piezoelectric nature of this semiconductor [26].**

These failure mechanisms can be divided into three main categories:

- Failure mechanisms which can be associated with the properties of GaN based material. (mechanisms 1 and 4 in Figure 4-3)
- Hot-electron induced degradation mechanisms (mechanisms 2 and 3 in Figure 4-3).
- Thermally-activated mechanisms (mechanisms from 5 to 8 in Figure 4-3).

### 4.2.3.1 Gate edge degradation

Under RF operating conditions, the large RF gate and drain voltage swings can involve high electric fields particularly concentrated at the edge of the gate contact, which may produce a degradation of the reliability. This high electric field condition can also be studied under DC excitation (when high reverse bias voltages are applied to the gate, with the drain and gate voltages set to zero). Consequently, a degradation of the electrical characteristics can appear:

- an increasing of gate leakage and CC;
- an increase of drain-source resistance;
- a decrease of saturation drain current.

This degradation involves the presence or the generation of defects at the edge of the gate by higher electric fields which can produce an injection of electrons from the gate to the AlGaIn barrier layer through a tunneling mechanism. A reverse-bias step-stress is carried out in OFF-state with  $V_D=V_S=0$  V, in order to verify the presence of this failure mechanism that appears when a strong gate leakage increase is obtained for a certain reverse voltage. Another powerful tool for reliability investigation that is normally used for the detection of hot-electron phenomena is electroluminescence (EL) microscopy. EL microscopy is used to detect the locations of a reverse current injection point and damaged areas. An example of false-color EL micrographs is shown in Figure 4-4. In the transfer length method (TLM), the device is submitted to a reverse bias step-stress with source and drain to ground. Figure 4-4 shows that after the step at -40 V, the EL spot and  $I_G$  increase by 100x after starting being observed. An increase in  $V_G$  shows an increase of the point density of the defects and an increase in the damage around each point. Moreover, the spots detected by EL were always located at the edge of the gate towards the drain and source, where the electric field is maximal.

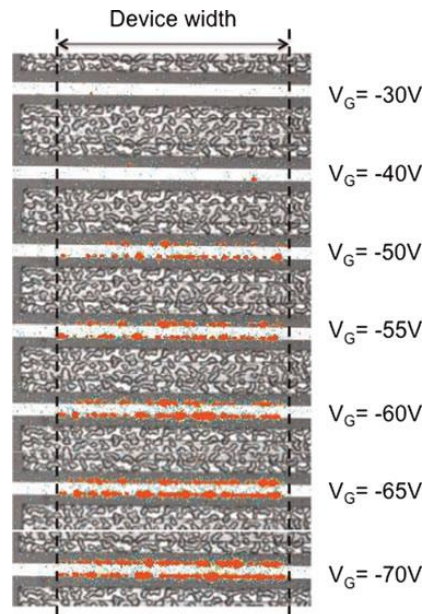


**Figure 4-4: EL microscopy images of a representative gated TLM HEMT sample. Images were taken at  $V_G = 10$  V (with  $V_S = V_D = 0$  V) after each step-stress. Dashed lines identify the device's active area [26].**

#### 4.2.3.2 Thermally activated failure mechanism

Figure 4-5 shows a DC life test carried out at  $V_{DS}=40$  V and  $I_{DS}=200$  mA for different base-plate temperatures. To investigate the degradation, the bias was stopped at regular intervals in order to carry out DC and pulsed I/V measurements of the device. The devices show in Figure 4-5 and Figure 4-6 an increase of gate leakage and a decrease of drain current. Moreover, Figure 4-7 shows an enhancement of the trapping effects.

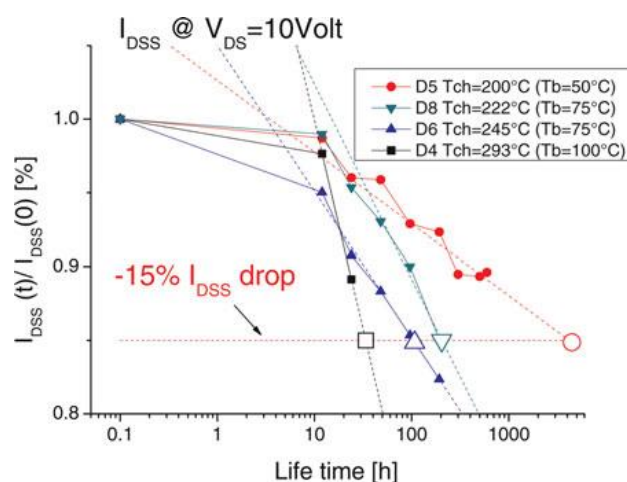


**Figure 4-5: Relative decrease in drain current for the four junction temperature of the DC test stress test at  $V_{DS} = 40$  V,  $I_D = 200$  mA. Devices periphery is 1.2 mm, gate length  $L_G = 0.5$   $\mu\text{m}$ , and the source-to-drain distance  $L_{SD}=3.7$   $\mu\text{m}$  [26].**

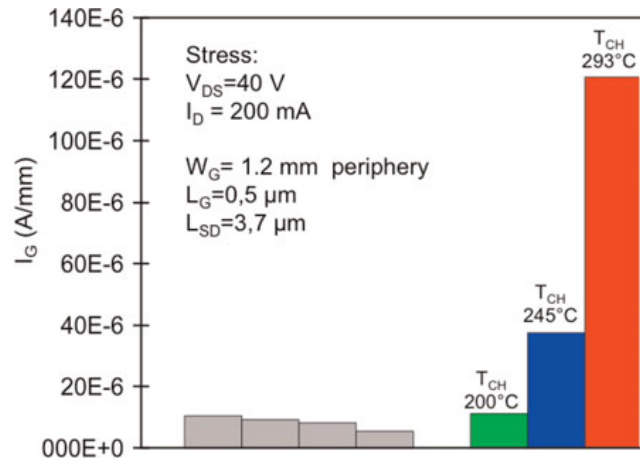


**Figure 4-6: Comparison of the gate leakage current in off-state in untreated (gray) and aged devices at  $V_{DS} = 40$  V,  $I_D = 200$  mA at different temperatures. Devices periphery is 1.2 mm, gate length  $L_G = 0.5$   $\mu\text{m}$ , and the source-to-drain distance  $L_{SD} = 3.7$   $\mu\text{m}$ .**

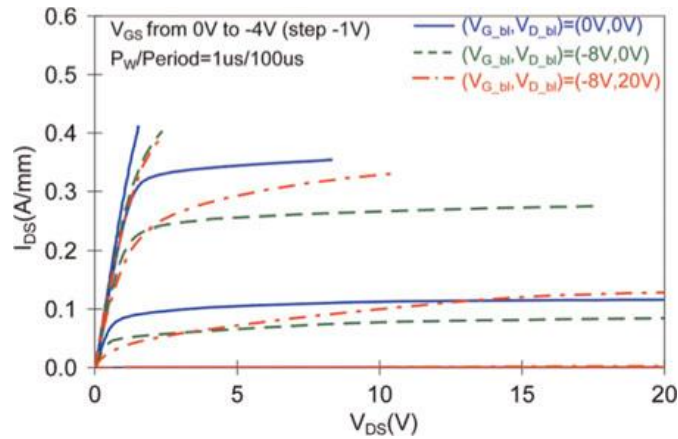


**Figure 4-7: Pulsed DC characteristics measured in a representative device after 200 h of DC testing at 245 °C, with  $V_{DS} = 40$  V,  $I_D = 200$  mA. Devices periphery is 1.2  $\mu\text{m}$ , gate length  $L_G = 0.5$   $\mu\text{m}$ , and the source-to-drain distance  $L_{SD} = 3.7$   $\mu\text{m}$  [26].**

#### 4.2.3.3 Hot electron degradation

Hot electron degradation is another failure mechanism that is involved when the device is driven in on-state at high  $V_{DS}$ . Thus, the 2DEG channel of electrons is accelerated by a high electric field and reaches a high energy. The electron become “hot” when the electron can overcome the energy barrier and when its energy decreases due to collision with the crystal and with the formation of defects or dangling bonds (i.e. the trapping effect in the surface or in the GaN buffer). In order to assess the reliability with respect to hot electron degradation, the EL microscopy is used.

In order to characterize hot electron effects, the EL measurements were carried out in [101] at different  $V_{GS}$  and  $V_{DS}$  levels as shown in Figure 4-8. At fixed  $V_{DS}$  EL intensity has a non-monotonic “bell-shaped” behavior. In OFF-state,  $V_{GS}$  is smaller than the pinch-off value.



Thus, the gate-drain voltage and the electric field are maximal. But, there are no carriers into the channel so that no light is emitted. When  $V_{GS}$  increases, the carriers begin to flow and they are accelerated by the electric field so that light is emitted. The emitted light is associated to the population of electrons in the channel. The light intensity increases with an increase in  $V_{GS}$  until a certain value of  $V_{GS}$  is reached. This value implies that the electrons have less energy so that the light intensity decreases. It is obvious that light is emitted with increasing  $V_{DS}$  because the electric field increases thus the electrons are more energetic. The light intensity increases and defect density due to hot electrons increases.

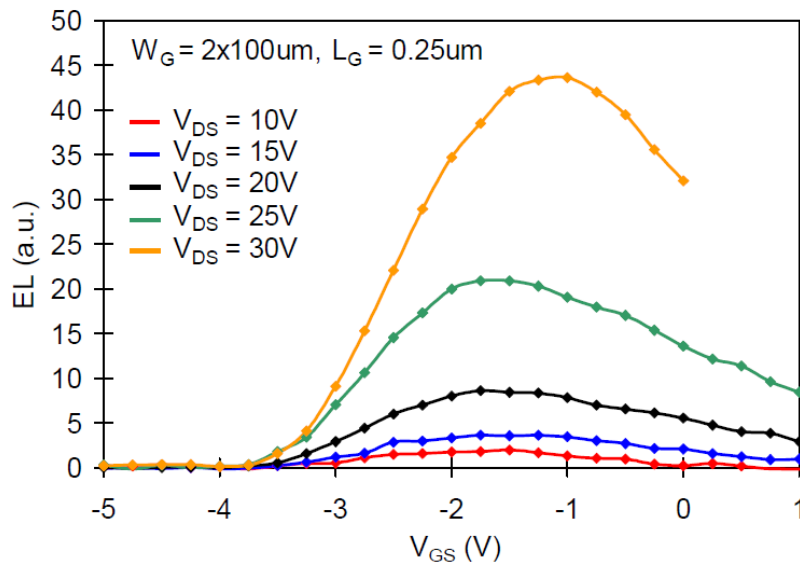


**Figure 4-8: EL intensity vs  $V_{GS}$  curves measured for different  $V_{DS}$  levels on one of the analyzed samples (before any stress) [101].**

### 4.3 Time-domain continuous RF waveform monitoring under stress overdrive condition

As is well explicated, among the various reliability tests, RF stress is an established technique to evaluate the lifetime of a transistor in RF power amplifiers, because the device works under realistic operating conditions. Conventional RF stress systems [102] are capable of measuring the DC parameters, and the input and output RF powers. An improved time-domain RF stress methodology with improved capabilities is proposed in this thesis. The system is extended to continually measure the calibrated time-domain RF waveforms at both ports of the nonlinear DUT, thanks to the use of an LSNA system. This methodology is expected to provide more information about the cause of the degradation mechanism. This approach is similar to [103]. In [103], the capability of the RF I/V waveform stress test procedure is shown. In this thesis, this approach is also applied to the GH50 technology, with an increase of stress time (240



hours) under very high compression operation mode in order to emulate a more realistic overdrive operating condition.

### 4.3.1 Time-domain continuous RF waveform stress set-up

The experimental set-up used for time-domain continuous RF waveform stress is based on the use of an LSNA measurement system configured in a load-pull test bench, as shown in Figure 4-9.

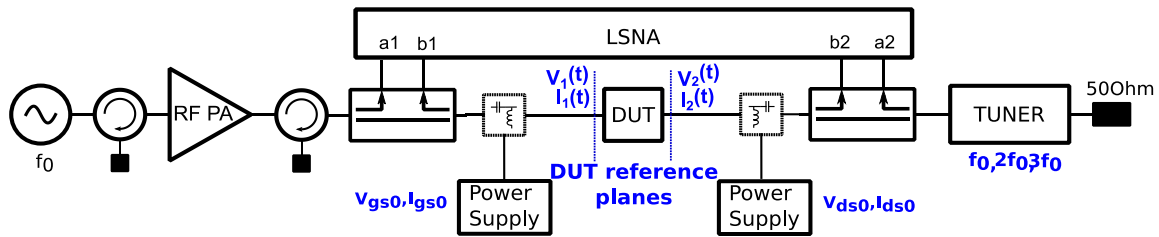


**Figure 4-9. Block diagram of the time-domain continuous RF waveforms stress set-up based on LSNA system.**

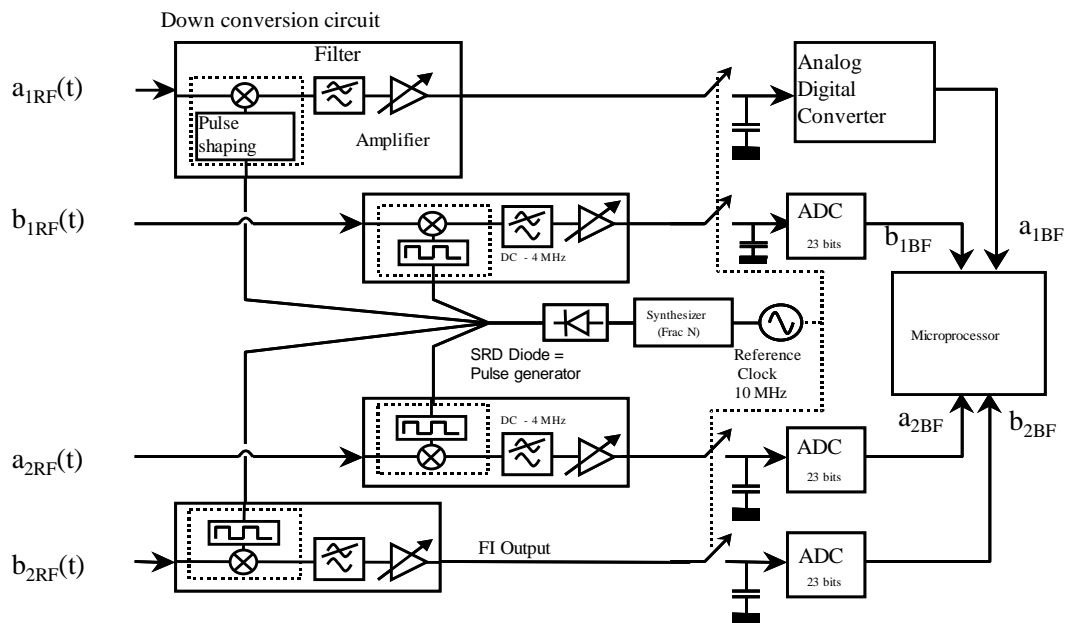


**Figure 4-10: LSNA internal block diagram.**

The simplified internal principle of LSNA is shown in Figure 4-10. LSNA measures four periodic RF waves: the incident and reflected waves at input and output of the DUT from 600 MHz up to 50 GHz with a dedicated test bench. The incident and reflected RF waves at both ports of the DUT are measured through two bidirectional couplers. These signals are then undersampled simultaneously by the four samplers of the front end of the LSNA. This undersampling principle allows the conversion and translation of the RF signal to IF bandwidth (10 MHz). The resulting IF signals are digitized by four synchronized ADCs.

Finally, a computer processes all the data to get the absolute phases and absolute amplitudes of the fundamental and harmonic frequencies [104]. The principle of frequency conversion-translation is shown in Figure 4-11. In this example, the fundamental frequency is equal to  $F_{RF}=1$  GHz, the frequency of the Fractional-N synthesizer is equal to  $F_{LO}=19.6$  MHz. Consequently, the IF frequency is calculated as  $F_{IF} = F_{RF} - N \times F_{LO}$  with  $N$  the number of periods required to obtain the final digitalized signal. In the given example, the IF frequency corresponding to the  $F_{RF}$  frequency is  $F_{IF}=400$  KHz. The same calibration is performed for other harmonics [104]. In order to obtain the calibrated RF voltage and current waveforms at the DUT planes, the LSNA needs a specific calibration protocol based on relative and absolute calibration. The error model used in the LSNA system is described in [106]. The error model in Equation (4-3) is only available for connectorized devices. The extension of the measurement system from connectorized devices to on-wafer devices implies an additional calibration between the *a1* and *b1* ports of the LSNA and the test set port1 RF input, because there are no power sensors or reference generators available on-wafer which can be used to determine  $K(f)$  [107], [108].

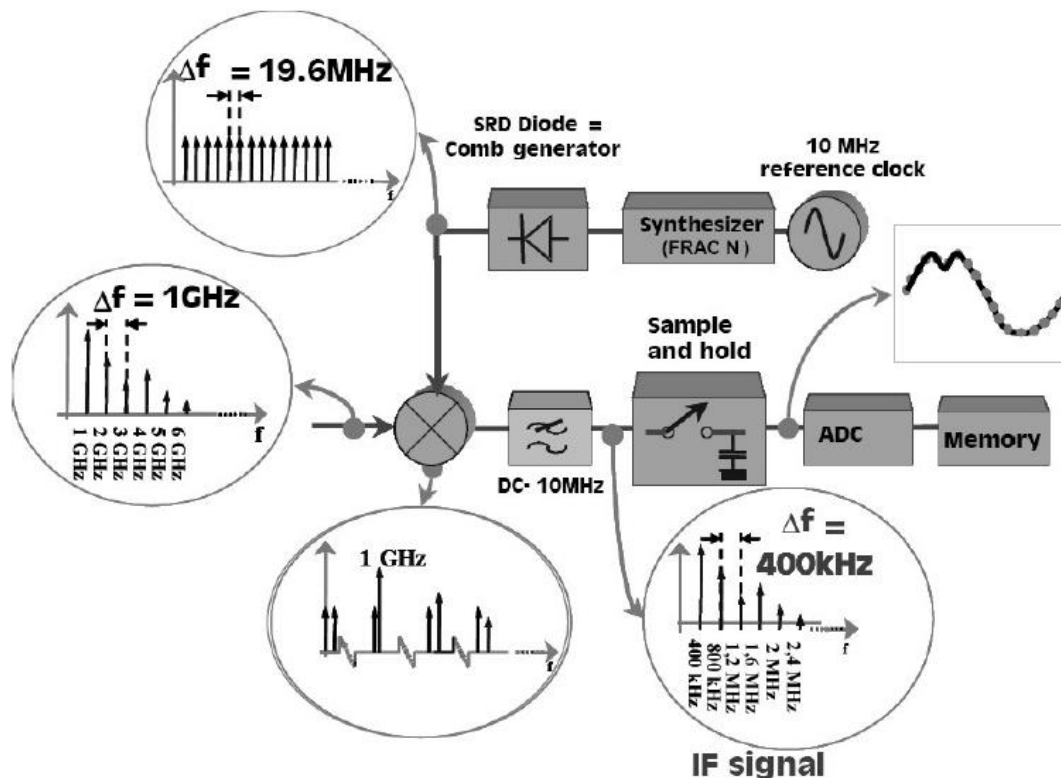


Figure 4-11: LSNA Frequency down-converter principle [105].

$$\begin{bmatrix} a_{1DUT}(f) \\ a_{2DUT}(f) \\ a_{3DUT}(f) \\ a_{4DUT}(f) \end{bmatrix} = |K(f)| \cdot e^{j\varphi(K(f))} \begin{bmatrix} 1 & \beta_1(f) & 0 & 0 \\ \gamma_1(f) & \delta_1(f) & 0 & 0 \\ 0 & 0 & \alpha_2(f) & \beta_2(f) \\ 0 & 0 & \gamma_2(f) & \delta_2(f) \end{bmatrix} \cdot \begin{bmatrix} a_{1m}(f) \\ a_{2m}(f) \\ a_{3m}(f) \\ a_{4m}(f) \end{bmatrix} \quad (4-3)$$

The absolute calibration elements, the power meter sensor and the harmonic phase reference (HPR) are therefore connected to the port1 RF input (as shown in Figure 4-13) and the measurement results are transformed to the port1 probe tip according to Equation (4-4).

$$\begin{bmatrix} a_{1port1}(f) \\ a_{2port1}(f) \end{bmatrix} = L(f) \cdot \begin{bmatrix} 1 & \lambda(f) \\ \mu(f) & \nu(f) \end{bmatrix} \cdot \left( K(f) \cdot \begin{bmatrix} 1 & \beta_1(f) \\ \gamma_1(f) & \delta_1(f) \end{bmatrix} \right)^{-1} \cdot \begin{bmatrix} a_{1DUT}(f) \\ a_{2DUT}(f) \end{bmatrix} \quad (4-4)$$

The error coefficients  $\beta_1(f)$ ,  $\gamma_1(f)$ ,  $\delta_1(f)$ ,  $\alpha_2(f)$ ,  $\beta_2(f)$ ,  $\gamma_2(f)$  and  $\delta_2(f)$  are calculated from the on-wafer relative (SOLT) calibration. The error coefficient  $\mu(f)$ ,  $\lambda(f)$  and  $\nu(f)$  are known after execution of the SOL calibration at the port1 RF input.  $L(f)$  is known after connecting the harmonic phase and a power meter at port1 RF input.

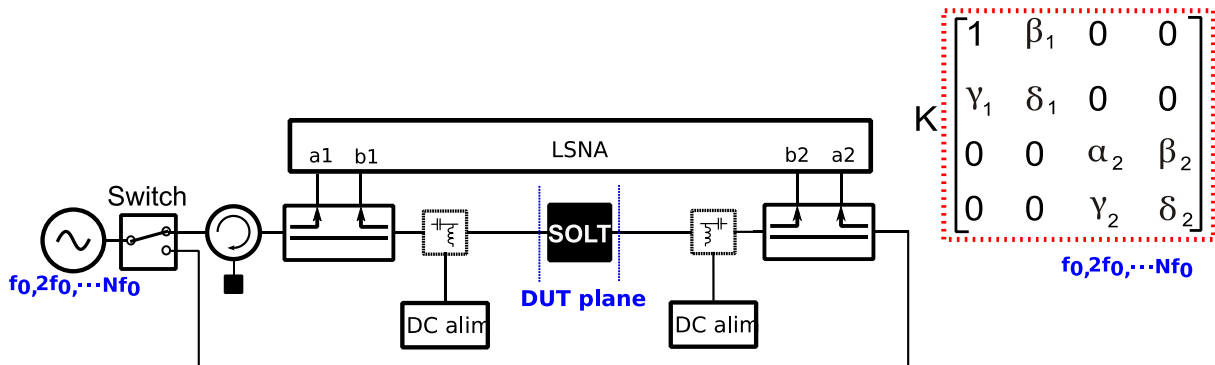


Figure 4-12: Configuration for on-wafer relative calibration.

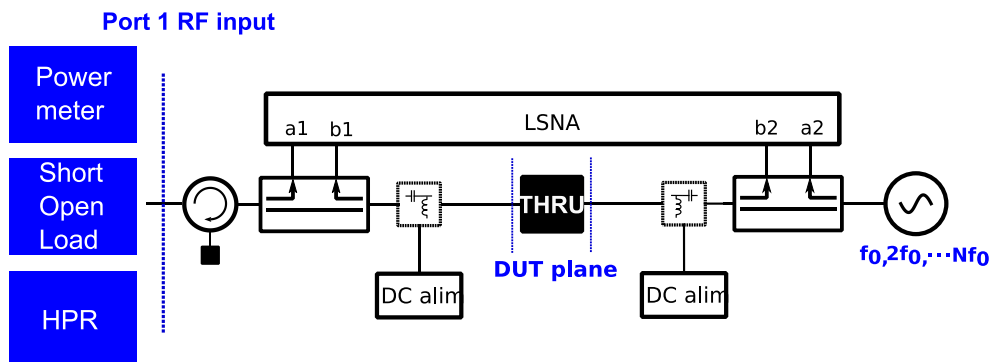


Figure 4-13: Configuration for on-wafer absolute magnitude and phase calibration.

### 4.3.2 Reliability test procedure

The measurements of the continuous RF waveforms during the RF stress under overdrive condition consists on recording (every 10 minutes) the calibrated time-domain voltage and current waveforms of the DUT driven by a CW large signal and loaded with a fixed impedance at fundamental and harmonic frequencies. The DUT used for all stress tests is an  $8 \times 250 \mu\text{m}$  GH 50 AlGaIn/GaN HEMT. The reliability test procedure includes a monitored RF stress considering a 24 h or a 240 h step stress under overdrive condition at different given compression levels. A specific characterization protocol is carried out before and after each RF step-stress. The reliability test procedure is an adaptation of the one used in [102].

#### 4.3.2.1 Characterization protocols

Two characterization protocols have been performed: the first, called the “short characterization protocol” is associated to a 24 h RF step-stress under overdrive operating condition. The second one, called the “full characterization protocol” is associated to 240 h step-stress under overdrive operating condition at a given compression value.

The short characterization protocol is carried out before and after each RF 24 h step-stress at different compression gain values. This protocol, in addition to a DC I/V characterization for classic device degradation assessments, is extended with pulsed I/V measurements to quantify trapping effects, with pulsed S-parameter measurements, and with power sweep measurements. This short characterization protocol is also used to determine a nonlinear electro-thermal model [69] taking into account the RF performance variation during the RF stress and its degradation. Thus, the short characterization protocol is composed of the following measurements:

- **DC I/V measurements** are carried out with a Keithley 4200 semiconductor characterization system (SCS) [109] equipped with two 4210 high power source measurement units (SMUs) for the gate and drain probes. In addition, the 4225-RPM (remote amplifier/switch module) are connected to the 4210 SMU that is at the gate, allowing a highly accurate characterization of the gate current. The DC I/V measurement allows the following characterizations:
  - Diode gate-source characterization with a  $V_{GS}$  sweep from -8 V to 1 V with a 0.05 V voltage step.
  - $I_D$ - $V_D$  characterization with a  $V_{DS}$  sweep from 0 to 10 V and  $V_{GS}$  sweep from -4 V to 0 V with a 0.5 V voltage step.

- $I_D$ - $V_G$  characterization with a  $V_{GS}$  sweep from -8 V to 1 V and with  $V_{DS}$  at 1 V, 2 V, 5 V and 10 V.
- **Pulsed I/V measurements** are carried out with the BILT AMCAD system described in Section 2.3.1.1 in order to quantify the impact of RF stress on trapping effects. The specific trapping pulsed I/V protocol developed in Section 2.3.1.2 is employed for this objective. The pulsed I/V measurements are performed at the following different quiescent bias points:
  - Cold network at bias point  $(V_{GQ}, V_{DQ})=(0 \text{ V}, 0 \text{ V})$ ;
  - Gate-lag network at bias point  $(V_{GQ}, V_{DQ})=(-5 \text{ V}, 0 \text{ V})$ ;
  - Drain-lag network at bias point  $(V_{GQ}, V_{DQ})=(-5 \text{ V}, 50 \text{ V})$ ;
  - Hot network at bias point  $(V_{GQ}, V_{DQ})=(-1.9 \text{ V}, 50 \text{ V})$  (under class AB bias condition with  $I_{DQ}=50 \text{ mA}$  and  $V_{DQ}=50 \text{ V}$ ).
- **Pulsed S-parameter measurements** are carried out with the same BILT AMCAD system and a Rohde & Schwarz ZVA40 VNA [110] equipped with ZVAX modules as described in Section 3.4.1.1. The pulsed S-parameters are determined for different biasing points corresponding to an ideal load-line (from 0.5 GHz to 20 GHz with frequency step of 0.5 GHz) obtained under the large-signal operating mode (quiescent point :  $V_{DQ}=50 \text{ V}$  and  $I_{DQ}=50 \text{ mA}$ ).
- **Time-domain power sweep measurements** are carried out with the properly calibrated LSNA system in the same conditions defined in the step-stress protocol.

The full characterization protocol includes all the measurements of the short characterization protocol with the addition of a thermal resistance characterization based on thermal pulsed I/V measurements and a trap characterization based on LF  $Y_{22}$  measurements. The advanced and full characterization protocol is performed before and after each 240 h RF step-stress under overdrive operating conditions at the same compression gain value. Thus, the full characterization protocol is composed of the following measurements:

- **DC I/V measurements** identical to the DC I/V measurements performed in the short characterization protocol.
- **Pulsed I/V measurements** identical to the pulsed I/V measurements performed in the short characterization protocol.
- **Pulsed S-parameter measurements** identical to the pulsed S-parameter measurements performed in the short characterization protocol.

- **Time-domain power sweep measurements** identical to the time-domain power sweep measurements performed in the short characterization protocol.
- **Additive  $R_{TH}$  measurements** are carried out with the BILT AMCAD system at different temperatures and different quiescent bias points, as described in Section 2.3.1.3.
- **Additive LF  $Y_{22}$  measurements** are carried out with an LF-HF vector network analyzer (Agilent E5061b) in 1-port configuration at different temperatures, as described in Section 2.3.4.

#### 4.3.2.2 24-hour RF step-stress in overdrive condition

An RF step-stress test is carried out in order to have a preliminary and quick evaluation of the degradation of the component's performance when driven by a large RF CW signal at different compression gain values (in the high overdrive region). The large RF signal excitations drive the transistor to ensure that it works with forward and reverse gate current and that it operates at high drain voltage peak values. This operating condition corresponds to a compressed mode allowing an accelerated RF life test under a high electric field. The 24 h RF step-stress condition is summarized below:

- The device is biased in class AB operation mode (50 mA of drain current at 50 V of drain voltage) at a 4 GHz fundamental frequency.
- The 24 h RF step-stress is carried out at 4 dB, 8 dB and 12 dB compression gain.
- Each RF operating test is carried out on two devices coming from the same wafer with similar characteristics.
- Two load impedances are used during this 24 h RF operating test in order to emulate different operating conditions corresponding to:
  - PAE optimum load ( $Z_{LOAD}(f_0) = 20.8 + j44 \Omega$ );
  - mismatched impedance for the transistor equals to  $50 \Omega$  ( $Z_{LOAD}(f_0) = 50 \Omega$ ).

The complete reliability test procedure with 24 h RF step-stress and the short characterization protocol is depicted in Figure 4-14.

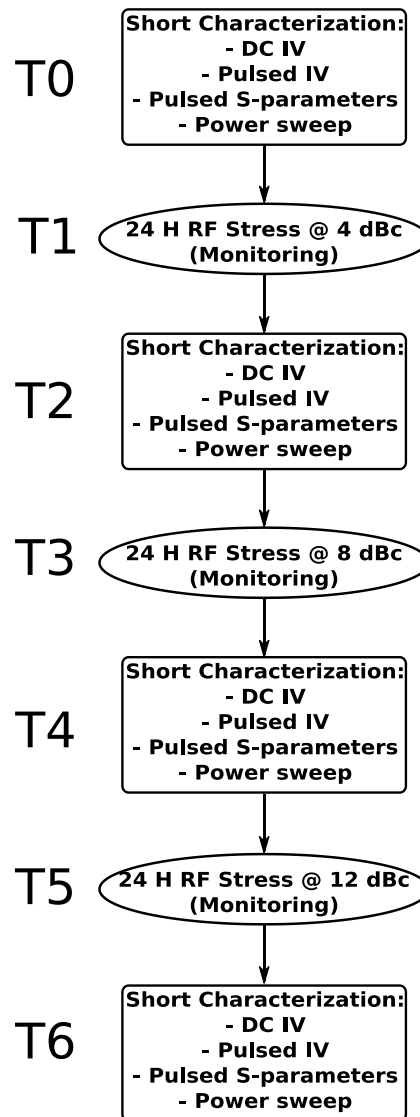


**Figure 4-14: Reliability test procedure with 24 h RF step-stress and short characterization protocol.**

#### 4.3.2.3 240-hour RF step-stress in overdrive condition

A 240-hours RF step-stress test in the overdrive region is a more realistic operation life stress condition for space equipment under a very high overdrive condition. The 12 dB compression step-stress corresponds to the last and the highest compression gain level applied during the 24 h step-stress protocol. The 240 h RF overdrive conditions (corresponding to the same stress conditions as the ones used in the previously described 24 h step-stress) are summarized below:

- The devices are biased in class AB operation mode (50 mA of drain current at 50 V of drain voltage) at a 4 GHz fundamental frequency.
- 240 hours of RF overdrive stress are carried out at 12 dB compression.

- Each RF operating test is carried out on two devices coming from the same wafer with similar characteristics.
- Two load impedances are used during this 240 h RF operating test in order to emulate different operating conditions correspond to:
  - PAE optimum load ( $Z_{LOAD}(f_0) = 20.8 + j44 \Omega$ );
  - mismatched impedance for the transistor equals to  $50 \Omega$  ( $Z_{LOAD}(f_0) = 50 \Omega$ ).

In order to detect an irreversible wear out mechanism, the full characterization protocol T3 described in Figure 4-15 (after the 240 h RF overdrive stress) is performed after seven days of the end of RF stress.

In order to measure the calibrated waveforms during the 240 hours, a calibration protocol is executed every 80 h. This value corresponds to the period for which the calibration coefficients remain valid in the XLIM laboratory environment. The completed reliability test procedure with 240 h RF overdrive stress and the full characterization protocol is depicted in Figure 4-15.

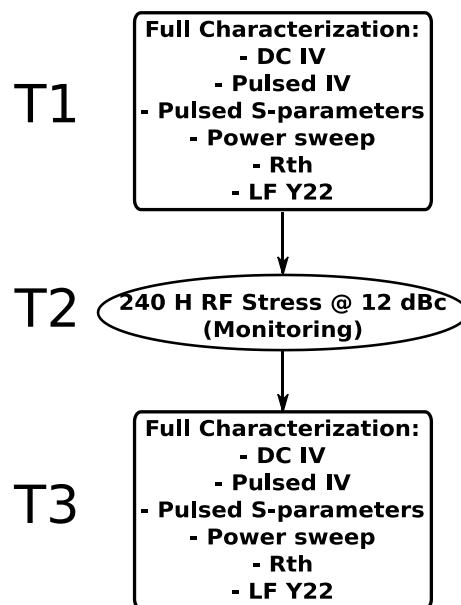


**Figure 4-15: Reliability test procedure with 240-hour RF overdrive stress and full characterization protocol.**

### 4.3.3 Time-domain stress test results

In this section, the time-domain results are presented firstly for the preliminary 24h RF step-stress test and secondly for the 240 h RF overdrive stress test. The results are shown for the two different load conditions (PAE optimum impedance and mismatched impedance). To



ensure a reliable characterization protocol all the measurements are carried out first on the reference sample and secondly on the stressed simple.

#### 4.3.3.1 24-hour RF step-stress test results

The time-domain RF performance measured during three consecutive applications of 24 hours of RF stress under PAE optimum load impedance and 50  $\Omega$  load impedance at 4 dB, 8 dB and 12 dB compression gains are shown in Figure 4-16 and Figure 4-17 for the two tested devices. The monitored parameters during the stress are: the output power, the DC drain and gate currents, and the modulus and phase of the I<sub>2</sub>, V<sub>2</sub>, I<sub>1</sub> and V<sub>1</sub> RF waveforms (as depicted in Figure 4-9). They have not shown any important degradation (e.g., output power varying during the stress but with a final minor variation for all stress of 0.2 dBm under PAE optimum load impedance in Figure 4-16(a) and of 0.3 dBm under 50  $\Omega$  load impedance in Figure 4-17(a)). In order to evaluate the degradation, the following figures of merit are determined by the short characterization protocol:

- DC figures of merit include saturation drain current (at  $V_{DS}$  equal to 10 V), peak of transconductance (at  $V_{DS}$  equal to 4 V), and threshold voltage.
- Trapping figures of merit include S.R. calculated in gate-lag, drain-lag and AB class condition.
- RF figures of merit include small-signal parameters at 4 GHz, output power, PAE and drain current in saturation condition (at 3 dBc).

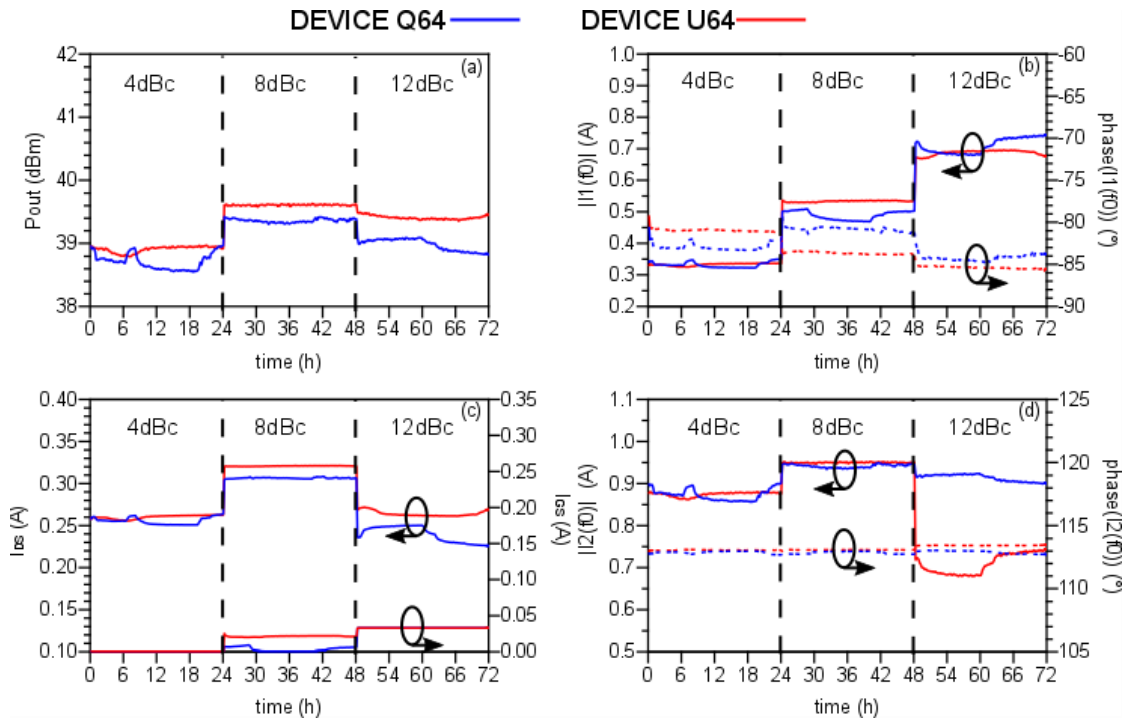


**Figure 4-16: (a) Output power, (b) modulus and phase of I1 at  $f_0$  extracted from I1 RF waveforms curves, (c) drain current and (d) modulus and phase of I2 at  $f_0$  extracted from I2 RF waveforms curves monitored during RF Pin step-stress with PAE optimum load impedance.**

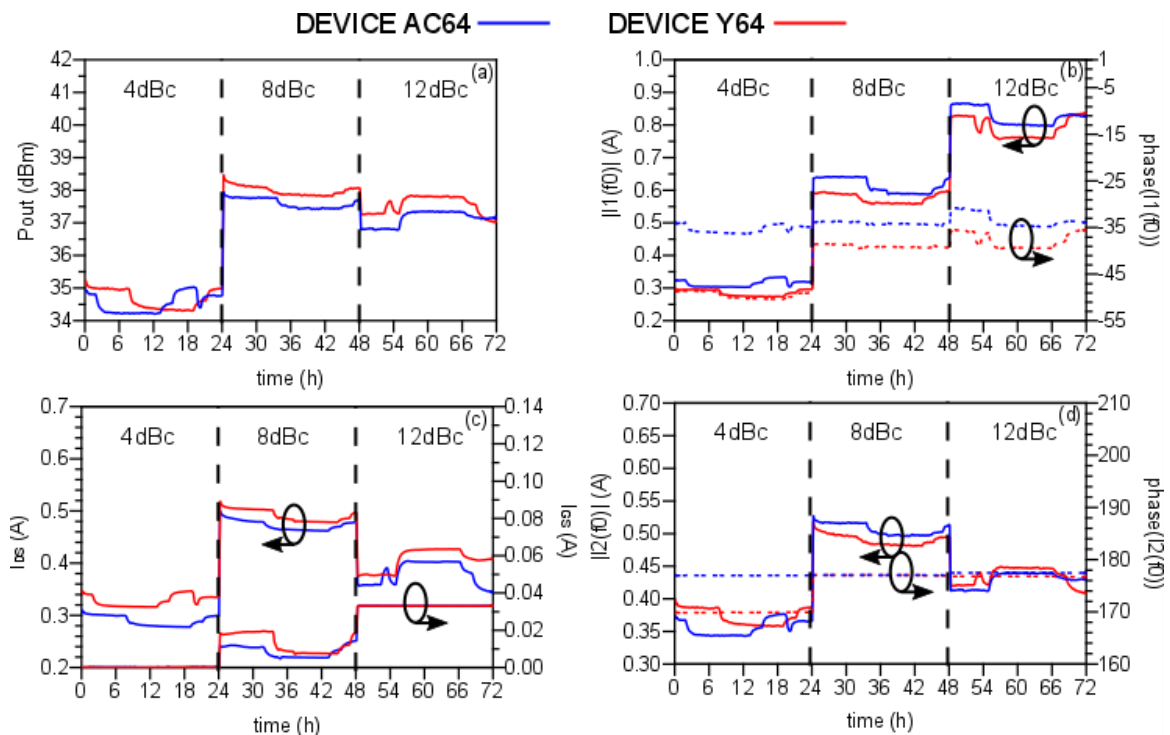


**Figure 4-17: (a) Output power, (b) modulus and phase of I1 at  $f_0$  extracted from I1 RF waveforms curves, (c) drain current and (d) modulus and phase of I2 at  $f_0$  extracted from (I2 RF waveforms curves) monitored during RF Pin step-stress with 50  $\Omega$  load impedance.**

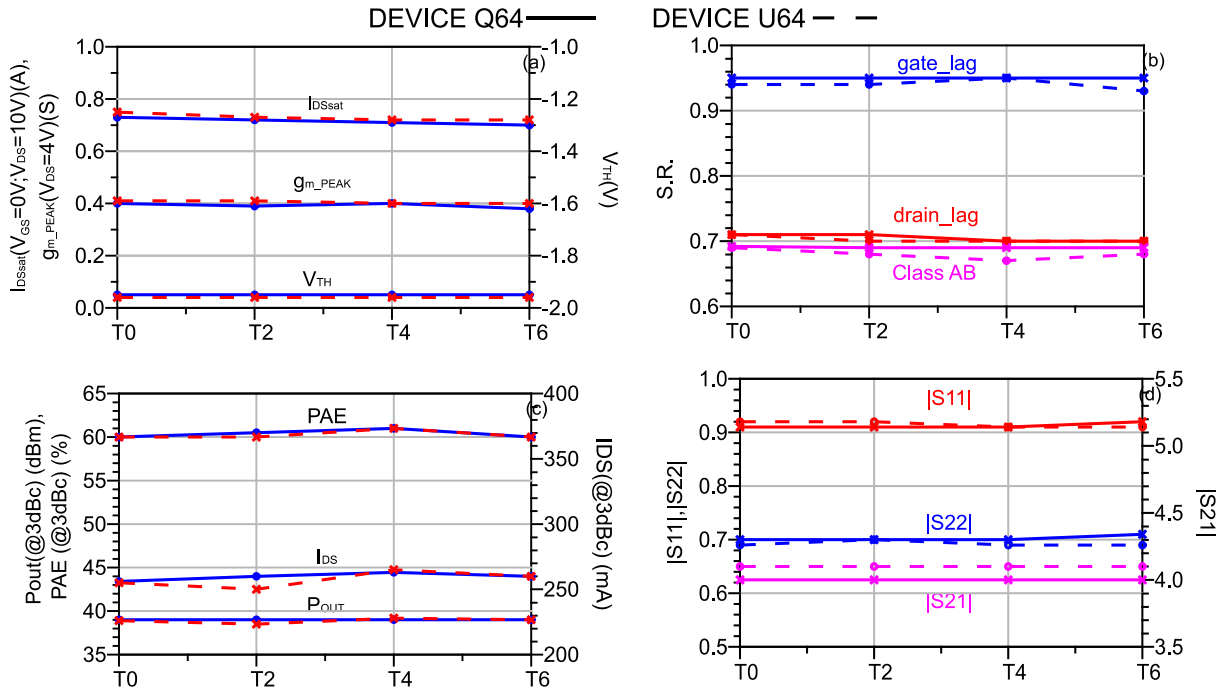


**Figure 4-18:** Comparison of figures of merit extracted from short characterization protocol before (T0) and after (T2, T4 and T6) each 24 h RF step-stress under the PAE optimum load impedance condition: (a) DC IV figures of merit, (b) trapping figures of merit (pulsed I/V measurements), (c) nonlinear power figures of merit and (d) small-signal figure of merit at 4 GHz for device Q64 (solid line) and device U64 (dashed line).

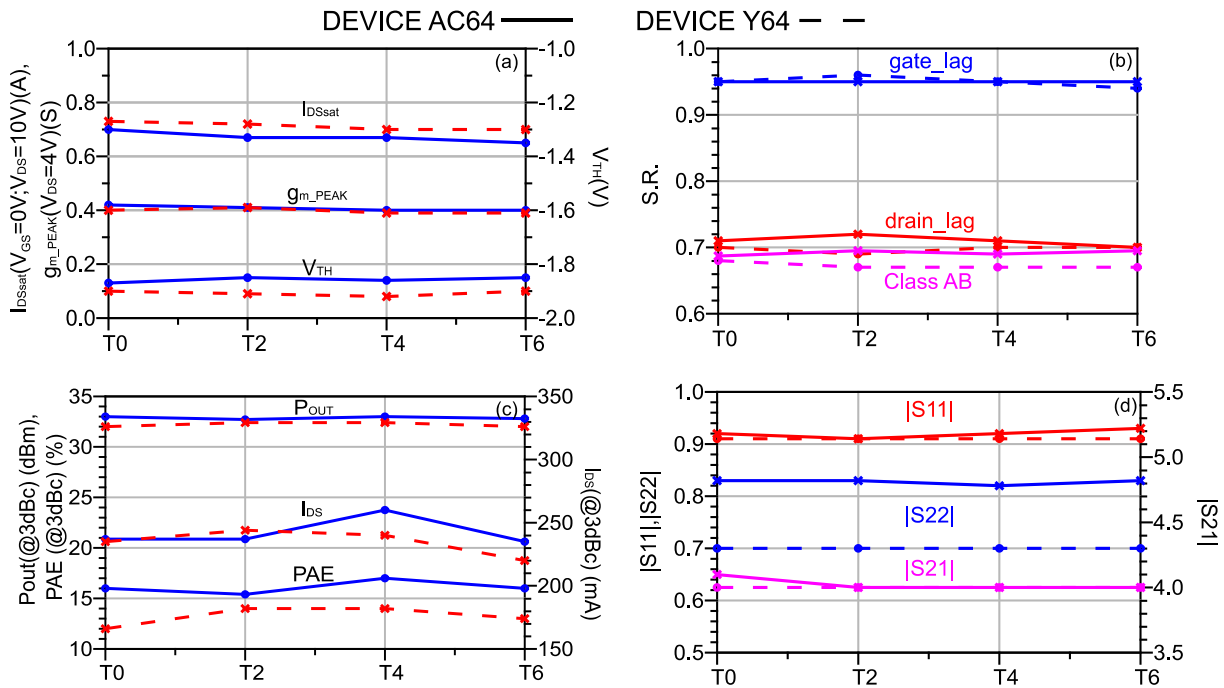


**Figure 4-19:** Comparison of figures of merit extracted from short characterization protocol before (T0) and after (T2, T4 and T6) each 24 h RF step-stress under the 50  $\Omega$  load impedance condition: (a) DC IV figures of merit, (b) trapping figures of merit (pulsed I/V measurements), (c) nonlinear power figures of merit and (d) small-signal figure of merit at 4 GHz for device AC64 (solid line) and device Y64 (dashed line).

In Figure 4-18 and Figure 4-19 are shown respectively the comparison of these figures of merit before and after the 24 h RF step-stress (T1, T3 and T5) under PAE optimum impedance and mismatched impedance (50  $\Omega$ ). The step-stress results are very different for the two devices and it is difficult to conclude whether or not they have the same degradation behavior. But, the comparison of the short characterization protocol before and after each 24 h step-stress in Figure 4-18 and Figure 4-19 for both load output impedances does not show any reduction of RF and DC performance and trapping effects. In conclusion, the short 24h stress period is not long enough to degrade the devices. Therefore, a longer stress period is applied.

#### 4.3.3.2 240-hour RF overdrive stress test results

The 240 h RF overdrive stress tests are applied to ensure that the device operates in a more realistic condition in order to determine an SOA during high overdrive condition at 12 dB compression. It corresponds to a constant 29 dBm input power applied to the devices under PAE optimum load impedance condition. But under the 50  $\Omega$  impedance load condition, it corresponds to a constant 31 dBm input power applied to the devices. The monitoring of the RF performance during the stress test is the same as that used for the 24 h step-stress, and is shown in Figure 4-20 and Figure 4-21, respectively for the PAE optimum load impedance condition and for 50  $\Omega$  load impedance condition. The variation of the RF and DC parameters during 240 hours of RF overdrive stress are summarized in Table 12 and Table 13 respectively for the PAE optimum load impedance condition and for the 50  $\Omega$  load impedance condition.

TABLE 12  
VARIATION OF RF AND DC PARAMETERS DURING 240 HOURS OF RF OVERDRIVE STRESS AT PAE OPTIMUM LOAD IMPEDANCE CONDITION

DEVICE	$\Delta P_{out}$ (dB)	$\Delta I_{DS}$ (mA)	$\Delta  I_2(f_0) $ (A)
M52	0.5	28	0.07
M64	0.4	19	0.03

TABLE 13  
VARIATION OF RF AND DC PARAMETERS DURING 240 HOURS OF RF OVERDRIVE STRESS AT 50  $\Omega$  LOAD IMPEDANCE CONDITION

DEVICE	$\Delta P_{out}$ (dB)	$\Delta I_{DS}$ (mA)	$\Delta  I_2(f_0) $ (A)
Q40	0.6	43	0.045
Q76	0.8	60	0.05
Q28	//	//	//

The time-domain stress results under the PAE optimum load impedance condition are shown in Figure 4-20. A decreasing trend for both devices (i.e., output power variation of 0.4 dB for device M64 and of 0.5 dB for device M52) is observed. In Figure 4-20, there can be observed a slight increase of drain current, output power and magnitude and phase of I2 during the first hour and a decrease of the same parameters after the first calibration at 80 hours of device M52. This variation is not observed with device M64. It can be concluded that the RF performance is not really affected by the stress. The time-domain stress results under 50  $\Omega$  load impedance condition are presented in Figure 4-21. A decreasing trend is seen for both devices: i.e., output power variation of 0.6 dB for the device Q40 and of 0.8 dB for the device Q76, which is twice as important a decrease of drain current than was observed under the PAE optimum load impedance condition. A catastrophic failure occurs for device Q28, as is clearly seen in Figure 4-22. After 200 hours of RF stress under the 50  $\Omega$  load impedance condition, device Q28 presents an increase of static gate current and an increase of static gate voltage that in dynamic behavior corresponds to increasing excursions of the input load cycles, as shown in Figure 4-22(a). This increase in the input load cycle excursion probably involves a degradation in the gate-source region which modifies the input impedance and that corresponds also to an increase of the input power of the device (the available power of the RF power generator is constant during the stress). Moreover, this increase in the input load cycle excursion corresponds to an increase of compression gain (until 18 dB compression before the catastrophic failure) and thus a decrease of output power and of output load cycles. Therefore, the static negative gate voltage increases until -6.5 V (Figure 4-22(f)) which in dynamic behavior corresponds to an increase of the V1 excursion until -30 V (Figure 4-22(a)) before catastrophic failure. The degradation and catastrophic failure of device Q28 is assumed to be due to the high compression operating condition during the overdrive condition and the higher device operating junction temperature (estimated to be 210 °C in Figure 4-23). The device operating junction temperature is estimated by using the following equation:

$$T_J = (P_{IN} - P_{OUT} + P_{DC}) \cdot R_{TH} + T_{AMB} \quad (4-5)$$

This equation is applied to the monitoring of the DC and RF parameters during the 240 hours of RF overdrive stress and  $R_{TH}$  is calculated as described in Section 2.3.1.3. The variations of estimated device operating junction temperatures during the 240 hours of RF overdrive stress under the PAE optimum load impedance condition and for the 50  $\Omega$  load condition are shown in Figure 4-23. It is possible to conclude that the wear out of device Q28 is probably due to

destruction by breakdown of the gate-source diode by the high reverse breakdown voltage (-6.5 V in static voltage and -30 V in dynamic voltage) applied in the gate to source terminals. The results of the full characterization protocol carried out before and after the 240 hours of RF overdrive stress under the PAE optimum load impedance condition are shown in Figure 4-24-Figure 4-28 and those under the 50  $\Omega$  load impedance condition are shown in Figure 4-29-Figure 4-33.

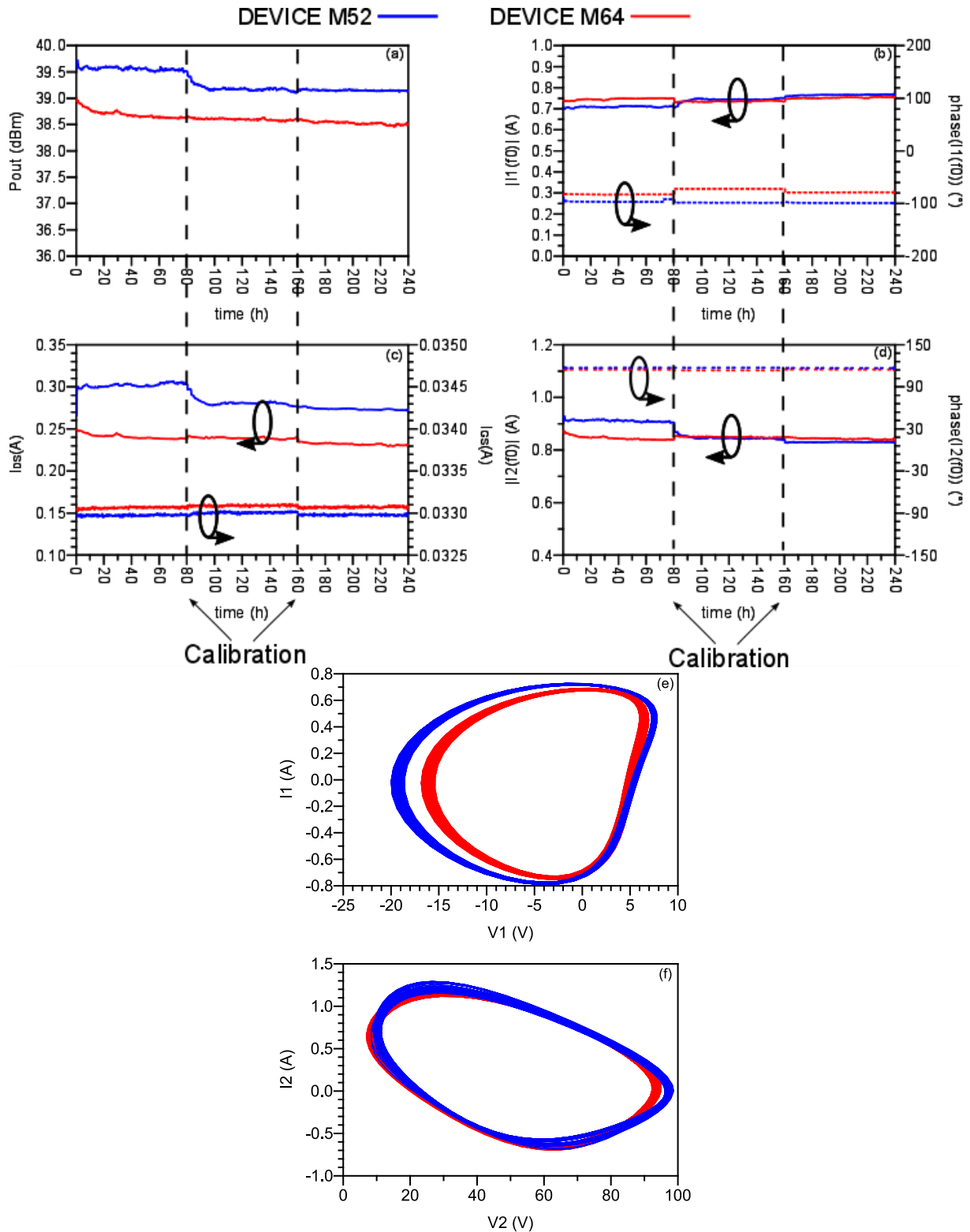
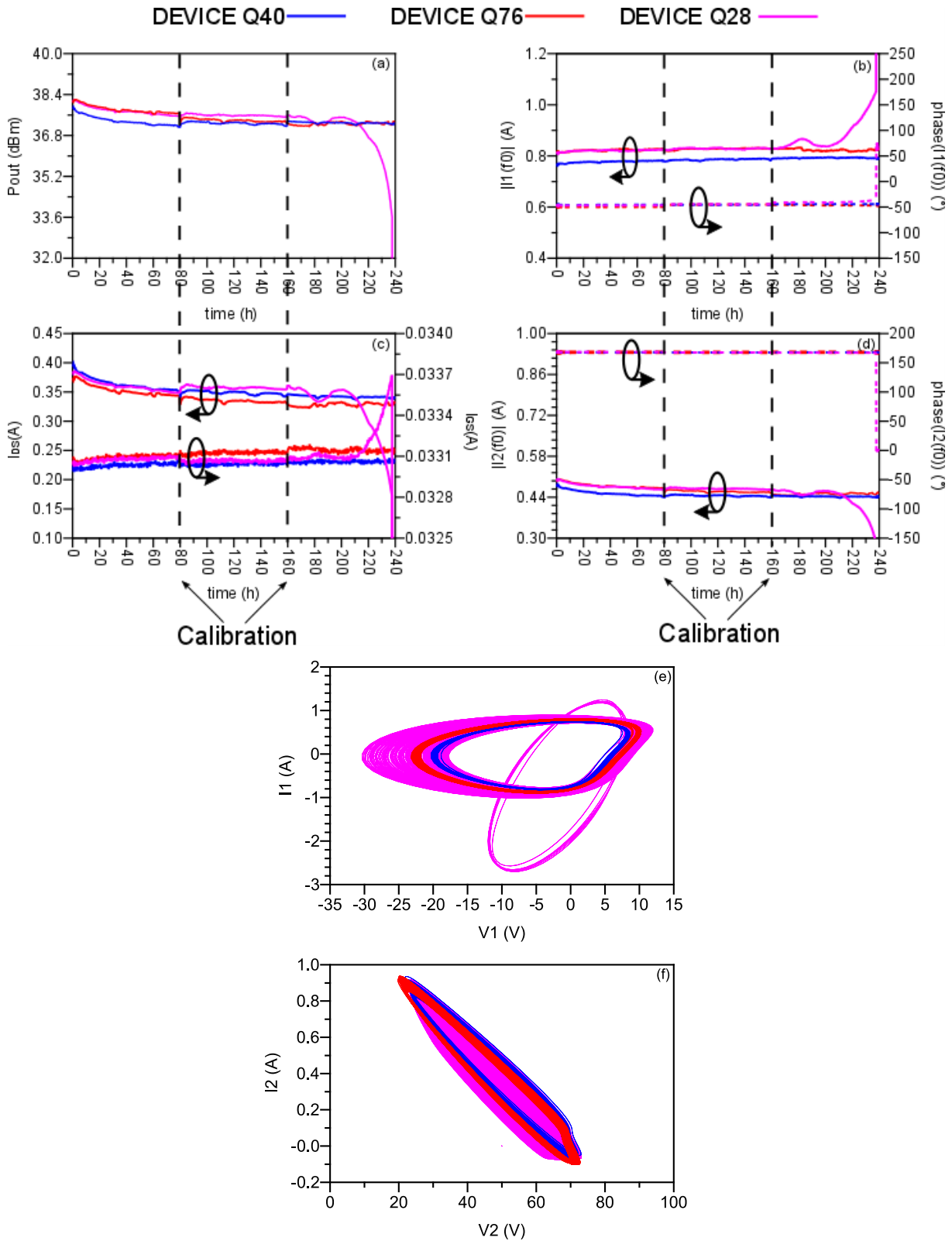
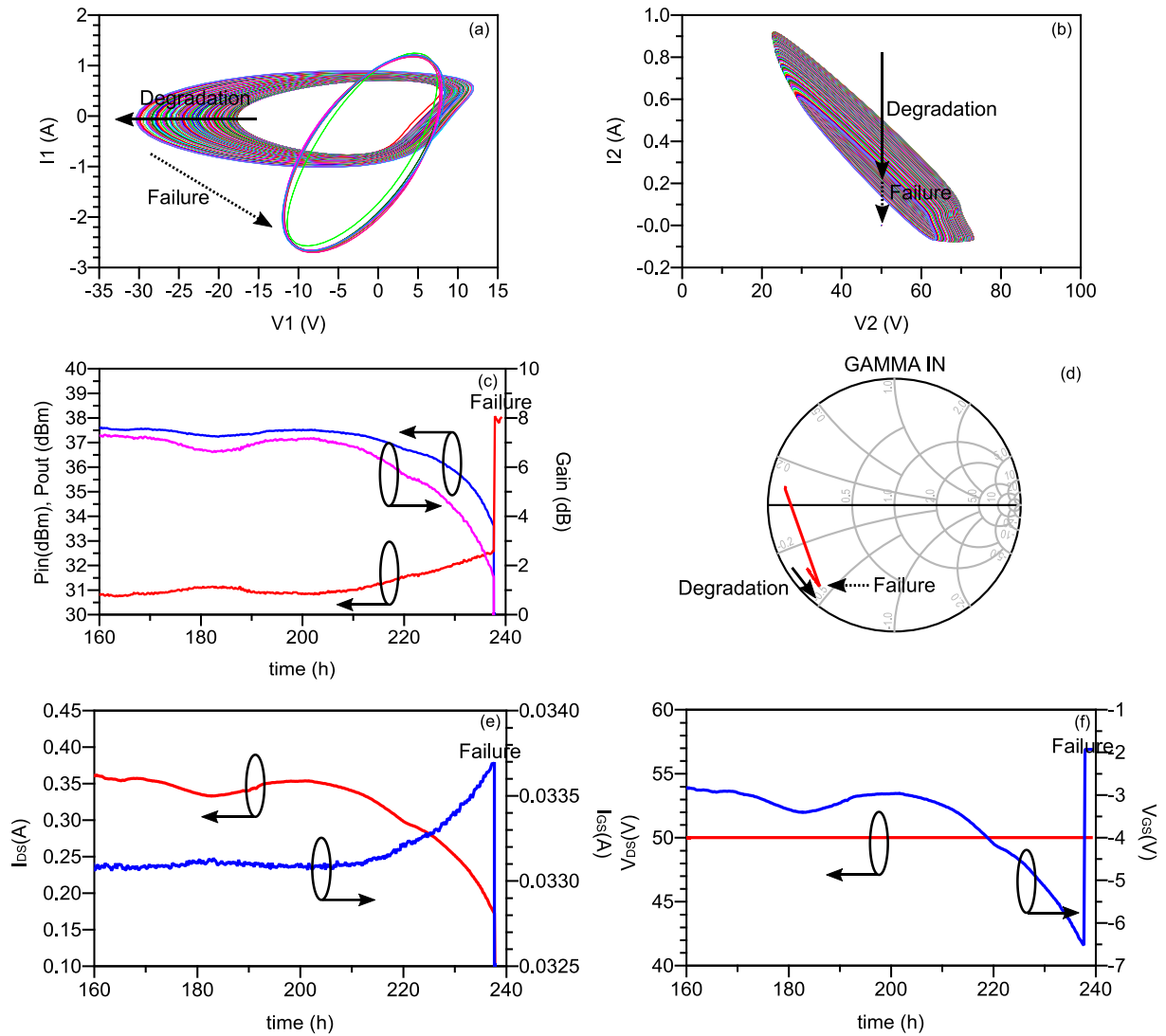


Figure 4-20:(a) Output power, (b) modulus and phase of  $I_1$  at  $f_0$  extracted from recorded extrinsic  $I_1$  RF waveforms, (c) drain current, (d) modulus and phase of  $I_2$  at  $f_0$  extracted from recorded extrinsic  $I_2$  RF waveforms, (e) extrinsic  $I_1$  RF waveforms vs extrinsic  $V_1$  RF waveforms and (f) extrinsic  $I_2$  RF waveforms vs. extrinsic  $V_2$  RF waveforms monitored during 240 hours of RF overdrive stress under the PAE optimum load impedance condition.



**Figure 4-21: (a) Output power, (b) modulus and phase of  $I1$  at  $f_0$  extracted from recorded extrinsic  $I1$  RF waveforms, (c) drain current, (d) modulus and phase of  $I2$  at  $f_0$  extracted from recorded extrinsic  $I2$  RF waveforms, (e) extrinsic  $I1$  RF waveforms vs extrinsic  $V1$  RF waveforms and (f) extrinsic  $I2$  RF waveforms vs. extrinsic  $V2$  RF waveforms monitored during 240 hours RF overdrive stress under the  $50 \Omega$  load impedance condition.**





**Figure 4-22: Measurement window zoom (from 160 hours to 240 hours) of failure of device Q28 during 240 hours RF overdrive stress at 50  $\Omega$  impedance load (a)  $I_1$  RF waveforms vs. extrinsic  $V_1$  RF waveforms, (b)  $I_2$  RF waveforms vs. extrinsic  $V_2$  RF waveforms, (c) input power, output power, gain, (d)  $\Gamma_{IN}$ , (e) drain and gate current and (f) drain and gate current variations.**

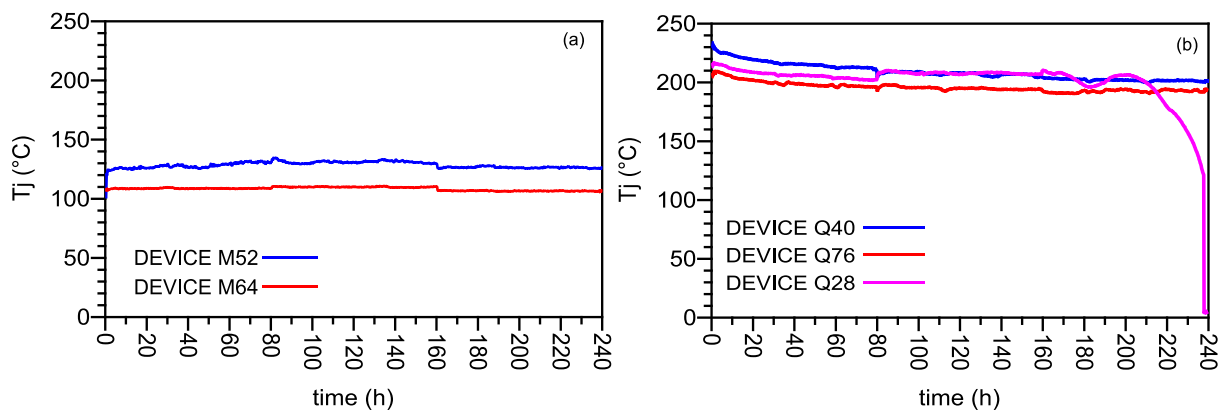


**Figure 4-23: Junction device temperature estimation during 240 hours RF overdrive stress at (a) PAE optimum impedance and (b) 50  $\Omega$  impedance.**

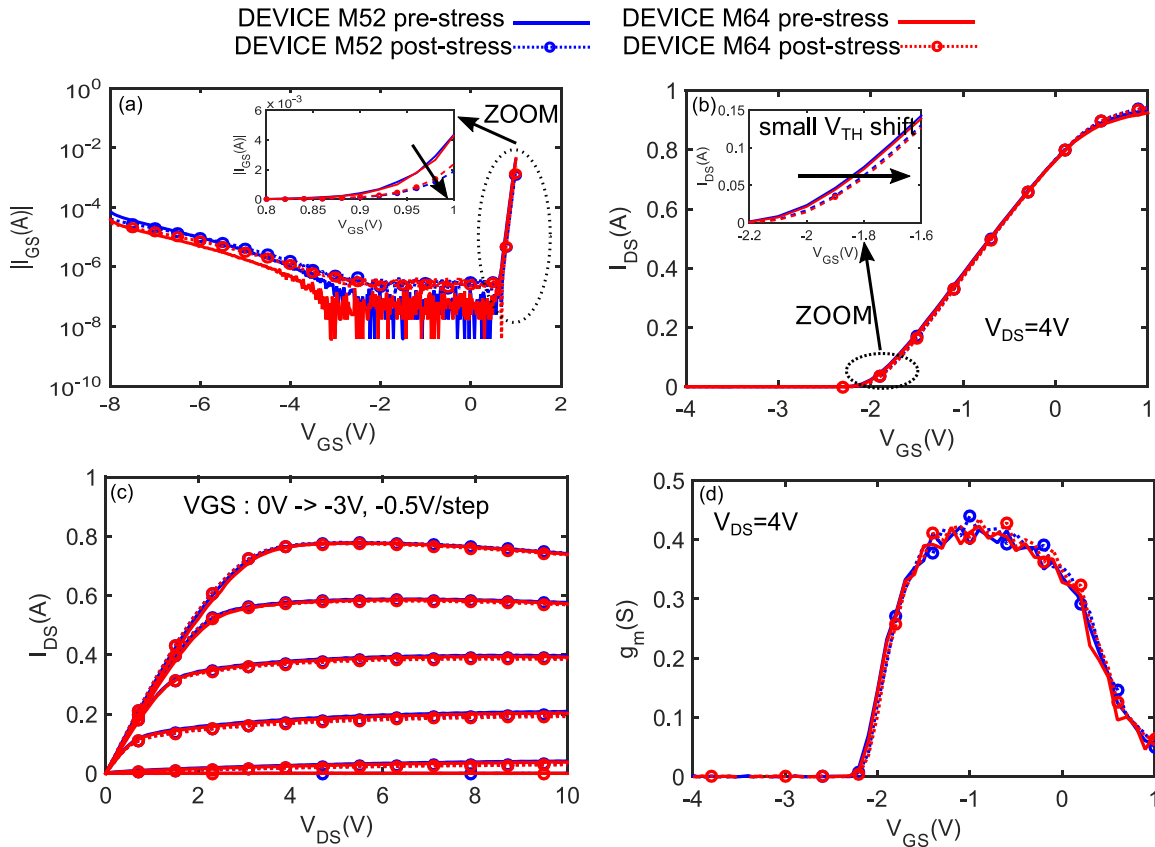


**Figure 4-24: Comparison of DC I/V measurements before (solid line) and after (dashed line) 240 hours RF overdrive stress under the PAE optimum load impedance condition: (a) gate to source diode characteristics, (b)  $I_{DS}$  vs.  $V_{GS}$  characteristics at  $V_{DS}=4$  V, (c)  $I_{DS}$  vs.  $V_{DS}$  characteristics ( $V_{GS}$  sweep from 0 V to -3 V, -0.5 V/step) and (d)  $g_m$  characteristics (extracted by  $I_{DS}$  vs.  $V_{GS}$  characteristics).**

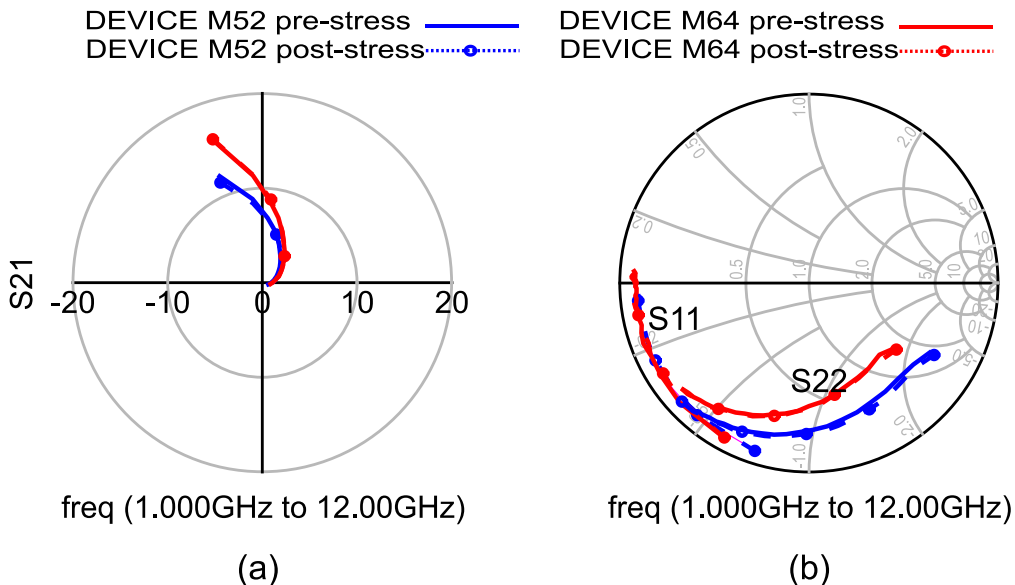


**Figure 4-25: Comparison of pulsed S-parameter measurements at quiescent bias point ( $I_{DQ}$ ,  $V_{DQ}$ )=(50 mA, 50 V) and pulsed bias point ( $V_{GM}$ ,  $V_{DM}$ )=(-2 V, 50 V) before (solid line) and after (dashed line) 240 hours RF overdrive stress under the PAE optimum load impedance condition: (a)  $S_{21}$ , (b)  $S_{11}$  and  $S_{22}$ .**

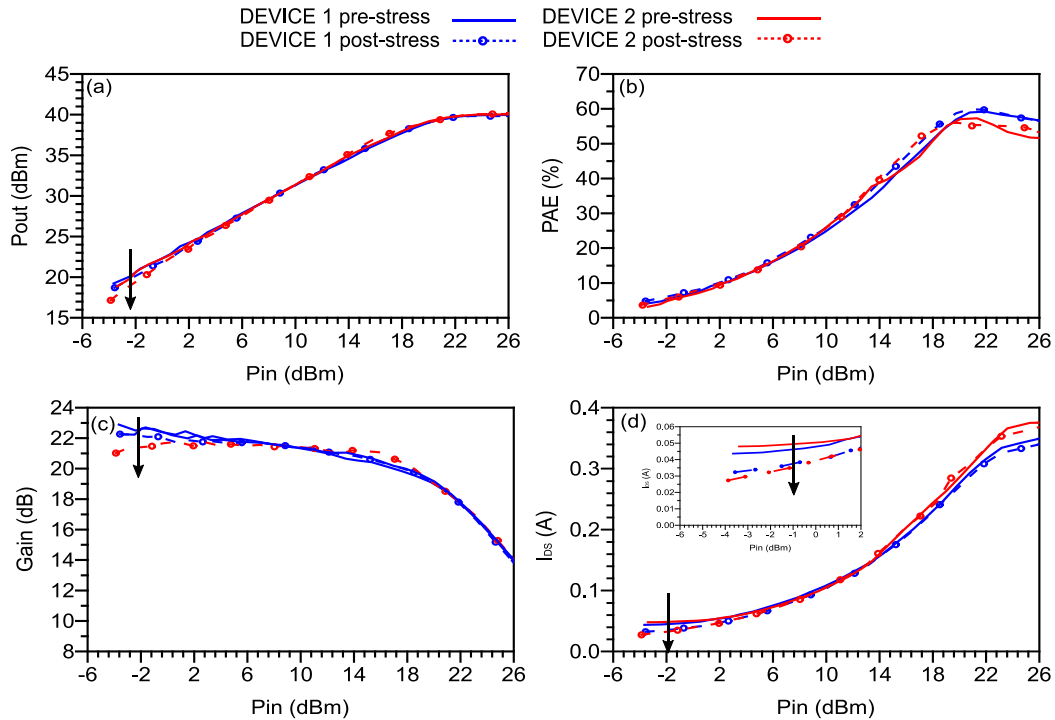


**Figure 4-26: Comparison of time-domain RF power sweep measurements under class AB condition ( $I_{ds0}=50$  mA and  $V_{ds0}=50$  V) before (solid line) and after (dashed line) 240 hours RF overdrive stress under the PAE optimum load impedance condition: (a) output power vs. input power, (b) PAE vs. input power, (c) Gain vs. input power and (d) drain current vs. input power characteristics.**

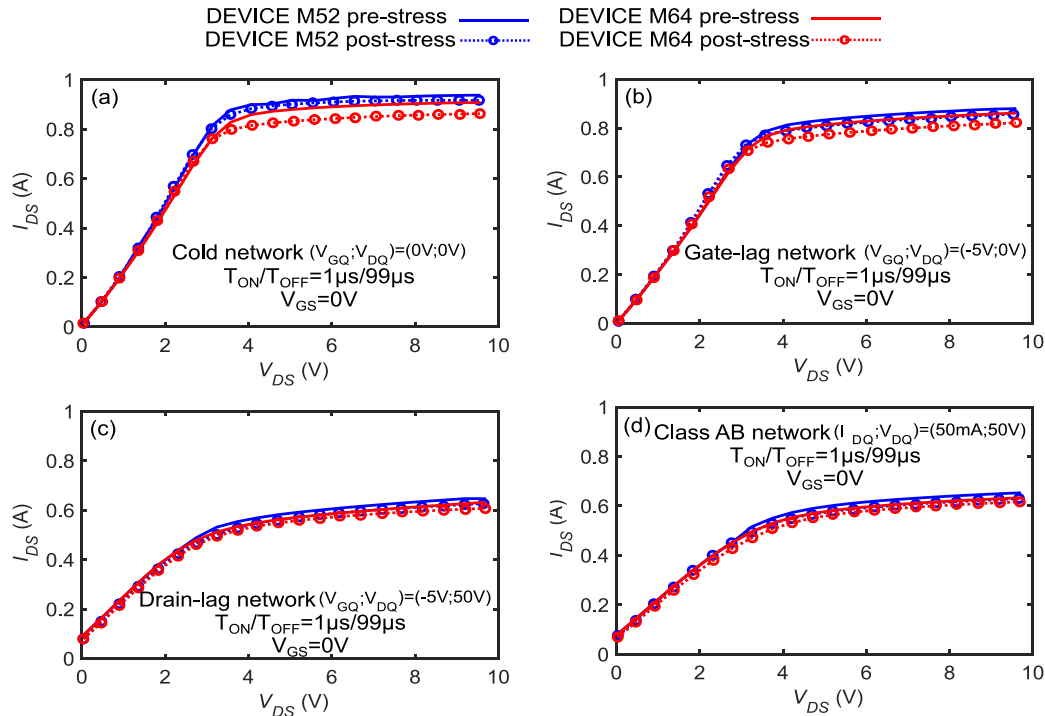


**Figure 4-27: Comparison of pulsed I/V measurements before (solid line) and after (dashed line) 240 hours RF overdrive stress under the PAE optimum load impedance condition: (a) cold network, (b) gate-lag network, (c) drain-lag network, and (d) class AB network.**

TABLE 14  
RTH ESTIMATION AT PRE- AND POST- 240 HOURS RF OVERDRIVE STRESS FOR PAE OPTIMUM LOAD IMPEDANCE CONDITION

DEVICE	R <sub>TH</sub> (°C/W)at T0 (pre-stress)	R <sub>TH</sub> (°C/W)at T2 (post-stress)
M52	~14	~14
M64	~14	~14

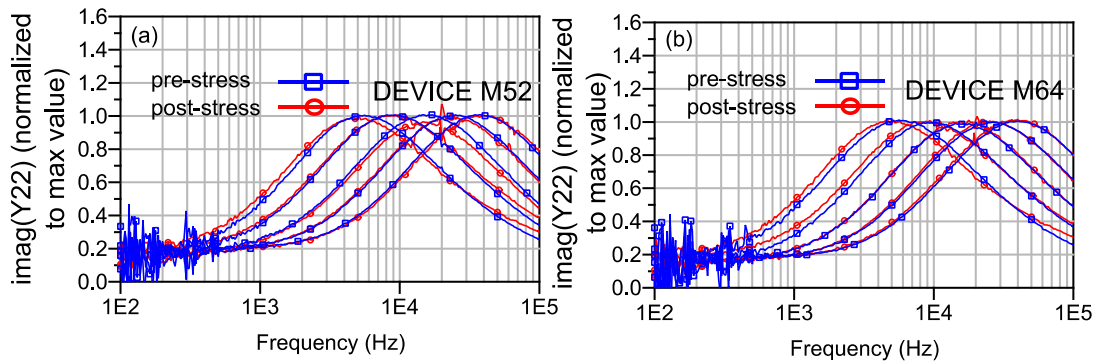


Figure 4-28: Comparison of LF Y22 measurements before (in blue) and after (in red) 240 hours RF overdrive stress at PAE optimum load impedance (a) of device M52 and (b) of device M64.

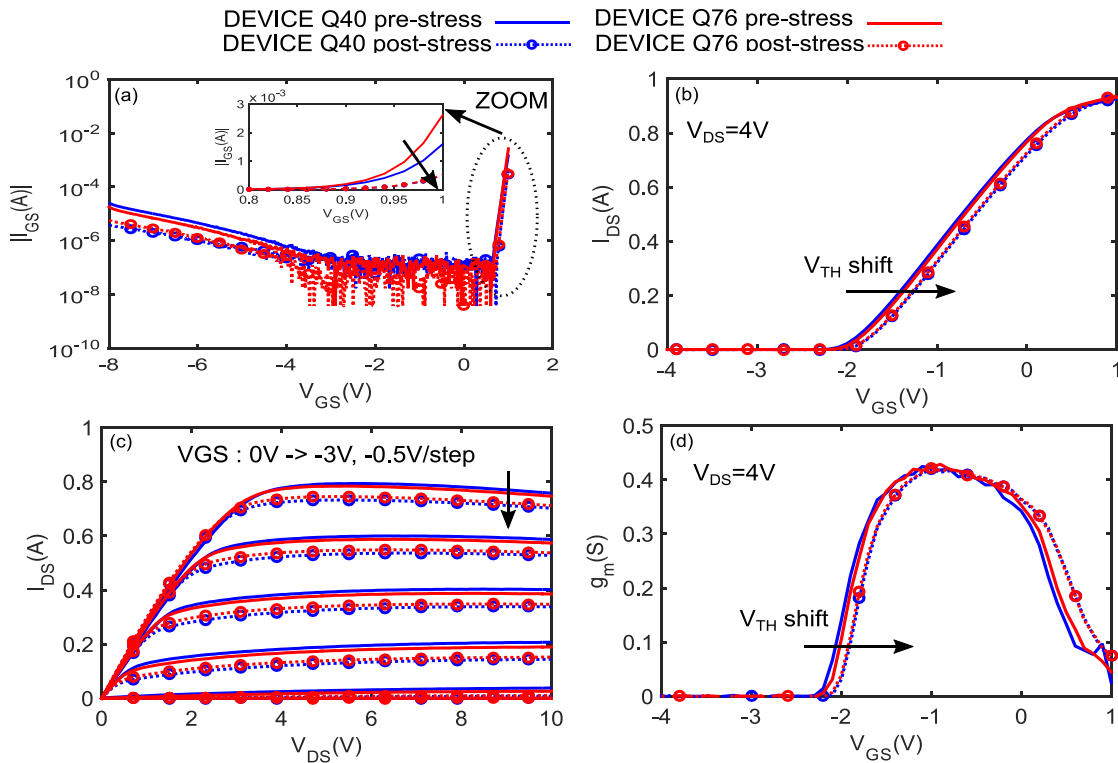
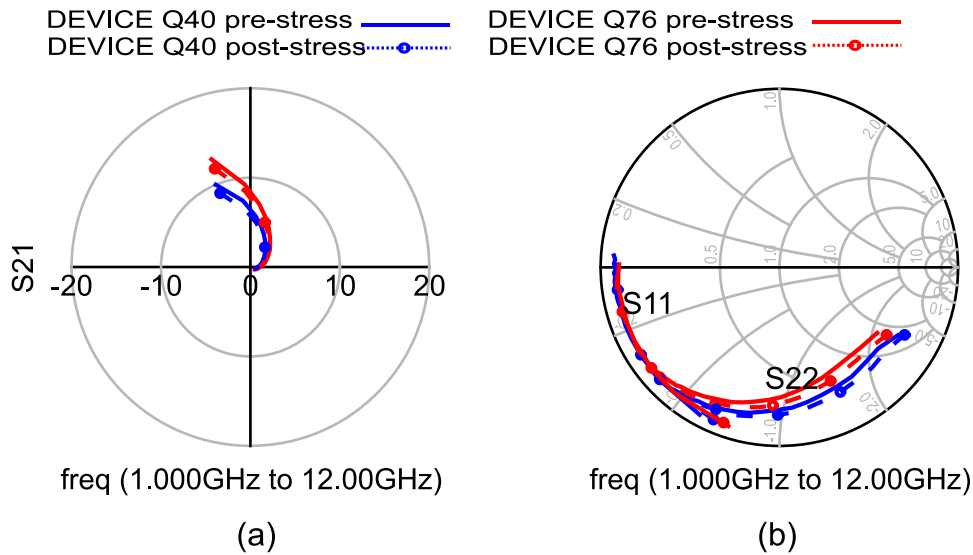
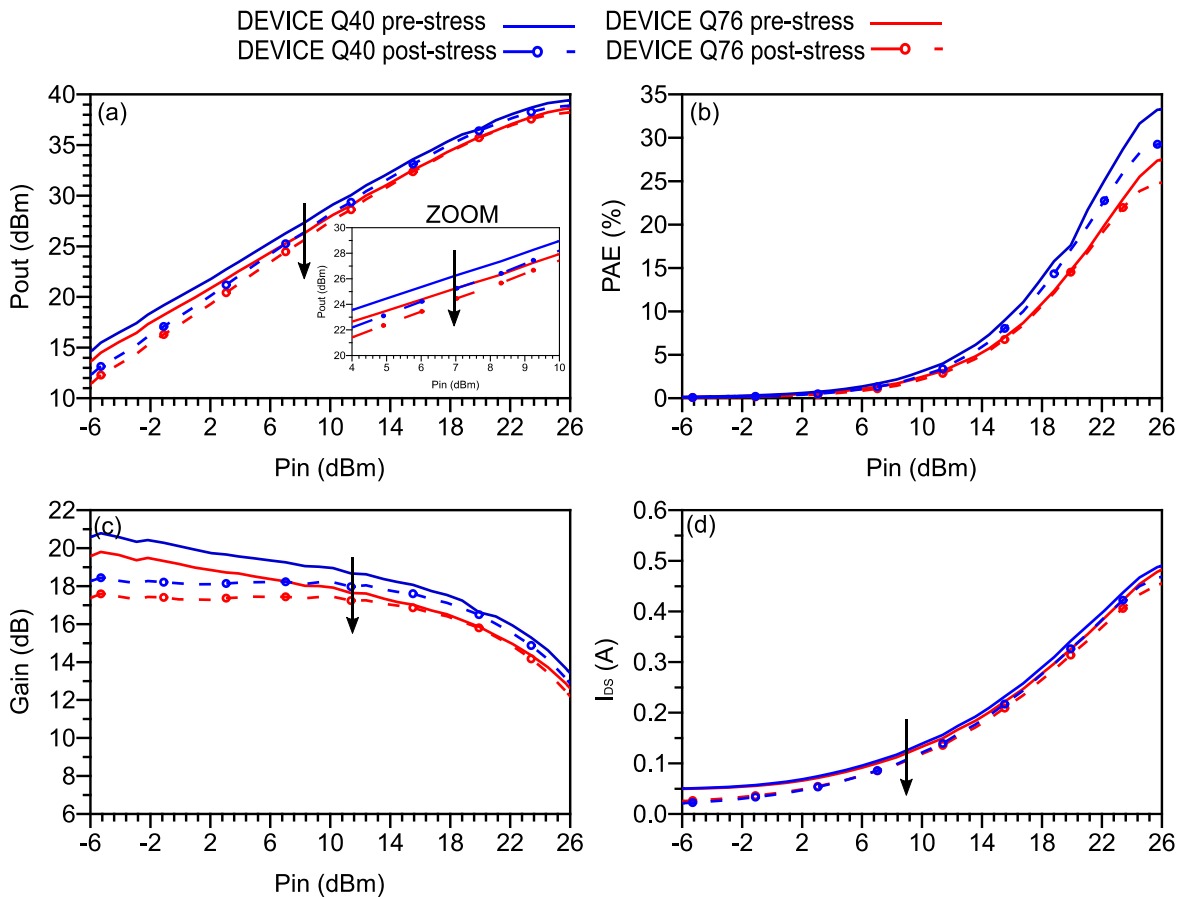


Figure 4-29: Comparison of DC I/V measurements before (solid line) and after (dashed line) 240 hours RF overdrive stress under the 50 Ω load impedance condition: (a) gate to source diode characteristics, (d) I<sub>DS</sub> vs. V<sub>GS</sub> characteristics at V<sub>DS</sub>=4 V, (c) I<sub>DS</sub> vs. V<sub>DS</sub> characteristics (V<sub>GS</sub> sweep from 0 V to -3 V, -0.5 V/step) and (d) g<sub>m</sub> characteristics (extracted by I<sub>DS</sub> vs. V<sub>GS</sub> characteristics).



**Figure 4-30: Comparison of pulsed S-parameter measurements at quiescent bias point ( $I_{DQ}$ ,  $V_{DQ}$ )=(50 mA, 50 V) and pulsed bias point ( $V_{GM}$ ,  $V_{DM}$ )=(-2 V, 50 V) before (solid line) and after (dashed line) 240 hours RF overdrive stress under the 50  $\Omega$  load impedance condition: (a) S21, (b) S11 and S22.**



**Figure 4-31: Comparison of time-domain RF power sweep measurements under class AB condition ( $I_{DS0}$ =50 mA and  $V_{DS0}$ =50 V) before (solid line) and after (dashed line) 240 hours RF overdrive stress under the 50  $\Omega$  load impedance condition: (a) output power vs. input power, (b) PAE vs. input power, (c) Gain vs. input power and (d) drain current vs. input power characteristics.**

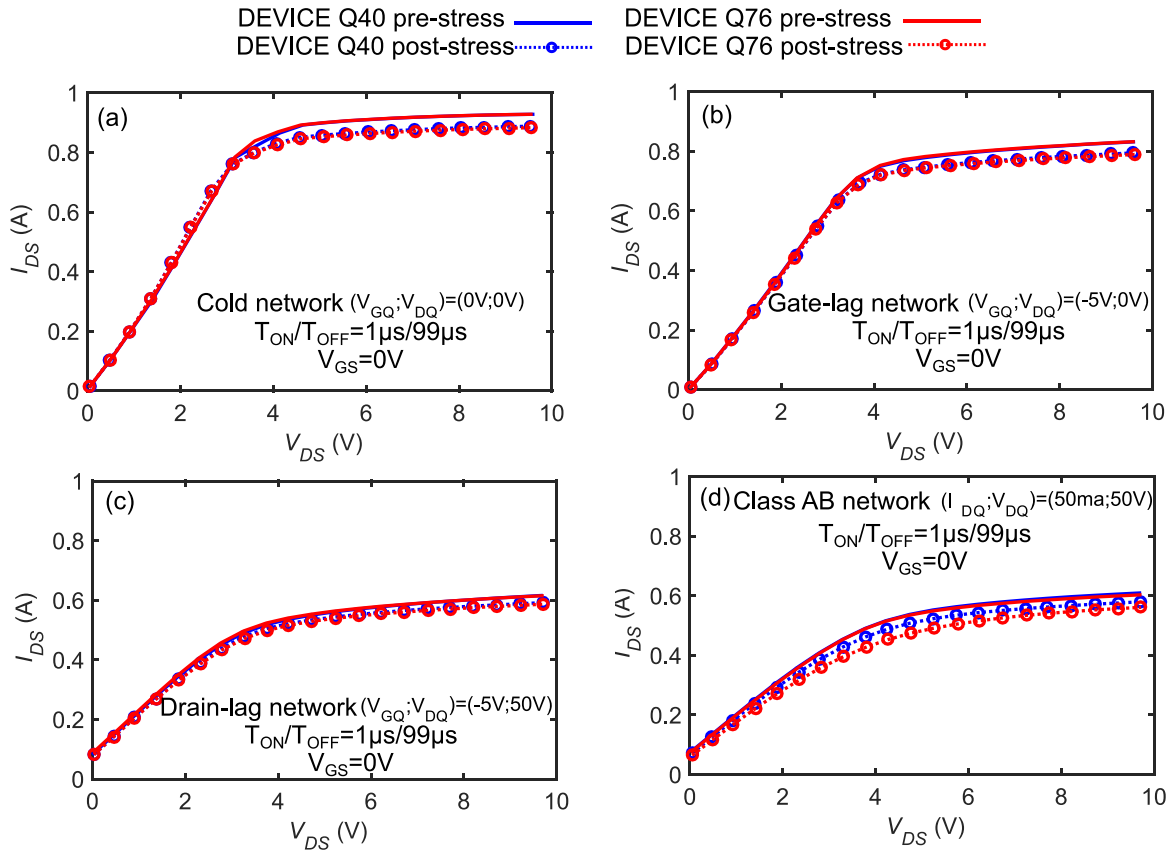


**Figure 4-32: Comparison of pulsed I/V measurements before (solid line) and after (dashed line) 240 hours RF overdrive stress under the 50 Ω load impedance condition: (a) cold network, (b) gate-lag network, (c) drain-lag network and (d) class AB network.**

TABLE 15

RTH ESTIMATION AT PRE- AND POST- 240 HOURS RF OVERDRIVE STRESS FOR 50 Ω LOAD IMPEDANCE CONDITION

DEVICE	R <sub>TH</sub> (°C/W) at T <sub>0</sub> (before stress)	R <sub>TH</sub> (°C/W) at T <sub>2</sub> (after stress)
Q40	~14	~13
Q76	~14	~13

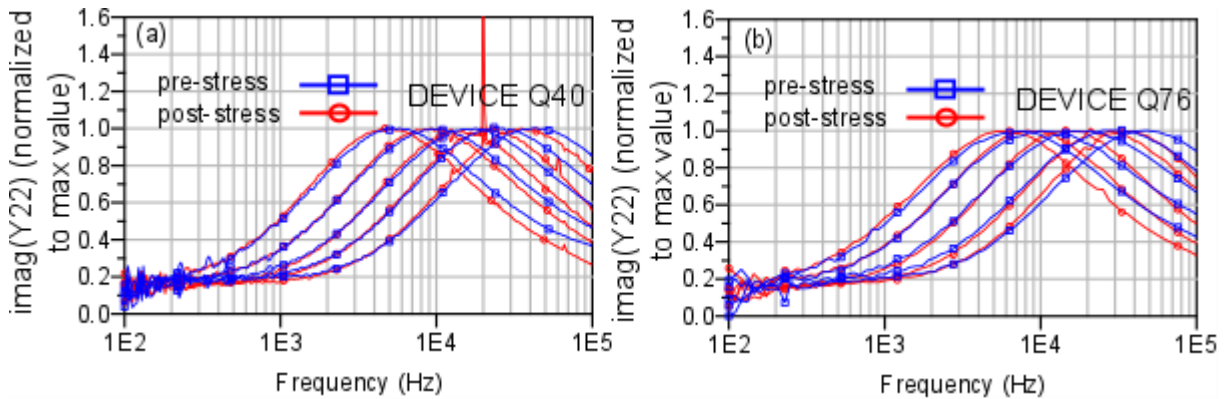


**Figure 4-33: Comparison of LF Y22 measurements before (in blue) and after (in red) 240 hours RF overdrive stress under the 50 Ω load impedance condition (a) of device Q40 and (b) of device Q76.**

The comparison of the DC I/V curves and CW RF performance before and after 240 hours of RF overdrive stress under the 50  $\Omega$  load impedance condition (in Figure 4-29 and Figure 4-31 respectively) shows a positive threshold voltage shift (around  $\Delta V_{TH}=0.05$  V) in the  $I_{DS}-V_{GS}$  characteristic (Figure 4-29(b)) which corresponds to a saturation drain current drop in the  $I_{DS}-V_{DS}$  characteristic (Figure 4-29(c)). Consequently, the average drain current, output power, gain and PAE versus input power curve are affected, as shown in Figure 4-31. This degradation mechanism is supposed to be strongly thermally activated; in fact, the stress has a stronger effect under the 50  $\Omega$  load condition, corresponding to a lower drain voltage excursion, higher average current, and thus higher device operating junction temperature (the average estimate during RF stress is around 220°C and 200°C from Figure 4-23). Under the optimum PAE load impedance condition, as shown in Figure 4-20, the DC and RF parameters during the RF life test have a minor variation, then the comparison of the DC I/V curves shows a slight positive threshold voltage shift which corresponds to a slight degradation of the average drain current versus input power characteristic (Figure 4-26(d)) at lower input power levels, indeed the device operating junction temperature obtained with the optimum PAE load impedance is 50% less than that reached with 50  $\Omega$  load impedance. The positive and negative pinch-off voltage shifts are one more common degradation and have been noticed during DC stress [111], [112] and RF stress [113]. In our case a positive pinch-off voltage shift is observed. This mechanism is similar to the trapping pinch-off voltage shift observed in Section 2.3.3.2.2 but in the stress study-case, it is irreversible.

A decrease of static gate current in forward zone is observed in Figure 4-24(a) and Figure 4-29(a) for both load output impedance condition. That is probably due to the high  $V_{GS}$  sweep excursion (in Figure 4-20(e) and Figure 4-21(e)) under overdrive operating conditions.

The trapping measurements (pulsed I/V measurements and LF  $Y_{22}$  measurements) included in the full characterization protocol show any trapping effects variation between the measurements carried out before and after stress. Indeed, the pulsed I/V measurements at different bias different quiescent bias points in Figure 4-27 and Figure 4-32, respectively for stress under the PAE optimum load impedance condition and under the 50  $\Omega$  load condition (the  $V_{GQ}$  is corrected in post-stress measurements of the Class AB network to reach the same drain current used in the pre-stress measurements) do not show any important variations. This is also in accordance with the dynamic study of trapping phenomena with CW LF  $Y_{22}$  measurements. The LF  $Y_{22}$  measurements carried out at different temperatures do not show any variations of frequency peaks between the pre-stress and post-stress measurements for both load impedance conditions in Figure 4-28 and Figure 4-33 (the  $V_{GS0}$  is corrected in the

post-stress measurements to reach the same drain current used in the pre-stress measurements).

Therefore, the 240 hours RF overdrive stress test does not impact the trapping effect when the gate voltage in the post-stress measurements is corrected to reach the same drain current used in the pre-stress measurements.

The results for the S-parameters measured at the quiescent bias point ( $I_{DQ}$ ,  $V_{DQ}$ )=(50 mA, 50 V) and the measurement bias point ( $V_{GM}$ ,  $V_{DM}$ )=(-2 V, 50 V) are shown Figure 4-25 and Figure 4-30 respectively for stress under the PAE optimum load impedance condition and under the 50  $\Omega$  load condition. The change in the S-parameters after the stress under the 50  $\Omega$  load condition is probably due to the fact that the measurement bias point ( $V_{GM}$ ,  $V_{DM}$ )=(-2 V, 50 V) has not been corrected to reach the same drain current used in the pre-stress measurements.

The estimation of the thermal resistance is obtained with an electrical method described in Section 2.3.1.3 based on thermal pulsed I/V measurements. The results of the thermal resistance estimation are summarized in Table 14 and Table 15 respectively for stress under the PAE optimum load impedance condition and under the 50  $\Omega$  load condition. For both stresses under the different load impedance conditions,  $R_{TH}$  is not impacted.

## 4.4 Conclusion

In this chapter, a continuous monitoring of RF waveforms during an RF operating life test under overdrive conditions to assess the degradation of devices for space applications is presented. This time-domain methodology is applied first to a 24 h step-stress (short stress) and secondly to a 240 h RF overdrive stress (long stress). A short and full characterization protocol have been performed respectively in order to determine the nonlinear electro-thermal model described in the previous chapter.

The first part of this chapter presented some methods of performing reliability analysis and tests. Moreover, an overview of the failure modes and mechanisms in GaN technology is also described.

The second part of this chapter presents the time-domain reliability set-up based on an LSNA measurement system in load-pull configuration and the results of a 24 h step-stress and a 240 h RF overdrive stress and their respective characterization protocols. The monitoring of RF waveforms during the 24 h step-stress for both load impedance conditions shows no variation of RF and DC performances. It is possible to conclude that the short step-stress period (24 h)



is not long enough to degrade the devices. Indeed, the monitoring of 240 hours of RF overdrive stress has shown that in this GaN technology, the RF degradation in class AB operation mode is due principally to a threshold voltage shift, which is more important under the 50  $\Omega$  condition with lower drain voltage excursion and higher average drain current (higher operating temperature) than for the PAE optimum load condition with higher drain voltage excursion. For future investigation one has the perspective of employing this time-domain methodology to perform the same stress protocol at a high temperature fixed with a thermal chuck in order to investigate the effects of temperature on the degradation mechanisms.

In conclusion, the potential of this set-up for analysing failures is demonstrated. For a more realistic reliability study, it is necessary to perform the time-domain RF stress with more devices and it will also be interesting to increase the period of stress.

Due to the complexity of the set-up and the numerous calibrations required to cover the whole of the stress period, it is suggested to combine this time-domain technique with classic RF stress: using firstly the classical accelerated RF stress for a preliminary stress to identify the degradation, and then using the time-domain RF stress to obtain supplementary information on the degradation mechanism based on the analysis of time-domain RF waveforms.

## 5 Conclusion

The work of this thesis is focused on three main topics: a trapping characterization methodology, a nonlinear electro-thermal model with a new thermal-trap model, and a time-domain methodology to investigate the device reliability of GaN-based HEMTs.

After a brief introduction of the properties and capabilities of GaN technology for space applications, the second chapter presented several characterization techniques in order to cover a broad frequency analysis from DC to radio-frequency range of the charge-trapping phenomena and the related parasitic effects in GaN-based HEMTs. This trapping characterization methodology is based on pulsed I/V measurements, DC and RF drain current measurements, and low-frequency dispersion measurements. This allows quantifying the effects of charge-trapping phenomena and the related mechanisms. These measurements are also used to identify the involved deep trap states and their location in the structure of the HEMT, through the analysis of their activation energy and their capture cross-section. With this trapping investigation, four deep levels are detected and labeled as “E1”, “E2”, “E3” and “E4.” In particular, deep level “E2” was identified with a DC DCT technique and LF dispersion technique. Furthermore, the deep level “E4” was detected with the DCT technique during DC and RF excitations but with an increasing density of ionized traps. The trap sensitivity has been investigated as a function of the input power level, pulse-width, temperature, load impedance (for two different output load impedances corresponding to the optimum of PAE and to a mismatched impedance) and operating bias points. The analysis of the dependence of the trapping effect on the bias during the RF CW mode operation condition has demonstrated that the choice of the correct operating bias point value allows making the GaN-based HEMTs insensitive to trapping effects.

The third chapter presents a methodology to extract a nonlinear electro-thermal model with a new additional thermal-trap model to take into account the dynamic behavior of the trap states and their associated temperature variations. For the extraction of a linear model of GaN-based HEMTs, a new technique, based on LF S-parameter measurements, is used. The new thermal-trap model allows accurately modeling the physical pinch-off voltage shift and the trap temperature activation. The nonlinear electro-thermal model also allows accurately predicting the dynamic behavior during large-signal RF excitation.

A time-domain RF waveform monitoring during an RF operating life test under overdrive conditions for reliability investigation is presented in the fourth chapter. The monitoring of RF waveforms is carried out for different step-stress periods of 24 h and 240 h and for two different output load impedances corresponding to the optimum of PAE and to a mismatched impedance. The RF waveform monitoring has shown the robustness, the capability to withstand very RF excitation, and great stability at very high compression levels without important degradation of this technology during 24h step-stress for both output load impedances. The conclusions are the same for 240 h step-stress for the optimum PAE load condition. But the 240 h step-stress, in overdrive condition, with a mismatched load impedance shows a stronger degradation, with a positive threshold voltage shift and a drop in saturation drain current, due principally to the high junction temperature reached by the devices during the RF stress. The time-domain reliability set-up has also shown its abilities to monitor failure events, for reliability analysis.

In conclusion, both the trapping and reliability investigations show that the trapping effects and RF degradation respectively are more important under mismatched impedance conditions with lower drain voltage excursions and higher average drain currents (higher operating temperatures) than for the optimum PAE load condition with higher drain voltage excursions.



## 6 Publications

### Journals

**A. Benvegnù**, S. Laurent, O. Jardel, J.-L. Muraro, M. Meneghini, D. Barataud, G. Meneghesso, E. Zanoni, and R. Quere, "Characterization of Defects in AlGa<sub>N</sub>/Ga<sub>N</sub> HEMTs Based on Nonlinear Microwave Current Transient Spectroscopy," in *IEEE Transactions on Electron Devices*, vol. 64, no. 5, pp. 2135-2141, May 2017.

**A. Benvegnù**, D. Bisi, S. Laurent, M. Meneghini, G. Meneghesso, D. Barataud, E. Zanoni and R. Quere, "Drain current transient and low-frequency dispersion characterizations in AlGa<sub>N</sub>/Ga<sub>N</sub> HEMTs," *International Journal of Microwave and Wireless Technologies*, available on CJO2016. doi:10.1017/S1759078716000398.

**A. Benvegnù**, S. Laurent, M. Meneghini, D. Barataud, G. Meneghesso, E. Zanoni, and R. Quere, "On-Wafer Single-Pulse Thermal Load–Pull RF Characterization of Trapping Phenomena in AlGa<sub>N</sub>/Ga<sub>N</sub> HEMTs," *IEEE Trans. Microw. Theory Tech.*, pp. 1–9, 2016.

### Conference Proceedings

**A. Benvegnù**, S. Laurent, M. Meneghini, R. Quere, J.-L. Roux, E. Zanoni and D. Barataud "Continuous Time-Domain RF waveforms monitoring under overdrive stress condition of AlGa<sub>N</sub>/Ga<sub>N</sub> HEMTs" *ESREF 2016*, vo. 64, pp 535-540, Sep 2016.

**A. Benvegnù**, O. Jardel, S. Laurent, D. Barataud, E. Zanoni and R. Quere, "Non-linear electro-thermal Ga<sub>N</sub> Model Including Large-Signal Dynamic Thermal-Trapping effects " in *IEEE MTT-S Int. Microw. Symp. Dig.*, San Francisco, CA, USA, May 2016, pp. 1–4.

**A. Benvegnù**, D. Bisi, S. Laurent, M. Meneghini, G. Meneghesso, J.-L. Muraro, D. Barataud, E. Zanoni, and R. Quere, "Trap investigation under class AB operation in AlGa<sub>N</sub>/Ga<sub>N</sub> HEMTs based on output-admittance frequency dispersion, pulsed and transient measurements," in *2015 10th European Microwave Integrated Circuits Conference*, pp. 136–139.

**A. Benvegnù**, S. Laurent, R. Quere, J.-L. Roux, J.-L. Muraro, E. Zanoni and D. Barataud, "Étude de la fiabilité de transistors de Nitrure de Gallium pour des applications spatiales: mesures de formes d'ondes temporelles en régime d'overdrive" in *2015 XIXèmes Journées Nationales Micro-ondes*, Bordeaux, France, Jun 2015.

**A. Benvegnù**, S. Laurent, M. Meneghini, G. Meneghesso, J.-M. Muraro, D. Barataud, E. Zanoni and R. Quere, "Trap characterization of AlGa<sub>N</sub>/Ga<sub>N</sub> HEMTs through Drain Current Measurements under Pulsed-RF Large-Signal excitation," in *IEEE MTT-S Int. Microw. Symp. Dig.*, Phoenix, AZ, USA, May 2015, pp. 1–4.

**A. Benvegnù**, S. Laurent, R. Quere, J.-L. Roux, J.-L. Muraro, E. Zanoni and D. Barataud, and "Protocole de de caractérisations avancées pour l'étude de la fiabilité de transistor Ga<sub>N</sub>" in *JNRDM 2015*, Bordeaux, France, May 2015.

**A. Benvegnù**, S. Laurent, T. Reveyrand, R. Quere, J.-L. Roux, J.-L. Muraro and D. Barataud, "Time-Domain Waveform Measurements under Large Signal RF Overdrive Stress in HEMT Technology" in *7th Space Agency–MOD Workshop on Wideband Gap Semiconductors and Components*.



## 7 References

- [1] T. Reveyrand *et al.*, “GaN transistor characterization and modeling activities performed within the frame of the KorriGaN project,” *Int. J. Microw. Wirel. Technol.*, vol. 2, no. 01, p. 51, Mar. 2010.
- [2] A. R. Barnes and F. Vitobello, “ESA perspective on the industrialisation of European GaN technology for space application,” in *European Microwave Integrated Circuit Conference (EuMIC), 2014 9th*, 2014, pp. 233–236.
- [3] Takashi Mimura, Satoshi Hiyamizu, Toshio Fujii, and Kazuo Nanbu, “A New Field-Effect Transistor with Selectively Doped GaAs/n-Al<sub>x</sub>Ga<sub>1-x</sub>As Heterojunctions,” vol. 19, no. 5, p. L225, 1980.
- [4] R. Dingle, H. L. Störmer, A. C. Gossard, and W. Wiegmann, “Electron mobilities in modulation-doped semiconductor heterojunction superlattices,” *Appl. Phys. Lett.*, no. 33, p. 665, 1978.
- [5] P. Nakkala, “pulsed I-V and RF characterization and modeling of AlGaIn/GaN HEMTs and graphene FETs,” Université de Limoges, 2015.
- [6] D. W. Runton, B. Trabert, J. B. Shealy, and R. Vetry, “History of GaN: High-Power RF Gallium Nitride (GaN) from Infancy to Manufacturable Process and Beyond,” *IEEE Microw. Mag.*, vol. 14, no. 3, pp. 82–93, 2013.
- [7] U. K. Mishra, P. Parikh, and Y.-F. Wu, “AlGaIn/GaN HEMTs—An overview of device operation and applications,” *Proc.-IEEE*, vol. 90, no. 6, pp. 1022–1031, 2002.
- [8] O. Ambacher *et al.*, “Two dimensional electron gases induced by spontaneous and piezoelectric polarization in undoped and doped AlGaIn/GaN heterostructures,” *J. Appl. Phys.*, vol. 87, no. 1, p. 334, 2000.
- [9] R. Giofré *et al.*, “A first step towards a 230 W SSPA for Galileo System exploiting European GaN technology,” in *2015 10th European Microwave Integrated Circuits Conference*, pp. 317–320.
- [10] B. Lefebvre *et al.*, “GaN For Space Applications: Ready for Commercial Use,” *8th Wide Bandgap Semiconductors and Components Workshop*, ESA-ECSAT, Harwell, United Kingdom, 12 Sep. 2016.
- [11] J.-L. Muraro *et al.*, “GaN for space application: Almost ready for flight,” *Int. J. Microw. Wirel. Technol.*, vol. 2, no. 01, p. 121, Apr. 2010.
- [12] K. Hirche *et al.*, “GaN Reliability Enhancement and Technology Transfer Initiative (GREAT<sup>2</sup>).”
- [13] W. Shockley and W. T. Read, Jr., “Statistics of the recombinations of holes and electrons,” *Phys. Rev.*, vol. 87, no. 5, p. 835, 1952.
- [14] R. N. Hall, “Electron-hole recombination in germanium,” *Phys. Rev.*, vol. 87, no. 2, p. 387, 1952.
- [15] H. Morkoc, *Handbook of Nitride Semiconductors and Devices*, vol. 1. Wiley-VCH, 2008.
- [16] S. D. Nsele, L. Escotte, J.-G. Tartarin, S. Piotrowicz, and S. L. Delage, “Broadband Frequency Dispersion Small-Signal Modeling of the Output Conductance and Transconductance in AlInN/GaN HEMTs,” *IEEE Trans. Electron Devices*, vol. 60, no. 4, pp. 1372–1378, Apr. 2013.
- [17] M. Meneghini *et al.*, “Investigation of trapping and hot-electron effects in GaN HEMTs by means of a combined electrooptical method,” *Electron Devices IEEE Trans. On*, vol. 58, no. 9, pp. 2996–3003, 2011.

- [18] J. Joh and J. A. del Alamo, "A Current-Transient Methodology for Trap Analysis for GaN High Electron Mobility Transistors," *IEEE Trans. Electron Devices*, vol. 58, no. 1, pp. 132–140, Jan. 2011.
- [19] J. G. Tartarin, S. Karboyan, F. Olivie, G. Astre, L. Bary, and B. Lambert, "I-DLTS, electrical lag and low frequency noise measurements of trapping effects in AlGaIn/GaN HEMT for reliability studies," in *2011 European Microwave Integrated Circuits Conference*, pp. 438–441.
- [20] D. Bisi *et al.*, "Deep-Level Characterization in GaN HEMTs-Part I: Advantages and Limitations of Drain Current Transient Measurements," *IEEE Trans. Electron Devices*, vol. 60, no. 10, pp. 3166–3175, Oct. 2013.
- [21] J. M. Golio, M. G. Miller, G. N. Maracas, and D. A. Johnson, "Frequency-dependent electrical characteristics of GaAs MESFETs," *IEEE Trans. Electron Devices*, vol. 37, no. 5, pp. 1217–1227, May 1990.
- [22] G. A. Umana-Membreno *et al.*, "Low-temperature shallow-trap related output-admittance frequency dispersion in AlGaIn/GaN MODFETs," in *Proceedings of the 1998 Conference on Optoelectronic and Microelectronic Materials Devices.*, pp. 252–255.
- [23] P. B. Klein and S. C. Binari, "Photoionization spectroscopy of deep defects responsible for current collapse in nitride-based field effect transistors," *J. Phys. Condens. Matter*, vol. 15, no. 44, p. R1641, 2003.
- [24] S. C. Binari, P. B. Klein, and T. E. Kazior, "Trapping effects in GaN and SiC microwave FETs," *Proc. IEEE*, vol. 90, no. 6, pp. 1048–1058, 2002.
- [25] R. Vetury, N. Q. Zhang, S. Keller, and U. K. Mishra, "The impact of surface states on the DC and RF characteristics of AlGaIn/GaN HFETs," *Electron Devices IEEE Trans. On*, vol. 48, no. 3, pp. 560–566, 2001.
- [26] G. Meneghesso *et al.*, "Reliability issues of Gallium Nitride High Electron Mobility Transistors," *Int. J. Microw. Wirel. Technol.*, vol. 2, no. 01, p. 39, Apr. 2010.
- [27] G. Meneghesso *et al.*, "Trapping phenomena in AlGaIn/GaN HEMTs: A study based on pulsed and transient measurements," *Semicond. Sci. Technol.*, vol. 28, no. 7, p. 074021, Jul. 2013.
- [28] O. Mitrofanov and M. Manfra, "Mechanisms of gate lag in GaN/AlGaIn/GaN high electron mobility transistors," *Superlattices Microstruct.*, vol. 34, nos. 1–2, pp. 33–53, Jul. 2003.
- [29] N. Ramanan, B. Lee, and V. Misra, "Device Modeling for Understanding AlGaIn/GaN HEMT Gate-Lag," *IEEE Trans. Electron Devices*, vol. 61, no. 6, pp. 2012–2018, Jun. 2014.
- [30] O. Jardel, "Contribution à la Modélisation des Transistors pour l'Amplification de Puissance aux Fréquences Microondes. Développement d'un nouveau Modèle Electrothermique de HEMT AlGaIn/GaN incluant les Effets de Pièges," Université de Limoges, 2008.
- [31] Pulsed IV Bilt AMCAD System datasheet, <http://www.amcad-engineering.com/IMG/File/PIV%20Gate%20and%20Drain%20Probe%20Heads%20Specifications.pdf>.
- [32] J. Joh, J. A. Del Alamo, U. Chowdhury, T.-M. Chou, H.-Q. Tserng, and J. L. Jimenez, "Measurement of channel temperature in GaN high-electron mobility transistors," *IEEE Trans. on Electron. Devices*, vol. 56, no. 12, pp. 2895–2901, 2009.
- [33] G. Mougnot, R. Sommet, R. Quéré, Z. Ouarch, S. Heckmann, and M. Camiade, "Thermal and trapping phenomena assessment on AlGaIn/GaN microwave power transistor," in *2010 European Microwave Integrated Circuits Conference*, pp. 110–113.



- [34] A. Chini, F. Soci, M. Meneghini, G. Meneghesso, and E. Zanoni, "Deep Levels Characterization in GaN HEMTs," Part II: Experimental and Numerical Evaluation of Self-Heating Effects on the Extraction of Traps Activation Energy," *IEEE Trans. Electron Devices*, vol. 60, no. 10, pp. 3176–3182, Oct. 2013.
- [35] M. Ćapajna, R. J. T. Simms, Yi Pei, U. K. Mishra, and M. Kuball, "Integrated Optical and Electrical Analysis: Identifying Location and Properties of Traps in AlGaIn/GaN HEMTs During Electrical Stress," *IEEE Electron Device Lett.*, vol. 31, no. 7, pp. 662–664, Jul. 2010.
- [36] T. Mizutani, T. Okino, K. Kawada, Y. Ohno, S. Kishimoto, and K. Maezawa, "Drain current DLTS of AlGaIn/GaN HEMTs," *Phys. Status Solidi A*, vol. 200, no. 1, pp. 195–198, Nov. 2003.
- [37] D. Bisi, "Characterization of Charge Trapping Phenomena in GaN-based HEMTs," 2015.
- [38] H. K. Cho, C. S. Kim, and C.-H. Hong, "Electron capture behaviors of deep level traps in unintentionally doped and intentionally doped n-type GaN," *J. Appl. Phys.*, vol. 94, no. 3, p. 1485, 2003.
- [39] D. Bisi *et al.*, "Trapping mechanisms in GaN-based MIS-HEMTs grown on silicon substrate: Trapping mechanisms in GaN-based MIS-HEMTs," *Phys. Status Solidi A*, vol. 212, no. 5, pp. 1122–1129, May 2015.
- [40] M. Meneghini *et al.*, "Buffer Traps in Fe-Doped AlGaIn/GaN HEMTs: Investigation of the Physical Properties Based on Pulsed and Transient Measurements," *IEEE Trans. Electron Devices*, vol. 61, no. 12, pp. 4070–4077, Dec. 2014.
- [41] O. Jardel *et al.*, "Modeling of Trap Induced Dispersion of Large Signal Dynamic Characteristics of GaN HEMTs," in *IEEE International Microwave Symposium*, 2013.
- [42] R. Quéré *et al.*, "Low frequency parasitic effects in RF transistors and their impact on power amplifier performances," in *Wireless and Microwave Technology Conference*, 2012, pp. 1–5.
- [43] J. Delprato, D. Barataud, M. Campovecchio, G. Neveux, C. Tolant, and P. Eudeline, "Measured and Simulated Impact of Irregular Radar Pulse Trains on the Pulse-to-Pulse Stability of Microwave Power Amplifiers," *IEEE Trans. Microw. Theory Tech.*, vol. 62, no. 12, pp. 3538–3548, Dec. 2014.
- [44] G. Avolio, G. Pailloncy, D. Schreurs, M. V. Bossche, and B. Nauwelaers, "On-Wafer LSNA measurements including dynamic-bias," in *2009 European Microwave Conference*, pp. 930–933.
- [45] J. Brinkhoff and A. Parker, "Charge trapping and intermodulation in HEMTs," in *IEEE MTT S International Microwave Symposium Digest*, 2004, vol. 2, pp. 799–802.
- [46] O. Axelsson *et al.*, "Application Relevant Evaluation of Trapping Effects in AlGaIn/GaN HEMTs With Fe-Doped Buffer," *IEEE Trans. Electron Devices*, vol. 63, no. 1, pp. 326–332, Jan. 2016.
- [47] G. Meneghesso *et al.*, "Surface-Related Drain Current Dispersion Effects in AlGaIn/GaN HEMTs," *IEEE Trans. Electron Devices*, vol. 51, no. 10, pp. 1554–1561, Oct. 2004.
- [48] O. Mitrofanov, "Poole–Frenkel electron emission from the traps in AlGaIn/GaN transistors," *J. Appl. Phys.*, vol. 95, no. 11, p. 6414, 2004.
- [49] A. El Rafei *et al.*, "DC (10 Hz) to RF (40 GHz) output conduction by S-parameters measurements for in-depth characterization of AlInN/GaN HEMTs, focusing on low frequency dispersion effects," in *Microwave Integrated Circuits Conference (EuMIC), 2011 European*, 2011, pp. 5–8.
- [50] *E5061B ENA Series Network Analyzer Manual*, <http://cp.literature.agilent.com/litweb/pdf/E5061-90008.pdf>.

- [51] D. A. Frickey, "Conversions between S, Z, Y, H, ABCD, and T parameters which are valid for complex source and load impedances," *IEEE Trans. Microw. Theory Tech.*, vol. 42, no. 2, pp. 205–211, Feb. 1994.
- [52] S. S. Islam, A. F. M. Anwar, and R. T. Webster, "A physics-based frequency dispersion model of GaN MESFETs," *IEEE Trans. Electron Devices*, vol. 51, no. 6, pp. 846–853, Jun. 2004.
- [53] G. A. Umana-Membreno *et al.*, "Co gamma-irradiation-induced defects in n-GaN," *Appl. Phys. Lett.*, vol. 80, no. 23, p. 4354, 2002.
- [54] Y. S. Park *et al.*, "Deep level transient spectroscopy in plasma-assisted molecular beam epitaxy grown AlGaIn/GaN interface and the rapid thermal annealing effect," *Appl. Phys. Lett.*, vol. 97, no. 11, p. 112110, 2010.
- [55] A. R. Arehart *et al.*, "Comparison of deep level incorporation in ammonia and rf-plasma assisted molecular beam epitaxy n-GaN films," *Phys. Status Solidi C*, vol. 5, no. 6, pp. 1750–1752, May 2008.
- [56] T. Okino, M. Ochiai, Y. Ohno, S. Kishimoto, K. Maezawa, and T. Mizutani, "Drain Current DLTS of AlGaIn& 8211;GaIn MIS-HEMTs," *IEEE Electron Device Lett.*, vol. 25, no. 8, pp. 523–525, Aug. 2004.
- [57] G. Verzellesi, A. Mazzanti, C. Canali, G. Meneghesso, A. Chini, and E. Zanoni, "Study on the origin of dc-to-RF dispersion effects in GaAs-and GaN-based heterostructure FETs," in *Proceedings of the 2003 GaAs Reliability Workshop.*, pp. 155–156.
- [58] M. Caesar *et al.*, "Generation of traps in AlGaIn/GaN HEMTs during RF-and DC-stress test," in *2012 IEEE International Reliability Physics Symposium*, p. CD–6.
- [59] G. A. Umana-Membreno, G. Parish, N. Fichtenbaum, S. Keller, U. K. Mishra, and B. D. Nener, "Electrically Active Defects in GaN Layers Grown With and Without Fe-doped Buffers by Metal-organic Chemical Vapor Deposition," *J. Electron. Mater.*, vol. 37, no. 5, pp. 569–572, May 2008.
- [60] H. M. Chung *et al.*, "Electrical characterization of isoelectronic In-doping effects in GaN films grown by metalorganic vapor phase epitaxy," *Appl. Phys. Lett.*, vol. 76, no. 7, pp. 897–899, 2000.
- [61] P. Hacke, T. Detchprohm, K. Hiramatsu, N. Sawaki, K. Tadatomo, and K. Miyake, "Analysis of deep levels in type GaN by transient capacitance methods," *J. Appl. Phys.*, vol. 76, no. 1, pp. 304–309, Jul. 1994.
- [62] J. Osaka, Y. Ohno, S. Kishimoto, K. Maezawa, and T. Mizutani, "Deep levels in n-type AlGaIn grown by hydride vapor-phase epitaxy on sapphire characterized by deep-level transient spectroscopy," *Appl. Phys. Lett.*, vol. 87, no. 22, pp. 222112–222112–3, Nov. 2005.
- [63] D. Kindl *et al.*, "Deep defects in GaN/AlGaIn/SiC heterostructures," *J. Appl. Phys.*, vol. 105, no. 9, p. 093706, 2009.
- [64] D. W. Cardwell *et al.*, "Spatially-resolved spectroscopic measurements of  $E_c - 0.57$  eV traps in AlGaIn/GaN high electron mobility transistors," *Appl. Phys. Lett.*, vol. 102, no. 19, p. 193509, 2013.
- [65] C. D. Wang *et al.*, "Deep level defects in n-type GaN grown by molecular beam epitaxy," *Appl. Phys. Lett.*, vol. 72, no. 10, 1998.
- [66] M. Silvestri, M. J. Uren, and M. Kuball, "Dynamic Transconductance Dispersion Characterization of Channel Hot-Carrier Stressed 0.25- AlGaIn/GaN HEMTs," *IEEE Electron Device Lett.*, vol. 33, no. 11, pp. 1550–1552, Nov. 2012.
- [67] M. Asghar, P. Muret, B. Beaumont, and P. Gibart, "Field dependent transformation of electron traps in GaN p–n diodes grown by metal–organic chemical vapour deposition," *Mater. Sci. Eng. B*, vol. 113, no. 3, pp. 248–252, Nov. 2004.

- [68] A. Stocco *et al.*, “Proton induced trapping effect on space compatible GaN HEMTs,” *Microelectron. Reliab.*, Aug. 2014.
- [69] Z.-Q. Fang *et al.*, “Deep centers in a free-standing GaN layer,” *Appl. Phys. Lett.*, vol. 78, no. 15, p. 2178, 2001.
- [70] F. D. Auret, S. A. Goodman, F. K. Koschnick, J.-M. Spaeth, B. Beaumont, and P. Gibart, “Electrical characterization of two deep electron traps introduced in epitaxially grown n-GaN during He-ion irradiation,” *Appl. Phys. Lett.*, vol. 73, no. 25, p. 3745, 1998.
- [71] Z.-Q. Fang, D. C. Look, D. H. Kim, and I. Adesida, “Traps in AlGaIn/GaN/SiC heterostructures studied by deep level transient spectroscopy,” *Appl. Phys. Lett.*, vol. 87, no. 18, p. 182115, 2005.
- [72] A. R. Arehart, T. Homan, M. H. Wong, C. Poblenz, J. S. Speck, and S. A. Ringel, “Impact of N- and Ga-face polarity on the incorporation of deep levels in n-type GaN grown by molecular beam epitaxy,” *Appl. Phys. Lett.*, vol. 96, no. 24, p. 242112, Jun. 2010.
- [73] A. R. Arehart, A. A. Allerman, and S. A. Ringel, “Electrical characterization of n-type Al<sub>0.30</sub>Ga<sub>0.70</sub>N Schottky diodes,” *J. Appl. Phys.*, vol. 109, no. 11, p. 114506, 2011.
- [74] A. Sasikumar *et al.*, “Access-Region Defect Spectroscopy of DC-Stressed N-Polar GaN MIS-HEMTs,” *IEEE Electron Device Lett.*, vol. 33, no. 5, pp. 658–660, May 2012.
- [75] N. M. Schmidt *et al.*, “Effect of annealing on defects in as-grown and symbol (g)-ray irradiated n-GaN layers,” *Phys. Status Solidi(B)*, vol. 216, no. 1, pp. 533–536, 1999.
- [76] A. Y. Polyakov *et al.*, “Electrical properties and deep traps spectra of a-plane GaN films grown on r-plane sapphire,” *Mater. Sci. Eng. B*, vol. 166, no. 3, pp. 220–224, Feb. 2010.
- [77] G. Verzellesi *et al.*, “False surface-trap signatures induced by buffer traps in AlGaIn-GaN HEMTs,” in *Reliability Physics Symposium, 2009 IEEE International*, 2009, pp. 732–735.
- [78] S. DasGupta *et al.*, “Slow Detrapping Transients due to Gate and Drain Bias Stress in High Breakdown Voltage AlGaIn/GaN HEMTs,” *IEEE Trans. Electron Devices*, vol. 59, no. 8, pp. 2115–2122, Aug. 2012.
- [79] K. Tanaka, M. Ishida, T. Ueda, and T. Tanaka, “Effects of Deep Trapping States at High Temperatures on Transient Performance of AlGaIn/GaN Heterostructure Field-Effect Transistors,” *Jpn. J. Appl. Phys.*, vol. 52, no. 4S, p. 04CF07, Apr. 2013.
- [80] M. R. Hogsed, “Deep level defects in electron-irradiated aluminum gallium nitride grown by molecular beam epitaxy,” DTIC Document, 2005.
- [81] A. Armstrong, A. Chakraborty, J. S. Speck, S. P. DenBaars, U. K. Mishra, and S. A. Ringel, “Quantitative observation and discrimination of AlGaIn- and GaN-related deep levels in AlGaIn/GaN heterostructures using capacitance deep level optical spectroscopy,” *Appl. Phys. Lett.*, vol. 89, no. 26, p. 262116, 2006.
- [82] P. Kamyczek, E. Placzek-Popko, V. Kolkovskiy, S. Grzanka, and R. Czernecki, “A deep acceptor defect responsible for the yellow luminescence in GaN and AlGaIn,” *J. Appl. Phys.*, vol. 111, no. 11, p. 113105, 2012.
- [83] T. Brazzini *et al.*, “Electroluminescence of hot electrons in AlGaIn/GaN high-electron-mobility transistors under radio frequency operation,” *Appl. Phys. Lett.*, vol. 106, no. 21, p. 213502, May 2015.
- [84] S. Rochette *et al.*, “A high efficiency 140W power amplifier based on a single GaN HEMT device for space applications in L-band,” in *2012 7th European Microwave Integrated Circuits Conference*, pp. 127–130.
- [85] C. A. Liechti, “Microwave Field-Effect Transistors,” *IEEE Trans. Microw. Theory Tech.*, vol. 27, no. 6, pp. 279–300, Jun. 1976.

- [86] W. Demenitroux, C. Mazière, T. Gasseling, B. Gustavsen, M. Campovecchio, and R. Quéré, “A new multi-harmonic and bilateral behavioral model taking into account short term memory effect,” in *2010 European Microwave Conference*, pp. 473–476.
- [87] I. Angelov and H. Zirath, “A New Empirical Nonlinear Model for HEMT and MESFET Devices,” *IEEE Trans. Microw. Theory Tech.*, vol. 40, no. 12, Dec. 1992.
- [88] P. Roblin, D. E. Root, J. Verspecht, Y. Ko, and J. P. Teyssier, “New Trends for the Nonlinear Measurement and Modeling of High-Power RF Transistors and Amplifiers With Memory Effects,” *IEEE Trans. Microw. Theory Tech.*, vol. 60, no. 6, pp. 1964–1978, Jun. 2012.
- [89] J. Verspecht *et al.*, “Extension of X-parameters to include long-term dynamic memory effects,” in *Microwave Symposium Digest, 2009*, pp. 741–744.
- [90] C. Charbonniaud, “Caractérisation et modélisation électrothermique non linéaire de transistors à effet de champ GaN pour l’amplification de puissance micro-onde,” Université de Limoges, France, 2005.
- [91] G. Dambrine, A. Cappy, F. Heliodore, and E. Playez, “A new method for determining the FET small-signal equivalent circuit,” *IEEE Trans. Microw. Theory Tech.*, vol. 36, no. 7, pp. 1151–1159, 1988.
- [92] H. S. Sodhi, “Measuring and Modeling Low Frequency in GaAs MESFET’s,” Massachusetts Institute of Technology, 1996.
- [93] Y. Tajima, B. Wrona, and K. Mishima, “GaAs FET large-signal model and its application to circuit designs,” *Electron Devices IEEE Trans. On*, vol. 28, no. 2, pp. 171–175, 1981.
- [94] O. Jardel *et al.*, “An Electrothermal Model for AlGaIn/GaN Power HEMTs Including Trapping Effects to Improve Large-Signal Simulation Results on High VSWR,” *IEEE Trans. Microw. Theory Tech.*, vol. 55, no. 12, pp. 2660–2669, Dec. 2007.
- [95] H. Reisinger, T. Grasser, W. Gustin, and C. Schlunder, “The statistical analysis of individual defects constituting NBTI and its implications for modeling DC-and AC-stress,” in *2010 IEEE International Reliability Physics Symposium*, pp. 7–15.
- [96] B. Lambert *et al.*, “Reliability data’s of 0.5  $\mu\text{m}$  AlGaIn/GaN on SiC technology qualification,” *Microelectron. Reliab.*, vol. 52, no.s 9–10, pp. 2200–2204, Sep. 2012.
- [97] M. Ohring, *Reliability and Failure of Electronic Materials and Devices*. Academic Press, 1988.
- [98] R. Trew, D. Green, and J. Shealy, “AlGaIn/GaN HFET reliability,” *IEEE Microw. Mag.*, vol. 10, no. 4, pp. 116–127, Jun. 2009.
- [99] L. John, *Handbook of RF and Microwave Power Amplifiers*. Cambridge University Press, 2012.
- [100] J. H. Leach and H. Morkoc, “Status of reliability of GaN-based heterojunction field effect transistors,” *Proc. IEEE*, vol. 98, no. 7, pp. 1127–1139, 2010.
- [101] M. Meneghini, A. Stocco, R. Silvestri, N. Ronchi, G. Meneghesso, and E. Zanoni, “Impact of hot electrons on the reliability of AlGaIn/GaN high electron mobility transistors,” in *2012 IEEE International Reliability Physics Symposium*, p. 2C–2.
- [102] J. Joh and J. A. Del Alamo, “RF power degradation of GaN high electron mobility transistors,” in *2010 IEEE International Electron. Devices Meeting*, pp. 20–22.
- [103] W. McGenn, M. J. Uren, J. Benedikt, and P. J. Tasker, “Development of an RF IV waveform based stress test procedure for use on GaN HFETs,” *Microelectron. Reliab.*, vol. 52, no. 12, pp. 2880–2883, Dec. 2012.
- [104] J. Verspecht, “Large-signal network analysis,” *Microw. Mag. IEEE*, vol. 6, no. 4, pp. 82–92, 2005.

- [105]J.-P. Teyssier and F. De Groote, “An embedded controller for the LSNA with pulsed measurement capabilities,” in *Proceedings IEEE 2007 Instrumentation and Measurement Technology Conference*, pp. 1–4.
- [106]F. De Groote, “Mesures de formes d’ondes temporelles en impulsions : application à la caractérisation de transistors micro-ondes de forte puissance,” Université de Limoges, 2007.
- [107]J. Faraj, “Développement et validation d’un banc de caractérisation de transistors de puissance en mode temporel impulsionnel,” Université de Limoges, 2010.
- [108]J. Verspecht, “Calibration of a Measurement System for High Frequency Nonlinear Devices,” Vrije Universiteit Brussel, 1995.
- [109]Keithley 4200 Semiconductor Characterization System Manual, <http://www.imperial.ac.uk/media/imperial-college/research-centres-and-groups/centre-for-bio-inspired-technology/7290999.PDF>.
- [110]Rohde & Schwarz ZVA40 VNA Datasheet, <http://www.testequipmenthq.com/datasheets/Rohde-Schwarz-ZVA40-Datasheet.pdf>.
- [111]M. Dammann *et al.*, “Reliability status of GaN transistors and MMICs in Europe,” in *2010 IEEE International Reliability Physics Symposium*, pp. 129–133.
- [112]J. Joh and J. A. del Alamo, “Mechanisms for electrical degradation of GaN high-electron mobility transistors,” in *International Electron Devices Meeting, 2006*, pp. 1–4.
- [113]A. M. Conway, M. Chen, P. Hashimoto, P. J. Willadsen, and M. Micovic, “Failure mechanisms in GaN HFETs under accelerated RF stress,” in *CS MANTECH Conference*, 2007.









## Trapping and Reliability Investigations in GaN-based HEMTs

**Abstract :** GaN-based high electron mobility transistors (HEMTs) are promising candidates for future microwave equipment, such as new solid state power amplifiers (SSPAs), thanks to their excellent performance. A first demonstration of GaN-MMIC transmitter has been developed and put on board the PROBA-V mission. But this technology still suffers from the trapping phenomena, principally due to lattice defects. Thus, the aim of this research is to investigate the trapping effects and the reliability aspects of the GH50 power transistors for C-band applications. A new trap investigation protocol to obtain a complete overview of trap behavior from DC to radio-frequency operation modes, based on combined pulsed I/V measurements, DC and RF drain current measurements, and low-frequency dispersion measurements, is proposed. Furthermore, a nonlinear electro-thermal AlGaIn/GaN model with a new additive thermal-trap model including the dynamic behavior of these trap states and their associated temperature variations is presented, in order to correctly predict the RF performance during real RF operating conditions. Finally, an advanced time-domain methodology is presented in order to investigate the device's reliability and to determine its safe operating area. This methodology is based on the continual monitoring of the RF waveforms and DC parameters under overdrive conditions in order to assess the degradation of the transistor characteristics in the RF power amplifier.

**Keywords:** Gallium nitride, HEMTs, large-signal network analyzer (LSNA), microwave measurement, low-frequency dispersion, trapping effects, modeling, reliability.

### Investigation des effets de pièges et des aspects de fiabilité des transistors à haute mobilité d'électrons en Nitrure de Gallium

**Résumé :** Les transistors à haute mobilité d'électrons (HEMTs) en nitrure de gallium (GaN) s'affirment comme les candidats prometteurs pour les futurs équipements à micro-ondes - tels que les amplificateurs de puissance à état solide (SSPA), grâce à leurs excellentes performances. Une première démonstration d'émetteur en technologie GaN-MMIC a été développée et embarquée dans la mission spatiale PROBA-V. Mais cette technologie souffre encore des effets de pièges par des défauts présents au sein de la structure. L'objectif de ce travail est donc l'étude d'effets de pièges et des aspects de fiabilité des transistors de puissance GH50 pour des applications en bande C. Un protocole d'investigation des phénomènes de pièges est présenté, qui permet l'étude des dynamiques des effets de pièges du mode de fonctionnement DC au mode de fonctionnement radiofréquence, basé sur la combinaison des mesures IV impulsionnelles, des mesures de transitoires du courant de drain avec des impulsions DC et RF et des mesures de paramètres [S] en basse fréquence. Un modèle de HEMT AlGaIn/GaN non-linéaire électrothermique est présenté, incluant un nouveau modèle thermique de pièges restituant le comportement dynamique de ces pièges et leurs variations en température afin de prédire correctement les performances en conditions réelles de fonctionnement RF. Enfin, une méthodologie temporelle pour l'évaluation de la fiabilité et de limites réelles d'utilisation de transistors dans l'amplificateur de puissance RF en régime d'overdrive (très forte compression), basée sur la mesure monitorée de Formes d'Onde Temporelles (FOT), est proposée.

**Mots clés :** Nitrure de Gallium, HEMTs, large signal network analyzer (LSNA), mesures micro-ondes, dispersion basse fréquence, effets de pièges, modélisation, fiabilité.